THÈSE DE DOCTORAT DE

L'UNIVERSITÉ PIERRE ET MARIE CURIE

ÉCOLE DOCTORALE:
ED388 - Chimie physique et chimie analytique de Paris Centre
Présentée par

M. Jun Tao

Pour obtenir le grade de

DOCTEUR de l'UNIVERSITÉ PIERRE ET MARIE CURIE

Spécialité: Chimie physique des surface

Sujet de la thèse :

Surface composition and corrosion behavior of an Al-Cu alloy

Soutenue le: 07 juin 2016
Devant le jury composé de :

M. Roland Oltra	Directeur de recherche au CNRS Université de Bourgogne Franche-Comté	Rapporteur
M. Dominique Thierry	Président de l'Institut de la Corrosion Institut de la Corrosion	Rapporteur
Mme. Eliane Sutter	Professeur Université Pierre et Marie Curie	Examinateur
M. Jean-Michel Lameille	Ingénieur-chercheur CEA	Examinateur
M. Philippe Marcus	Directeur de recherche au CNRS Chimie ParisTech	Directeur de thèse
Mme. Jolanta Światowska	Chargée de recherche au CNRS Chimie ParisTech	Encadrante

Table of content

Abstract

Al-Cu series alloys are the most widely used heat treatable alloys for the aircraft materials, machine parts, and structural materials mainly due to their high strength to weight ratio and good mechanical properties. However, the Cu-rich precipitations (Al_2Cu intermetallic particles present in these alloys as the most important strengthening phase), have negative effects on the corrosion performances of these alloys. In this thesis, Al-Cu model alloy was employed to investigate the influence of thermal aging treatments in ultra-high vacuum (UHV) on the chemical modifications of the alloy using surface analytical techniques (XPS, ToF-SIMS).

The *in situ* XPS characterization showed that the Al-Cu alloy was oxidized as a function of exposure to the low pressure (LP) of O_2 and temperatures from 300 to 400 °C via the mechanism - the preferential oxidation of Al in the alloy leading to a growth of aluminium oxide layer, and the enrichment/segregation of the intermetallic particles (Al_2Cu) at the oxide/substrate, as evidenced by ToF-SIMS analyses.

Then, in a next chapter, the Al-Cu alloy samples thermally treated in a dedicated setup (at 540 °C in vacuum (1.0×10^{-5} mbar) and aged at 300 °C in air) were exposed to the neutral (pH≈6.2) and the alkaline electrolyte (pH=11.5) containing Cl^- ions. After immersion the surface characterization indicated different corrosion mechanisms influenced by the thermal treatment and aging. In neutral electrolytes trenching on the polished sample *vs.* hollow pits on the aged sample were observed due to a thicker Al oxide covering on Cu-rich intermetallics after aging treatment. However, in alkaline electrolytes, the corrosion of the polished and aged samples showed the general dissolution of aluminium matrix, which resulted in a formation of protruded Cu-rich intermetallics. Then in the next stages after the general corrosion, the preferential dissolution of matrix surrounding Cu-rich intermetallics occurred. Furthermore, grain boundaries of the aged sample were etched because of the

distribution of Cu intermetallics at the grain boundaries, which was not observed on the corroded surface of the polished sample. Formation of mixed aluminium-copper oxide/hydroxide layers rich in Cu_2O, CuO and/or $CuCl_2$ deposits were found by XPS on the corroded surface.

The last part of the thesis presents the corrosion protection of the Al-Cu alloy by nanometer-thick (20 nm) Al_2O_3 ALD layer (atomic layer deposition). This study was performed in order to confirm whether significant improvement of the corrosion resistance of aluminium alloys can be observed without a prior removal of the intermetallic particles. The immersion of the alumina coated Al-Cu alloy in neutral electrolyte containing Cl^- ions showed good corrosion resistance while a number of pits were observed by SEM on the Al-Cu sample after immersion in the alkaline electrolyte although no chemical surface modifications were observed by XPS. It was indicated that the OH^- promoted the corrosion, by enlarging the cracks/pinholes and dissolving the ALD layer by decreasing its thickness and increasing its porosity.

Keywords: Al-Cu alloy; aging treatment; intermetallic particles; corrosion; ALD film; XPS; ToF-SIMS; SEM; AFM;

Chapter 1 State-of-the-art and objectives

In this chapter, a general state-of-the-art related to the aluminium and aluminium alloys is presented. The most important bibliographic data on the age hardening of Al-Cu alloys used for the strengthening of aluminium alloys are presented. The corrosion performance and the corrosion mechanisms of aluminium alloys and the role of Cu-rich precipitations (intermetallic particles) in corrosion of aluminium alloys are introduced. Finally, different ways of corrosion protection of aluminium alloys are summarized. Atomic Layer Deposition (ALD) technique as a new way of corrosion protection of aluminium alloys by thin and well defined layers used in this PhD work is described. Then, in the last part of this chapter, the objectives and the content of the thesis are listed.

1.1 Aluminium and aluminium alloys

Aluminium as the most abundant metal in the Earth making up about 8% by weight of the Earth's solid surface is widely used in many applications due to its low density, high strength stiffness to weight ratio, good formability, recycling potential and good corrosion resistance[1-6].

In 1807, Humphry Davy first used the word "Aluminum", and tried to produce aluminum. In 1886, Charles Martin Hall and Paul Héroult found the method (named Hall–Héroult process) for producing the aluminum. So far, this electrochemical process, reducing alumina to aluminium, is still the main method of industrial production of aluminum[7-11].

There are two principal classifications, namely casting alloys and wrought alloys, both of which are further subdivided into the categories heat-treatable and non-heat-treatable. Alloying elements, *e.g.* copper, magnesium, manganese, silicon and zinc are often added to the aluminium to obtain various properties, such as high strength, fatigue resistance, high electrical, thermal conductivity and recyclability, which are quite vital to the aerospace industry and important in other areas of transportation and structural materials[12-14]. On the basis of the predominant alloying metal, aluminium alloys have been divided into different series, designated AA 1xxx series to the AA 8xxx series (as seen in the Tab.1-1).

Copper has been the most common alloying element for the AA2xxx series alloys by increasing the strength and fatigue resistance[15], and a variety of alloys in which copper is the major addition were developed. The Al-Cu series alloys are the most widely used heat treatable alloys for the aircraft materials, machine parts, and structural materials owing to its high strength to weight ratio, high damage tolerance, good fatigue resistance, as well as cutting properties.

Tab.1-1 Types designation for Aluminium Alloys (AA)[16].

Series	Main alloying elements	Common Usage	Cu (wt.%)	Heat Treatable
1xxx	-	Aluminium foil, package	0.05-0.20	No
2xxx	Cu, Mg	Aircraft	3.8-4.9	Yes
3xxx	Mn	Beverage cans	0.05-0.20	No
4xxx	Si	As cladding alloy on brazing sheet	0.3	No
5xxx	Mg	Structural alloys	＜0.2	No
6xxx	Mg, Si	Structural alloys, general purpose	0.1-0.4	Yes
7xxx	Zn	High strength	1.2-2.0	Yes
8xxx	Li & other additive elements	Automotive	0.7-1.3	No

1.2 Thermal treatments of Al-Cu series alloys

The most important cast aluminum alloy is the Al-Cu system. Copper is usually added to aluminum alloys to provide substantial increase in strength and to promote the precipitation hardening. The distribution of copper in aluminium alloys varies from copper atoms dispersed in solid solution through the formation of clusters of copper atoms and then into a range of intermetallic particles (IMP). Fig.1-1 shows the Al-Cu phase diagram, on at.% scale (with the corresponding wt.% scale across the top). This diagram is the basis of the age-hardening for the Al-Cu alloys. The liquidus boundaries fall to a eutectic point at 33wt. % Cu and 548°C.

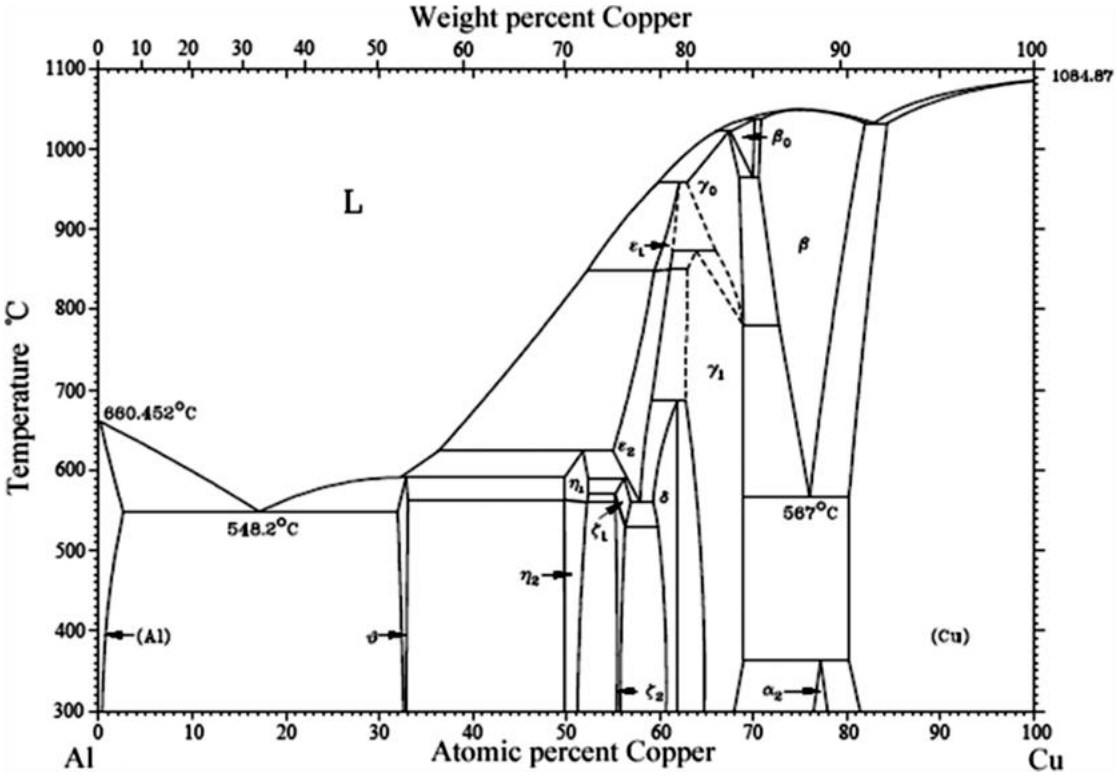

Fig.1-1 Phase diagram of the aluminium–copper system[17].

Age hardening or precipitation hardening is now one of the most widely used methods for the strengthening of aluminium alloys. Through this process the strength and hardness of aluminium alloys could be significantly enhanced by the formation of small (from micron to couple of microns) uniformly dispersed second-phase particles within the original phase matrix. The precipitation-hardening process for the Al-Cu series alloys involves three basic steps[18-20]: solution treatment, quenching, and aging (shown graphically in the Fig. 1-2).

During the 1st step, the alloys are heated to a high temperature (usually above the solvus line) that allows the alloying atoms (called the solute) to dissolve into the solution. This results in a homogeneous solid solution of one phase (α phase). Then in the 2nd step, quenching rapidly cools the solution and freezes the atoms in solution, indicating that the atoms of the alloying elements do not have time to diffuse out of the solution resulting in the formation of an unstable supersaturated solid solution (SSSS or α_{ss}). The 3rd step is the aging process where the solute particles diffuse out of solution and into clusters with a formation of finely dispersed precipitates, *i.e.* S

phase (Al_2CuMg) and θ phase (Al_2Cu) in the case of 2xxx series alloys, due to the low solid solubility of Cu in Al and the low stability of supersaturated α phase[21-26].

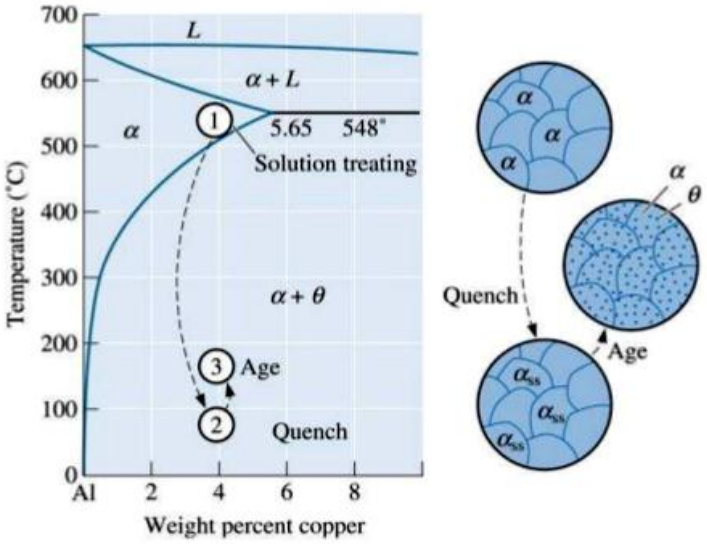

Fig.1-2 Three steps in the age-hardening heat treatment for the Al-Cu alloy[27].

As shown in the Fig. 1-3, the precipitate particles act as obstacles to dislocation movement and thereby strengthen the heat-treated Al-Cu alloys[28,29].

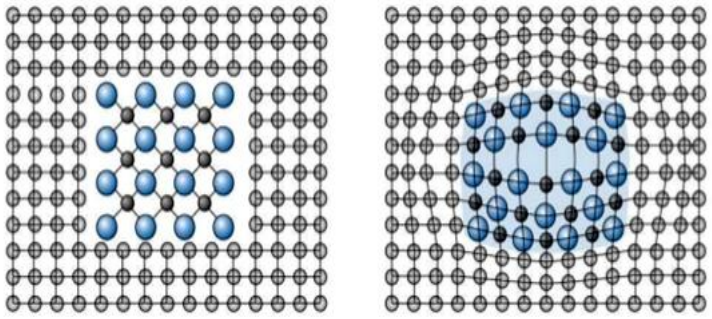

Fig.1-3 Schematic illustrations on diffusion out of solution and into clusters that distort and strengthen the material[30,31].

Precipitation usually starts from the formation of Guinier-Preston (GP) zones, which may be regarded as fully coherent metastable precipitates[32-36]. These GP zones are coherent in nature that is they have one to one lattice matching with the solvent crystal lattice. Subsequent evolution of the microstructure involves the replacement of the GP zones with more stable phases[37] as the following processes for Al-Cu Alloy

over many studies[38-42]: supersaturated solid solution (SSSS or α_{ss})→ GP zones (Discs)→ θ" (Discs)→ θ' (Plates)→ θ(Al_2Cu). Aaron *et al.*[43] found that the precipitates mainly grow via the grain boundaries (see Fig. 1-4). Rashkova *et al.*[44] found that the microstructure of the Al-Cu alloy consists of high-angle grain boundaries with incoherent Al_2Cu precipitates lying along the grain boundaries, either after aging at elevated temperatures, or at ambient temperature after longer time. In conventional bulk alloys, the Al_2Cu has one of the most common precipitate morphology[43] and the growing and coarsening mechanisms have been well established[45-48].

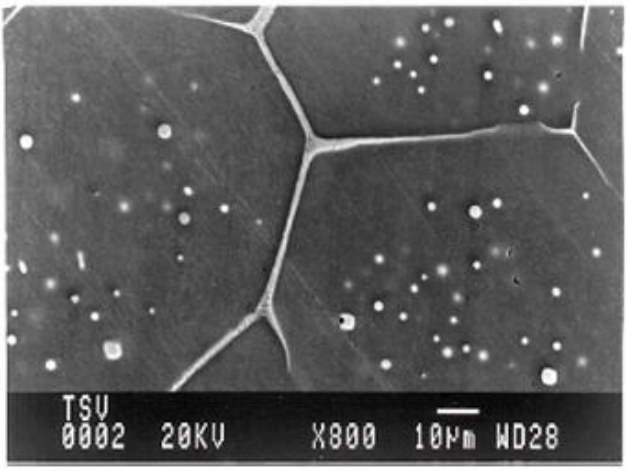

Fig.1-4 Scanning electron micrographs of the Al-3.35wt.%Cu alloy after aging treatment at 190 ºC for 24 hours, showing precipitates around grain boundaries[42].

In the early works, the hardening was generally attributed to the formation of the S' or S phase[49]. In the 1980s, Cuisiat *et al.*[50] suggested that a distinct precipitate termed S″ was responsible for the peak hardness. In the 1990s, using atom-probe field ion microscopy, Ringer *et al.*[51] proposed that the hardening peak was due to the formation of GP zones, which start to form near the end of the hardness plateau. However, using a combination of hardness tests, Wang *et al.*[52] reported different results that the S phase, a dense precipitation in an Al–Cu–Mg alloy that is quenched, stretched and aged to peak strength, is the main contributor to the peak hardness. Sharma *et al.*[53] raised that the microhardness increased with the aging time to a peak

value and then decreased with a prolonged aging time under all the heat treatment conditions. The peak hardness of the water quenched samples appeared at later stages of aging time, which can be attributed to the diffusion of copper atoms from the matrix to the interfacial region of the alloy resulting in reducing the copper concentration in the interparticle region required for precipitation.

As discussed above, it can be concluded that there are several studies on the influence of age hardening on the microstructure of aluminum alloys, and their mechanical properties. However, according to our knowledge there are only few studies, which show **the evolution of surface chemistry with age hardening process**. The studies related to surface chemistry of Al alloys will be presented in more details in the introduction part of chapter 3. The main object of this chapter is the chemical surface modifications of the Al-Cu model alloy studied by *in situ* X-ray Photoelectron Spectroscopy (XPS) and Time-of-flight Secondary Ion Mass Spectrometry (ToF-SIMS). The model Al-Cu alloy used in this work will be precisely defined in the experimental part.

1.3 Corrosion of Al-Cu alloys

1.3.1 Introduction to corrosion of aluminium alloys

The special characteristic of most corrosion processes is the oxidation and reduction, which occur at separate locations on the metallic surface. This is possible because metals are conductive, so the electrons can flow through the metal from the anodic to the cathodic regions. The presence of water and/or a liquid medium is necessary in order to transport ions to and from the metal, but a thin film of adsorbed moisture can be sufficient.

Aluminum and aluminium alloys are very reactive and can easily undergo passivation. The passivation of the aluminium and aluminium alloys can be explained by spontaneous formation of a protective amorphous native aluminum oxide film in air at room temperature[54-57], which impedes further reaction of aluminum with aggressive environments. The growth of oxide films on Al alloys at ambient

environment has been reported in details in a number of publications[58-61]. Oxide layers formed on aluminium in the ambient environment are generally considered to be non-crystalline, although short-range cubic ordered structure has been noted[62].The oxide film is naturally self-renewing and accidental abrasion or other mechanical damage of the surface film is rapidly self-repaired by re-oxidation.

In the presence of water, hydroxyl functionalities (such as AlOOH or $Al(OH)_3$) form at the alumina surface. Therefore, to obtain a hydroxyl-free alumina surface is very difficult in ambient conditions[63]. It is reported that water adsorbed at the surface of the air-formed film results in the formation and growth of an oxide/hydroxide surface film[64-67].

Although aluminium and aluminium alloys are highly resistant to most environments and to a great variety of chemical agents due to the inert and protective character of the thin aluminium oxide layer (usually between 50 and 100Å[68]); nevertheless, the protective oxide film may breakdown resulting in corrosion of the underlying matrix, when aluminium and its alloys are exposed to aqueous solutions. The corrosion resistance is highly determined by the pH of the environment[69-71].

The various equilibrium of the Al-H_2O system has been clarified by Pourbaix *et al.*[72] in a potential versus pH diagram (shown in the Fig. 1-5). It is revealed that aluminium corrodes in the range of4> pH>8 forming Al^{3+} ions at low pH values and AlO_2^- ions at high pH values[73]. Aluminium should show passivity (solubility constant $<10^{-32}$) forming $Al_2O_3 \cdot 3H_2O$ at near-neutral pH values and immunity at very negative potentials[74,75].

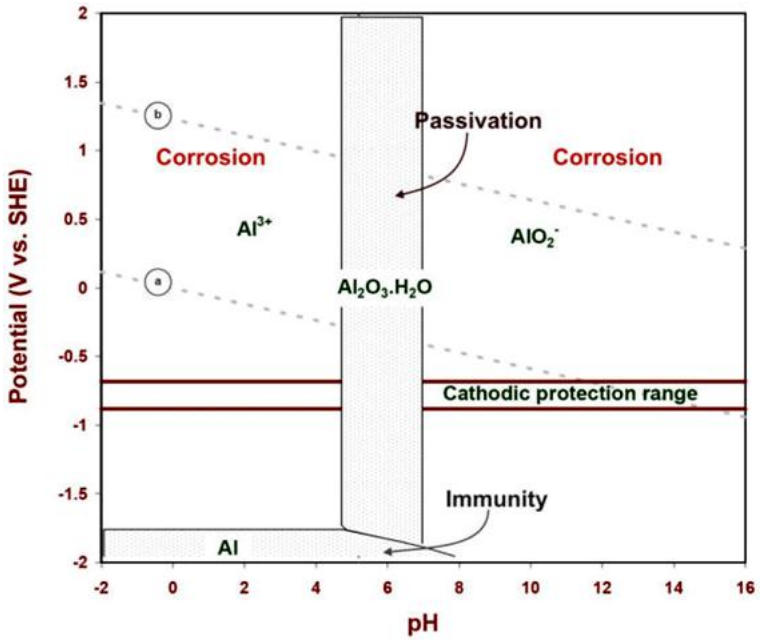

Fig.1-5 E-pH corrosion diagram (Pourbaix Diagram) for Al/H_2O system at 25 °C[76-78].

However, the introduction of copper into the aluminium alloys significantly influences the corrosion resistance of aluminium alloys. Copper is one of the noblest alloying elements used in aluminium alloys. Therefore, it generally behaves differently when comparing with the aluminium matrix (+0.24 V_{SCE} *vs.* -1.42 V_{SCE} in standard reduction potential). Copper-containing phases on the surface tend to be cathodically protected due to the cathodic reduction reaction[79]:

$$O_2 + 2H_2O + 4e^- \rightarrow 4OH^- \quad \text{Eq. 1-1}$$

$$O_2 + 4H^- + 4e^- \rightarrow 2H_2O \quad \text{Eq. 1-2}$$

$$2H^+ + 2e^- \rightarrow H_2\uparrow \quad \text{Eq. 1-3}$$

while the aluminium matrix has a net anodic reaction which provokes the anodic dissolution of aluminium matrix as follows:

$$Al \rightarrow Al^{3+} + 3e^- \quad \text{Eq. 1-4}$$

The presence of copper accelerates the rate of electrochemical reactions shown

above (Eq.1-1 to Eq. 1-4). Fig. 1-6 provides a summary of the effects of copper element on the corrosion potential (E_{corr} *vs.* 0.1 N calomel electrode) of aluminium alloys in a solution containing 53 g/L of sodium chloride (NaCl) and 3 g/L of hydrogen peroxide (H_2O_2)[80,81]. It was shown that the addition of copper to aluminium increases the electrode potential by approximately 37 mV per percent of copper, in which range Cu is completely in solid solution. Further increasing the copper content (from 4 to 7 wt.%), which forms a second phase, has limited effect on the electrode potential.

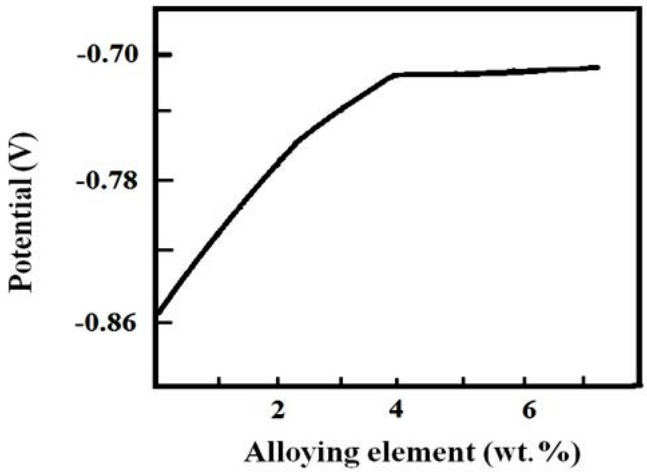

Fig.1-6 Effects of copper on corrosion potential of aluminium[80].

1.3.2 Corrosion behavior of aluminium alloys and influence of intermetallic particles

There are many different types of corrosion[82-84], such as uniform corrosion, galvanic corrosion, crevice corrosion, intergranular corrosion, pitting, stress corrosion cracking (SCC) and corrosion fatigue. Pitting and intergranular corrosion are the most common types of corrosion observed in the Al-Cu alloys[85]. It is widely known that the heterogeneous distribution of copper in Al-Cu series alloys is the predominant cause for susceptibility to pitting. Chlorides cause the most serious problems due to their presence in many environments such as seawater and salt on roads, and in the chemical industry. Pitting process can be divided into several steps[86,87,88,89]: 1) process leading to breakdown of passivity; 2) early stages of pit growth; 3) late stages of pit growth; 4) repassivation phenomena. In the stages of 2 and 3 (as shown in the Fig. 1-

7), aluminium oxidizes into aluminium ions at the bottom of the pits. A reduction of either water or hydrogen occurs in contact with the metal outside of the pit. With either reduction reaction the pH will increase outside of the pit to give an alkaline pH. The aluminium ions will form a film of aluminium chloride or aluminium oxychloride in the pit and stabilize it. After a while the aluminium chloride will hydrolyse into aluminium hydroxide. This leads to a decrease in the pH value to a more acidic environment, which increases the corrosion rate within the pit. Aluminium hydroxide precipitates at the rim of the pit and covers the opening, which eventually hinders exchange of ions and slows down the corrosion process[90-92].

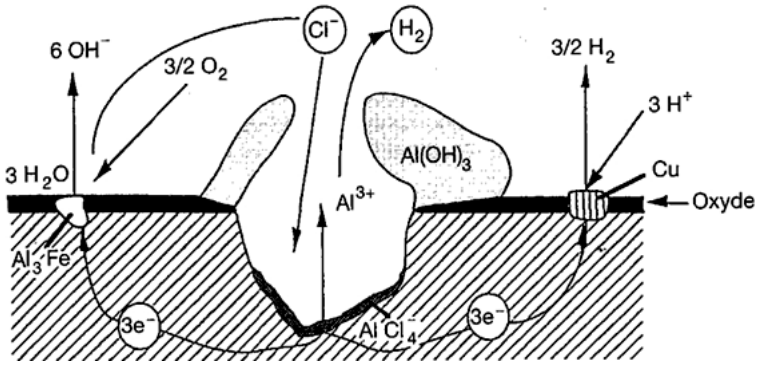

Fig. 1-7 Simple illustrations of mechanism of pitting corrosion of aluminium[93].

Intergranular corrosion consists of localized attack in which a path is corroded preferentially along the grain boundaries. The mechanism is electrochemical and it depends on the formation of local cells at the grain boundaries. The local cells are a result of second phase precipitates at the grain boundaries. During the formation of intermetallic second phase precipitates along the grain boundaries, an adjacent matrix zone is formed that has a different potential. For Al-Cu series alloys (such as AA2xxx series alloys), intergranular corrosion and pitting corrosion in the chloride-containing environments are encountered, owing to the heterogeneous microstructures and differences of chemical and electrochemical activities between aluminium and alloyed elements, *e.g.* copper and magnesium[94-97]. The precipitation of the θ phase around the grain boundary could lead to copper depletion in the neighborhood of the grain boundary[98]. The precipitate may be anodic to the matrix such as Al_8Mg_5, in which

case it corrodes preferentially; or it may be cathodic, such as Al_2Cu, in which case it does not corrode, but stimulates corrosion in the adjacent matrix zone. In either case, selective grain boundary corrosion occurs. The degree of susceptibility of an alloy to intergranular attack can vary depending on its microstructure, in particular, the amount, size, and distribution of second phases, which is a result of the metallurgical history and thermal treatment. Heat treatments that cause precipitation throughout the grain tend to diminish the intergranular attack. It is significant that in certain aged conditions, Al-Mg-Cu alloys may suffer intergranular corrosion, but not stress corrosion cracking, as a result of different precipitate distribution.

Pitting corrosion of Al-Cu alloys is mainly attributed to the IMPs[99]. Birbilis *et al.*[100,101] proposed that the electrochemical behavior of Cu-containing intermetallics in aluminium alloys can be either noble or active with respect to the aluminium matrix based upon the composition of the intermetallics. The introduction of copper or other elements into aluminium alloys can increase or decrease the corrosion potential compared with pure aluminium as indicated in the Tab1-2. Particles containing Al, Cu, Fe, and Mn (*e.g.* Al_2Cu, θ-phase) act as cathodes and promote matrix dissolution at their periphery[102-106] (as shown in the Fig. 1-8), while particles containing Al, Cu, and Mg (*e.g.* Al_2CuMg, S-phase) show anodic behavior and dissolve with preferential dealloying of Mg and Al[107-110]. In addition, copper tends to precipitate at grain boundaries, making the metal very susceptible also to stress corrosion cracking[111-113]. Due to high corrosion activity of these IMPs they have been widely studied as the active sites corrosion initiation[114-118]. The IMPs which have a size of few hundreds of nanometers participate in intergranular corrosion and lead to anodic dissolution of areas with lower copper concentration near the grain boundaries[119-121].

Trenching of the matrix surrounding intermetallic particles may be interpreted as a galvanic corrosion between the matrix and the particle. In addition, it could also be related to the etching under high pH conditions generated by cathodic reactions (oxygen and/or water reduction), reported by several publications revealing high pH (around 9.5) at the edge of cathodic intermetallic particles[122,123].

Tab. 1-2 Changing of the corrosion potential compared with pure aluminium after introduction of copper or other elements into aluminium alloys[124,125].

	Nature of phases	E_{corr} (mV *vs* ECS)
Cathodic particles	Cu	+100
	Si	-170
	Al_3Ni	-430
	Al_2Cu (θ-phase)	-440
	Al_3Fe	-470
	Al_6Mn	-760
Anodic particles	Al	-840
	Al_2CuMg(S-phase)	-910
	$MgZn_2$	-960
	Al_3Mg_2	-1150
	Mg_2Si	-1190
	Al_8Mg_5	-1240

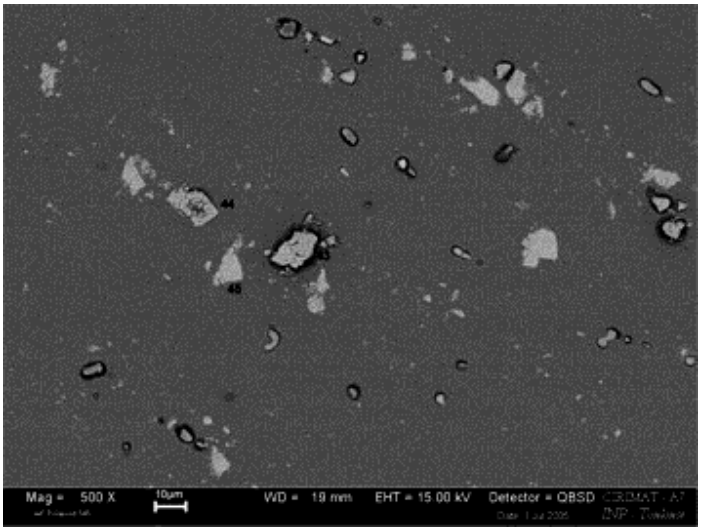

Fig.1-8 SEM images of corrosion surrounding the cathodic Al-Cu-Fe-Mn particles in the AA2024 alloy after immersion in 0.1 M NaCl solution[98].

The efficiency of copper containing intermetallics to act as cathodes also enable them to support copper plating reactions whereby soluble copper ions are reduced back to copper metal. Chen *et al.*[126] investigated the corrosion processes on the polished AA 2024 alloy, and found the deposition of Cu on the surface of cathodic

intermetallic particles. Blackwood *et al.*[127] studied the Cu deposition onto the AA 6063 alloy from $CuSO_4$ solutions with and without Cl^- ions, and revealed that the deposition of Cu onto the Cu metal was more favored than onto the Al metal. However, the presence of Cl^- ions leads to $CuCl^+$, which lowered the energy barrier for deposition of Cu onto Al metal.

Several publications have shown the role of cathodic Cu-containing intermetallics in controlling pit initiation and growth. Leblanc *et al.*[128] proposed that the Al-Cu-Fe-Mn phases are crucial for pit initiation in Cl-containing environments. Liao *et al.*[129] confirmed that the cathodic particles in the AA 2024 alloy performed as initiation sites of pitting and pit growth. However, the pits were shallow. The cluster of intermetallic particles would promote deeper pitting.

The cathodic intermetallic phases (*e.g.* the Al-Cu-Fe-Mn family) support high cathodic reaction rates under most solution condition. The ability of cathodic intermetallic phases to support high cathodic reaction rates results in pitting initiation near these particles. Muster e*t al.*[130] reported that in a corrosive environment, slow dissolution of the cathodic intermetallics was combined with the pitting on these particles themselves. Trenches were seen around the cathodic intermetallics, which are maybe owing to a galvanic corrosion between the particle and the matrix, or perhaps related to etching under the high pH conditions generated by cathodic reactions (oxygen and water reduction)[131].

In situ and a real-time monitoring ask for applying local probes techniques to demonstrate of the localized corrosion around the intermetallic phases[132]. Oltra *et al.*[133]investigated the local probing of the galvanic coupling between micrometer-sized aged Al_2Cu phases and the surrounding aluminum-based matrix of a specially heat-treated 2011 alloy using a microcapillary electrochemical cell, and confirmed the mass transport control of the oxygen reduction on the galvanic coupling of the particle with the surrounding matrix based on the local electrochemical behavior of an isolated particle after aging.

Particles containing Al, Cu, and Mg show anodic behavior and dissolve with preferential dissolution of Mg and Al (as seen in the Fig. 1-9). The S-phase is initially

anodic and then being transformed to a net cathode after the dealloying of magnesium and aluminium resulting in the enrichment in copper[134]. As shown in the Fig. 1-9, the intermetallic particle itself has been attacked, with preferential dealloying of magnesium and aluminium, owing to its anodic characteristic with respect to the matrix. Then, the cathodic properties of the copper-rich phase lead to dissolution and depletion of the matrix surrounding the original particle. Guillaumin *et al.*[135] reported what appeared to be on the matrix directly adjacent to the copper-rich intermetallic remnants. Buchheit *et al.*[136] also reported copper enrichment at the surface of aluminium alloys associated with anodic intermetallics.

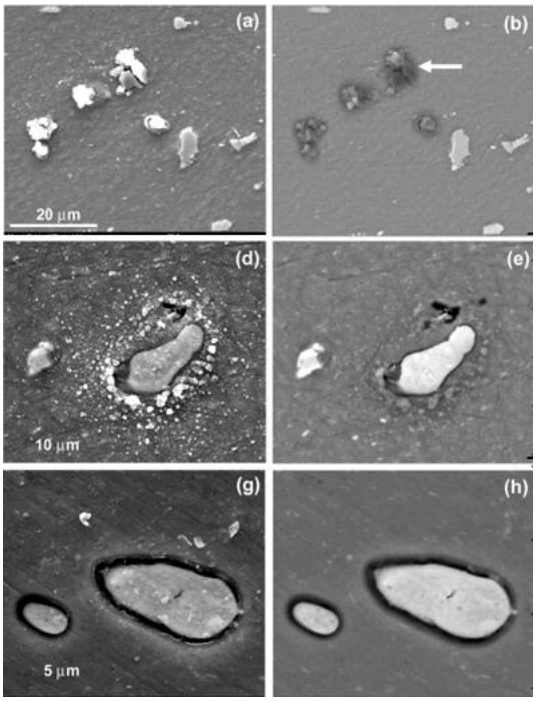

Fig.1-9 Secondary (left) and backscattered (right) electron images of corrosion around the anodic Al-Cu-Mg particles in the AA 2024 alloy after (a,b)2.5, (d,e) 5 and (g,h) 15 min exposure to 0.1 M NaCl[137].

There is a huge number of papers related to corrosion resistance and corrosion behavior of aluminium alloys and still a lot of discussion about the possible mechanisms of corrosion of these alloys as a function of type of intermetallic particles. Here in this PhD thesis, the studies are focused on the influence of one type of intermetallic particles (Al_2Cu) present in the Al-Cu model alloy. The aim of this

study was to work on a model Al-Cu alloy with a simplified chemical composition and to have more insight into the influence of the thermal treatments on the electrochemical/corrosion performances of this alloy. These results will be presented in details in chapter 4. The state-of-the-art focused on the corrosion performance and the surface physical-chemical properties studied by the surface sensitive techniques (principally by XPS and ToF-SIMS) on the alloy containing Al_2Cu intermetallic particles will be presented in details in chapter 4.

1.4 Corrosion protection of aluminium alloys

1.4.1 Generalities about corrosion protection of aluminium alloys

Aluminium is an active metal and its resistance to corrosion depends on the formation of the protective oxide film[138]. Since aluminium alloys have the anodic and cathodic sites in constant electrical contact, the only way to inhibit corrosion is to eliminate the contact with electrolyte and the cathodic reactant. The main methods to prevent such corrosion are by barrier coatings[139,140]. The barrier coatings are used to suppress the cathodic reaction by limiting the diffusion of the electrolyte, oxygen and water to the substrate. It also limits the transport of electrons to the metal interface.

There are different ways[141 - 144] to protect the aluminium and its alloys from corrosion as below:

- conversion coatings, such as the chromium chemical conversion (CCC) and the trivalent chromium process (TCP),
- anodization,
- organic coatings (*i.e.* electroconducting polymers, and polyaniline),
- coatings prepared by Atomic Layer Deposition technique.

1.4.2 Conversion coatings

To achieve the full protective properties on aluminum alloys, most organic coatings require the metal surface to be pre-treated. This provides a surface film, which becomes an integral part of the metal surface involving virtually no

dimensional changes. After the aluminium alloy surface pretreatment (degreasing and deoxidation) the conversion coatings can be deposited. Chromates conversion coatings, the most efficient and the most widely used coatings up to now, contain hexavalent chromium species(Cr^{6+}) [145 - 147] .Chromate coatings allow subsequent deposition of an organic coating (such as a primer and a top-coat). During the conversion process, Cr^{6+} is reduced to Cr^{3+}, with the exception of approximately 5–15% remaining as Cr^{6+} as an integral part of the layer. A chromate conversion coating layer deposited on the alloy substrate can provide an active barrier layer reducing the rate of the cathodic oxygen reaction[148]. Nevertheless, the use of hexavalent chromium species is highly restricted because of the carcinogenic effect of chromate (Cr^{6+}), thus a lot of research has been carried out to develop new chromate-free coatings in order to meet strict European REACH[1] and RoHS[2] environmental regulations.

Recently, a new conversion coating system based on trivalent chromium species (Cr^{3+}), known as the Trivalent Chromium Processes (TCP), has been developed by the NAVAIR (the U.S. Naval Air Systems Command)[149,150]. It should be emphasized that trivalent chrome compounds by definition are not chromates, which specifically describe chromium in the +6 oxidation state. The new technology is based on low levels of Cr^{3+}. The process solution and the coating it produces are totally free of Cr^{6+}. It provides a total replacement for traditional hexavalent chromium conversion coatings[151]. The functional advantages of trivalent chromium are less energy, higher cathode efficiency and better throwing power, which mean better production rates. The TCP bath, typically containing hexafluorozirconate, chromium sulfate and pH-adjusters, allows a deposition of a coating providing good corrosion properties. The structure of the TCP layer is composed of an hydrated zirconium-rich outer layer that also contains chromium species and an inner, aluminum-rich layer[152-154]. Suib *et al.*[155] reported that in TCP-coated AA2024T3 samples, no hexavalent chromium was detected even after exposure of coated samples to ASTM G 85 SO_2 salt spray for up to 744 hours. Similarly, none was detected after exposure to indoor or outdoor

[1]REACH (Regulation concerning the Registration, Evaluation, Authorisation and Restriction of Chemicals)

[2]RoHS (Restriction of Hazardous Materials)

environments. It was also confirmed that no hexavalent chromium is produced in the TCP treatment solution or in treated parts under production conditions. Lyer *et al*.[156] also reported similar results that Cr^{6+} species were not detected in TCP solutions.

In recent time, it has been showed that long immersion time in a pickling bath is detrimental for the TCP deposition because of the formation of holes and high surface roughness[157]. However, there is still a lack of understanding of the deposition mechanism of the TCP layer[158,159], and the pretreatments conditions allowing for good corrosion efficiency of the TCP coatings[160].

1.4.3 Anodizing

From a historical perspective, the first protection applied on aluminium was anodization (architectural profiles) around 1930[161]. Aluminium anodizing is an electrochemical process in which a protective or decorative oxide (anodic) layer is electrochemically built on the surface of the metal[162,163]. Although aluminum alloys naturally form aluminum oxide on their surface, this film is very thin. Anodizing provides much thicker oxide layers. The anodic coating consists of hydrated aluminium oxide and is considered resistant to corrosion and abrasion. The thickness of the anodized layer is dependent on the applied current, the voltage and the time of polarization[164]. The voltage required by various solutions may range from 1 to 300 V DC, mostly falling in the range of 15 to 21 V, and the anodizing current varies with the area of aluminium being anodized, typically ranging from 30 to 300 A/m². The film thickness can range from under 0.5 μm for decoration up to 150 μm for architectural applications[165]. The properties of the oxide layer are affected by the nature and composition of the electrolyte and by the aluminium substrate[166, 167]. Anodizing provides surface corrosion protection along with an excellent substrate for decorative finishes.

Generally, the production lines perform a multiple-step process that includes (as shown in the Fig. 1-10):

- cleaning – to remove fabrication oils and buffing compounds,
- pretreatment –to improve the appearance of a surface prior to the anodizing

step,

- anodizing – produces the actual coating. Acting as the positive electrode, a direct current is passed through the item to be anodized while submerged in a bath of water and acid (sulfuric, chromic, phosphoric) used as the electrolyte,
- sealing – the pores on the surface of the finished pieces need to be closed.

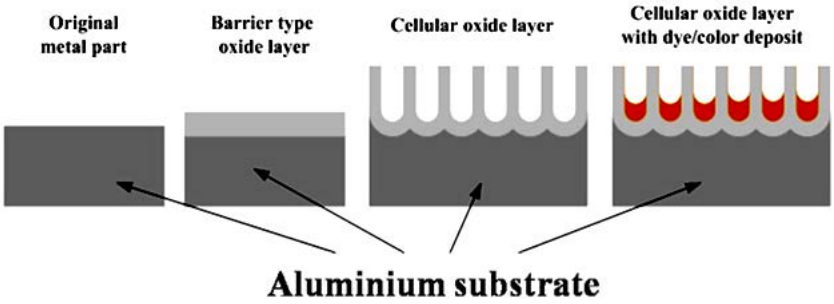

Fig. 1-10 Simplified diagrams of the anodizing process of aluminium or aluminium alloy substrates[168].

O'Sullivan *et al.*[169] studied quantitatively the morphology of porous anodic oxide films formed on aluminium in phosphoric acid electrolytes by electron microscopy, and found that at constant current density, relatively non-aggressive electrolytes give thicker barrier layers, larger cells and larger pores next to the barrier layer than aggressive media, although subsequent pore widening at the outer surface of the film by simple chemical dissolution is more severe in aggressive electrolyte.

Lee *et al.*[170]reported a novel approach termed "pulse anodization" that combines the advantages of the mild and hard anodization processes on the aluminium substrate using under a regulated cell voltage of 25 V by using 0.3 M H_2SO_4. By designing the pulse sequences it is possible to control both the composition and pore structure of the anodic aluminium oxide films while maintaining high throughput. It was found that the effective electric field strength has profound implications on the anodic alumina, determining not only its chemical stability but also its mechanical properties.

Although anodizing is generally a good technique, it has several disadvantages. Anodized aluminum has much lower thermal conductivity than regular aluminium,

making it a bad material for some applications calling for good thermal conductivity, such as the aluminium cookware. In addition, the color selection is greatly limited on products because of the chemicals used in the anodizing process. Furthermore, anodized specimens exhibit worse mechanical properties, *e.g.* the reduced fatigue life and decreased modulus of elasticity compared to the aluminum alloy, which can be attributed to the porosity and the crack sites initiated at the oxide layer[171,172].

1.4.4 Organic coatings

Organic coatings provide protection either by the action of a barrier from the layer or from active corrosion inhibition provided by pigments in the coating. Liquid coatings were introduced in the 1950's. Eventually, powder coating was invented, which took aluminium coating to a new level[173,174].The most common organic coatings are polyesters, polyurethane, polyvinyl chloride (PVC), and polyvinylidene fluoride (PVDF)[175].

Pirhady *et al*.[176] have developed silica-based organic-inorganic hybrid nanocomposite films by sol-gel method for corrosion protection of the AA2024 alloy. The sol-gel films were synthesized from 3-glycidoxypropyltrimethoxysilane (GPTMS) and tetraethylorthosilicate (TEOS) precursors. They have utilized the potentiodynamic scanning and salt spray tests to study the corrosion protection properties of the films. Their results indicate that the hybrid films provided exceptional barrier and corrosion protection in comparison with untreated aluminium alloy substrate.

The corrosion resistance strongly depends on the thickness of the applied coating. However, thicker organic coatings usually have bad adhesion to the substrate, leading to the detachment of the coating. Gonzalez *et al*.[177] identified that at sufficiently long exposure times, swelling through the coating may eventually reach an irreversible stage where detachment of the coating occurs.

1.4.5 Coatings prepared by Atomic Layer Deposition

ALD (Atomic Layer Deposition) treatment has recently been described as a

promising technique for the surface treatment of the Al-Cu series alloys, and already shown its versatility in industrial applications[178-181]. ALD is a thin film deposition technique in which a film is grown on a substrate by exposing its surface to alternate gaseous species (typically referred to as precursors)[182,183]. These precursors react with the surface of a material one at a time in a sequential, self-limiting, manner. Through the repeated exposure to separate precursors, a thin film is slowly deposited. The cyclical growth process of ALD film for deposition of a binary compound can be represented schematically in four steps (as shown in the Fig. 1-11)[184,185]:

1) exposure of the substrate to the first precursor,
2) purging (with an inert gas) or evacuation of the chamber,
3) exposure of the substrate to the second precursor,
4) purging (with an inert gas) or evacuation of the chamber.

The cycle (steps 1 to 4) is repeated as many times as needed to obtain a specific film thickness.

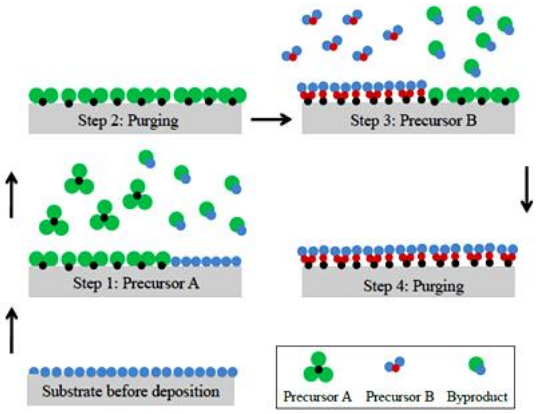

Fig. 1-11 Schematic representation of an ALD cycle, from references[186].

ALD provides coatings and material features which either cannot be achieved cost–efficiently with existing techniques, or they cannot be achieved at all. ALD, as a thin film coating method, offers:

1) precise control of the film thickness, at true nanometer scale,
2) pinhole–free films for, *e.g.*, superior barriers and surface passivation,
3) conformal coating of batches, large–area substrates and complex 3D objects, including porous bulk materials, as well as powders,

4) engineered and new functional materials and structures, such as nanolaminates,
5) a highly repeatable and scalable process.

The ALD of Al_2O_3 has developed as a model ALD system. An earlier extensive review by Puurunen[187] has discussed the details of Al_2O_3 ALD. Al_2O_3 ALD has high dielectric properties, uniform good adhesion to many surfaces, amorphous structure at chosen deposition temperature, good thermal stability[188]. Consequently, this section will only mention the highlights of Al_2O_3 ALD. Al_2O_3 ALD is usually deposited using trimethyl aluminum (TMA) and H_2O as aluminium and oxygen precursors, respectively.

More recent works[189-192] in the semiconductor industry presented the application of TMA and ozone for Al_2O_3 ALD. Here, we will concentrate on Al_2O_3 ALD using TMA and H_2O. The surface chemistry during Al_2O_3 ALD can be described as:

$$AlOH^* + Al(CH_3)_3 \rightarrow AlOAl(CH_3)_2^* + CH_4 \qquad \text{Eq. 1-5}$$

$$AlCH_3^* + H_2O \rightarrow AlOH^* + CH_4 \qquad \text{Eq. 1-6}$$

where the asterisks denote the surface species. The Al_2O_3 ALD growth occurs during alternating exposures to TMA and H_2O. Al_2O_3 ALD is a model system because the surface reactions are very efficient and self-limiting.

ALD alumina for corrosion protection has already been studied on many kinds of materials[193-197,], principally in the group of Physical Chemistry of Surfaces at IRCP, Chimie ParisTech[198-207]. Several papers[208-210] have reported that high quality ALD films with a uniform in-depth stoichiometry on the metals and alloys can efficiently decrease the corrosion of alloys, and thicker ALD films can provide better corrosion resistance because of its lower porosity.

The former studies performed on the efficiency of the ALD alumina layer deposited on Al 2024-T3 showed a poor coating adhesion[211]. However, the neutral salt spray (NSS) results show a clear influence of the coating thickness (5 to 70 nm alumina ALD layer on aluminum Al 2024-T3) and the deposition temperature on the

corrosion resistance[212]. A decreased coating porosity was also observed for increased coating thickness.

As before mentioned, the uncoated aluminium alloys with the IMPs, which can be either cathodes (particles containing Al, Cu, Fe, and Mn), or anodes (particles containing Al, Cu, and Mg) with respect to the surrounding aluminium matrix, have a weak corrosion resistance. So far, according to our knowledge, not many works have been published to investigate the protection of aluminium alloys by thin ALD layers. In this PhD thesis, thin alumina ALD coatings (20 nm) were deposited on the model Al-Cu alloy in order to investigate the corrosion behavior of the coated system in neutral and alkaline chloride solutions. The aim of this work was to study the mechanism of the corrosion protection of the alumina ALD layer/Al-Cu alloy and the influence of the intermetallic Cu-containing particles present in the coated system. The idea was also to look more precisely at the role of the well-controlled alumina layer (ALD layer), which can mimic a passive film, on the corrosion performances of the oxide layer/aluminium alloy substrate system. This study is the first approach into understanding the role of the oxide layer usually present on the aluminium alloys. As widely known, usually the oxide layers are removed from the surface of the aluminium alloys along with a partial removal of intermetallic particles in the pretreatment processes before anodization or conversion coating deposition stages. These studies with a more precise description of the state-of-the art related to the ALD layer applied for corrosion protection of metals and alloys will be presented in chapter 5 of this PhD thesis.

1.5 Objectives of this thesis

In this thesis, an Al-4.87wt.% Cu (Al-2.11at.% Cu) model alloy (which definition will be presented in more details in the experimental part) was employed to investigate:

1) The influence of thermal treatments(aging) of the Al-Cu alloy on the surface chemical modifications related to the oxide formation and formation and distribution of the intermetallic particles by *in situ* X-ray Photoelectron Spectroscopy (XPS) and by *ex situ* ion Time-of-Flight Secondary Ion Mass Spectrometry (ToF-SIMS) depth profiling and imaging;
2) The influence of thermal treatments (aging) of Al-Cu alloy and resulting chemical surface modifications on the corrosion performances by exposure to the neutral and alkaline electrolytes containing chloride ions;
3) The corrosion protection efficiency of the Al-Cu alloy by thin alumina layer deposited by atomic layer deposition (ALD) and the effect of well-defined aluminium oxide layers on the corrosion resistance of the Al-Cu alloy with the presence of Cu-rich intermetallic particles.

Our approach aims at elucidating the mechanisms of corrosion and corrosion protection as a function of the surface state of Al-Cu alloy modified either by thermal treatments or deposition of the ALD alumina layer, using principally surface analytical techniques XPS, ToF-SIMS and AFM.

1.6 Contents of the thesis

This thesis is composed of six chapters as follows: **chapter 1** presenting the bibliographic chapter presenting the state-of-the-art related to the corrosion and corrosion protection of aluminium alloys; **chapter 2** introducing the experimental methods including the surface sensitive techniques used along this research, and then three chapters of results (chapter 3, 4 and 5) and the last concluding **chapter 6,** containing also the research perspectives.

Chapter 3 investigates the influence of thermal aging treatments (at elevated temperatures and low pressure (LP) of O_2) on the chemical modifications of the model Al-Cu alloy such as the oxide growth, the modifications at the oxide/substrate interface and the evolution of the Al-Cu intermetallic particles. These studies were performed using a model Al-4.87wt.% Cu alloy which was polished, sputtered and thermally treated at LP of O_2 (around 1.0×10^{-7} mbar) at temperatures ranging from 300 °C to 400 °C. *In situ* X-ray Photoelectron Spectroscopy (XPS) was employed to investigate the chemical modifications of the model Al-Cu alloy starting from polished surface, then ion-sputtered surface in the UHV preparation chamber and then after each step of thermal treatment. Time-of-Flight Secondary Ion Mass Spectrometry (ToF-SIMS) depth profiling and imaging were employed to investigate surface, interface and bulk modifications of the Al-Cu model alloy induced by thermal treatments. The ToF-SIMS characterization was performed after the final stage of thermal treatments.

Chapter 4 presents the comparison of the corrosion performance of the polished Al-Cu sample and the thermally aged Al-Cu alloy. The polished, model Al-4.87wt.% Cu alloy was annealed and aged at high temperatures at atmospheric pressure (details are presented in the experimental part) in order to form Al_2Cu intermetallic particles. The polished and polished-aged samples were then exposed to the neutral (pH=6.2) and alkaline (pH=11.5) electrolytes to investigate their corrosion performances and to

study the influence of the well-formed intermetallic particles. Scanning Electron Microscopy (SEM) was used to observe the modifications of micro morphology of the samples after aging treatments and corrosion tests in chloride solutions. XPS and ToF-SIMS were employed to investigate chemical modifications of the polished and the aged Al-Cu alloys before and after immersion in neutral and alkaline electrolytes.

Chapter 5 explores thoroughly the corrosion protection of the Al-Cu alloy coated by a thin nanometric alumina ALD (atomic layer deposition) layer. The corrosion efficiency of the ALD was investigated by immersion in a neutral solution and an alkaline solution of chlorides. The SEM was combined with atomic-force microscopy (AFM) for a surface morphological characterization and with XPS and ToF-SIMS for the surface and bulk chemical characterizations.

Each chapter presenting results (chapters 3, 4 and 5) is structured as a scientific paper and contains the introduction part focused on the state-of-the art tightly related to the topic of the chapter, experimental part, results and discussion and conclusions.

References

[1] P.G. Sheasby and R. Pinner, *The Surface Treatment and Finishing of Aluminum and Its Alloys, 6th Edition*, ASM International, Materials Park, 2001

[2] W.S. Miller, L. Zhuang, J. Bottema, A.J. Wittebrood, *Mater. Sci. Eng.: A*, 280, 37–49 (2000)

[3] R. Molina, P. Amalberto, M. Rosso, *Metall. Sci. Tech.*, 29, 5-13 (2011)

[4] J. R. Galvele and S. M. De Micheli, *Corros. Sci.*, 10, 795 (1970)

[5] I. L. Muller and J. R. Galvele, *Corros. Sci.*, 17, 179 (1977)

[6] G.O. Ilevbare, J.R. Scully, Yuan, R.G. Kelly, *Electrochem. Soc. Meet.*, San Diego CA, May, 1998

[7] Ph. Mandin, R. Wüthrich, H. Roustan, *ECS Trans.*, 26, 1-10 (2009)

[8] *Aluminum,*.Los Alamos National Laboratory, 2013

[9] W.B. Frank, *Aluminum*. Ullmann's Encyclopedia of Industrial Chemistry. Wiley VCH, 2009

[10] *Production of Aluminum: The Hall-Héroult Process*. National Historic Chemical Landmarks. American Chemical Society, Ohio, 2014

[11] I.J. Polmear, *Light Alloys: Metallurgy of the Light Metals (3rd edition)*. Butterworth-Heinemann, 1995

[12] A. Lipski, S. Mrozinski, *Acta Mechanica et Automatica*, 6, 62-66 (2012)

[13] L. Quan, S. Gao, B. Muddle, ARC centre of excellence, Monash University, Melbourne, 2009

[14] *Alloy 2024 sheet and plate*, Alcoa Mill Products., Bettendorf, SPD-10-036

[15] I.J. Polmear, *Mater. Forum.*, 28, 1-14 (2004)

[16] T.H. Muster, A.E. Hughes, and G.E. Thompson, *Copper Distributions in Aluminium Alloys*, Nova Science Publishers Inc., New York, 2009

[17] J.R. Davis, *Aluminum and Aluminum Alloys*, ASM International, 1993

[18] T.B. Massalski, *Bull. Alloy Phase Diagr.*, 1, 27-33 (1980)

[19] S.P. Ringer, K. Hono, I.J. Polmear, T. Sakurai, *Appl. Surf. Sci.*, 94–95, 253–260 (1996)

[20] I.J. Polmear, *Mater. Forum.*, 28, 3-4 (2004)

[21] S.P. Ringer, T. Sakurai, I.J. Polmear, *Acta Mater.*, 45, 3731–3744 (1997)

[22] K. Raviprasad, S. Moutsos, *Mater. Forum.*, 28, 412–417 (2004)

[23] R.K.W. Marceau, G. Sha, R. Ferragut, A. Dupasquier, S.P. Ringer, *Acta Mater.*, 58, 4923–4939 (2010)

[24] W.R.Osório, J. E. Spinelli, C.M.A. Freire, et al, *J. Alloys Compd.*, 443, 1-2 (2007)

[25] E.L. Rooy, *Metals Handbook*, ASM International, Materials Park, Ohio, 743-770 (1988)

[26] T. Suter and R.C. Alkire, *J. Electrochem. Soc.*,148, B36 (2001)

[27] B. Lu, K. Chen, W.J. Meng, A.K. and R. Jin, *J. Micro Nano-Manuf.*, 3, 03-10 (2013)

[28] S.C. Wang, M.J. Starink and N. Gao, *Scripta Mater.*, 54, 287–291 (2006)

[29] S.P. Ringer, K. Hono, T. Sakurai, I.J. Polmear, *Scripta Mater.*, 36, (517–521) 1997

[30] O. Schneider, G.O. Ilevbare, and J.R. Scully, *J. Electrochem. Soc.*, 151, B465 (2004)

[31] R.P. Wei, and M. Gao, *Metall. Mater. Trans. A*, 29A, 1153 (1998)

[32] A. Guinier, *J. Physique Rad.*, 8, 124 (1942)

[33] C.B. Walker, A. Guinier, *Acta Met*., 1, 568 (1953)

[34] K. Toman, *Acta Crystallogr.*, 13, 60 (1960)

[35] D. Dew-Hughes, W.D. Robertson, *Acta Metall.*, 8, 156–167 (1960)

[36] M. Voncina, A. Smolej, J. Medved, P.Mrvar, R. Barbič, *Mater. Geoenvironment*, 57, 295-304 (2010)

[37] M.J. Starink, A.M. Zahra, *J. Mater. Sci. Lett.*, 16, 1613-1615 (1997)

[38] E.D. Boyes and F.L. Gai, *Proc. EMAG 75*, Academic Press, NY, 267 (1976)

[39] T. Abe, K. Miyazaki, and K. Hirano, *Acta Metall.*, 30, 57–366 (1982)

[40] M. Wada, H. Kita, and T. Mori, *Acta Metall.*, 33, 1631–1635 (1985)

[41] K. Hono, T. Satoh, and K. Hirano, *Philos. Mag.*, 53A, 495–504 (1986)

[42] R.J. Rioja and D.E. Laughlin, *Metall. Trans.*, 8A, 1257–1261 (1977)

[43] H.B. Aaron, H.I. Aaronson, *Acta Metall.*, 16, 789–798 (1968)

[44] B. Rashkova, M. Faller, R. Pippan, G. Dehm, *J. Alloys Compd.*, 600, 43–50 (2014)

[45] J.W. Martin, R.D. Doherty, *Stability of Microstructure in Metallic Systems*, Cambridge University Press, 1976

[46] D.A. Porter, K.E. Easterling, *Phase Transformations in metals and alloys*, Van Nostrand Reinhold (UK) Co. Ltd., 1983

[47] L.C. Brown, *Acta Metall.*, 33, 1391–1398 (1985)

[48] L. Bourgeois, Ch. Dwyer, M. Weyland, J.F. Nie, B. Muddle, *Acta Matter.*, 59, 7043–7050 (2011)

[49] J.M. Silcock, *J. Inst. Met.*, 89, 203 (1960–1961)

[50] F. Cuisiat, P. Duval, R. Graf, *Scripta Metall.*, 18, 1051 (1984)

[51] S.P. Ringer, T. Sakurai, I.J. Polmear, *Acta Mater*, 45, 3731 (1997)

[52] S.C. Wang, M.J. Starink, N. Gao, *Scripta Mater.*, 54, 287–291 (2006)

[53] A. Sharma, S. Das, *Mater. Design*, 30, 3900–3903 (2009)

[54] N. Cabrera and N.F. Mott, *Rep. Prog. Phys.*, 12, 163 (1948)

[55] M. Schmid, G. Leonardelli, R. Tscheliessnig, A. Biedermann, P. Varga, *Surf. Sci.*, 478, L355–L362 (2001)

[56] P.C. Snijders, L.P.H. Jeurgens, W.G. Sloof, *Surf. Sci.*, 496, 97–109 (2002)

[57] F.P. Fehlner and N.F. Mott, *Oxid. Met.*, 2, 59 (1970)

[58] J. Evertsson, F. Bertram, F. Zhang, et al, *Appl. Surf. Sci.*, 349, 826–832 (2015)

[59] I. Popova, Z. Zhukov, J.T. Yates, *J. Appl. Phys.*, 87, 8143 (2000)

[60] Z. Zhukov, I. Popova, J.T. Yates, *J. Vac. Sci. Technol. A*, 17, 1727 (1999)

[61] D.R. Jennison, C. Verdozzi, P.A. Schultz, M.P. Sears, *Phys. Rev. B*, 59, R15605 (1999)

[62] K. Wefers, C. Misra, *Alcoa Technical Paper*, 19, 1987

[63] J.B. Peri, *J. Phys. Chem.,* 69, 211 (1965)

[64] M. Texter, M. Amstutz, *Anal. Chim. Acta.*, 15, 297 (1994)

[65] M.R. Alexander, G.E. Thompson, G. Beamson, *Surf. Interf. Anal.*, 29, 468 (2000)

[66] M.R. Alexander, G.E. Thompson, G. Beamson, *Aluminium Surface Scienceand Technology*, ATBMetallurgie, Brussels, 133–138 (2000)

[67] M.R. Alexander, G.E. Thompson, X. Zhou, G. Beamson and N. Fairley, *Surf. Interf. Anal.*, 34, 485–489 (2002)

[68] L.P.H. Jeurgens, W.G. Sloof, F.D. Tichelaar, E.J. Mittemeijer, *Surf. Sci.*, 506, 313–332 (2002)

[69] J.W. Diggle, T.C. Downie, C. Goulding, *Electrochim. Acta,* 15, 1079 (1970)

[70] W.A. Badawy, M.S. El-Basiouny, M.M. Ibrahim, *J. Technol.*, 24, (1986)

[71] F.M. Al-Kharafi, W.A. Badawy, *J. Chem. Technol*. 3, 212 (1996)

[72] E.H. Hollingsworth, H.Y. Hunsicker, *Corrosion of aluminum and aluminum alloys*, ASM Handbook, 1987

[73]C.M.A. Brett, I.A.R. Gomes, J.P.S. Martins, *Corros. Sci.*, 369,15 (1994)

[74] W.M. Carroll, C.B. Breslin, *Corros. J.,* 26, 255 (1991)

[75] P.L.Cabot, F.A. Centellas, J.A. Garrido, et al., *Electrochim. Acta*, 36, 179 (1991)

[76] E. McCafferty, *Introduction to Corrosion Science*, Springer, New York, 2009

[77] W.G. Cook, R.P. Olive, *Corros. Sci.*, 58, 291-298 (2012)

[78] M.Sc. Ahmed Younis, *Protection of Aluminum Alloy (AA7075) from Corrosion by Sol-Gel Technique*, Technischen Universität Chemnitz, 30.08. 2011

[79] K.S. Rao and K.P. Rao, *Trans. Indn. Ins.Met.*, 57, 593-610 (2004)

[80] J.R. Davis, *Corrosion of aluminium and aluminium alloys*, ASM international, Novelty, USA, 1999

[81] H. Böhni and H.H. Uhlig, *J. Electrochem. Soc.*, 116, 906-910 (1969)

[82] E. Kunze, *Aluminium*, 52, 296-301 (1976)

[83] T. Singe, *Aluminium*, 187-189 (1981)

[84] J.P. Moran, et al., *Corros.*, 43, 374-382 (1987)

[85] C. Vargel, *The behaviour of aluminium and its alloys* , Dunod, 1979

[86] T. Suter, R.C. Alkire, *J. Electrochem. Soc.*, 148, B36 (2001)

[87] H.M. Obispo, L.E. Murr, R.M. Arrowood, et al, *J. Mater. Sci.*, 35, 3479 (2000)

[88] P.A. Schweitzer, *Metallic materials*, Marcel Dekker, INC., Pennsylvania, USA, 2003

[89] P. Marcus, *Corrosion mechanisma in Theory and Practice, third edition*, CRC Press, 2011

[90] Z. Szklarska-Smialowska, *Corros. Sci.*, 41, 1743-1767 (1998)

[91] G.S. Frankel, *J. Electrochem. Soc.*, 145, 2186-2197 (1998)

[92] R. Ambat, A.J. Davenport, G.M. Scamans, A. Afseth, *Corros.Sci.*, 48, 3455-3471 (2006)

[93] C. Vargel, *Corrosion of Aluminium*, Elsevier, 2004

[94] I.T.E. Fonseca, N. Lima, J.A. Rodrigues, et al, *Electrochem.Commun.*, 4, 353–357 (2002)

[95] K. Kowal, J. DeLuccia, J.Y. Josefowicz, et al, *J.Electrochem.Soc.,* 143, 2471 (1996)

[96] R.M. Rynders, C.H. Paik, R. Lee, C. Alkire, *J. Electrochem. Soc*., 141, 1439 (1994)

[97] P. Leblanc and G.S. Frankel, *J. Electrochem. Soc.*, 149, B239-B247 (2002)

[98] T.H. Muster, A.E. Hughes, G.E. Thompson, *Copper Distributions in Aluminium Alloys*, Nova Science Publishers Inc., New York, 9-23 (1958)

[99] Z. Szklarska-Smialowska, *Corros. Sci.*, 41, 1743–1767 (1999)

[100] N. Birbilis, and R.G. Buchheit, *J. Electrochem. Soc*., 152,B140-B151 (2005)

[101] R.G. Buchheit, L.P, Montes, M.A. Martinez, J. Michael and P.F. Hlava, *J. Electrochem. Soc*.,146, 4424-4428 (1999)

[102] G.S. Chen, M. Gao, R.P. Wei, *Corros.*, 52, 8-15 (1996)

[103] J.R. Scully, K.O. Knight, R.G. Bucheit, D.E. Peebles, *Corros. Sci.*, 35, 185 (1993)

[104] G.O. Ilevbare, O. Schneider, R. G. Kelly, and J. R. Scully, *J. Electrochem. Soc.*, 151, B453 (2004)

[105] J.R. Scully, K.O. Knight, R.G. Bucheit, D.E. Peebles, *Corros. Sci.*, 35, 185 (1993)

[106] J.R. Scully, D.E. Peebles, A.D. Romig, D.R. Frear, C.R. Hills, *Metall. Trans. A*, 23A, 1365 (1990)

[107] G.S. Chen, M. Gao, R.P. Wei, *Corros.*, 52, 8-15 (1996)

[108] J.R. Scully, K.O. Knight, R.G. Bucheit, D.E. Peebles, *Corros. Sci.*, 35, 185 (1993)

[109] R.G. Buchheit, R.P. Grant, P.F. Hlava, B. Mckenzie and G.L. Zender, *J. Electrochem. Soc*., 144,2621-2628 (1997)

[110] Z. Szklarska-Smialowska, *Corros. Sci.*, 41, 1743-1767 (1999).

[111] H.N. Girisha, K.V. Sharma, *Inter. J. Sci. Eng. Res.*, 3 (2012)

[112] N. Nafsin, H.M.M.A. Rashed, *Inter. J. Sci. Adv. Techno. (IJEAT),* 2 (2013)

[113] K.A. Son, N. Missert, J.C. Barbour, et al, *J.Electrochem.Soc.*,148, B260-B263 (2001)

[114] C. Blanc, B. Lavelle, G. Mankowski, *Corros.Sci.*, 39, 495-510 (1997)

[115] P. Schmutz, G. S. Frankel, *J. Electrochem. Soc*., 145, 2295-2306 (1998)

[116] T. Dimogerontakis, L. Kompotiatis, I. Kaplanoglou, *Corros. Sci.*, 40, 1939-1951 (1998)

[117] P. Campestrini, E. P. M. van Westing, H. W. van Rooijen, J. H. W. Wit, *Corros.Sci.*, 42, 1853-1861 (2000**)**

[118] C. Blanc, S. Gastaud, G. Mankowski, *J. Electrochem. Soc*., 150, B396-B404 (2003)

[119] M. C. Reboul, T. Magnin, T. J. Warner, *Conference proceedings volume II*, 1992

[120] V. Guillaumin, G. Mankowski, *Corros. Sci.*, 41, 421-438(1999)

[121] M. Reboul, *Techniques de l'Ingénieur*, 2005.

[122] J.O. Park, C.H. Paik, Y.H. Huang, R.C. Alkire, *J. Electrochem. Soc*., 146, 517-523 (1999)

[123] M.B. Vukmirovic, N. Dimitrov, K. Sieradzki, *J. Electrochem. Soc.*, 149, B428-439 (2002)

[124] C. Vargel, *Corrosion de l'aluminium*, Dunod, Paris, 1999

[125] M.C. Reboul, T.J. Warner, H. Mayer, B. Barouk, *Mater. Sci. Forum*, 217 - 222, 1553-1558 (1997)

[126] G.S. Chen, M. Gao, R.P. Wei, *Corros.*, 52, 8-15 (1996)

[127] D.J. Blackwood, A.S.L. Chong, *Brit. Corros. J.*, 33, 225-229 (1998)

[128] P. Leblanc, G.S. Frankel, *J. Electrochem Soc.*, 149, B239-B247 (2002)

[129] C.M. Liao, J.M. Olive, M. Gao, R.P. Wei, *Corros.*, 54, 451-458 (1998)

[130] J.O. Park, C.H. Apik, Y.H. Huang, et al, *J. Electrochem. Soc.*, 146, 517-523 (1999)

[131] M.B. Vukmirovic, N. Dimitrov, K. Sieradzki, *J. Electrochem. Soc.*, 149, B428-B439 (2002)

[132] R. Oltra, V. Maurice, R. Akid, P. Marcus, *Local Probe Techniques for Corrosion Research*, Woodhead Publishing Limited Cambridge, England, 2007

[133] R. Oltra, B. Vuillemin, F. Rechou and C. Henon, *Electrochem. Solid-State Lett.*,12, , C29-C31 (2009)

[134] H. Habazaki, K. Shimizu, P. Skeldon, et al, *Corros. Sci.*, 39, 731-737 (1997)

[135] V. Guillaumin, G. Mankowski, *Corros. Sci.*, 41, 421-438 (1999)

[136] R.G. Buchheit, R.P. Grant, P.F. Hlava, et al, *J. Electrochem Soc.*, 144, 2621-2628 (1997)

[137] A. Boag, A.E. Hughes, A.M. Glenn, T.H. Muster, D. McCulloch, *Corros.Sci.*, 53, 17–26 (2011)

[138] S.M. Cohen, *Corros.*, 51, 71-78 (1995)

[139] S.E. Manahan, *Environmental Chemistry*, CRC Press, Ann Arbor, MI, 1994

[140] R.L. Twite, G.P. Bierwagen, *Progress in Organic Coatings*, 33, 91-100 (1998)

[141] R.S. Razavi, *Recent Researches in Corrosion Evaluation and Protection*, InTech, Shanghai, 2012

[142] M. Sheffera, A. Groysmanb,D. Mandler, *Corros. Sci.*, 4, 2893–2904 (2003)

[143] A.J. Epsteina, J.A.O. Smallfieldb, H. Guana, M. Fahlman, *Synthetic Metals*, 102, 1374–1376 (1999)

[144] D. W. DeBerry, *J. Electrochem. Soc.*, 132, 1022 (1985)

[145] V.S, Protsenko, F.I. Danilov, *Clean Technologies and Environmental Policy*, 16, 1201-1206 (2004)

[146] X.C. Dong, P. Wang, S. Argekar, D.W. Schaefer, *Langmuir*, 26, 10833-10841 (2010)

[147] D. Ende, W. Kessler, D. Oelkrug, R. Fuchs, *Electrochim. Acta*, 38, 2577-2580 (1993)

[148] H.L. Jamese, *Plat. Surf. Finish.*, 86, 40-42 (1999)

[149] B.D. Fonte, *Trivalent chromium passivate solution and process*, US 4359345 A, 16.11.1982

[150] D.E. Crotty, R.J. Lash, *Trivalent chromium passivate composition and process*, US 4384902 A, 24.05.1983

[151] *Pollution Prevention Technology Profile-Trivalent Chromium Replacements for Hexavalent Chromium Plating*, The Northeast Waste Management Officials' Association (NEWMOA), Boston, 2003

[152] X. Dong, P. Wang, S. Argekar, D.W. Schaefer, *Langmuir*, 26, 10833 (2010)

[153] J. Qi, T. Hashimoto, J. Walton, X. Zhou, P. Skeldon, and G. E. Thompson, *J. Electrochem. Soc.*, 163, C25-C35 (2016)

[154] B. Kagajwala, T.D. Hall, M. Inman, E.J. Taylor, B. Griffin, G. Cushnie, R. Taylor, M. Jaworowski and J. Bonivel, *NASF SUR/FIN 2012*, Las Vegas, Nev., 2012

[155] S.L. Suib, J.L. Scala, W. Nickerson, A. Fowler, and N. Zaki, *Metal finish.*, 2009

[156] A. Lyer, W. Willis, S. Frueh, A. Fowler, J. Barnes, L. Hagos, *Plat. Surf. Finish.*, 97, 2010

[157] Zh. Zeng, L. Wang, A. Liang, J. Zhang, *Electrochim. Acta*, 52, 1366–1373(2006)

[158] X. Dong, P. Wang, S. Argekar and D.W. Schaefer, *Langmuir*, 26, 10833–10841 (2010)

[159] L. Li and G.M. Swain, *ACS Appl. Mater. Interf.*, 5, 7923–7930 (2013)

[160] X. Dong, S. Argekar, P. Wang, and D.W. Schaefer, *ACS Appl. Mater. Interf.*, 3, 4206–4214 (2011)

[161] J.C. Hecker. Jr., *Aluminum Consultants*, Madison, Wisconsin, USA, 1994

[162] T. Ohgai, X. Hoffer, L. Gravier, J.Ph. Ansermet, *J. Appl. Electrochem.*, 34, 1007-1012 (2004)

[163] T.M. Whitney, J.S. Jiang, R. C. Searson and C.L. Chien, *Science,* 261**,** 1316 (1993)

[164] A. Belwalkar, E. Grasing, W. Van Geertruyden, Z. Huang, and W.Z. Misiolek, *J Memb Sci.*, 319, 192–198 (2008)

[165] J. Edwards, *Coating and Surface Treatment Systems for Metals*, Finishing Publications Ltd. and ASM International, 1997

[166] T. Thurn-Albrecht, J. Schotter, G.A. Kästle, N. Emley, T. Shibauchi, L. Krusin-Elbaum, K. Guarini, C.T. Black, M.T. Tuominen and T.P. Russell, *Sci.,* 290**,** 2126 (2000)

[167] J. Vereecken, G. Goeminne, I. De Graeve, H. Terryn, *Proc. 13th Int. Corros. Congr.*, Melbourne, Australia, 25–29, 1148 (1996)

[168] C. Ban, Y. He, X. Shao, L. Wang, *J. Mater. Sci.*, 25, 128-133 (2014)

[169] J.P. O'Sullivan, G.C. Wood, *The Royal Society*, 1970

[170] W. Lee, K. Schwirn, M. Steinhart, E. Pippel, R. Scholz, U. Gösele, *Nature Nanotechnology*, 3, 234-239 (2008)

[171] X. Zhao et al, *Surf. Rev. Lett.*, 22, 1550002 (2015)

[172] V. Soko, I. Vrublevsky, V. Parkun, K. Moskvichev, *Ana.l Bioanal. Chem.*, 375, 968-973 (2003)

[173] D.A. Wrobleski, B.C. Benicewicz, K.G. Thompson, and C.J. Bryan, *ACS Polymer Preprints,* 35, 265 (1994)

[174] S. Jasty and A.J. Epstein, *Mater. Sci. Eng.*, 72, 565 (1995)

[175] M.M. Gvozdenović, B.Z. Jugović, J.S. Stevanović, T.Lj. Trišović and B.N. Grgur, *Electropolymerization*, 78-96 (2004)

[176] N. Tavandashti, S. Sanjabi, T. Shahrabi, *Prog. Org. Coat.*, 65, 182–186 (2008)

[177] S. González, F. Cáceres, V. Fox, R.M. Souto, *Prog. Org. Coat.*, 46, 317–323 (2003)

[178] M. Leskela, M. Ritala, *Thin Solid Films*, 409, 138-146 (2002)

[179] S.M. George, *Chem. Rev.*, 110, 111–131 (2010)

[180] R.L. Puurunen, *J. Appl. Phys.,* 97 (2005) 121301

[181] T. Suntola, J. Antson, US Patent, 4,058,430, n.d

[182] A.C. Dillon, A.W. Ott, J.D. Way, S.M. George, *Surf. Sci.*, 322, 230 (1995)

[183] M. Ritala, M. Leskela, J.P. Dekker, C. Mutsaers, P.J. Soininen, J. Skarp, *Chem.Vapor Depos.*, 5, 7 (1999)

[184] M. Leskelä, M. Ritala, Angew. *Chem. Int. Ed*. 42, 5548 (2003)

[185] H.S. Nalwa, *Handbook of Thin Film Materials*, Academic Press, 2001

[186] V. Miikkulainen, M. Leskel , M. Ritala, R.L. Puurunen, *J. Appl. Phys*., 113 (2013)

[187] R.L. Puurunen, M. Putkonen, *Handbook of Silicon Based MEMS Materials and Technologies (Second Edition)*, Elsevier, 2015

[188] R.L. Puurunen, *Chem. VaporDepos.*, 20, 332–344 (2014)

[189] C.A. Wilson, R.K. Grubbs, and S.M. George, *Chem. Mater.*, 17, 5625–5634 (2005)

[190] S.M. Prokes, M.B. Katz and M.E. Twigg, *APL Mater.* 2, (2014)

[191] D.N. Goldstein, J.A. McCormick, and S.M. George, *J. Phys. Chem. C*, 112, 19530–19539 (2008)

[192] M.D. Groner, F.H. Fabreguette, J.W. Elam, and S.M. George, *Chem. Mater.*, 16, 639-645 (2004)

[193] M. Ritala, M. Leskela, *Handbook of Thin Film Materials*, Academic Press: San Diego, CA, 2001

[194] R.W. Johnson, A. Hultqvist, S.F. Bent, *Materials Today*, 17, 236–246 (2014)

[195] E. Marin, A. Lanzutti, L. Guzman, L. Fedrizzi, *J. Coat. Technol. Res.*, 8, 655-659 (2011)

[196] A.W. Ott, J.W. Klaus, J.M. Johnson, S.M. George, *Thin Solid Films*, 292, 135 (1997)

[197] M.D. Groner, J. W. Elam, F.H. Fabreguette, S.M. George, *Thin Solid Films*, 413, 186 (2002)

[198] B. Díaz, J. Światowska, V. Maurice, A. Seyeux, B. Normand, E. Härkönen, M. Ritala, P. Marcus, *Electrochim. Acta*, 56, 10516 -10523 (2011)

[199] S. Mirhashemihaghighi, J. Światowska, V. Maurice, A. Seyeux, L.H. Klein, E. Härkönen, M. Ritala, and P. Marcus, *J. Electrochem. Soc.,* 162, C377-C384 (2015)

[200] B. Díaz, J. Światowska, V. Maurica, A. Seyeux, E. Härkönen, M. Ritala, S. Tervakangas, J. Kolehmainen, P. Marcus, *Electrochim. Acta*, 90, 232–245 (2013)

[201] E. Härkönen, B. Díaz, J. Światowska, V. Maurice, A. Seyeux, M. Vehkamäki, T. Sajavaara, M. Fenker, P. Marcus, and M. Ritala, *Electrochim. Acta*, 90, 232–245 (2013)

[202] B. Díaz, E. Härkönen, J. Światowska, A. Seyeux, V. Maurice, M. Ritala, P. Marcus, *Corros.Sci.*, 56, 208-217 (2014)

[203] B. Diaz, E. Harkonen, J. Swiatowska, V. Maurice, A. Seyeux, P. Marcus, M. Ritala, *Corros. Sci.*, 53, 2168-2175 (2011)

[204] B. Diaz, E. Harkonen, V. Maurice, J. Swiatowska, A. Seyeux, M. Ritala, P. Marcus, *Electrochim. Acta*, 56, 9609-9618 (2011)

[205] S. Mirhashemihaghighi, J. Swiatowska, V. Maurice, A. Seyeux, L.H. Klein, E. Salmi, M. Ritala, P. Marcus, *Electrochim. Acta*, 193, 7-15 (2016)

[206] E. Härkönen, S.E. Potts, W.M.M. Kessels, B. Díaz, A. Seyeux, J. Światowska, V. Maurice, P. Marcus, G. Radnóczi, L. Tóth, M. Kariniemi, J. Niinistö, M. Ritala, *Thin Solid Films*, 534, 384-393 (2013)

[207] E. Härkönen, S. Tervakangas, J. Kolehmainen, B. Díaz, J. Światowska, V. Maurice, A. Seyeux, P.Marcus, M. Fenker, L. Tóth, G. Radnóczi, M. Ritala, *Mater. Chem. Phys*., 147, 895-907 (2014)

[208] B. Díaz, E. Härkönen, J. Światowska, V. Maurice, A. Seyeux, P. Marcus, M. Ritala, *Corros. Sci.*, 53, 2168–2175 (2011)

[209] Z. Chai, Y. Liu, J. Li, X. Lu and D. He, *RSC Advances*, 4, 50503-50509 (2014)

[210] Z. Chai, J. Li, X. Lu, and D. He, *RSC Advances*, 4, 39365-39371 (2014)

[211] S.E. Potts, L. Schmalz, M. Fenker, B. Díaz, J. Światowska, V. Maurice, A. Seyeux, P. Marcus, G. Radnóczi, L. Tóth, *J. Electrochem. Soc.*, 158, C132-C138 (2011)

[212] E. Härkönen, M. Ritala, L. Schmalz, M. Fenker, B. Diaz, J. Światowska, B. Normand, V. Maurice, P. Marcus, *J. Electrochem. Soc.,* 216th ECS Meeting, Abstract, 2009

Chapter 2 Techniques and sample preparations

In this chapter, two main surface analytical techniques used in the thesis—X-ray photoelectron spectroscopy (XPS) and Time-of-Flight secondary ion mass spectrometry (TOF-SIMS) are described. The principles of their techniques and instrumentations are introduced. The preparation procedure of the Al-Cu alloy samples is also presented. The detailed experimental procedures related to measurements and/or sample treatments are presented in each chapter.

2.1 X-ray Photoelectron Spectroscopy (XPS)

X-ray photoelectron spectroscopy (XPS), also known as ESCA (Electron Spectroscopy for Chemical Analysis), is a technique for analyzing the surface chemistry of a material. XPS can measure the elemental composition, empirical formula, chemical state and electronic state of the elements within a material. XPS was developed in the mid 1960s by K. Siegbahn and his research group. K. Siegbahn was awarded the Nobel Prize for Physics in 1981 for his work in XPS[1,2]. XPS spectra are obtained by irradiating a solid surface with a beam of X-rays while simultaneously measuring the kinetic energy and electrons that are emitted from the top 1-10 nm of the material being analyzed. A photoelectron spectrum is recorded by counting ejected electrons over a range of electron kinetic energies. Peaks appear in the spectrum from atoms emitting electrons of a particular characteristic energy. The energies and intensities of the photoelectron peaks enable identification and quantification of all surface elements (except hydrogen). The main characteristics of the XPS are as follows[3]:

- XPS requires high vacuum (P~10^{-8} millibar) or ultra-high vacuum (UHV; P $<10^{-9}$ millibar) conditions, although a current area of development is ambient-pressure XPS, in which samples are analyzed at pressures of a few tens of millibar.
- In principle XPS detects all elements. In practice, using typical laboratory-scale X-ray sources, XPS detects all elements with an atomic number (Z) of 3 (lithium) and above. It cannot easily detect hydrogen (Z = 1) or helium (Z = 2).
- Detection limits for most of the elements (on a modern instrument) are in the parts per thousand range. Detection limits of parts per million (ppm) are possible, but require special conditions: concentration at top surface or very long collection time (overnight).
- XPS is routinely used to analyze inorganic compounds, metal alloys, semiconductors, polymers, elements, catalysts, glasses, ceramics, paints, paper, inks,

woods, plant parts, make-up, teeth, bones, medical implants, bio-materials, viscous oils, glues, ion-modified materials and many others.

- XPS is less routinely used to analyze the hydrated forms of some of the above materials by freezing the samples in their hydrated state in an ultra pure environment, and allowing or causing multi layers of ice to sublime away prior to analysis. Such hydrated XPS analysis allows hydrated sample structures, which may be different from vacuum-dehydrated sample structures, to be studied in their more relevant as-used hydrated structure. Many bio-materials such as hydrogels are examples of such samples.

2.1.1 Principle

The phenomenon is based on the photoelectric effect outlined by Einstein in 1905 (as shown in the Eq. 2-1) where the concept of the photon was used to describe the ejection of electrons from a surface when photons impinge upon it. The energy of a photon of all types of electromagnetic radiation is given by the Einstein relation:

$$E = h\nu \qquad \text{Eq. 2-1}$$

where

h - the Planck constant (6.62×10^{-34} Js)

ν - the frequency (Hz) of the radiation.

In the case of XPS, electrons are liberated from the specimen as a result of a photoemission process. When a solid surface is irradiated with soft X-ray photons, mostly from an Al-Kα or Mg-Kα primary source, an incident photon of energy hν can be absorbed by an electron with binding energy E_B below the vacuum level: the entire photon energy is transferred to the electron, which is then promoted to an unoccupied state above the vacuum level. As a result, this photoelectron is ejected into the vacuum with kinetic energy, and its energy can be detected by an electron energy analyzer. The XPS process is schematically represented in Fig. 2-1(a) for the emission

of an electron from the 1s shell of an atom.

The experimental quantity that is measured is the kinetic energy of the electron, which depends on the energy hν of the primary x-ray source. For a solid surface the binding energy (E_B) is conventionally measured with respect to the Fermi level rather than to the vacuum level (Fig. 2-1(b)), and the previous relationship is written in the form[4]:

$$E_B = h\nu - E_K - W \qquad \text{Eq. 2-2}$$

where E_B and E_K are respectively the binding and the kinetic energy of the emitted photoelectron, hν is the photon energy, and W is the spectrometer work function and represents the minimum energy required to remove an electron from the solid. In a first approximation, the work function is the difference between the energy of the Fermi level E_F and the energy of the vacuum level E_V, which is the zero point of the electron energy scale:

$$W = E_F - E_V \qquad \text{Eq. 2-3}$$

This quantity is to be determined by calibration for the spectrometer used. From Eq. 2-3 it is clear that only binding energies lower than the exciting radiation (1486.6 eV for Al-Kα and 1253.6 eV for Mg-Kα) are probed. If one measures the electron kinetic energy, and perhaps also knows the spectrometer work function, it is thus possible to measure the binding energies of various inner (or core) electrons, as well as those of the outer (or valence) electrons that are involved in chemical bonding. Such measurements have been found to reveal a broad array of phenomena that can be used to characterize a given material, in particular the near-surface regions of solids from which most photoelectrons are emitted. Each element has a characteristic electronic structure and thus a characteristic XPS spectrum.

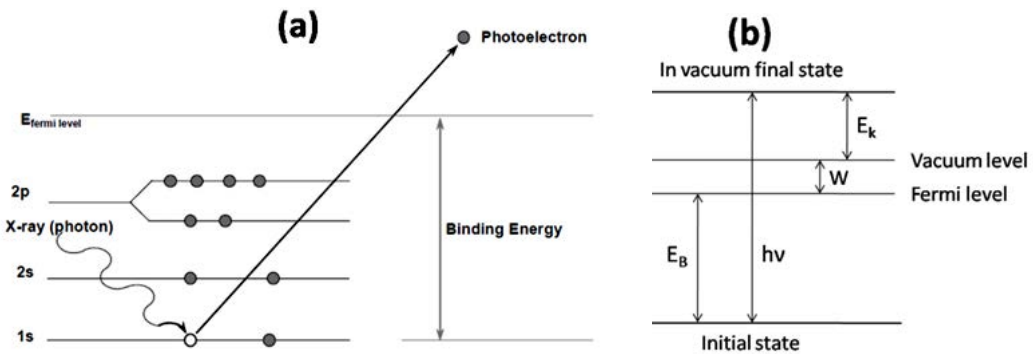

Fig. 2-1 Schematic view of the photoemission process: (a) the emission of an electron from the 1s shell of an atom; (b) corresponding energy balance within the framework of one electron picture[5].

2.1.2 Instrument

The XPS analyses were performed with the ESCALAB250 spectrometer of Thermo Electron Corporation with an Al Kα monochromated radiation (hν=1486.6 eV), was used to in this thesis, as illustrated in Fig. 2-2. In this thesis, survey spectra were recorded with pass energy of 100 eV and the high resolution spectra of the C1s, O1s, Al2p and $Cu2p_{3/2}$, core level regions were collected with pass energy of 20 eV. Spectra were recorded and analyzed using the Thermo Scientific™ Avantage Software (version 5.954).

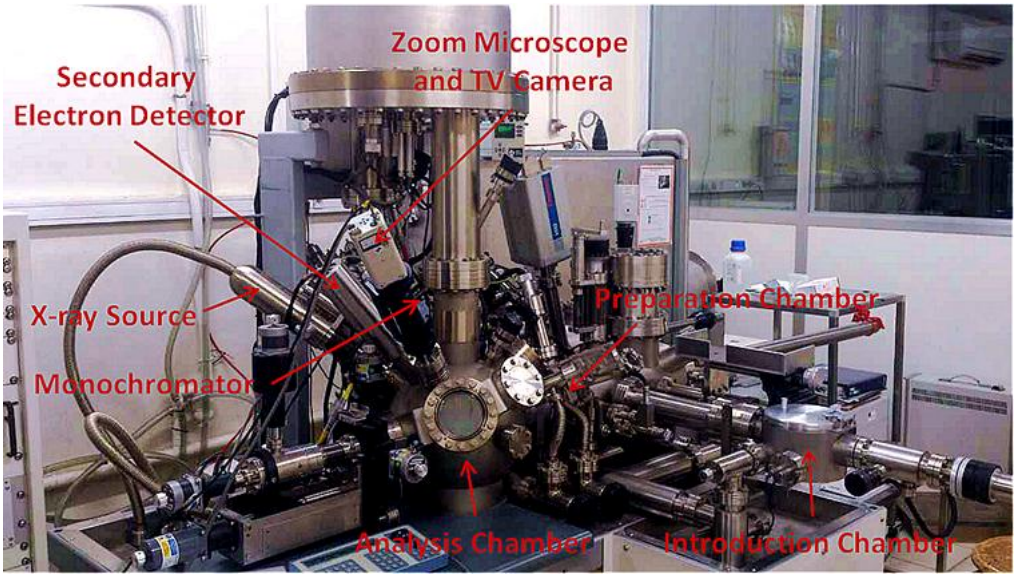

Fig. 2-2 Illustrations of the ESCALAB250 spectrometer of Thermo Electron Corporation employed in this thesis.

2.1.3 Characterization

Generally in an XPS spectrum sharp peaks and extended tails are shown in the allowed energy range. The shape and energy positions of these peaks indicate the presence of elements as well as their chemical state, especially in the valence band zone. Some spectral features are introduced below.

Core level

At low energy resolution, XPS spectra provides qualitative and quantitative information on the elements present, whereas at high-resolution core level it gives information on the chemical state and bonding of those elements. As illustrated in the Fig. 2-3, high-resolution core level XPS spectra provides improved chemical selectivity by narrowing the spectral peaks, lower spectral background, and elimination of unwanted x-ray from satellites and anode impurities, which simplifies spectral analysis.

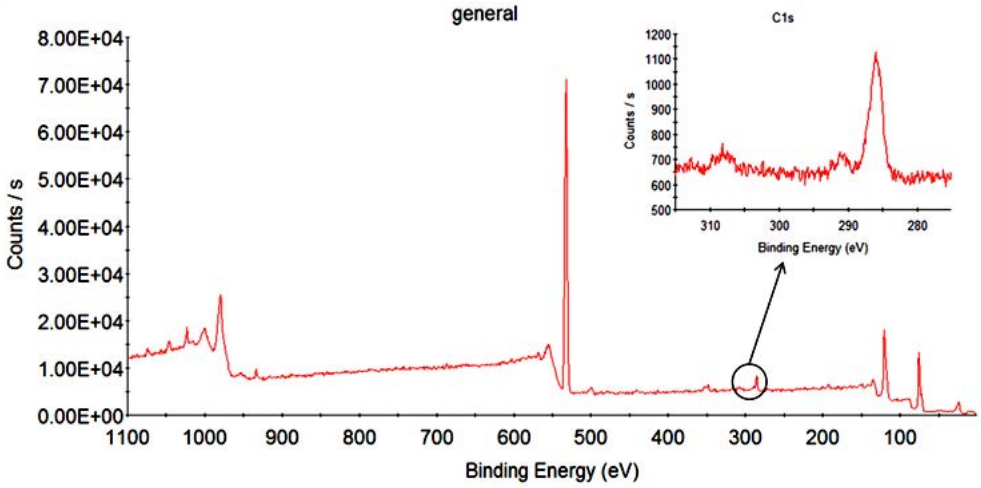

Fig. 2-3 Survey XPS spectra of the bulk Al-4.87wt.% Cu alloy. The inset shows high-resolution core level XPS spectra of C1s peak.

Backgrounds

Quantifying the intensity of peaks in XPS data requires properly modeling the background signal. In general, three types of backgrounds are used:

1) a simple straight line or linear background,

2) the Shirley background in which the background intensity at any given binding energy is proportional to the intensity of the total peak area above the background in the lower binding energy peak range (*i.e.* the background goes up in proportion to the total number of photoelectrons below its binding energy position),

3) the Tougaard background, which is a methodology for integrating the intensity of the background at a given binding energy from the spectral intensities to higher kinetic energies.

The simple linear background suffers from large peak area changes depending on the position of the chosen end points and is the least accurate. The Tougaard background is the most accurate but suffers from complications in practical use, particularly if there are numerous peak overlaps. The Shirley background falls somewhere in between for accuracy, however its ease of use has resulted in its widespread adoption. In this thesis, Shirley background was used and the shape of fitting curves was determined by a 70% Gaussian/30% Lorentzian distribution, typical for the spectra fitting for metals/oxides.

Binding energy and chemical shift

For each and every element, there will be a characteristic binding energy (E_B) associated with each core atomic orbital *i.e.* each element will give rise to a characteristic set of peaks in the photoelectron spectrum at kinetic energies determined by the photon energy and the respective binding energies.

Chemical shift is the change in binding energy of a core electron of an element due to a change in the chemical bonding of that element, *e.g.*, the formation of chemical bonds with other atoms resulting in a change of the oxidation state.

Atoms of a higher positive oxidation state exhibit a higher binding energy due to the extra coulombic interaction between the emitted electron and the ion core. This ability to discriminate between different oxidation states and chemical environments is one of the major strengths of the XPS technique. For example, Titanium exhibits very large chemical shifts between different oxidation states of the metal, as shown in

the Fig. 2-4, in which a Ti 2p spectrum from the pure metal (Ti) is compared with a spectrum of titanium dioxide (Ti^{4+}).

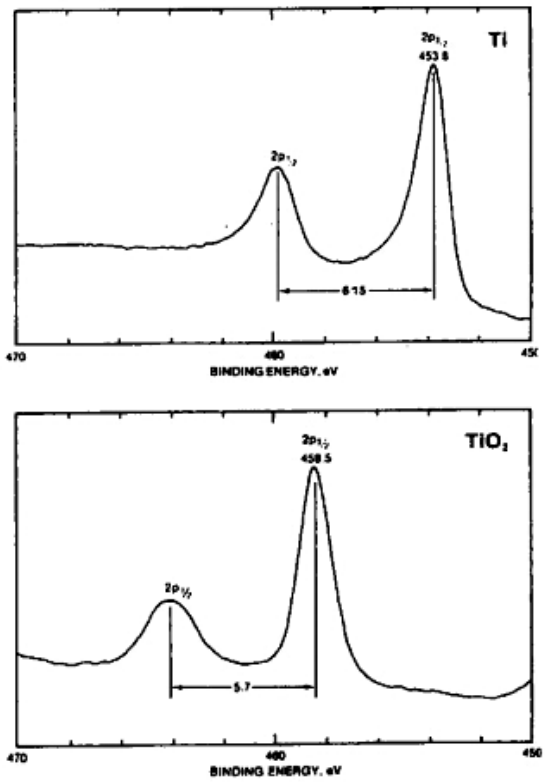

Fig. 2-4 Illustration of Ti2$p_{1/2}$ and 2$p_{3/2}$ chemical shift for Ti and Ti^{4+}[6].

Full width at half maximum (FWHM)

Full width at half maximum (FWHM) is an expression of the extent of a function given by the difference between the two extreme values of the independent variable at which the dependent variable is equal to half of its maximum value. In other words, it is the width of a spectrum curve measured between those points on the y-axis which are half the maximum amplitude.

FWHM is applied to such phenomena as the duration of pulse waveforms and the spectral width of sources used for optical communications and the resolution of spectrometers.

The term full duration at half maximum (FWHM) is preferred when the independent variable is time.

The convention of "width" meaning "half maximum" is also widely used in signal processing to define band width as "width of frequency range where less than half the signal's power is attenuated", *i.e.*, the power is at least half the maximum. In signal processing terms, this is at most −3 dB of attenuation, called "half power point".

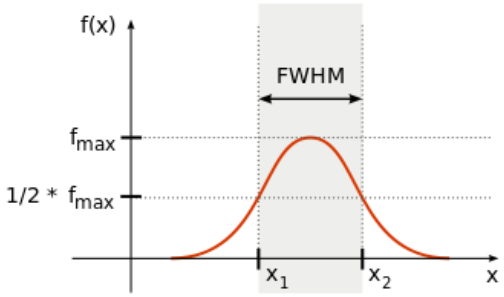

Fig. 2-5 A legend of full width at half maximum[7].

Shake-up satellites

Shake-up satellites arise when a core electron is removed by a photoionization. For some materials, there is a finite probability that the photoelectronic process leads to the formation of an ion in its excited state with a few eV above the ground state.

Shake-up features especially common in transition metal oxides associated with paramagnetic species. Generally, the shake-up satellites have intensities and energy separations from the parent photoelectron line that are unique to each chemical state, which can be used to analyze the chemical state of the elements. Such strong shake-up satellite in the Cu2p spectrum of CuO can be observed but not for Cu_2O. It's possible to distinguish Cu oxidation states using satellite features of Cu2p, as shown in the Fig. 2-6. Cu (II) has observable collection of satellite features 943 eV, and $Cu2p_{3/2}$ peak in Cu (II) oxide is shifted and is much broader compared to Cu (I) oxide. In Cu (I) oxide, there is only a very weak satellite at 945 eV. $Cu2p_{3/2}$ peak in Cu (I) oxide is not shifted but is broader compared to Cu metal.

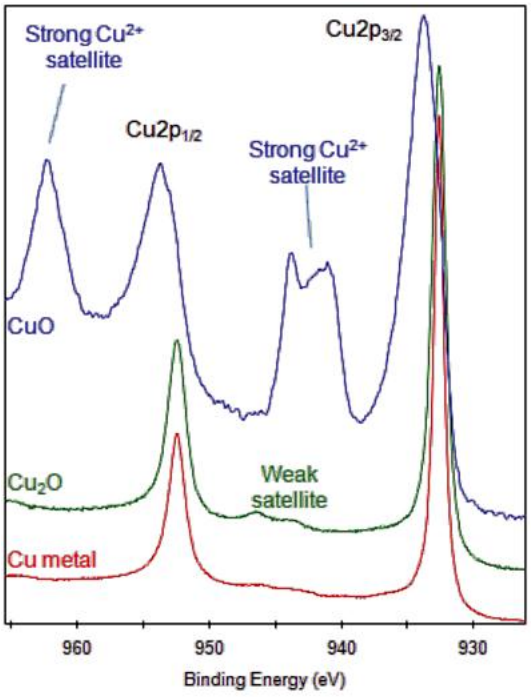

Fig. 2-6 Representation of the XPS Cu2p peaks with satellite peaks[8].

Spin-Orbit Splitting

Core levels in XPS use the nomenclature *nlj* where *n* is the principal quantum number, *l* is the angular momentum quantum number and $j = l + s$ (where *s* is the spin angular momentum number and can be ±½). All orbital levels except the *s* levels ($l = 0$) give rise to a doublet with the two possible states having different binding energies. This is known as spin-orbit splitting (or *j-j* coupling)[9]. The peaks will also have specific area ratios based on the degeneracy of each spin state, *i.e.* the number of different spin combinations that can give rise to the total j. For example, for the 2p spectra, where n is 2 and *l* is 1, *j* will be 1/2 and 3/2. The area ratio for the two spin orbit peaks ($2p_{1/2}$:$2p_{3/2}$) will be 1:2 (corresponding to 2 electrons in the $2p_{1/2}$ level and 4 electrons in the $2p_{3/2}$ level). These ratios must be taken into account when analyzing spectra of the *p*, *d* and *f* core levels.

For example, as shown in the Fig. 2-7, the Al2p peak has closely spaced spin-orbit components $2p_{1/2}$ (higher BE) and $2p_{3/2}$ (lower BE) with Δmetal=0.44 eV, and the peak intensity of $Al2p_{3/2}$ should be twice the intensity of $Al2p_{1/2}$. Splitting only observed for Al metal and under typical experimental conditions, and may be ignored

for Al2p peaks from aluminium compounds, such as Al oxide. These values will be needed when fitting spectra where the chemical shifts are larger than the spin-orbit splitting.

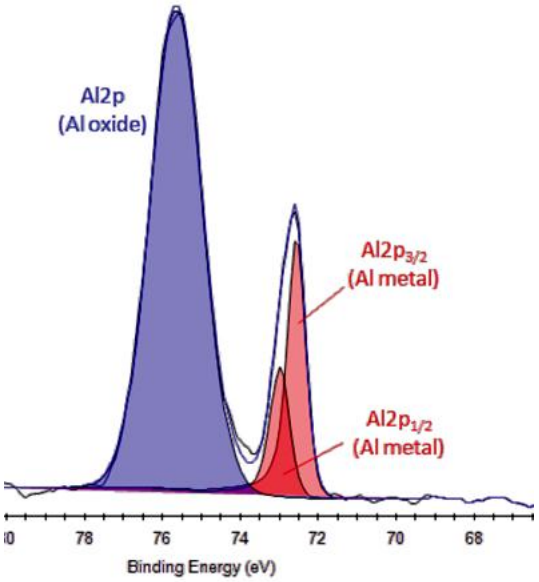

Fig. 2-7 Al2p spectrum of native oxide on Al metal showing the Al2p spin-orbit splitting[8].

Auger parameter

Core ionization by photoelectron emission an outer shell electron can fill the created vacancy and the energy released can result in the emission of an Auger electron. Auger spectra have unique peak shapes and positions and are useful for both elemental identification and chemical state analyses. A calculated value from both photoelectron and Auger peak positions is the Auger parameter (α). This parameter is particularly useful for chemical state analysis and can be used without interference of surface charging.

The Auger parameter (α) is defined as the difference in BE between two chemical states. This depends on the change in core electron level energy and the change in intra and extra-atomic relaxation energies. The Auger electron kinetic energy is always independent from the source nature. It is defined as follows[10]:

$$\alpha = E_{KLL} - E_K \qquad \text{Eq. 2-5}$$

and

$$E_K = h\nu - E_B \qquad \text{Eq. 2-6}$$

therefore

$$\alpha + h\nu = E_{KLL} + E_B \qquad \text{Eq. 2-7}$$

where E_{KLL} is Auger peak in KE and E_B is core level peak in BE.

For example, as shown in the Fig. 2-8, the binding energy of $Cu2p_{3/2}$ = 932.6 eV, and the kinetic energy of Cu LMM = 918.6 eV, hence, α= Cu2p (BE) + Cu LMM (KE) = 1851.2 eV, which indicates the presence of metallic Cu.

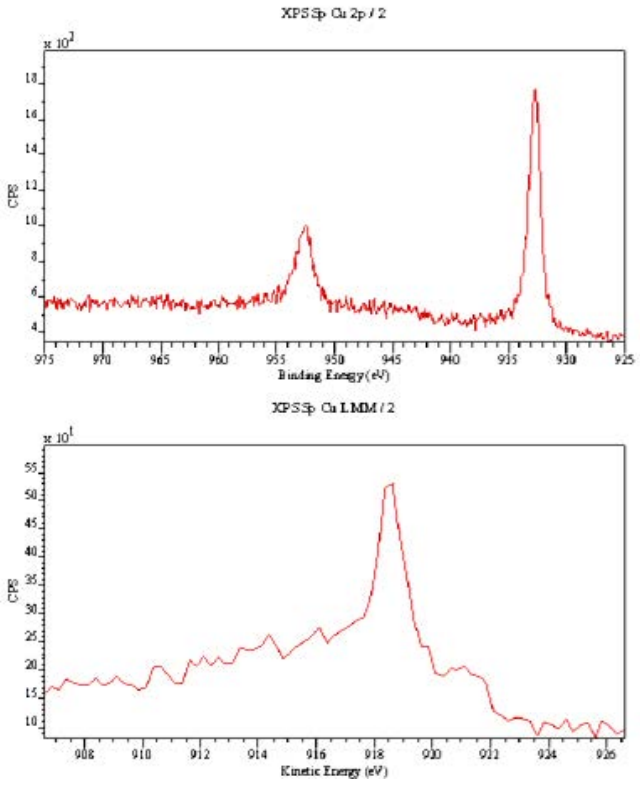

Fig. 2-8 XPS spectra of Cu2p in BE and Cu LMM in KE.

2.2 Time-of-Flight Secondary Ion Mass Spectrometry (ToF-SIMS)

Time-of-Flight secondary ion mass spectrometry (ToF-SIMS) is a very sensitive

surface analytical technique, well established for many industrial and research applications. ToF-SIMS is an acronym for the combination of the analytical technique SIMS (Secondary Ion Mass Spectrometry) with Time-of-Flight mass analysis (ToF). The technique provides detailed elemental and molecular information about the surface, thin layers, interfaces of the sample, and gives a full three-dimensional analysis. The use is widespread, including semiconductors, polymers, paint, coatings, glass, paper, metals, ceramics, biomaterials, pharmaceuticals and organic tissue. The average depth of analysis for a ToF-SIMS measurement is approximately 1 nm[11,12].

2.2.1 Principle

ToF-SIMS uses a focused, pulsed particle beam (typically Cs or Ga) to dislodge chemical species on a materials surface. The sample surface is pulsed by an ion beam (primary ions) with a kinetic energy (KE) of a few keV, resulting in the emission of various secondary particles, such as electrons, neutral species, atoms and molecules from the surface, as illustrated in the Fig. 2-9[13].

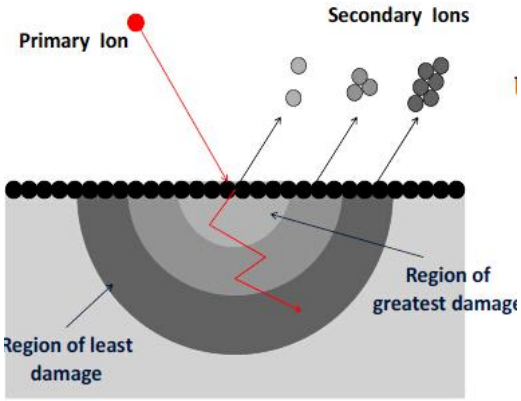

Fig. 2-9 Schematic diagram of the SIMS process[14].

A basic equation is always used to describe the quantitative relation[15,16]:

$$I_s^m = I_p y_m \alpha^{\pm} \theta_m \eta \qquad \text{Eq. 2-8}$$

where I_s^m is the secondary ion current of species m;

I_p is the primary particle flux;

y_m is the sputter yield;

$\alpha^{\pm}$ is the ionization probability to positive or negative ions;

θ_m is the fractional concentration of m in the surface layer;

η is the transmission of the analysis system.

Particles produced closer to the site of impact tend to be dissociated ions (positive or negative). Secondary particles generated farther from the impact site tend to be molecular compounds, typically fragments of much larger organic macromolecules. The ionized secondary ions are collected and detected by a time of flight (ToF) mass analyzer (Fig. 2-9). When these secondary ions are ejected from the sample surface, they are accelerated to a given potential (V) and thus all possess the approximately same kinetic energy (KE). All these secondary ions are then accelerated into a flight path on their way towards a detector. It follows that[17,18]:

$$t = L\left(\frac{m}{2zV}\right)^{1/2} \qquad \text{Eq. 2-9}$$

where t, L, m, z, and V are the flight time, travel distance, mass, charge, and speed of the secondary particle, respectively.

Because it is possible to measure the "time-of-flight" of the particles from the time of impact to detector on a scale of nano-seconds, it is possible to produce a mass resolution as fine as 0.00X atomic mass units (*i.e.* one part in a thousand of the mass of a proton).

ToF-SIMS is also referred to as "static" SIMS because a low primary ion current is used to "tickle" the sample surface to liberate ions, molecules and molecular clusters for analysis. In contrast, "dynamic" SIMS is the method of choice for quantitative analysis because a higher primary ion current results in a faster sputtering rate and produces a much higher ion yield. Thus, dynamic SIMS creates better counting statistics for trace elements. Organic compounds are effectively destroyed by "dynamic" SIMS, and no diagnostic information is obtained.

2.2.2 Instrument

In this work, a ToF-SIMS V spectrometer (ION TOF GmbH-Munster, Germany) was employed to analyze elemental species presented on the sample surface, and asses their status and distribution in high resolution, as shown in the Fig. 2-10.

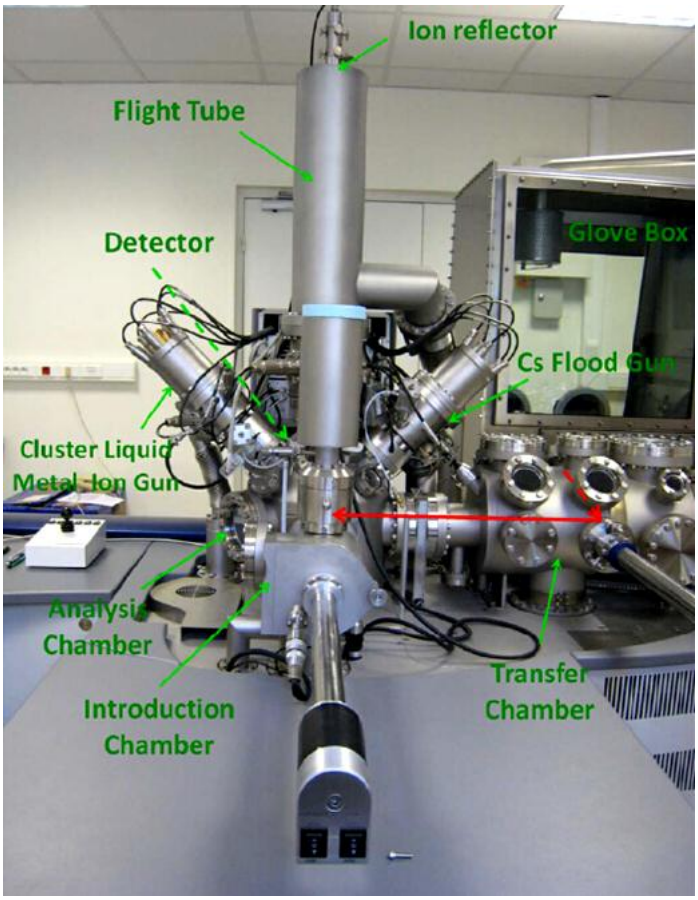

Fig. 2-10 Illustrations of a ToF-SIMS V spectrometer (ION TOF GmbH-Munster, Germany) employed in this thesis.

The ToF-SIMS spectrometer consists of a precisely pulsed primary Bi ion gun, a sputtering Cs ion gun, a highly accurate computer clock, a flight tube, a detector and a considerable computing power for data acquisition. The polyatomic primary Bi^{n+} cluster ions source has the advantage of high intensity of cluster emission and good focusing characteristics. Furthermore, doubly charged Bi^{3+} ions are formed in a significant proportion which gives double impact energy and excites more secondary

ions. Depth profiling is performed by the sputtering of Cs^+ ions that enhance significantly the ionization probability of negative secondary ion species. The reflector includes a series of precisely spaced rings that can control the path of the energetic ions to make sure the ions with the same mass arrive to the detector at same time: the more energetic the ions the longer path in the rings will be used.

2.2.3 Characterization

Depending on the primary ion dose, SIMS can be classified into static SIMS and dynamic SIMS. Normally the acceptable primary ion dose density is less than 1013 ions cm^{-2} per experiment for static SIMS, and at least 1017 ions cm^{-2} per experiment for dynamic SIMS. In the case of static SIMS, the objective is to eliminate the modification of the probed surface region brought by the ion impact. In contrast for dynamic SIMS, it is just to maintain a steady state of erosion and surface chemistry. In the near surface region the primary ions dose attains a stationary value. The most used three modes of ToF-SIMS analysis are surface spectrometry, depth profiling and chemical imaging[19]. In this thesis, only depth profiling and chemical imaging modes are employed for the analysis.

Depth profiling mode

Depth Profiling is a process where the element or chemical content of a sample is measured as a function of depth. For depth profiling two ion beams operate in the dual beam mode: the first beam is sputtering a crater, the second beam is progressively analyzing the crater bottom (Fig. 2-11).

Many analysis techniques that perform depth profiling use a beam of ions such as Ar^+, Ga^+, Cs^+, or O_2^+. Other depth profiling techniques use pulses of laser light, plasma beams, glow discharge or confocal manipulation of the sample in the Z axis. The depth profile process involves the repeated removal (or in certain cases, the movement of the sample) down to the desired depth.

The "Y" axis of a depth profile plot represents the quantity of the element or

chemical state measured at each measured depth. The "X" axis of a depth profile plot represents the depths that were analyzed by the repeated cycling of ion beam, the laser pulse etc.

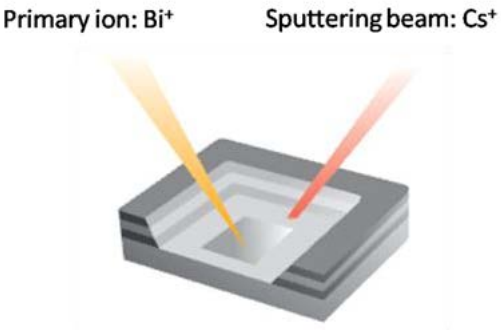

Fig. 2-11 Illustrations of dual beam mode depth profiling, from ToF-SIMS V brochure (ION-ToF GmbH).

The expected thickness of the layers of interest and detection limits are important factors to consider before starting any depth profiling. For example, as shown in the Fig. 2-12, the depth profiles provide plenty of information on the elemental species as a function of sputtering time for an as-polished binary Al-4.87wt.% Cu alloy sample, which is quite convenient for characterizing different surface layers, *e.g.* the surface native oxide and the metallic substrate, by analyzing the intensities changing of elemental species.

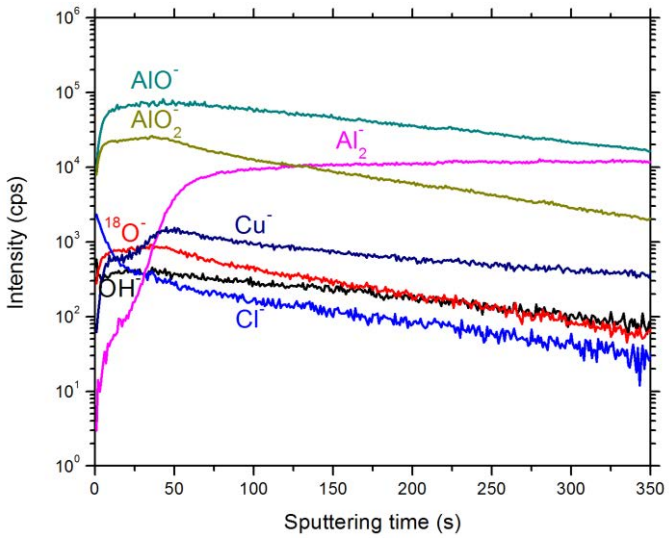

Fig. 2-12 Illustrations of the ToF-SIMS negative ions depth profiles obtained from an as-polished binary Al-4.87wt.% Cu alloy sample used in this thesis.

Chemical imaging mode

If the aim of the measurement is to obtain compositional images of the surface formed from the secondary ion spectrum with minimum possible damage to the surface, then the main problem is to ensure that sufficient signal is obtained at the desired spatial resolution whilst minimizing the ion flux incident on any part of the surface.

This is most easily achieved by switching from the traditional instrumental approach of using continuous-flux ion guns and quadrupole mass spectrometer detectors, to using pulsed ion sources and time-of-flight (TOF) mass spectrometers. By rastering a fine-focused ion beam over the surface, like an electron beam in an electron microprobe, mass resolved secondary ion images (chemical maps) can be obtained simultaneously (Fig. 2-13). The TOF mass spectrometers are a much more efficient way of acquiring spectral data, and also provide good resolution and sensitivity up to very high masses. Using such instruments, SIMS images with a spatial resolution of better than 50 nm are obtainable.

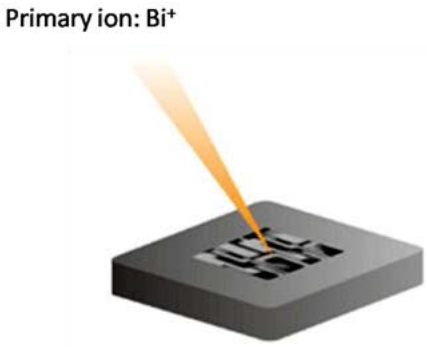

Fig. 2-13 Illustrations of chemical imaging mode, from ToF-SIMS V brochure (ION-ToF GmbH).

Still taking the as-polished binary Al-4.87wt.% Cu alloy sample for example, the 100×100 μm^2 negative ion images (Fig. 2-14) are obtained after 10 s, 60 s, and 310 s of sputtering, corresponding to the oxide region, the oxide/metal interfacial region and the metallic substrate, respectively. These three rows of images clearly demonstrate

the status and distribution of elemental species ($^{18}O^-$, AlO^-, and Al_2^-).

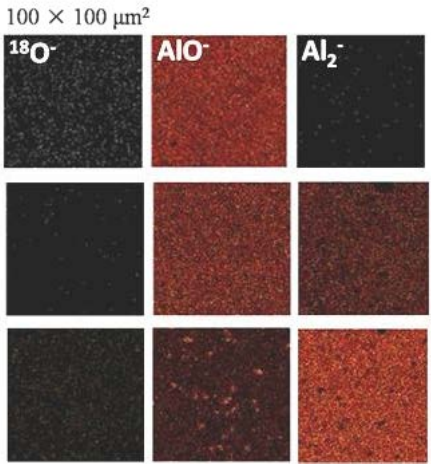

Fig. 2-14 Illustrations of the ToF-SIMS negative ion images of $^{18}O^-$, AlO^-, Al_2^-, obtained from an as-polished binary Al-4.87wt.% Cu alloy sample used in this thesis.

2.3 Scanning Electron Microscopy (SEM) and Energy-dispersive X-Ray spectroscopy (EDX)

Scanning electron microscopy with energy dispersive x-ray spectroscopy (SEM/EDX), the best known and most widely-used of the surface analytical techniques, was used as additional techniques to visualize the surface of some of the coated samples. SEM uses a focused beam of high-energy electrons to generate a variety of signals at the surface of solid specimens. The signals that derive from electron-sample interactions reveal information about the sample including external morphology (texture), chemical composition, and crystalline structure and orientation of materials making up the sample. In most applications, data are collected over a selected area of the surface of the sample, and a 2-dimensional image is generated that displays spatial variations in these properties. Areas ranging from approximately 1 cm to 5 microns in width can be imaged in a scanning mode using conventional SEM techniques (magnification ranging from 20X to approximately 30,000X, spatial resolution of 50 to 100 nm). The SEM is also capable of performing analyses of selected point locations on the sample. The EDX technique detects x-rays emitted from the sample during bombardment by an electron beam to characterize the

elemental composition of the analyzed volume. Features or phases as small as 1 μm or less can be analyzed[20-22].

Secondary electron images were taken at LISE (Laboratoire Interfaces et Systèmes Electrochimiques) in UPMC with a digital SEM S440 LEICA with a tungsten filament (FEG-SEM) as shown in the Fig. 2-15.

Fig. 2-15 Illustrations of a FEG-SEM (LEICA, Germany) employed in this work.

2.4 Sample preparations

2.4.1 Mechanical polishing

The Al-Cu polycrystalline alloy samples were containing 4.87 wt.% of Cu as characterized by EDX. This Al-Cu alloy called here a model alloy (purchased from *Goodfellow*) was made with initial purity of Cu and Al 99.99 %. The samples in the form of discs (Φ=1cm) were polished with SiC papers (#1200; #2400; #4000) with water, and then with polishing cloth with alumina suspensions (OP-AN, ESCIL Inc.) in order of 3 μm, 1 μm, and 0.3 μm (Fig. 2-16), cleaned separately with acetone, ethanol and ultrapure water (Millipore® water, resistivity $>$ 18 MΩ cm) in an ultrasonic bath for 5, 3, and 1 minute, respectively and dried with compressed air.

Figure 2-16 Polishing cloth, and suspensions for the Al-Cu alloy samples employed in this thesis.

2.4.2 The annealing and aging thermal treatments

The Al-Cu polycrystalline alloy samples were thermally treated in two different ways:

1) the first thermal treatment was to oxidize the as prepared Al-Cu alloy samples *in situ* XPS at low pressure by exposure to O_2 at 1.0×10^{-7} mbar at different temperatures (300 °C, 350 °C, and 400 °C) for 54 h totally, which was described detailed in the chapter 3.

2) the second thermal treatment was to anneal and age the as prepared Al-Cu alloy samples in the system shown in Fig. 2-17. After cleaning, the sample was placed inside a quartz tube, and pumped to vacuum (of around 1.0×10^{-5} mbar). Prior to the formal thermal treatment, the optimization of the annealing temperature among 520 °C, 540 °C, and 560 °C was performed on the Al-Cu samples, respectively. Afterwards, during the formal annealing treatment, the quartz tube with the sample inside was placed in the oven and the pressure of O_2 was kept below 1.0×10^{-5} mbar at the optimized temperature for 1 hour. When the annealing was finished, the oven was moved away and the tube was quenched by ice water to room temperature rapidly. After a quick polishing (#1200→#2400→#4000→3μm→1μm, to obtain a mirror-like

surface without modifying the surface significantly), the sample was placed inside the quartz tube again for aging treatment in air at 300 °C for 10 h followed by 450 °C for 5 minutes. When the aging treatment was finished, the sample was cooled down in the quartz tube and then transported directly to the XPS preparation and analysis chambers for the following measurements.

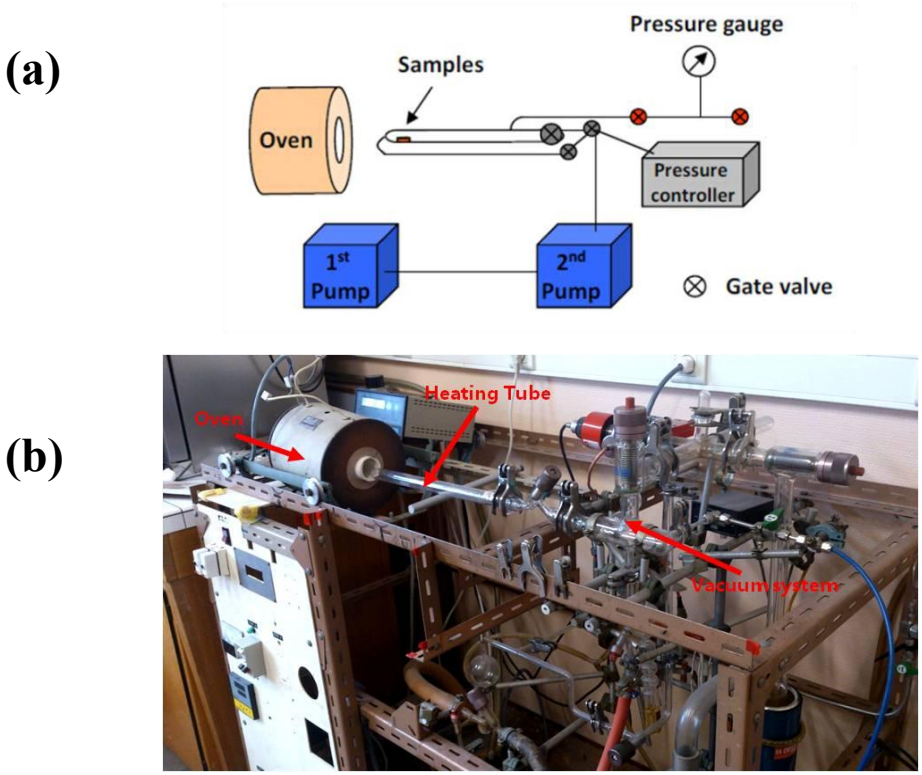

Fig. 2-17 Schema (a) and a picture of the equipment for the annealing and aging treatments by application of a special vacuum system (or around 1.0×10^{-5} mbar).

Fig. 2-18 shows the micrographs of Al-Cu samples after annealing and aging treatments at 520 °C, 540 °C, and 560 °C, respectively, for the optimization of the annealing temperature. Coarse grain boundaries with adjacent dendritic network structures (intermetallic phase) can be observed in the Al-Cu alloy after annealing at 520 °C and aging as shown in the SEM images (Fig. 2-18(a)). As measured by EDX the atomic ratio of Al/Cu of intermetallic phase at the grain boundary is 5.1 ± 1.5, which indicates that the phases are transitional phases, far from the equilibrium θ-phase (Al_2Cu).

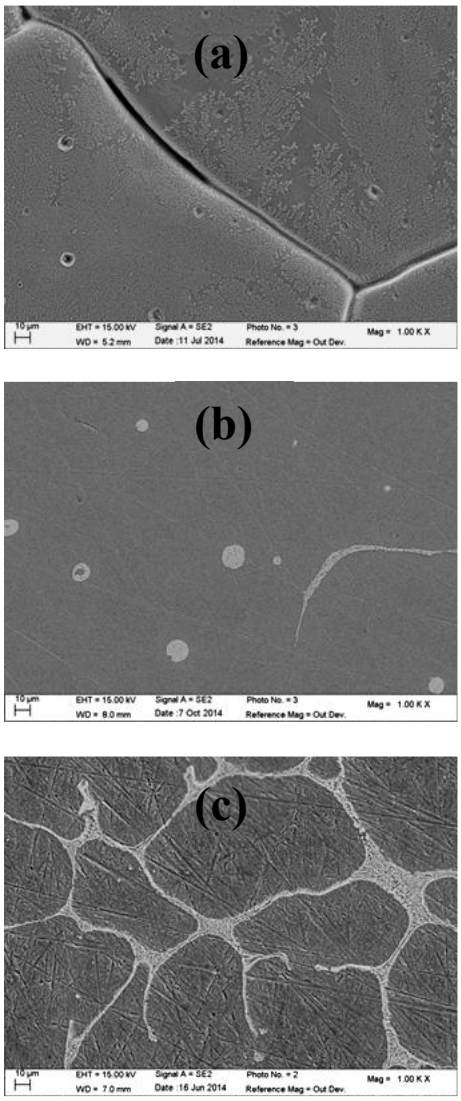

Fig. 2-18 SEM (SE2) images of the Al-Cu samples after annealing and aging treatments: (a) at 520 °C; (b) 540 °C; (c) 560 °C.

Fig. 2-18(b) illustrates the presence of round and dendritic intermetallics distributed uniformly in the Al-Cu alloy after annealing at 540 °C and aging. From the EDX analysis, it can be confirmed that these phases are the near equilibrium θ-phase (Al_2Cu), according to the values of atomic ratio: 2.4 ± 0.5, which is quite close to the atomic ratio of Al_2Cu.

The annealing at 560 °C led to sample melting, and severe modification of surface morphology with a very high roughness with drum-like shape features. SEM (in Fig. 2-18(c)) shows large number of coarse dendritic-like network structure at the grain boundaries with atomic ratio of Al/Cu: 2.7 ± 0.6.

It can be concluded that 540 °C is an optimal temperature combined with the aging treatment to obtain a relatively homogeneous Al-Cu alloy with dispersive intermetallic particles (close to the equilibrium θ-phase (Al_2Cu)). This is also in agreement with the observations reported by Fujda *et al.*[23], in which 540 °C was confirmed as an adequate annealing temperature for Al 2024 alloy generating the dissolution and coagulation of the dispersive intermetallic particles during the following artificial aging, and avoiding the coarse intermetallic phases (as shown in the Fig. 2-18(c)).

References

[1] K. Siegbahn, C. Nordling, A. Fahlman, et al, *Atomic, molecular and solid-state structure studied by means of electron spectroscopy*, Nova Acta Regiae Soc. Sci. Ups., Almqvist and Wiksells, 1967

[2] K. Siegbahn, C. Nordling, G. Johansson, et al, *ESCA Applied to Free Molecules*, North-Holland, Amsterdam, The Netherlands, 1969

[3] J.M. Hollander, W.L. Jolly, *Acc. Chem. Res.*, 3, 193–200 (1970)

[4] J.F. Watts, *Vacuum*, 45, 653-671 (1994)

[5] E. Paterson, R. Swaffield, *Clay Mineralogy: Spectroscopic and Chemical Determinative Methods*, Springer Netherlands, 1994

[6] C. Molina, K. Dahmouche, P. Hammer, et al, *J. Braz. Chem. Soc.*,17, 2006

[7] W.E. SwartzJr., *Anal. Chem.*, 45, 788A–800a (1973)

[8] *Knowledge base*, Thermo Scientific XPS website

[9] D. Briggs, J.T. Grant, *Surface Analysis by Auger and X-ray Photoelectron Spectroscopy*, IM Publications, Chichester, 31-56, 2003

[10] C.D. Wagner, *Faraday Discuss. Chem. Sot.*, 60, 291 (1975)

[11] A.M. Belu, D.J. Graham, D.G. Castner, *Biomaterials*, 24, 3635–3653 (2003)

[12] R.N.S. Sodhia, *Show Affiliations Analyst*, 129, 483-487 (2004)

[13] A. Schnieders, *Microscopy Today*, 19, 30-33 (2011)

[14] D. Pleul, F. Simon, *Poly.Surf. Interf.*, Springer Berlin Heidelberg, 2008

[15] A. Benninghoven, *Chem. Phys. Lett.*, 6, 616 (1970)

[16] P. Sigmund, *Rev. Roum. Phys.*, 17, 823–870, 969–1000, 1079–1106 (1972)

[17] A. Benninghoven, F.G. Rüdenauer, H.W. Werner, *Secondary Ion Mass Spectrometry*, Wiley, New York, 1987

[18] A. Benninghoven, *Surf. Sci.*, 35, 427 (1973)

[19] J.C. Vickerman, A. Brown, N.M. Reed, *Secondary ion mass spectrometry – Priciples and Applications*, Oxford Science, Clarendon Press, Oxford, 1989

[20] J.M. Cowley, *Electron Diffraction Techniques*, 1 and 2, Oxford University Press, New York,1992

[21] N.J. Unakar, J.Y. Tsui, C.V. Harding, *Ophthalmic Res.*, 13, 20–35 (1981)

[22] P. Echlin, C.E. Fiori, J. Goldstein, D.C. Joy, D.E. Newbury, *Advanced Scanning Electron Microscopy and X-Ray Microanalysis*, Springer Science & Business Media, 2013

[23] M. FUJDA, R. MIŠIČKO, L. RUSŇÁKOVÁ and M. SOJKO, *J. Met., Mater. Miner.*, 17, 35-40 (2007)

Chapter 3 Influence of thermal aging treatments on surface chemical modifications of model Al-Cu alloy studied by *in situ* XPS and ToF-SIMS

In this chapter, the Al-4.87wt.% Cu model alloy was employed to investigate the influence of thermal aging treatment on the surface chemical modifications by *in situ* XPS and ToF-SIMS analyses. The Al-Cu alloy samples were heated at temperatures 300 °C→350 °C→400 °C in low pressure (LP) of O_2 for up to 54 hours. XPS revealed that the surface dehydration and/or dehydroxylation offset the oxide growth in the initial stages. The oxidation of Al-Cu alloy is governed by two kinds of mechanisms: the oxidation of Al substrate evidenced by Al oxide growth, and the preferential oxidation of Al in the intermetallic particles (Al_2Cu). In addition, it was evidenced by ToF-SIMS analysis that the thermal treatment promoted the significant segregation of Cu-rich intermetallic particles at the oxide/substrate interface.

3.1 Introduction

Aluminium is remarkable for its low density and high corrosion resistance due to the phenomenon of passivation. However, pure aluminium is too soft thus different alloying elements (*e.g.* Cu, Mn, Mg, Cr, and Si) are usually added to aluminium to provide substantial increase in yield strength in aluminium alloys (AA)[1].

Age hardening is one of the most widely used methods for the strengthening of aluminium alloys. As already discussed in the Bibliographic part (Chapter 1) the age hardening consists in three different stages: a solution treatment at high temperature (548 °C), a quenching and a controlled decomposition leading to formation of finely dispersed precipitates, accompanied by aging at appropriate temperatures. Through this process the strength and hardness of aluminium alloys could be significantly enhanced by the formation of small (from micron to dozens of microns) uniformly dispersed second-phase intermetallic particles (IMP) present within the original phase matrix. The IMPs act as obstacles to dislocation movement and thereby strengthen the heat-treated Al alloys[2]. In the case of the AA 2xxx-series, having copper as a principal alloying element, two types of second phase particles can be formed: θ phase (Al_2Cu) and S phase (Al_2CuMg).

These second phase particles (precipitates) formed during the age-hardening process are known to have negative effects on the corrosion resistance of aluminium alloys, as evidenced by many research groups[3-8]. Bucheit and Birbilis[9,10] revealed that the electrochemical behavior of intermetallic particles in aluminium alloys is much more complicated than the electrochemical behavior of a simple element – *i.e.* metal. About 60% of particles present in 2024-T3 alloy greater than about 0.5 to 0.7 μm are Al_2CuMg (the S phase particles). These types of particles appeared to be more active (anodic IMPs) with respect to the matrix phase[11], which is consistent with bibliographic data presented in the chapter 1. The S phase particles exhibited severe dealloying, which resulted in the formation of Cu-rich particle remnants. Some particle remnants remained largely intact and induced pitting at their periphery once

ennobled by dealloying. Other particle remnants decomposed into 10 to 100 nm Cu clusters that became detached from the alloy surface and can be dispersed by mechanical action of growing corrosion product or solution movement, which can lead to a redistribution of Cu across the surface. However, cathodic intermetallic particles, such as Al_2Cu, which are also present in the aluminium alloy 2024-T3, have noble corrosion potentials significantly nobler than the matrix[12,13]. Copper–containing intermetallic phases support high cathodic reaction rates under most solution conditions, and assist in the initiation of localized pitting corrosion.

As before mentioned there are several studies on the influence of age hardening on the metallurgy of aluminium alloys, their mechanical properties and their corrosion behavior, however there are only few studies which show the evolution of surface chemistry as a function of thermal treatments. Rampulla *et al.*[14] studied the origins of the corrosion resistance of Al-Cu-Fe alloy film annealed in ultrahigh vacuum (UHV) using *in situ* XPS, and found that oxidation occurs *via* the formation of a passivating Al_2O_3 overlay. The oxidation rate during exposure to H_2O vapor (from 8×10^{-9} Torr to 1×10^{-8} Torr at 300 K) was significantly higher than that during exposure to O_2 (from 1×10^{-8} Torr to 8×10^{-8} Torr at 300 K) leading to formation of much thicker layers under H_2O than under O_2. During low exposure to O_2 the oxide coverage rises rapidly and then at higher exposures saturates. Saturation occurs as a result of the passivation of the surface with a thin film of Al_2O_3. Alexander *et al.*[15] found that the air-formed film formed on the pure aluminium stored under ambient conditions resembled oxyhydroxide, while in vacuum (pressure=2.5×10^{-7} mbar) under ambient temperature Al_2O_3 was produced, which revealed significant rehydration upon exposure to the ambient atmosphere. They also reported incomplete dehydration of Al_2O_3 by elemental and functional stoichiometry changes upon vacuum. Jeurgens *et al.*[16] investigated the growth of oxide layers in the UHV processing chamber (base pressure < 2.5 Pa) as function of total oxygen exposure time by heating a clean, recrystallized, pure aluminium (>99.999 wt.%) substrate, and subsequent exposure to pure oxygen gas (99.998 vol%) at an oxygen pressure of 1.33 Pa. They found that at

low temperatures (T≤573 K), an amorphous, Al deficient (as compared to γ-Al_2O_3) oxide film of relatively uniform thickness was formed, while at higher temperatures (T ≥ 673 K), an amorphous Al-enriched oxide film was formed initially, which gradually became crystalline γ-Al_2O_3 with the stoichiometric composition of Al_2O_3 after prolonged oxidation.

The surface chemistry of Al alloys has been more often studied by surface sensitive techniques such as XPS, AES, ToF-SIMS after different pre-treatments (like degreasing and deoxidation processes) usually applied on the classical metal/oxide systems such as Al/Al_2O_3 of the thermally aged alloys[17-23]. These *ex situ* Al alloy pre-treatment can have an important influence on the formation of the oxide layer, enrichment in copper or other elements being the components of the alloy and/or the intermetallic particles, diffusion and or segregation of these elements at the oxide/substrate interface and finally on the formation and/or dissolution of the intermetallic particles. It should be noted that the surface state of the Al alloys will then depend not only on the thermal aging treatment but also on the following pre-treatment processes applied to the surfaces of Al alloys before application of the corrosion protection coatings (conversion coatings or anodization, etc.).

The aim of this work was to investigate the influence of thermal aging treatments (at low oxygen pressure around 1.0×10^{-7} mbar and temperatures ranging from 300 to 400°C) on the modifications of the model Al-Cu alloy such as the oxide growth, the chemical modifications at oxide/substrate interface and the evolutions of the Al-Cu intermetallic particles by *in situ* XPS and ToF-SIMS. The model Al-Cu alloy (with composition of Al-4.87wt.% Cu similar to commercial aluminium alloy AA2024) was used in this study, in order to focus on the particular θ phase (Al_2Cu), and exclude the interferences of other phases (such as Al_2CuMg and $Al_2Mg_3Zn_3$) present in the commercial AA2024 alloys. The surface chemical composition was studied by XPS on the polished Al-Cu alloy, then on the ion-sputtered sample prepared in the UHV preparation chamber of the XPS and then after each step of thermal treatment. ToF-SIMS depth profiling and imaging were employed to investigate the surface, interface

and bulk modifications of the Al-Cu model alloy after the final stage of thermal treatment (performed in the UHV XPS preparation chamber).

3.2 Experimental

Sample preparation. The Al-Cu polycrystalline alloy samples (Goodfellow) contain 4.87 wt.% of Cu as characterized by EDX. The samples in the form of discs (Φ=1cm) were polished on the SiC papers (#1200; #2400; #4000) with water, and then on the polishing cloth with alumina suspensions (OP-AN, ESCIL Inc.) up to 0.3 μm, cleaned separately with acetone, ethanol and ultrapure water (Millipore® water, resistivity＞18 MΩ cm) in an ultrasonic bath for 5, 3, and 1 minute, respectively, and dried with compressed air.

Thermal treatments. Thermal treatment of the as prepared Al-Cu model alloy sample was performed in the XPS UHV preparation chamber. Following the chemical analysis of the polished Al-Cu model alloy sample by XPS (before thermal treatment at low oxygen pressure), the surface of the sample was sputtered with the XR5 gun (15 kV, 150W) for 90 seconds principally to remove the surface contaminations. The slight surface sputtering was used to avoid a preferential sputtering of aluminium and enrichment in copper. Then, the as prepared sample was oxidized at low pressure (LP) by exposure to O_2 at 1.0×10^{-7} mbar (where exposition at 1.0×10^{-7} mbar for 100 s corresponds to 7.5 Langmuir (L)) at different temperatures:

- the first stage of treatment was performed at 300 °C for 6 hours four times,
- the second stage was performed at 350 °C for 6 h two times,
- the last stage was done at 400 °C during 6 h and then during 12 h.

At each step of the thermal treatment, the chemical composition of the thermally treated Al-Cu sample was performed by the XPS analysis. ToF-SIMS profiling and chemical mapping were performed on the polished Al-Cu alloy sample and on the Al-Cu alloy sample after final stage of thermal treatment.

X-ray Photoelectron Spectroscopy Analysis. A Thermo Scientific ESCALAB 250

X-ray Photoelectron spectrometer (XPS) with an Al Kα monochromated radiation (hν=1486.6 eV), was used to analyze the surface chemical composition of the sample (before and after each step of thermal treatment at low oxygen pressure). The energy reference of the spectrometer was calibrated with binding energy (BE) of hydrocarbons (C1s at 285.0 eV). The pressure in the analysis chamber was kept at 1×10^{-9} mbar. The Al Kα monochromated source (hν=1486.6 eV) was operated at 15 kV and the samples were analyzed at a take-off angle of 90°. Survey spectra (BE=0~1060 eV) and the high-resolution spectra (C1s, O1s, Al2p, Al2s, Cu2p and Auger Cu LMM) were recorded with a pass energy of 100 and 20 eV, respectively. Spectra were recorded and analyzed using the Thermo Scientific™ Avantage Software (version 5.954). For curve fitting and decomposition, a Shirley-type background subtraction was used and the shape of fitting curves was determined by a 70% Gaussian / 30% Lorentzian distribution, typical for the spectra fitting for metals/oxides[24].

Time-of-Flight Secondary Ion Mass Spectrometry Analysis. Time-of-Flight Secondary Ion Mass Spectrometry (ToF-SIMS) was employed to analyze elemental species present on the sample surface, and asses the distribution in high resolution following the XPS analysis (sample was exposed in air during the transferring), using a ToF-SIMS V spectrometer (ION TOF GmbH-Munster, Germany). The analysis was carried out on the sample after polishing and after the final thermal treatments (during 54 h, at low O_2 pressure at different temperatures from 300 °C to 400 °C) as described above. The analysis chamber was maintained at about 1×10^{-9} mbar. Depth profiles were performed using sputtering with Cs ion gun: Cs^+ 2 keV, 100 nA (300×300 μm^2) and analysis with Bi ion gun: Bi^+ 25 keV, 1.1 pA (100×100 μm^2). Chemical images of the polished Al-Cu model alloy and after thermal treatments were performed by using a pulsed Bi^+ 25 keV primary ion source, delivering 0.1 pA current over a 100×100 μm^2 area.

3.3 XPS results

3.3.1 Surface chemistry of polished Al-Cu model alloy

Fig. 3-1 presents the XPS core level C1s, Al2p, Al2s, Cu2p, Auger Cu LMM and O1s spectra recorded on the polished Al-Cu model alloy sample.

The high resolution C1s core level spectrum can be fitted with three peaks, attributed to the CH_2-CH_2 bonds (BE= 285.0 ± 0.1 eV), the C-O bonds (BE= 286.1 ± 0.1 eV), the C=O bonds (carboxyl groups, BE= 288.6 ± 0.1 eV), and the carbonates (BE= 290.0 ± 0.1 eV), respectively[25]. These peaks can be explained by the presence of low quantity of organic contaminations on the metallic substrates after exposure to ambient air.

The Al2p core level can be decomposed into the lower binding energy peaks at 72.3 ± 0.1 and at 72.8 ± 0.1 eV assigned to the $Al2p_{3/2}$ and $Al2p_{1/2}$ spin orbit doublet of metallic aluminium. The FWHM of the $Al2p_{1/2}$ spin orbit component (1.00) is larger than that of $Al2p_{3/2}$ (0.63), and the $Al2p_{1/2}$:$Al2p_{3/2}$ area ratio is 0.50 ± 0.01, which is consistent with the theoretical value[26]. The higher Al2p peak with BE=74.6 ± 0.1 eV is attributed to the Al hydroxide ($Al(OH)_3$ and/or AlOOH), and the Al2p peak at 75.5 ± 0.1 eV is assigned to the Al oxide[27,28,29]. The peaks at 76.1 ± 0.1 eV and 78.1 ± 0.1 eV can be assigned to the spin orbit doublet $Cu3p_{3/2}$ and $Cu3p_{1/2}$ of metallic copper[30-32] overlapping the Al2p area. The peaks at binding energy of 15.8 eV higher than the metallic aluminium peak (*i.e.* at around 88.2 ± 0.1 eV) correspond to bulk plasmon losses[33-36].

The Al2s core level is also included here in Fig. 3-1 in order to confirm the correct decomposition of Al2p core level spectra where the interference of the Cu2p is present. The Al2s peak can be decomposed into four peaks: a peak at 117.8 ± 0.1 eV assigned to the Al metal[37,38], a peak at 119.1 ± 0.1 eV assigned to the Al hydroxide ($Al(OH)_3$ and/or AlOOH)[39], and a peak at 120.6 ± 0.1 eV assigned to the Al oxide[40]. The ratio between the oxide and hydroxide here in the Al2s core level region is basically the same as that in the Al2p core level (7.3 *vs* 7.7), which verified the correct

decomposition of Al2p core level. However, the contribution of copper in the region of the Al2s is also observed, which can be confirmed by the presence of the highest binding energy peak at 122.6 ± 0.1 eV assigned to the Cu3s (corresponding the metallic copper)[41,42].

The nature of copper was determined from the Cu2p core level spectra (with the $Cu2p_{3/2}$ at 932.9 ± 0.1 eV) and the Cu LMM (not shown here). According to Auger parameter (α) of 1851.8 ± 0.1 eV the presence of metallic copper was confirmed (Tab. 3-1)[43-45]. In addition, the presence of CuO is thought to be unlikely also because the characteristic shake-up satellites expected at 943.5 ± 0.1 eV are not observed[46,47].

Tab. 3-1 Auger parameter (α) for Cu calculated for the polished Al-Cu alloy surface.

BE of Cu LMM	Cu Auger	$Cu2p_{3/2}$	α	Status
568.97	918.9	932.9	1851.8	Metallic Cu

The O1s core level can be fitted with two peaks attributed to the Cu oxides (530.2 ± 0.1 eV), oxide ions of the alumina matrix (531.4 ± 0.1 eV)[48], hydroxyl groups (like AlOOH or $Al(OH)_3$ species) or contaminants (carboxyls and/or carbonates) (532.3 ± 0.1 eV) already observed in the C1s core level region, and water molecules adsorbed on the sample surface (533.2 ± 0.1 eV), respectively[49-54]. Although the lower binding energy peak is unanimously attributed to oxide, the presence of hydroxyl groups cannot be completely excluded as it has been observed that the presence of oxide may favor the dissociative adsorption of water[55,56]. It indicates that under ambient conditions the air-formed film on the aluminium alloys appeared to be oxyhydroxide instead of the stoichiometric composition of γ-Al_2O_3 owing to the rehydration upon exposure to the ambient atmosphere. Similar results have been reported for the pure aluminium and aluminium alloys[23,24,57,58].

The O:Al atomic ratio calculated from O1s (at 531.4 ± 0.1 eV) and Al2p (at 75.5 ± 0.1 eV) corresponding to the Al_2O_3 is around 1.5, which is consistent with the theoretical stoichiometry of Al_2O_3 (O:Al = 1.5). This atomic ratio is an evidence of a

correct decomposition of O1s and Al2p core levels indicating the presence of the metallic aluminium, the aluminium oxide (Al_2O_3), the hydroxyl groups ($Al(OH)_3$ or AlOOH) and also the metallic copper (Cu3p peak overlapping Al2p)[59].

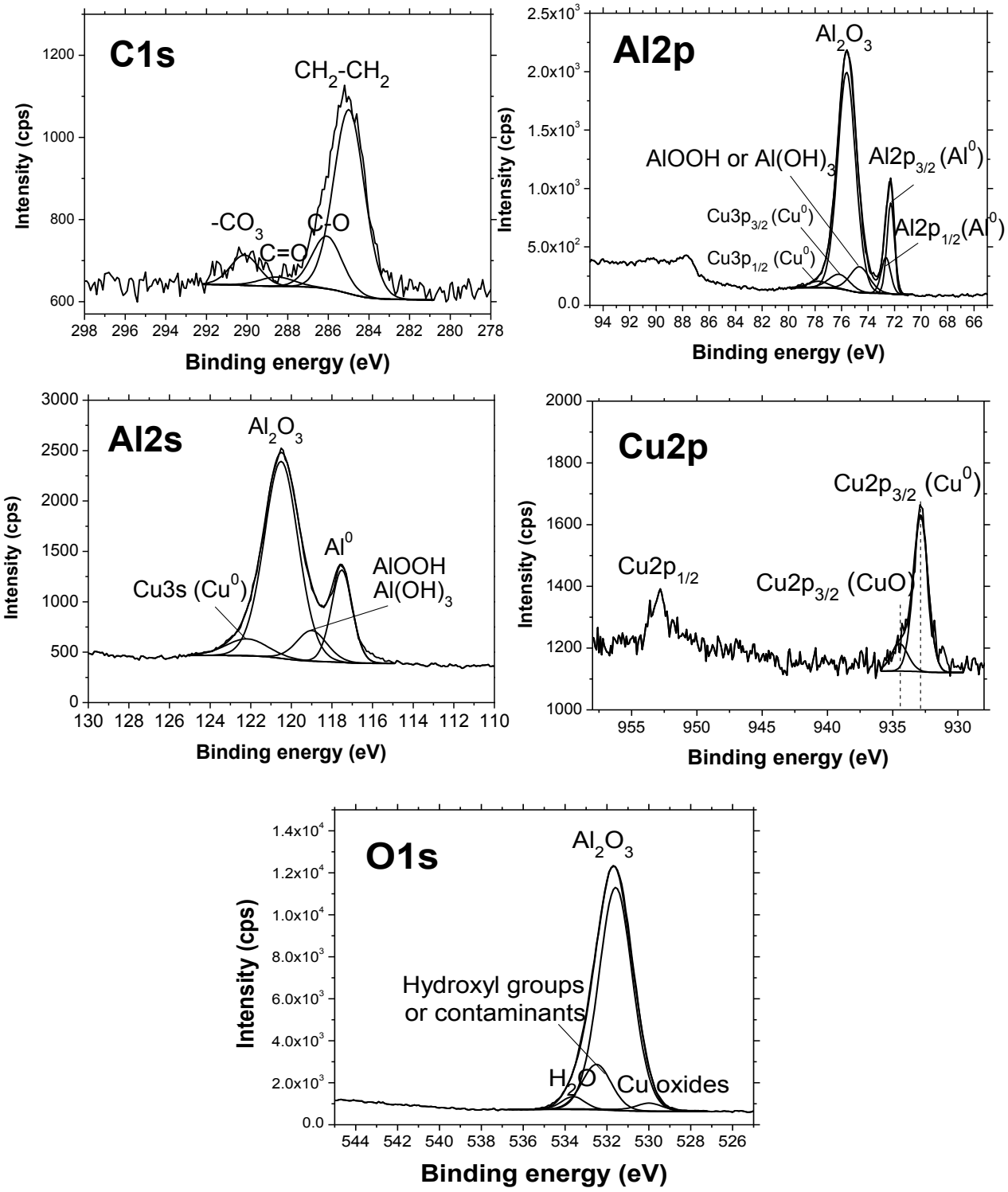

Fig. 3-1 High resolution C1s, Al2p, Al2s, Cu2p and O1s XPS spectra recorded on the polished Al-Cu model alloy.

3.3.2 Chemical surface modifications induced by thermal treatments

The very low sputtering applied to the Al-Cu model surface, as specified in the experimental part, removed principally the carbonaceous contaminations decreasing by about 79.7 at.% on the sputtered surface compared with the polished surface.

Fig.3-2 shows the changes in the O1s core-level peak as a function of thermal treatment of the Al-Cu surface, starting from 0 Langmuir corresponding to the sputtered surface. For the sputtered surface before thermal treatment (0 L), the main component at lower binding energy of 530.4 ± 0.1 eV (BE) is attributed to Cu oxide, at higher BE of 531.4 ± 0.1 eV (BE) is attributed to Al oxide, and the peak at highest BE of 532.3 ± 0.1 eV to the hydroxyl groups (like AlOOH or $Al(OH)_3$ species) and the contaminants (carboxyls and/or carbonates). After the low-pressure O_2 exposure at 300°C for 6 hours (1620 L) the contributions of hydroxyl decreased significantly, what can be concluded from the more symmetrical shape of O1s. After 24-hour exposure to O_2 (6481 L), the contributions from the hydroxyls groups is not observed anymore in the O1s region.

The change in the total area of O1s peak as a function of the exposure to LP O_2 is presented in Fig. 3-3. The data (the binding energies (BE), the full-widths at half maximum (FWHM)) of the high resolution main O1s peak core level spectra are compiled in Tab.3-2. The significant increase of O1s peak area can be observed when the sample was exposed to O_2 in the initial stage (about the first 3200 L) at 300 °C, which can be attributed to the growth of the Al oxide. However, the area of O1s peak decreased as the exposure to O_2 at 300 °C went on (after about 3200 L), probably related to the surface dehydration and/or dehydroxylation, which has been reported by Papee *et al*.[60] that heating of Al substrate covered by oxide/hydroxide layer (under vacuum at T ≥170 °C) leads to dehydration.

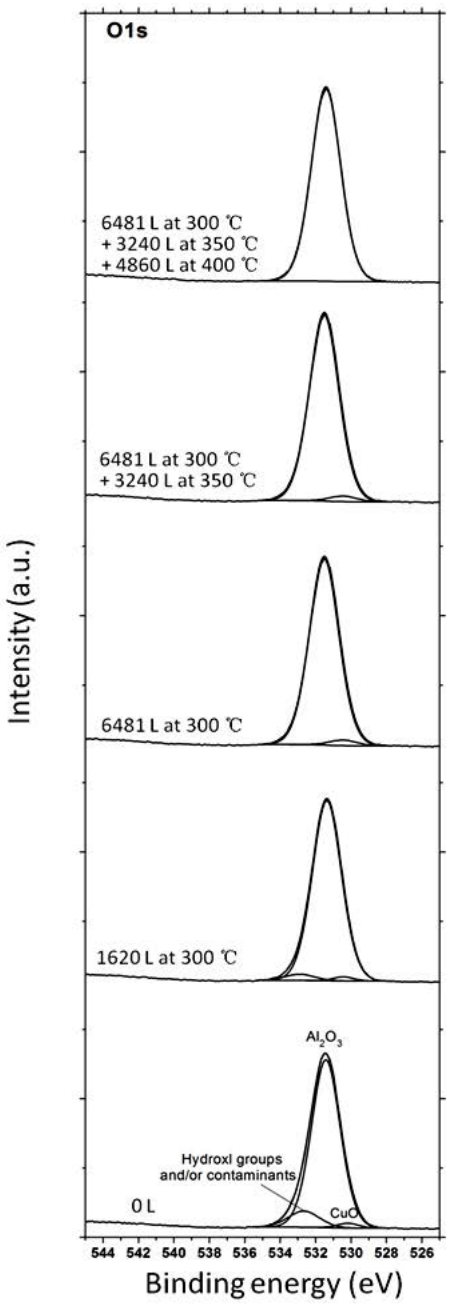

Fig. 3-2 XPS spectra of the O1s core level after LP exposure of the Al-Cu alloy to O_2 at 300, 350, 400°C. The exposure to oxygen at different temperatures is expressed in Langmuir (L).

During the following stage of exposure (from 6481 L to around 11300 L) at higher temperatures 350 °C and 400 °C, the area of the O1s peak re-increased, which indicates the continuous oxide growth[61,62]. Nevertheless, the area of O1s peak slightly decreased once again after about 11300 L of exposure at 400 °C. By comparing two last O1s peaks (one obtained at 350°C and the last one at 400°C, Fig. 3-2), it can be revealed that the peak assigned to the Cu oxide disappeared completely, which can be

explained by the reduction of CuO with CO or preferential aluminium oxidation and segregation of copper and copper oxide at surface defects or at grain boundaries or at surface oxide/substrate interface region. The possible copper reduction can take place under high-temperature conditions (≥250 °C at the ambient pressure) according to reaction 3-1 as already reported in the literatures[63-66]:

$$CuO + CO \rightarrow Cu + CO_2 \qquad \text{Eq. 3-1}$$

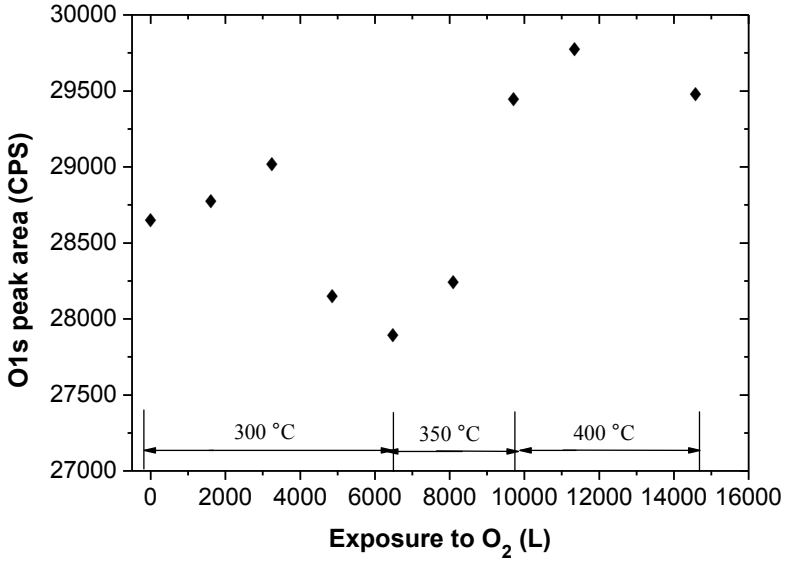

Fig. 3-3 Change in the O1s core level peak area as a function of LP exposure to O_2 at different temperatures.

Fig. 3-4 shows the changes of the Al2p and $Cu2p_{3/2}$ core levels as a function of LP oxygen exposure of the Al-Cu surface at different temperatures. Similar contributions can be observed on the sputtered Al-Cu model alloy as on the polished Al-Cu sample presented above (Fig. 3-1). The peak attributed to the Al hydroxide disappears completely after 24-hour-exposure (6481 L) at 300 °C and only higher peak at 75.5 ± 0.1 eV attributed to the Al oxide can be observed, which is consistent with the O1s peak decomposition (shown in the Fig. 3-2). In addition, the peaks at 76.1 ± 0.1 eV and 78.1 ± 0.1 eV assigned to the spin orbit doublet $Cu3p_{3/2}$ and $Cu3p_{1/2}$[67] can be observed up to (6481 + 3240) L of exposure to O_2.

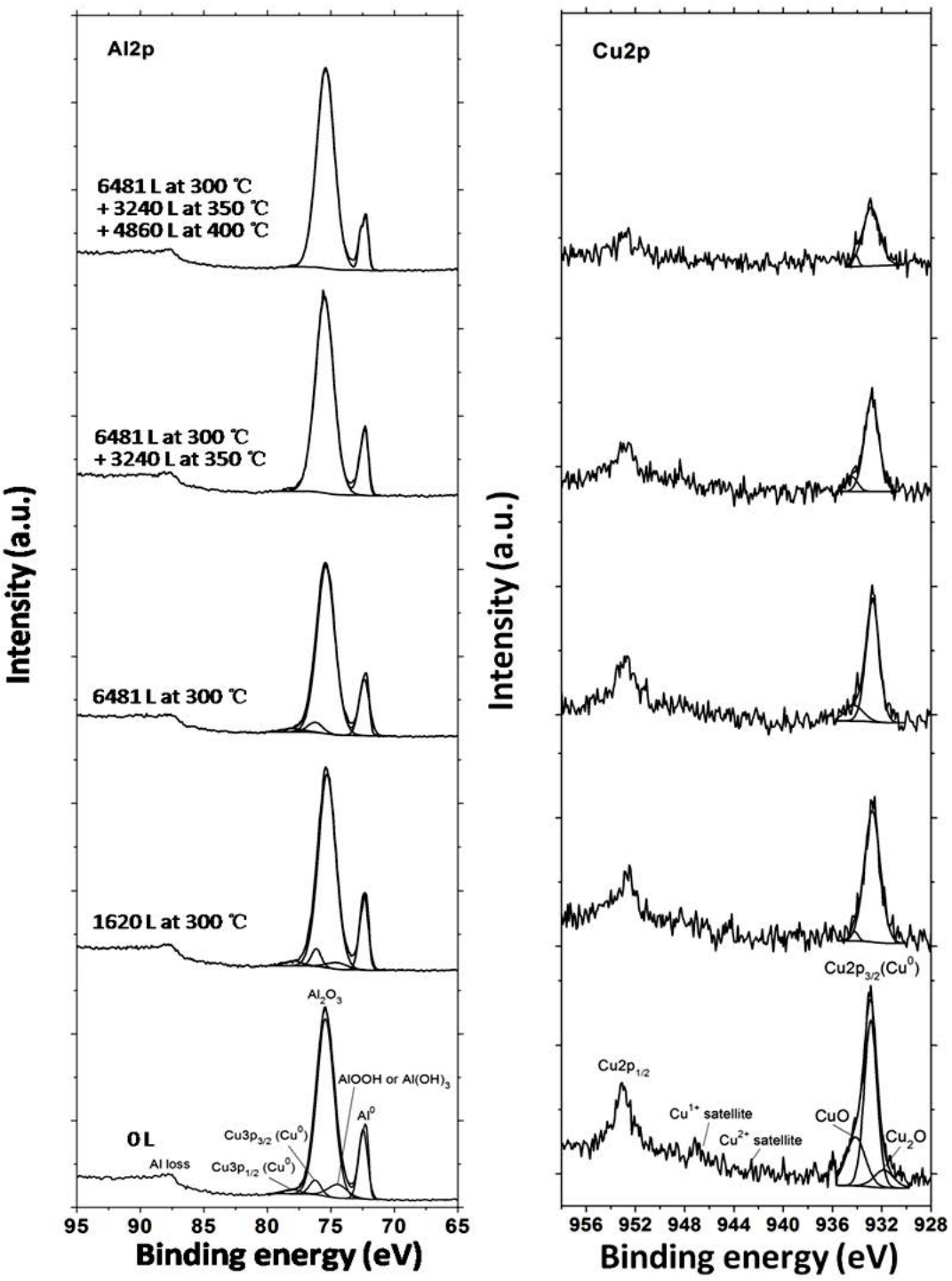

Fig. 3-4 XPS spectra of Al2p and Cu2p core levels as a function of LP exposure of the Al-Cu alloy to O_2 at 300, 350, 400°C. The exposure to oxygen at different temperatures is expressed in Langmuir (L).

On the sputtered surface before thermal treatment, small-intensity peaks can be observed at higher BE of 934.2 ± 0.1 eV and lower BE of 932.0 ± 0.1 eV than the metallic copper (932.8 ± 0.1 eV). These small-intensity peaks can be attributed to

CuO and Cu_2O, respectively, confirmed by the presence of satellite features at 943.5 ± 0.5 eV and 945.5 ± 0.5 eV[68]. However, due to the high signal-to-noise ratio and the low intensity, the existence of CuO and Cu_2O cannot be confirmed.

At further stages of the thermal treatment (from 300 °C up to 400 °C), although the Cu signal attenuated quite rapidly, the existence of CuO/Cu_2O can still not be totally excluded on the surface. Furthermore, the peak assigned to the Cu_2O on the sputtered surface disappeared during the thermal treatments, which may also be attributed to the oxidation of Cu_2O forming CuO during the heating[69].

The data (binding energies (BE) and full-widths at half maximum (FWHM) of the high resolution main Al2p peak core level spectra for metal and oxide components) are compiled in Tab.3-2. Upon exposure to oxygen, the O:Al atomic ratios calculated with the corresponding O1s (at 531.4 ± 0.1 eV) and to Al2p (at 75.5 ± 0.1 eV) attributed to the Al_2O_3 are 1.42 ± 0.08, which is consistent with the theoretical stoichiometry of Al_2O_3 (O:Al = 1.5). Small variations in the O:Al ratio can be related to the uncertainty in the peaks decompositions, which is beyond 10%.

Estimation of the Al and Cu concentrations and the thickness of the aluminium oxide layer are feasible from the Al2p core level based on the prior studies[70,71]. However, it should be noted that the contribution of Al hydroxide to the passivation layer on the polished surface and the sputtered surface (as shown in the Fig. 3-1) was not taken into account; therefore, a slight underestimation of the true film thickness can be predicted.

Tab. 3-2 BE and FWHM for the O1s and Al2p (metallic aluminium) and Al2p (aluminium oxide) peaks as a function of LP exposure to O_2 at different 300, 350 and 400 °C.

Exposure (L)	O1s (oxide)		Al2p (metal)		Al2p (oxide)	
	BE (eV)	FWHM (eV)	BE (eV)	FWHM (eV)	BE (eV)	FWHM (eV)
0	531.3	2.01	72.7	0.66	75.5	1.78
1620@300 ℃	531.4	2.03	72.8	0.59	75.4	1.78
3240@300 ℃	531.4	2.02	72.7	0.67	75.4	1.77
4860@300 ℃	531.3	2.03	72.7	0.62	75.3	1.82
6481@300 ℃	531.5	2.02	72.6	0.61	75.5	1.80
6481@300 ℃ +1620@350 ℃	531.5	2.00	72.8	0.65	75.6	1.71
6481@300 ℃ +3240@350 ℃	531.4	1.99	71.5	0.65	75.7	1.77
6481@300℃ +3240@350℃ +1620@400℃	531.5	2.01	72.7	0.61	75.5	1.78
6481@300℃ +3240@350℃ +4860@400℃	531.5	1.96	72.8	0.50	75.6	1.71

The calculation of the oxide thickness assuming a homogenous distribution of the Al_2O_3 on the Al-Cu alloy substrate (before and after thermal treatment) was performed using the intensites of the Al2p and $Cu2p_{3/2}$ peaks with the following equations[72]:

$$I_{Alm} = K\delta_{Al}\lambda_{Alm}D_{Alm}\tau_{Al}exp\ (-d/\lambda_{Al}^{Alox}) \quad \text{Eq. 3-2}$$

$$I_{Cum} = K\delta_{Cum}\lambda_{Cum}D_{Cum}\tau_{Cu}exp\ (-d/\lambda_{Cu}^{Alox}) \quad \text{Eq. 3-3}$$

$$D_{Alm} + D_{Cum} = 1 \quad \text{Eq. 3-4}$$

$$I_{Alox} = K\delta_{Al}\lambda_{Alox}D_{Alox}\tau_{Al}[1-exp(-d/\lambda_{Al}^{Alox})] \quad \text{Eq. 3-5}$$

where d is the oxide thickness; D_{Alox} and D_{Alm} are the densities of Al in the oxide and the metal phases, respectively; λ_{Al}^{Alox} and λ_{Cu}^{Alox} are the attenuation lengths of the Al and Cu photoelectrons in the oxide; λ_{Alm}, λ_{Alox}, and λ_{Cum} are the attenuation lengths of the Al and Cu photoelectrons in the metal; $I_{X(Y)}$ is the intensity of the X peak (element

X) corresponding to *Y* species, τ is the result of experimental photoelectron yield multiplied by $sin\theta$ (θ is the photoelectron take-off angle, θ = 90°); δ is the experimental photoelectron yield, which is assumed to be the same for Al in the metal and in the oxide; and *K* is an instrument constant. The values of λ are: λ_{Alm} = 19.3 Å, λ_{Al}^{Alox} = 21.9 Å and λ_{Cu}^{Alox} = 13.7 Å, D_{Alm}= 0.100, D_{Alox} = 0.078 moles cm^{-3}, τ_{Al} = 45853, τ_{Cu} = 63468, δ_{Al} = 0.537, δ_{Cum} = 16.73.

After combining and rearranging Eq.3-2 and Eq.3-3, the I_{Alm}/I_{Cum} can be expressed as follows:

$$\frac{I_{Alm}}{I_{Cum}}=\frac{\delta_{Al}\lambda_{Alm}D_{Alm}\tau_{Al}exp\ (-d/\lambda_{Al}^{Alox})}{\delta_{Cum}\lambda_{Cum}D_{Cum}\tau_{Cu}exp(-d/\lambda_{Cu}^{Alox})} \qquad \text{Eq. 3-6}$$

And the Eq.3-2 and Eq.3-5 can be combined, and the I_{Alm}/I_{Alox} can be expressed as:

$$\frac{I_{Alm}}{I_{Alox}}=\frac{\lambda_{Alm}D_{Alm}exp\ (-d/\lambda_{Al}^{Alox})}{\lambda_{Alox}D_{Alox}exp[1-exp(-d/\lambda_{Al}^{Alox})]} \qquad \text{Eq. 3-7}$$

Combined with the Eq.3-2, Eq.3-4 and Eq.3-5, the thickness of the oxide and the concentrations of Al and Cu can be calculated by solving the Eq.3-8 and Eq.3-9. The obtained data are shown in Table 3-3, and the oxide thickness modifications as a function of the thermal treatment at low oxygen pressure are graphically presented in Fig. 3-7.

$$\frac{I_{Alm}}{I_{Cum}}=\frac{\delta_{Al}\lambda_{Alm}D_{Alm}\tau_{Al}exp\ (-d/\lambda_{Al}^{Alox})}{\delta_{Cum}\lambda_{Cum\,(}1-D_{Alm)}\tau_{Cu}exp(-d/\lambda_{Cu}^{Alox})} \qquad \text{Eq. 3-8}$$

$$\frac{I_{Alm}}{I_{Alox}}=\frac{\lambda_{Alm}D_{Alm}exp\ (-d/\lambda_{Al}^{Alox})}{\lambda_{Alox}D_{Alox}exp[1-exp(-d/\lambda_{Al}^{Alox})]} \qquad \text{Eq. 3-9}$$

Tab.3-3 Atomic percentage (AA) of metallic Al and metallic Cu determined from above equations using the Al2p and Cu2p$_{3/2}$ core level intensity.

Exposure (L)	AA.% of Al	AA.% of Cu	Thickness of Al oxide/Å
0 (Polished surface)	75.6	24.4	70.7
0 (Sputtered surface)	67.0	33.1	70.4
1620@300 ℃	67.6	32.4	73.4
3240@300 ℃	71.3	28.7	74.6
4860@300 ℃	72.1	27.9	73.4
6481@300 ℃	71.1	28.9	75.1
6481@300 ℃+1620@350 ℃	77.0	23.0	75.2
6481@300 ℃+3240@350 ℃	76.4	23.6	78.2
6481@300℃+3240@350℃+1620@400	75.4	24.6	81.5
6481@300℃+3240@350℃+4860@400	73.7	26.3	81.7

As already discussed above, the thinner oxide layer present on the sputtered surface is related to the small removal of contamination layer as well as oxide/hydroxide layer. However, it should be noted that sputtering led to remarkable surface enrichment with Cu (from 24.4 at.% to 33.1 at.%) (Fig. 3-5(b)), because the lighter Al atoms in the binary Al-Cu system are more easily sputtered away[73,74]. Since the first stage of the thermal treatment of the Al-Cu model sample, the Al oxide layer shows a thickness increase as a function of the thermal treatments from 300 °C to 350 °C, as indicated in a Table 3-3 and in Fig. 3-5(a). At the same time a decreasing concentration of Cu near the surface from around 33.1 to 23.6 at.% as a function of the thermal treatment can be observed, which can be attributed to the attenuation of detected Cu signal as the oxide grew and the low diffusion rate of Cu atoms from the bulk to the surface at the beginning stage of thermal treatments. Nevertheless, during the last stage of heating at higher temperatures from 350 °C to 400 °C, the concentration of Cu raised slightly (from 23.6 at.% to 26.3 at.%). This rebound could be related to the higher diffusion speed of Cu atoms from bulk of Al-Cu alloy to the

interface region (oxide /substrate) at higher temperatures (>350° C) [75, 76]. The confirmation of this hypothesis will be presented hereafter by means of ToF-SIMS depth profiles and ToF-SIMS chemical mapping performed on the Al-Cu sample after the final stage of thermal treatment.

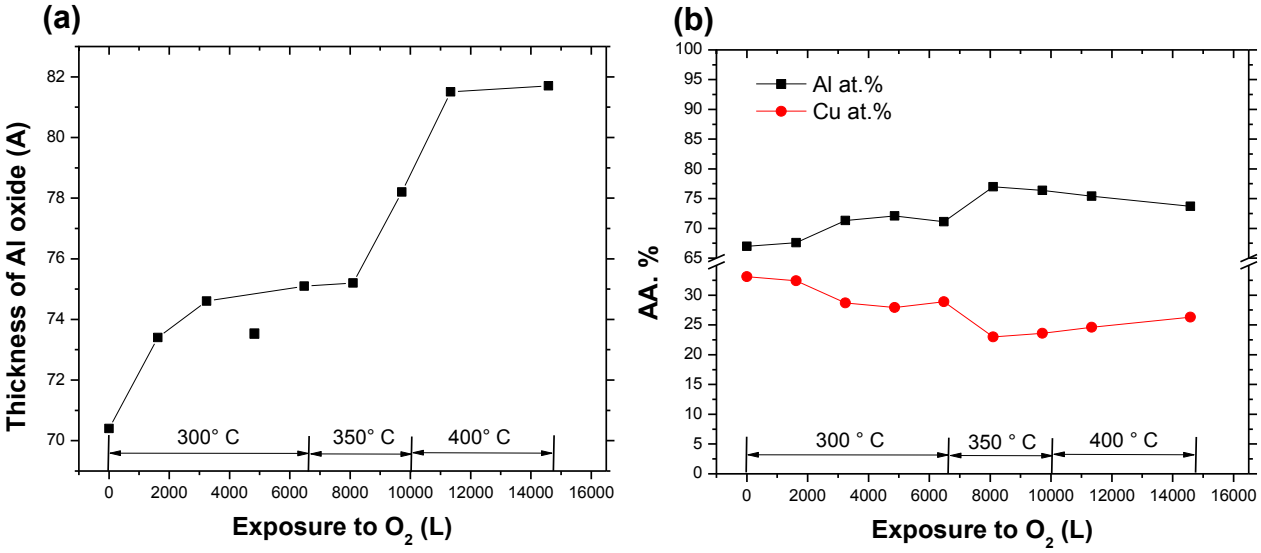

Fig. 3-5 The evolution of Al_2O_3 thickness a) and the atomic concentration of Al at.% (black squares) and Cu at.% (red dots) b) as a function of LP O_2 exposure at 300, 350 and 400 °C temperatures.

3.4 ToF-SIMS results

ToF-SIMS negative ion depth profiles of the Al-Cu polished sample before and after the final thermal treatment including LP O_2 exposition at 300 °C (6481 L), 350 °C (3240 L) and 400 °C (4860 L) are presented in Fig. 3-6. For both samples, three main regions can be identified:

- the first one characterized by high and relatively constant intensity of AlO^-, AlO_2^- and $^{18}O^-$ signals assigned to the presence of an aluminium oxide film formed on the substrate alloy,
- the second interfacial region characterized by drastic decreasing intensities of AlO^-, AlO_2^- and $^{18}O^-$ ions and increasing intensities of Al_2^- signal,
- the third substrate region with a large and constant Al_2^- signal.

Slight difference in the sputtering time of the first region can be observed for both samples. The increase of the sputtering time from 30 (for polished sample) to 47 s (for a thermally treated sample) confirms a growth of oxide layer as confirmed by the XPS results (seen in the Fig. 3-2 and Fig. 3-5). However, the increased thickness values of the oxide are different indicated by XPS and ToF-SIMS. This might be due to several reasons: 1) the XPS results and ToF-SIMS results were obtained from different Al-Cu alloy samples, on which the oxide layers differed; 2) the measurement of XPS and ToF-SIMS were not carried out exactly at the same time, which resulted in the growth of the oxide exposed to the air; 3) the identification of the oxide layer region based on the sputtering time could not be strictly accurate, in which errors is not excluded. A constant Cu^- signal in the oxide region present on the polished Al-Cu surface indicates a more homogenous distribution of copper in this case than in the case of thermally treated sample. A significant depletion in copper can be observed in the oxide grown at LP O_2 (for the thermally treated sample) as it can be deduced by much lower signal intensity of Cu^-, which is almost identical with intensity of Al^- ion signal in the first region. The copper decrease at the Al-Cu alloy surface with increasing the LP O_2 exposition at higher temperatures was clearly evidenced by XPS results presented above (as shown in the Fig. 3-4 and 3-5). However, a higher Cu^- signal gradient between the first and the second region for thermally treated sample can indicate a thermally induced accumulation of the copper at the interfacial aluminium oxide/metallic substrate region. This type of Cu enrichment at the oxide/metal interface during oxide formation has been previously reported on Al-Cu series alloys[77,78,79]. It should be also noted that the increase Cu intensity in the interfacial region can be related to the higher density and bigger sizes of the Cu-rich intermetallic particles. To confirm this hypothesis a ToF-SIMS chemical mapping was performed on both samples.

The third region corresponding to Al-Cu substrate does not show particular differences for both polished and thermally aged samples.

Fig. 3-7(a) and (b) show 100×100 μm^2 negative ion images for polished Al-Cu

sample and for Al-Cu sample after a final stage of thermal treatment (Bi^+ current: 0.2 pA, Cs^+ current: 100mA). The images acquired at different depths, corresponding to surface, interface and substrate regions were performed according to depth profiles presented in Fig. 3-6. For the polished Al-Cu alloy sample the surface, interface and substrate region correspond to 3 s, 48 s, and 148 s of sputtering, respectively.

The images obtained after 3 s of sputtering in the near surface region showed an intact native aluminium oxide film formed on the Al-Cu alloy. However, there are already small intermetallic particles (weak Cu^- signal intensity) in the surface layer after polishing. With a sputtering depth closer to the metal/oxide interface, large isolated areas with higher Cu^- intensity, and some corresponding areas of low Al_2^- intensity are detected. After 48 seconds of sputtering, there is clear evidence for isolated Cu-rich regions. After 148 seconds of sputtering, no further evidence of localized Cu enrichment was obtained on ion images, and homogenous distribution of copper in the Al-Cu alloy matrix could be observed.

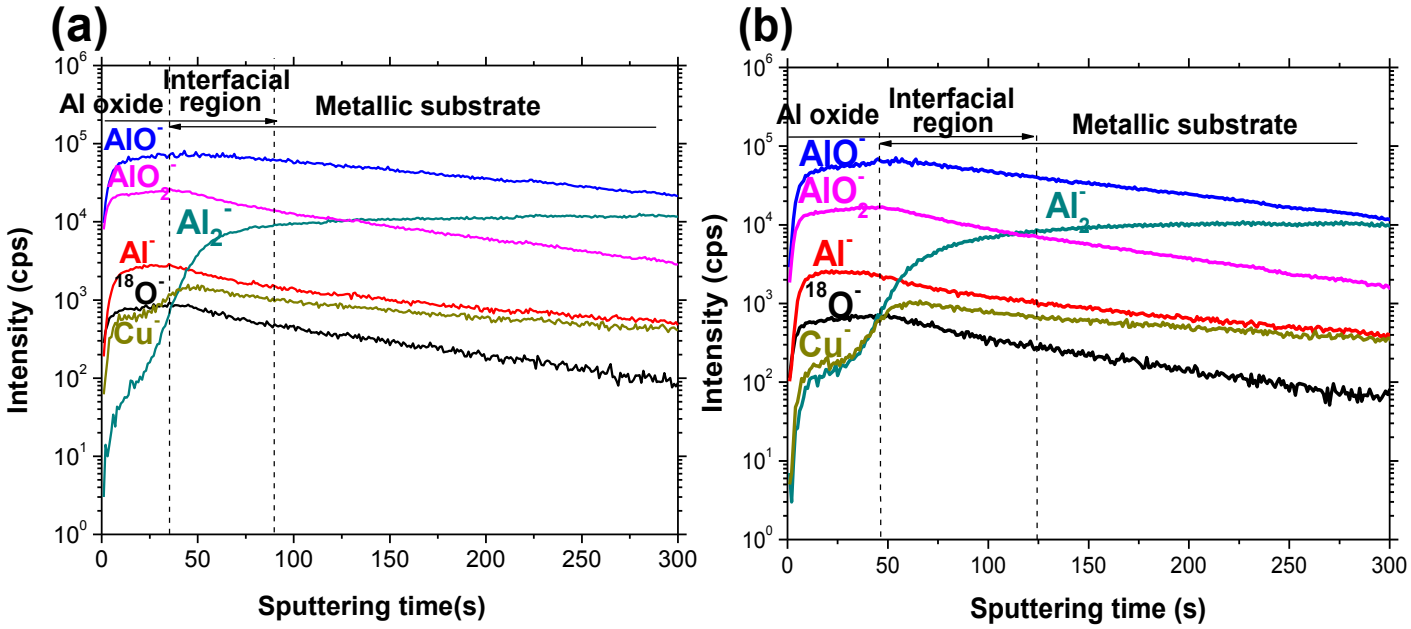

Fig. 3-6 ToF-SIMS negative ion depth profiles obtained on the Al-Cu model samples: (a) after mechanical polishing; (b) after final thermal treatments performed at the LP O_2 at 300 °C (6481 L), 350 °C (3240 L) and 400 °C (4860 L).

Fig. 3-7(b) shows 100×100 μm^2 negative ion images ($^{18}O^-$, AlO^-, Al_2^-, Cu^-) in high lateral resolution mode for Al-Cu sample after thermal treatments for 10 s, 60 s, and 310 s of sputtering, which correspond to the near surface region, the interface between the oxide layer and metallic substrate and to the metallic substrate, respectively. The images for the polished and thermally treated samples obtained in the near surface region indicate the formation of a homogeneous aluminium oxide film. As the sputtering time increases close to the oxide/substrate interface, the isolated areas showing higher Cu^- intensity indicate a large-amount of the intermetallic particles (Al enriched in Cu). Compared to the polished sample, a thermally treated Al-Cu alloy shows much more significant Cu^- signals in the interfacial region resulting from sample exposition to higher temperatures under LP O_2. High intensity Cu signals indicates formation of Cu-enriched, cluster-like particles with a round and elliptical shape with diameters ranging from 2~20 μm. After 310 seconds of sputtering when reaching the alloy substrate, some spots with high intensity of AlO_2^- signals corresponding to low Al_2^- signals are detected. These spots correspond to high intensity of Cu^- signal observed previously in interfacial region. The lack of the high intensity copper signal in the substrate region can indicate that the copper-rich intermetallic particles are surrounded by aluminium oxide layer. The size and position of AlO^- and Cu^- indicate a preferential oxidation of Al around the Cu-rich intermetallic particles, resulting in intrusions of particles with Al oxide and formation of a core-shell structure with copper rich as a core and aluminium oxide as a shell.

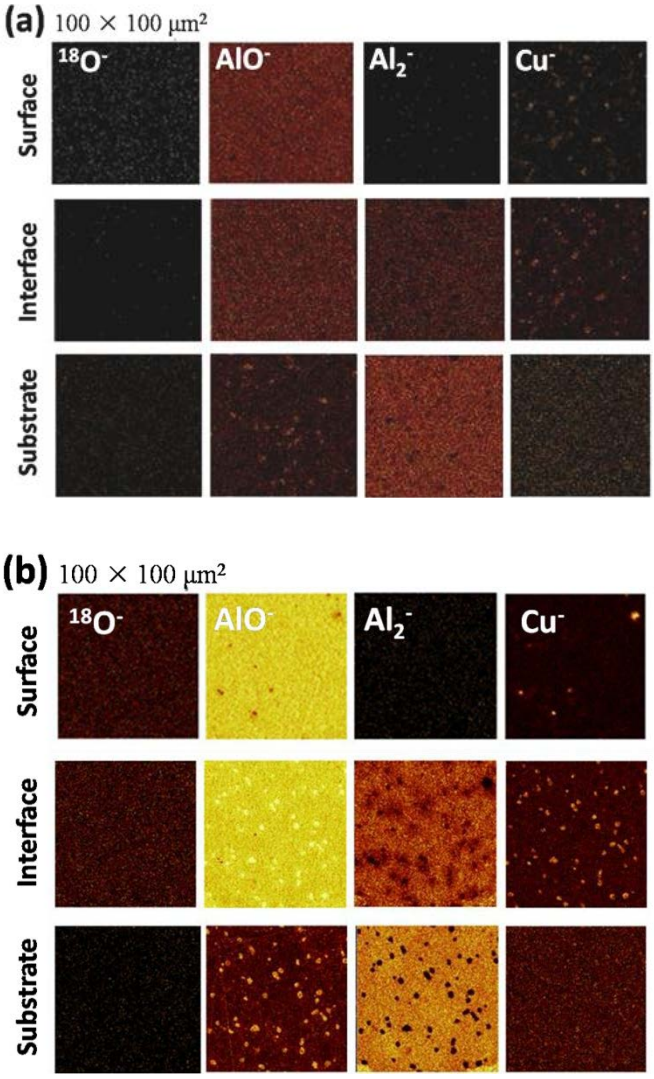

Fig. 3-7 ToF-SIMS negative ion images of $^{18}O^-$, Al_2^-, AlO_2^- and Cu^- recorded on the Al-Cu model alloy sample: (a) after mechanical polishing; (b) after final thermal treatment performed at the LP O_2 exposition at 300 °C (6481 L), 350 °C (3240 L) and 400 °C (4860 L).

However, the ToF-SIMS imaging performed on the polished sample does not exclude that the intermetallic particles already present in the non-treated Al-Cu alloy are slightly oxidized on the surface (which can be deduced from high intensity AlO^- signal observed in the substrate region, and can be superimposed with high intensity of Cu^- signal in the interface region in Fig. 3-7(a)). The copper enrichment at the oxide/substrate interface region induced by thermal treatments was not observed by the surface analysis made by XPS. The XPS data show the aluminium oxide growth and the depletion of the oxide layer with copper (see Fig. 3-5). The clearly discernable

AlO^-, Al^- and Cu^- signals observed by ToF-SIMS at different sputerring depth for sample after thermal treatments indicate the formation of copper-rich intermetallic particles and their segregation at oxide/metal interfacial region.

The evolution of the distribution of intermetallic particles in the Al-Cu sample before and after thermal treatments is illustrated in Fig. 3-8. On the surface of the polished Al-Cu alloy, the presence of small intermetallic particles can be observed but their size and distribution within the oxide layer is different than in the case of thermally treated sample. Similar intermetallic particles with similar characteristics and distribution have been already observed by Seyeux *et al.*[80] in the case of an Al-0.5% Cu matrix containing Al_2Cu intermetallic particles formed in air. During the thermal treatments at elevated temperatures under LP of O_2, two kinds of preferential oxidation occurred:

- first, a progressive uptake of the oxide layer as evidenced by *in situ* analysis by XPS with Al oxide layer growth with a thickness of around 0.5 nm (Fig. 3-8(b)), and diffusion and precipitation and growth of Cu-rich intermetallic particles at the oxide/metal interfacial region as observed from the ToF-SIMS imaging,

- second, a preferential oxidation of the intermetallic particles with formation of a core-shell structure with copper inside and aluminium oxide formed at the intermetallic particles surface (Fig. 3-8(c)).

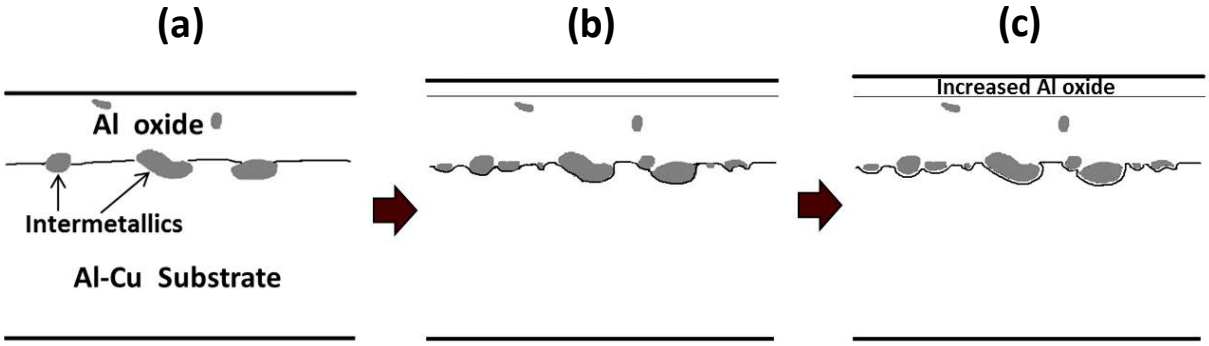

Fig. 3-8 Schematic illustrations of the growth and oxidation of intermetallic particles during thermal treatments: (a) after sputtering (0 L), and after aging under LP O_2 (b) at 300 °C (6481 L) and 350 °C (3240 L), (c) at 400 °C (4860 L).

3.5 Conclusions

(1) The XPS analyses evidenced the growth of aluminium oxide layer as a function of thermal treatments from 300 °C to 400 °C, and the increase of Cu concentration in the surface oxide layer from 23.0 at.% to 26.3 at.% at higher temperatures from 350 °C to 400 °C, which is due to the higher diffusion speed of Cu atoms from bulk of Al-Cu alloy to the interface region (oxide/substrate) at higher temperatures (>350 °C);

(2) The significant decrease of O1s peak area at 300 °C indicated the dehydration and/or decomposition of hydroxide layer at high temperatures, formerly present at the native alumina surface. The slight decrease of O1s at 400 °C can be explained by the reduction of Cu oxides with CO under high-temperature conditions (≥250 °C at the ambient pressure), or preferential aluminium oxidation and segregation of Cu/Cu oxides at surface defects or at grain boundaries or at oxide/substrate interface region;

(3) ToF-SIMS depth profiles confirmed a formation of thicker oxide layer for the thermally treated sample and decrease of the copper signal in the oxide layer region and higher intensity at the interfacial region pointing to diffusion and segregation of copper at the oxide/substrate interface region; ToF-SIMS imaging also confirmed the growth of the Cu-rich intermetallics during the thermal treatments;

(4) It can be concluded that thermal treatments of Al-Cu alloy occurs according to following mechanism: the preferential oxidation of Al, resulting in the growth of the aluminum oxide layer, and accumulation/growth of Cu-rich intermetallic at the oxide/metal interfacial region.

References

[1] I.J. Polmear, *Aluminum alloys—A century of age hardening*, Materials Forum, 28, 1-14 (2004)

[2] S.C. Wang,M.J. Starink and N. Gao, *Scripta Mater.*, 54, 287–291 (2006)

[3] K.A. Son, N. Missert, J.C. Barbour, J.J. Hren, R.G. Copeland, K.G. Minor, *J. Electrochem. Soc.*,148, B260-B263 (2001)

[4] R.G. Buchheit, *J. Electrochem. Soc.*, 142, 3994-3996 (1995)

[5] S.S. Wang, I.W. Huang, L. Yang, J.T. Jiang, J.F. Chen, S.L. Dai, D.N. Seidman, G.S. Frankel, and L. Zhen, *J. Electrochem. Soc.*, 162, C150-C160 (2015)

[6] B.L. Hurley, S.Qiu and R.G. Buchheit, *J. Electrochem. Soc.*,158, C125-C131 (2011)

[7] J.R. Scully, D.E. Peebles, A.D. Romig, D.R. Frear, C.R. Hills, *Metall. Trans. A*, 23A, 1365 (1990)

[8] J.R. Scully, K.O. Knight, R.G. Buchheit, D.E. Peebles, *Corros. Sci.*,35, 185 (1993)

[9] N. Birbilis, and R.G. Buchheit, *J. Electrochem. Soc.*,152, B140-B151 (2005)

[10] R.G. Buchheit, L.P, Montes, M.A. Martinez, J. Michael and P.F. Hlava, *J. Electrochem. Soc.*, 146, 4424-4428 (1999)

[11] R.G. Buchheit, R.P. Grant, P.F. Hlava, B. Mckenzie and G.L. Zender, *J. Electrochem. Soc.*, 144, 2621-2628 (1997)

[12] J.R. Scully, R.P. Frankenthal, K.J. Hanson, D.J. Siconolfi, and J.D. Sinclair, *J. Electrochem. Soc.*,137, 1365 (1990)

[13] O. Schneider, G.O.Ilevbare, and J.R.Scully, *J. Electrochem. Soc.*,151, B465 (2004)

[14] D.M. Rampulla, C.M. Mancinelli, I.F. Brunell, A.J. Gellman, *Langmuir*, 21, 4547-4553 (2005)

[15] M.R. Alexander, G.E. Thompson and G. Beamson, *Surf. Interf. Anal.*, 29, 468–477 (2000)

[16] L.P.H. Jeurgens, W.G. Sloof, F.D. Tichelaar, E.J. Mittemeijer, *Thin Solid Films*, 418, 89–101 (2002)

[17] T.S. Sun, J.M. Chen, J.D. Venables, *Appl. Surf. Sci.*, 1, 202-214 (1978)

[18] M.Collinet-Fressancourt, N. Nuns, S. Bellayer, M. Traisnel, *Appl. Surf. Sci.*, 277, 186-191 (2013)

[19] I. Popova, Z. Zhukov, J.T. Yates, *J. Appl. Phys.*, 87, 8143 (2000)

[20] Z. Zhukov, I. Popova, J.T. Yates, *J. Vac. Sci. Technol. A*, 17, 1727 (1999)

[21] D.R. Jennison, C. Verdozzi, P.A. Schultz, M.P. Sears, *Phys. Rev. B*, 59, R15605 (1999)

[22] A. Bogicevic, D.R. Jennison, *Phys. Rev. Lett.*, 82, 4050 (1999)

[23] L.P.H. Jeurgens, W.G. Sloof, F.D. Tichelaar, C.G. Borsboom,E.J. Mittemeijer, *Appl. Surf. Sci.*, 11, 144-145 (1999)

[24] S. Doniach, *Physical Review B*, 2, 3898-3905 (1970)

[25] V. Crist, *Handbook of Monochromatic XPS Spectra (Elements and Native Oxides)*, XPS International LLC, CA, USA, 2004

[26] N.H. Chen, C.Y. Wang, J.C. Hwang, F.S. Huang, *J. Solid Stat. Sci. Technol*, 1, 190-196 (2012)

[27] P. Marcus, C. Hinnen, I. Ofefjord, *Surf. Interf. Anal.*, 20, 923–929 (1993)

[28] Y.C. Kim, H.H. Park, J.S. Chun, W.J. Lee, *Thin Solid Films*, 237, 57 (1994)

[29] I. Ofefjord, H.J. Mathieu, P. Marcus, *Surf. Interf. Anal.*, 15, 681 (1993)

[30] A.N. Mansour, *Surf. Sci. Spectra*, 3, 202 (1994)

[31] A. Ayame, et al, *Bunseki Kagaku*, 40, 673 (1991)

[32] S. Moon, S. Pyun, Corros. Sci., 39, 399-408 (1997)

[33] R.J. Baird, C.S. Fadley, S.M. Goldberg, P.J. Feibelman, and M. Sunjic, *Surf. Sci.*, 72, 495–512 (1978)

[34] L.P. H. Jeurgens, W. G. Sloof, F. D. Tichelaar, C. G. Borsboom, and E. J. Mittemeijer, *Surf. Sci*., 144–145, 11–15 (1999)

[35] B.V. Crist, *Handbook of Monochromatic XPS Spectra-The Elements of Native Oxides*, Wiley, New York, US, 2000

[36] L.H. Zhang, C. Zheng, F. Li, D.G. Evans, X. Duan, *The Journal of Materials Science*, 43, 237-243 (2008)

[37] L. Ley, F.R. McFeely, S.P. Kowalczyk, J.G. Jenkin , D.A. Shirley, *Phys. Rev. B*, 11, 600 (1975)

[38] K. Domen, T.J. Chuang, *J. Chem. Phys.*, 90, 3318 (1989)

[39] F. Rueda, J. Mendialdua, A. Rodriguez, R. Casanova, Y. Barbaux, et al, *J. Electron Spectrosc. Relat. Phenom.*, 82, 135 (1996)

[40] B. Ealet, M.H. Elyakhloufi, E. Gillet, M. Ricci, *Thin Solid Films*, 250, 92 (1994)

[41] A.N., Mansour, *Surf. Sci. Spectra*, 3, 202 (1994)

[42] R.J. Bird, P. Swift, *J. Electron Spectrosc. Relat. Phenom.*, 21, 227 (1980)

[43] J.P. Espinós,P. Espinós, J. Morales, A. Barranco, A. Caballero, J.P. Holgado, and A.R. González-Elipe, *J. Phys. Chem.B*, 106, 6921-6929 (2002)

[44] P. Brand, H. Freiser, *Anal. Chem.*, 46, 1147 (1974)

[45] F.M. Capece, V.Di Castro, C.Furlani, G.Mattogno, *J. Electron Spectrosc.,* 27, 119 (1982)

[46] G. Schon, *Surf. Sci.*, 35, 96-108 (1973)

[47] N. Pauly, S.Tougaard, F.Yubero, *Surf. Sci.*, 620, 17-22 (2014)

[48] A.K. Dua, V.C. George, R.P. Agarwala, *Thin Solid Films*, 165, 163 (1988)

[49] G. Beamson, D. Briggs, *High Resolution XPS of Organic Polymers*, TheScienta ESCA 300 Database, John Wiley and Sons, 1992

[50] J.A. Rotole, P.M.A. Sherwood, *Surf. Sci.Spectros.*,5, 18-25 (1998)

[51] J.T. Kloprogge, L.V. Duong, B.J. Wood, L. Ray, *J. Colloid Interf. Sci.,*296, 572-576 (2006)

[52] J.T. Kloprogge, L.V. Duong, B.J. Wood, R.L. Frost, *J. Colloid Interf. Sci.,* 296, 572-576 (2006)

[53] M.R. Alexander, G.E. Thompson, G. Beamson, *Surf. Interf. Anal.,* 29, 468-477 (2000)

[54] B. Diaz, E. Harkonen, J. Swiatowska, V. Maurice, A. Seyeux, P. Marcus, M. Ritala, *Corros. Sci.*, 53, 2168-2175 (2011)

[55] S. Andersson, J.W. Davenport, *Solid State Communications,* 28, 677 (1978).

[56] H. Hopster, C.R. Brundle, *J. Vac. Sci. Technol.*, 16, 548 (1979).

[57] P. Marcus, C. Hinnen, I. Olefjord, *Surf. Interf. Anal.*, 20, 923-929 (1993)

[58] P. Marcus, C. Hinnen, D. Imbert, J. M. Siffre, *Surf. Interf. Anal.*, 19, 127-132 (1992)

[59] J. Zähra, S. Oswaldb, M. Türpec, H.J. Ullricha, U. Füssela, *Vacuum*, 86, 1216-1219 (2012)

[60] D. Papee, R. Tertian Bull, *Soc. Chim. Fr.*, 983, 1955

[61] Eric C. Guyer, *Handbook of Applied Thermal Design*, Taylor & Francis, USA, 1999

[62] S. Mrowec, *Defects and diffusion in solids: An Introduction*, Elsevier Scientific Pub. Co., 1980

[63] E.A. Goldstein, R.E. Mitchell, *Proceedings of the Combustion Institute*, 33, 2803-2810 (2011)

[64] J.A. Rodriguez, J.Y. Kim, J.C. Hanson, M. Perez, A.I. Frenkel, *Catal. Lett.*, 85, 247-254 (2003)

[65] X. Wang, J.C. Hanson, A.I. Frenkel, J.Y. Kim, J.A. Rodriguez, *J. Phys. Chem. B*, 108, 13667-13673 (2004)

[66] J.Y. Kim, J.A. Rodriguez, J.C. Hanson, A.I. Frenkel, P.L. Lee, *J. Am. Chem. Soc.*, 125, 10684–10692 (2003)

[67] T. Robert, G. Offergeld, *Phys. Status Solidi A*, 14, 277 (1972)

[68] M. Scrocco, *Chem. Phys. Lett.*, 63, 52-56 (1979)

[69] Y. Zhu, K. Mimura, and M. Isshiki, *Oxidation of Metals*, 62, 207-222 (2004)

[70] M.R. Alexander, G.E. Thompson, X. Zhou, G. Beamson, N. Fairley, *Surf. Interf. Anal.*, 34, 485-489 (2002)

[71] B.R. Strohmeier, *Surf. Interf. Anal.*, 15, 51 (1990)

[72] I. Olefjord, H.J. Mathieu, and P. Marcus, *Surf. Interf. Anal.*, 15, 681-692 (1990)

[73] N. Andersen, P. Sigmund, K. Selsk, *Mat-Fys. Medd.*, 39, (1974)

[74] W.K. Chu, J.K. Howard, and R.F. Lever, *J. Appl. Phys.*, 47, 4500-4503 (1976)

[75] E. Fleury, J.S. Kim, D.H. Kim, W.T. Kim, *J. Mater. Res.*, 18, 1837-1841(2003)

[76] C.D. Wagner, A .Joshi, *J. Electron Spectrosc.*, 47, 283-313 (1988)

[77] Y. Liu, G.E. Thompson, P. Skeldon, *Surf. Interf. Anal.*, 36, 339 (2004)

[78] Y. Liu, M.A. Arenas, P. Skeldon, *Corros. Sci.*, 50, 1475 (2008)

[79] R.G. Buchheit, *J. Appl. Electrochem.*, 28, 503-510 (1998)

[80] A. Seyeux, G.S. Frankel, and P. Marcus, *J. Electrochem. Soc.*, 158, C165-C171 (2011)

Chapter 4 Corrosion performances of model Al-Cu alloy after thermal treatments (annealing and aging) – surface studies by means of XPS and ToF-SIMS

In this chapter, the influence of thermal treatments (annealing at 540 °C and aging at 300 °C and 450 °C) of Al-Cu model alloy on its corrosion performance in neutral (0.01 M NaCl＋0.3% vol H_2O_2 at pH 6.2) and in alkaline (0.01M NaCl＋NaOH at pH 11.5) electrolytes was investigated. The adapted immersion tests were followed by surface characterization by means of XPS and ToF-SIMS and completed by morphology characterization by Scanning Electron Microscopy (SEM). Various mechanisms of corrosion influenced by the size and distribution of IMPs formed due to thermal treatment were evidenced: different types of pitting corrosion in case of immersion in neutral electrolytes and general corrosion in the case of immersion in alkaline electrolytes. Increase of corrosion layer thickness and copper enrichment on the surface of Al-Cu alloys after immersion tests were clearly demonstrated.

4.1 Introduction

The strength and hardness of aluminium alloys are substantially increased by the formation of extremely small uniformly dispersed second-phase particles containing Cu within the original phase matrix in a process which we know as precipitation or age hardening[1,2]. Other elements (*i.e.* Cu, Si, Fe, Mg and Cr) are usually added to the aluminium to obtain diverse properties to meet the demands in industries. Age hardening or precipitation hardening is now one of the most widely used mechanism for the strengthening of Al-Cu alloys. The precipitate particles, as described in the bibliographic part (chapter 1), act as obstacles to dislocation movement and thereby strengthen the heat-treated Al-Cu alloys[3]. Generally, the age-hardening for the Al-Cu alloys involves a three-step heat treatment as follows:

- first step: the Al-Cu alloy is solution heat treated - held above 548 ℃ [4] to make the alloying elements (Cu, Mg, Zn, Si, etc) dissolve [5] and obtain a homogeneous solid solution (α phase)[6],
- second step: the material is quenched from the solution-treatment temperature, typically by dunking or spraying it with cold water, which traps the alloying elements in solution. Quenching is a fierce treatment that can cause distortion and create internal stresses that may require correction in industry, such as rolling,
- third step: the material is aged, meaning that it is heated at moderate temperatures ranging from 100 to 400 ℃ [7] for several hours during which the alloying elements condense into nano-scale dispersions of intermetallics (Al_2Cu, Al_2CuMg, Mg_2Si, etc.)[8]. This process often starts from clustering of alloying components called Guinier-Preston (GP) zones that will grow larger and more intensively with increasing heating temperature and time. For the Al-Cu binary alloy, the forming processes of the θ-phase (Al_2Cu) are supersaturated solid solution (α_{ss})→ GP zones (Discs)→ θ" (Discs)→ θ'

(Plates)→ θ(Al_2Cu)[9-16]. Many studies[17-21] have reported that the precipitates mainly grow *via* the grain boundaries of the alloys.

Nevertheless, as discussed in the bibliographic chapter (chapter 1), these Cu-rich intermetallic particles present in the Al-Cu alloys have negative effects on the corrosion resistance of the alloy, due to the galvanic interactions between intermetallic particles (IMPs) and the Al-alloy matrix[22-27]. Copper is a nobler element than aluminium, and has a significant effect on the corrosion susceptibility of the Al-Cu alloys. The Al-Cu alloys with IMPs mainly undergo corrosion *via* the pitting and intergranular corrosion[28,29]. However, in general, IMPs can be either passive or active with respect to the aluminium matrix based upon the composition of the intermetallics[30,31].

Particles containing Al, Cu, Fe, and Mn (*e.g.* Al_2Cu, θ-phase) act as cathodes, where oxygen or water reduction leads to pH increase (local OH^- accumulation), which in further stages promotes oxide and matrix dissolution at their periphery (leading to localized corrosion)[32]. The pitting potential of Al_2Cu particles is low enough so that metastable pitting can occur at the OCP[33]. The oxide present on these particles might be more conductive or catalytic, which provides more cathodic current from oxygen reduction promoting localized corrosion[34 - 37]. Schneider et al.[38] investigated the mechanism of trenching formation around the cathodic intermetallic particles on a polished AA 2024-T3 alloy *in situ* using confocal laser scanning microscopy. It was revealed that the propensity to promote trenching of the Al matrix is not the same for all Al-Cu and Al-Cu-Mn-Fe particles in solutions of low chloride content. Al-Cu particles are more susceptible, while Al-Cu-Mn-Fe particles hardly trench at low Cl^- concentrations. However, it was also reported that a pH increase around the cathodic particles can explain trenching formation only for the bulk in a neutral pH environment.

In the case of active particles containing Al, Cu, and Mg (*e.g.* Al_2CuMg, S-phase), the anodic dissolution with preferential dealloying of Mg and Al can occur[39-45]. The preferential dissolution of Al-alloy matrix surrounding the intermetallics could lead to

copper depletion in the neighborhood of the grain boundary[46], or accumulation of copper on the surface. Once a certain level of enrichment occurs, copper atoms are thought to arrange themselves into clusters through diffusion processes and eventually protrude from the alloy surface due to undermining of the surrounding Al-alloy matrix[47]. The copper clusters could be released as elemental copper into the oxide layer when they are undermined or oxidized. The defects existing in the aluminium oxide may also be increased by the enrichment of copper at the alloy surface[48], which promotes the pit propagation rate and pit germination rate[49]. Seyeux et al.[50] investigated the pitting corrosion of Al-Cu thin film alloys heat treated (aged in air at 300 °C for 10 h followed by 450 °C for 5 min) where the Al_2Cu particles were formed within an Al-0.5wt.% Cu matrix, and reported the localized enrichment of metallic Cu at the metal/oxide interface. Following exposure to an aggressive environment, where localized corrosion was initiated, the pit density closely matched that of the Cu-rich interfacial regions.

In this chapter, the influence of thermal treatment of Al-4.87wt.% Cu model alloy on the corrosion performances (immersion tests at open circuit potential) in near neutral electrolyte (pH=6.2) and in alkaline electrolyte (pH=11.5) is presented. The corrosion behavior of thermally treated sample (after annealing at 540 °C for 1 h under primary vacuum of 1.0×10^{-5} mbar, quenching, and aging in air at 300 °C for 10 h followed by 450 °C for 5 minutes) is compared with non-treated (just polished) sample. For the sake of comparison some results obtained on the pristine, polished Al-Cu alloy sample already presented in the chapter 3 will be repeated here in this chapter. The scanning electron microscopy (SEM) and surface sensitive techniques: x-ray photoelectron spectroscopy (XPS) and time-of-flight secondary ion mass spectrometry (ToF-SIMS) were combined to compare the thermally formed oxide with the native oxide on the Al-Cu alloy, evaluate the structural and chemical modifications induced by the immersion tests, and to get more insight into the influence of the size and distribution of the Cu-containing intermetallic particles (Al_2Cu) on the corrosion susceptibility. The goal of this study was also to assess

whether the type of oxide layer (native or thermal) and its heterogeneity (above the particles or the alloy matrix) could be related to differences in local reactivity.

4.2 Experimental

Sample preparation. As already introduced in the experimental part (chapter 2) the Al-Cu polycrystalline alloy samples containing 4.87wt.% of Cu (*Goodfellow),*were used in this studies. The samples in the form of discs (Φ=1cm) were mechanically polished first with SiC papers (#1200; #2400; #4000), and then with alumina polishing slurries (OP-AN, ESCIL Inc.) of 2-3 μm, 1 μm and 0.3 μm, successively, and cleaned separately with acetone, ethanol and ultrapure water (Millipore® water, resistivity＞18 MΩ cm) in an ultrasonic bath for 5, 3, and 1 minute, respectively and blow-dried with compressed air.

Thermal treatments. Thermal treatments of as prepared Al-Cu alloy sample was performed in dedicated equipment presented in the experimental chapter (chapter 2) and used previously in our group for preparation of well-crystallized single crystal surfaces[51]. The sample was annealed at 540 °C in vacuum (pressure of 1.0×10^{-5} mbar) for 1 hour, to create a homogeneous Al-Cu solid solution, ice water quenched, then roughly polished to 1μm with SiC papers (#1200; #2400; #4000) and alumina polishing slurries (2-3 μm, 1 μm), and then aged in air at 300 °C for 10 h followed by next aging step at 450 °C for 5 minutes in order to form Al_2Cu intermetallic particles in the Al-Cu matrix, as applied in the ref. 51.

Immersion tests. Immersion tests of non-thermally and thermally treated Al-Cu alloy samples were performed using a three-electrolyte system: a working electrode (Al-Cu alloy), a counter electrode (Pt wire) and a reference electrode (Ag/AgCl) using an Autolab/PGSTAT128N instrument. The electrolytes were prepared with ultra-pure Millipore® water and reagent grade chemicals (NaCl Analar Normapur analytical reagent, VWR® BDH Prolabo®). The open circuit potential (OCP) was registered during the immersion tests. The surface of working electrode area was delimited to

0.29 cm^2 by a Viton O-ring. The immersion was performed for the non-thermally treated samples in a neutral electrolyte containing 0.01 M NaCl＋0.3% vol H_2O_2 (pH≈6.2) for duration of 7 min, and in an alkaline electrolyte containing 0.01 M NaCl ＋NaOH (pH=11.5) for (7+30) minutes. The thermally treated samples were immersed only for 7 minutes both in the neutral and in the alkaline electrolyte. All the tests were assisted with the Autolab/PGSTAT128N instrument.

X-ray Photoelectron Spectroscopy Analysis. A Thermo Scientific ESCALAB 250 X-ray Photoelectron spectrometer (XPS), with an Al Kα monochromatized radiation (hv= 1486.6 eV), was used to acquire all spectra and analyze the surface chemical composition of the sample. The pressure in the analysis chamber was kept at 1×10^{-9} mbar. The Al Kα monochromatized source was operated at 15 kV and the samples were analyzed at a 90° take-off angle normal to the surface. The survey spectra (at 0~1060 eV) were recorded with a pass energy of 100 eV, and the high-resolution spectra (C1s, O1s, Al2p, $Cu2p_{2/3}$ or Cu2p) were recorded with a pass energy of 20 eV and a resolution of 0.1 eV. All spectra were calibrated versus the binding energy (BE) of hydrocarbons (at 285.0 eV). Spectra were recorded and analyzed using the Thermo Scientific™ Avantage software (version 5.954). For curve fitting and decomposition, a Shirley-type background subtraction was used and the shape of fitting curves was determined by a 70% Gaussian/30% Lorentzian distribution, typical for the spectra fitting for metal/oxides[52].

Time-of-Flight Secondary Ion Mass Spectrometry Analysis. Time-of-Flight Secondary Ion Mass Spectrometry (ToF-SIMS) was employed to analyze elemental species present on the sample surface, and assess their status and distribution in high resolution following the XPS analysis (the sample was exposed to air during transfer), using a ToF-SIMS V spectrometer (ION TOF GmbH-Munster, Germany). The analysis chamber was maintained at about 1×10^{-9} mbar. Depth profiles were performed using sputtering with Cs ion gun: Cs^+ 2 keV, 100 nA (300×300 μm^2) and analysis with Bi ion gun: Bi^+ 25 keV, 1.1 pA (100×100 μm^2). Chemical images of the polished Al-Cu model alloy and after thermal treatment were performed by using a

pulsed Bi^+ 25 keV primary ion source, delivering 0.1pA current over a 100×100 μm^2 area.

Scanning Electron Microscopy. Scanning Electron Microscopy (SEM) images of the polished and aged samples were obtained with a Carl Zeiss Ultra 55 Field Emission Scanning Electron Microscopy (FE-SEM, Germany).

4.3 Results and discussions

4.3.1 Surface characterization of the polished and aged Al-Cu alloy before corrosion

Fig. 4-1 shows the SEM morphologies of the Al-Cu samples after polishing (a) and after thermal treatments (annealing & aging) (b), respectively. As shown in Fig. 4-1 (a), the polished Al-Cu sample exhibits a homogeneous distribution of round particles, with diameters of 1-5 μm in Al-4.87wt.% Cu matrix. The particles were analyzed by electron diffraction (EDX) analysis, indicating the composition of Cu/Al= 33/66 [at.%], consistent with the stoichiometry of the θ-phase (Al_2Cu).

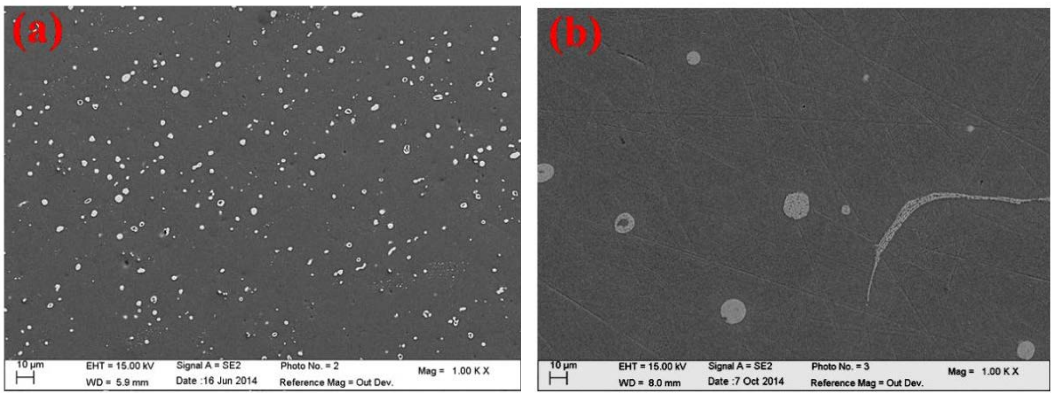

Fig. 4-1 SEM micrographs of Al-4.87wt.% Cu samples after: (a) polishing, (b) annealing at 540 °C & aging treatments at 300 and 450 °C.

After thermal treatments (annealing & aging) (Fig. 4-1(b)) clear modifications of the alloy microstructure can be observed. The round intermetallic particles have bigger sizes ranging from 5-20 μm. Moreover, additional irregular dendritic network structures (suggesting the accumulation of IMPs at grain boundaries) can be observed.

According to the EDX analysis the composition of the particles (Cu/Al) is ranging from 27/73 to 33/66 [at.%], indicating that these intermetallics should be equilibrium θ (Al_2Cu) precipitates essentially with few θ' particles undergoing the θ'→θ transformation[53,54].

As already mentioned, the chemical surface characterization of the polished Al-Cu alloy sample was presented in details in chapter 3. Here, in Fig. 4-2 (a) and (b), we present a comparison of Al2p, $Cu2p_{3/2}$ core level spectra for pristine, non-treated and thermally treated samples, and in Fig. 4-2 (c) the Al2p and $Cu2p_{3/2}$ peak decompositions for the sample after thermal treatment. It was concluded (in chapter 3) that the surface of the polished Al-Cu model alloy is covered by a thin aluminium oxide and aluminium hydroxide ($Al(OH)_3$ and AlOOH) layer. The presence of metallic copper was also evidenced. After annealing & aging treatments, the Al2p spectra still show the presence of the hydroxyls groups (usually observed at 74.8 ± 0.1 eV[55,56] and detected formerly at the non-thermally treated, polished surface as specified in the previous chapter 3), which could be related to the adsorption and/or re-formation of hydroxides on the surface during a quick transfer in laboratory air from the thermal treatment setup to the XPS analysis chamber. Due to the quick polishing applied on the surface of the Al-Cu alloy after annealing step, even though after the following aging treatment in air at 300 and 450 °C (as indicated in the experimental part), very low Al oxide increase (Al2p peak at BE of 75.7 ± 0.1 eV corresponding to Al oxide, Fig. 4-2(a) and (c)) can be observed (7 nm for the non-treated sample and 8 nm for the thermally treated sample)[57-59]. The decomposition of the Al2p also shows the spin orbit doublet $Cu3p_{3/2}$ (at 76.2 ± 0.1 eV) and $Cu3p_{1/2}$ (BE of 77.8 ± 0.1 eV) of Cu oxide[60-62] overlapping the Al2p area (Fig. 4-2(c)). The decomposition of the $Cu2p_{3/2}$ signal indicates a formation of CuO (at 933.9 ± 0.1 eV)[63-67] after the annealing and aging treatments (Fig. 4-2(d)). Moreover, the intensity of CuO peak is more significant in the case of thermally treated than in the case of the polished, non-treated sample, pointing to more important quantity of oxidized than metallic form of copper (Fig. 4-2(b)). However, it should be noted that a low signal

intensity of the Cu2p core level spectra can cause some inaccuracy in a peak decomposition and data interpretation.

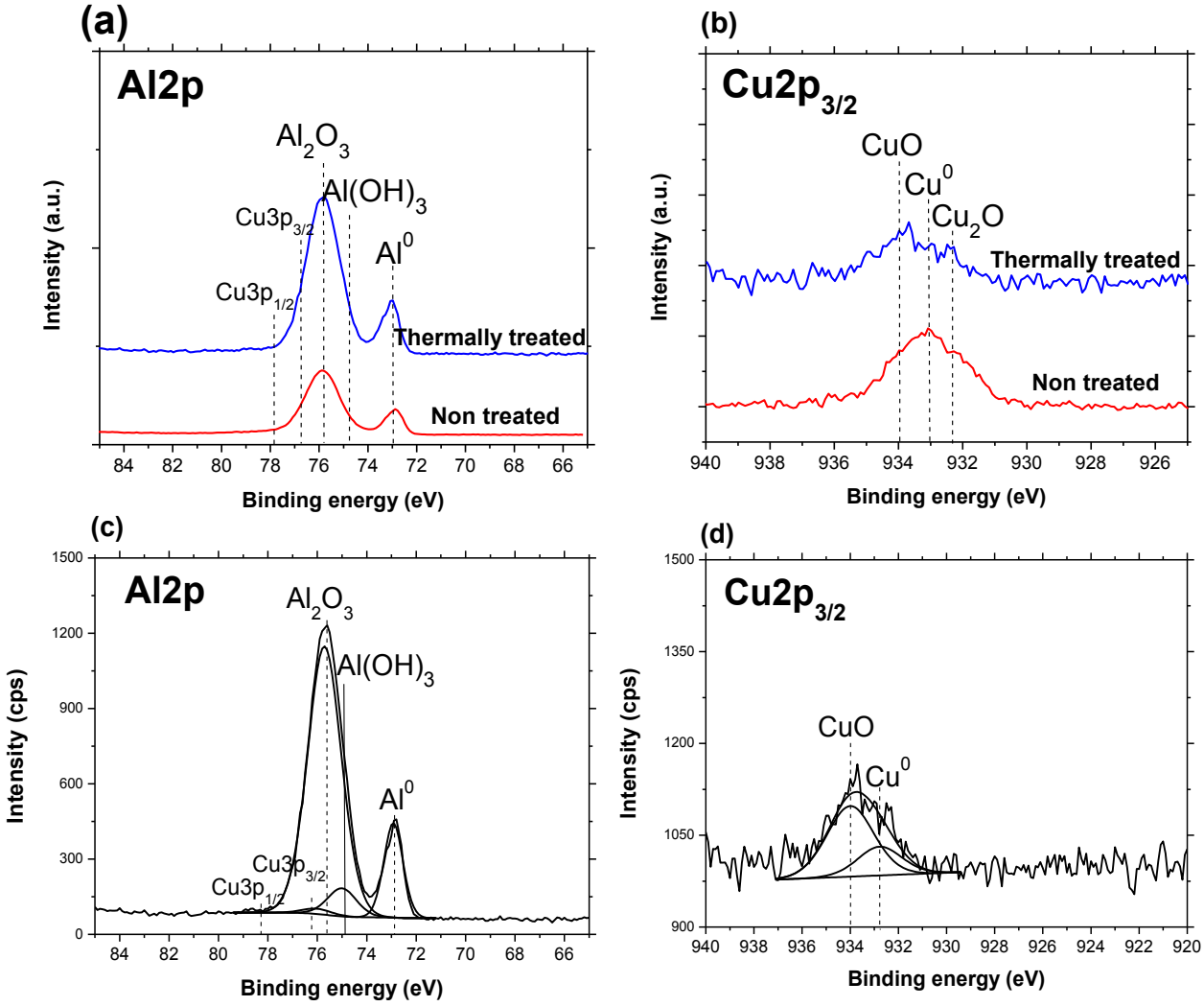

Fig. 4-2 The comparison of Al2p(a) and Cu2p$_{3/2}$ (b) core level spectra obtained for the non-thermally treated, polished Al-Cu sample and after annealing at 540 °C & aging treatments at 300 and 450 ℃ and decomposition of Al2p (c) and Cu2p$_{3/2}$ (d) peaks for the thermally treated Al-Cu sample (annealing and aging).

The data of the high resolution main O1s, Al2p and Cu2p$_{3/2}$ (binding energy (BE) and full-width at half maximum (FWHM)) are depicted in Tab.4-1. The O:Al atomic ratio calculated with the corresponding O1s (at 531.4 ± 0.1 eV) and Al2p (at 75.7 ± 0.1 eV) is around 1.5, which is consistent with the atomic stoichiometry of Al_2O_3 (O:Al = 1.5). The similar atomic ratio calculated for the pristine, polished Al-Cu alloy (in chapter 3) indicates that no significant chemical modifications occur on the alloy

surface due to thermal treatments (annealing and aging).

Tab. 4-1 Binding energies (BE), full-widths at half maximum (FWHM) and intensities (converted in atomic percentages) for the main peaks ofAl2p, $Cu2p_{3/2}$ and O1s core level obtained for the thermally treated sample after annealing at 540 °C & aging at 300 and 450 ℃ .

XPS peaks	BE (eV)	FWHM (eV)	Species
Al2p	72.9	0.9	Metallic Al
	74.8	1.5	AlOOH/$Al(OH)_3$
	75.7	1.7	Al_2O_3
$Cu2p_{3/2}$	932.8	2.2	Metallic Cu
	934.0	2.3	CuO
O1s	530.3	1.3	CuO
	531.3	2.0	Al_2O_3
	532.3	1.5	Hydroxyl groups/Contaminants

ToF-SIMS negative ion depth profiles and images for both polished and thermally treated (annealed and aged) Al-Cu samples are shown in Fig.4-3 and 4-4, respectively. For both samples, three main regions can be distinguished: 1) the aluminium oxide region (identified by high and relatively constant intensities of AlO^-, AlO_2^- and $^{18}O^-$ signals), 2) the oxide/metal interfacial region (identified by decreasing intensities of AlO^-, AlO_2^- and $^{18}O^-$ and increasing intensity of Al_2^-) and 3) the metallic substrate region (identified by a constant Al_2^- signal). The description of the ToF-SIMS depth profiles obtained for the polished Al-Cu alloy sample was given in details in the chapter 3.

Only slight increase of the sputtering time observed for the Al-Cu sample from around 35 s (for polished sample, Fig. 4-3 (a)) to around 40 s (for thermally aged sample, Fig. 4-3 (b)) confirms a formation of slightly thicker Al oxide, the increasing rate of which is perfectly consistent with the observations by the previous XPS (from 7 nm for the non-treated sample to 8 nm for the thermally treated sample). As discussed already, this not significant growth should be related to the quick polishing

(up to 1 µm) between the annealing and aging treatments, which removed the thermally oxidized layer remarkably. In addition, the Cu signal shows a decrease from 600 cps (for polished, (a)) to 200 cps (for thermally treated sample, (b)) in the beginning of sputtering time and a higher gradient between the first (oxide) and the second (interfacial) region (b). This higher gradient indicates a thermally induced precipitation and accumulation of Cu-rich intermetallic particles at the oxide/metallic substrate interface during the thermal aging treatment, which has been previously observed on a thin film air formed oxide on an Al_2Cu model alloy[68]. It should be emphasized that similar results have been obtained for the same Al-Cu alloy sample thermally treated at different temperatures and at low oxygen pressure in the XPS preparation chamber, as discussed in chapter 3. Furthermore, the higher OH^- and Cl^- signal intensities can be observed on the extreme surfaces of both samples than in a bulk, which should be attributed to the sample cleaning process and/or sample transfer through the laboratory air resulting in presence of some traces of contaminations and formation of hydroxides.

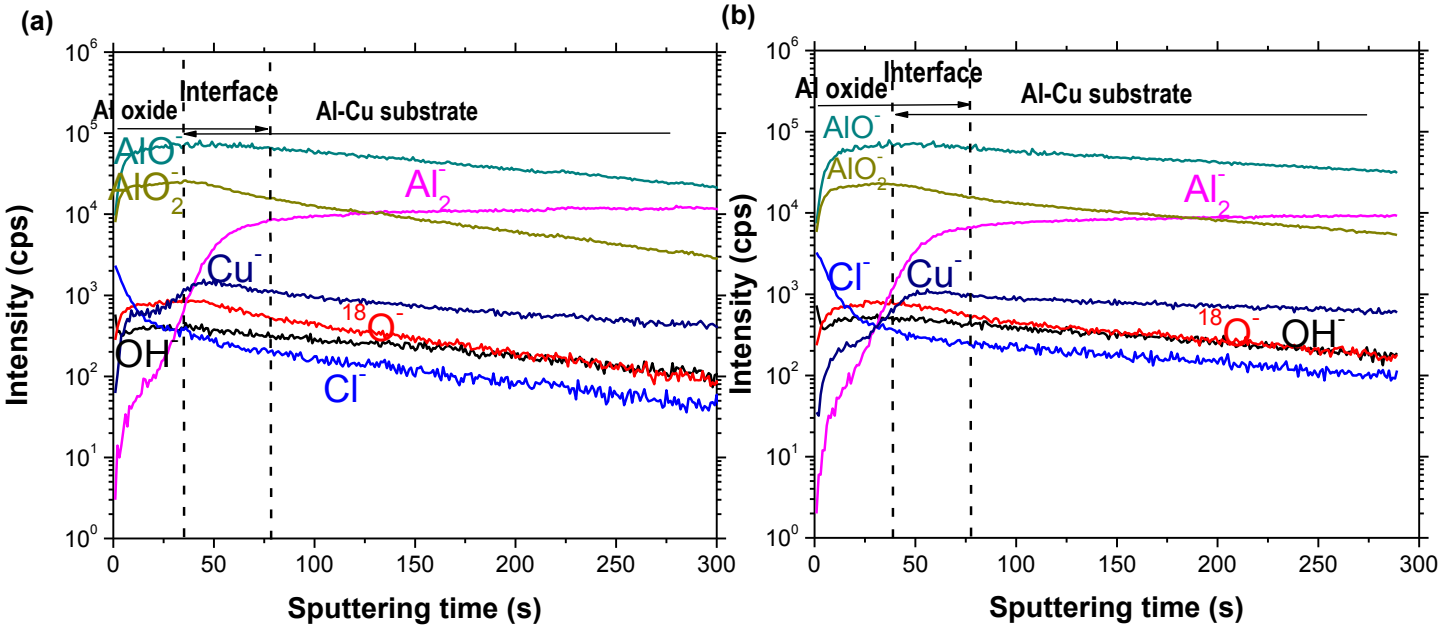

Fig. 4-3 ToF-SIMS negative ion depth profiles obtained on (a) the pristine, polished Al-Cu sample; (b)the thermally treated sample after annealing at 540 °C & aging treatments at 300 and 450 ℃ .

ToF-SIMS negative ion 100×100 μm^2 chemical images, similarly to previous chapter 3, were performed at different depths of sputtering corresponding to: 1) the extreme surface of the oxide layer (surface), 2) the interfacial region (oxide/substrate interface) (interface) and 3) the area corresponding to the metallic substrate (substrate). However, here only the first two regions are presented: the region 1) corresponding to the surface and the region 2) corresponding to the interface (Fig. 4-4(a) and (b) for the pristine, polished and the thermally treated samples, respectively). To confirm the presence of the intermetallic particles in the interfacial region for the sample after thermal treatment the second region of analysis was chosen (named as "Interface 2" in Fig. 4-4(b)). The images obtained in the near surface region show a homogeneous native aluminium oxide film on the pristine, polished Al-Cu sample. The presence of small-size (1~5 μm) Cu-rich intermetallic particles in surface layer of the polished sample was already evidenced and described in details in the previous chapter 3 and confirmed by the SEM data presented above.

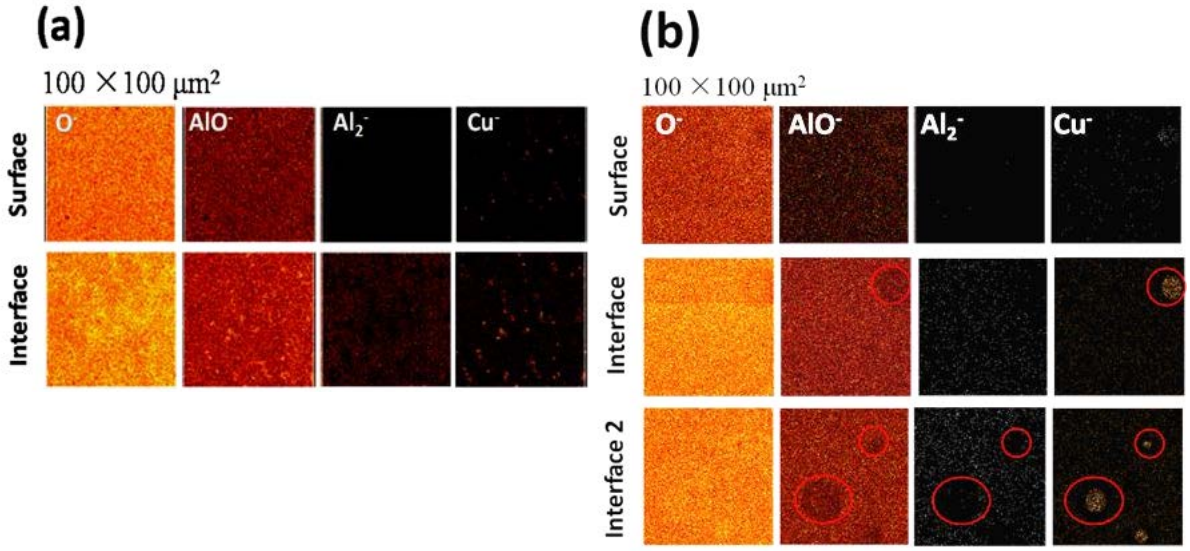

Fig. 4-4 ToF-SIMS negative O^-, AlO_2^-, Al_2^- and Cu^- ion images obtained at different depths of sputtering surface, interface and substrate regions on:(a) the pristine, non-treated Al-Cu sample and (b) the thermally treated sample after annealing at 540 °C & aging treatments at 300 and 450 °C. Regions of Cu enrichment and Al depletion are circled in (b) images for clarity.

However, significant modifications related to Cu-rich intermetallic particles can

be observed for the thermally treated Al-Cu sample (after annealing & aging). As shown in the Cu^- images performed in the interfacial region, the round high intensity Cu-ion spots corresponding to Cu-rich intermetallic particles can be observed (Fig. 4-4(b)). In areas showing Cu enrichment, the lower intensity of O^- signal can be observed indicating an oxide layer heterogeneity on the surface of Al-Cu alloy (*i.e.* difference in the oxide layer formed on the alloy matrix area and in the Cu-rich intermetallic particles). Contrary to what can be observed for the pristine, polished Al-Cu alloy (Fig. 4-4(a)) at the substrate region, the AlO^- signal depletion matches the enrichment of Cu^- signal intensity for the thermally treated sample (as seen in two rows of images: ~~–in~~terface" and ~~–in~~terface 2" in Fig. 4-4(b)). This reveals that the Cu-rich intermetallic particles wedge into the Al substrate. However, it is difficult to conclude about the heterogeneity of the oxide layer in the case of the pristine, polished Al-Cu alloy (Fig. 4-4(a)) due to the significantly smaller Cu-rich intermetallic particles and a low spatial resolution of the ToF-SIMS images. The sizes of the spots for the thermally treated sample ranging from 5 to 20 μm are much larger than those observed for the polished one. These data are in agreement with the SEM images (Fig. 4-1) discussed above. The presented ToF-SIMS data are in agreement with the previous results obtained on the thin film Al-4wt.% Cu alloy after annealing (at 560 °C) and thermally treated (at 300 °C followed by 450 °C) by Seyeux et al.[51].

4.3.2 Corrosion performance of the polished and thermally treated Al-Cu alloys – immersion tests

Prior to this study, series of immersion tests (with different times of immersion) were carried out for measurement optimization in the neutral and alkaline electrolytes. The goal of these tests was to be able to observe the first signs of corrosion initiation and to control the surface state by surface sensitive techniques such as XPS and ToF-SIMS. Finally, the 7-minute-immersion test in near neutral, chloride electrolyte resulting in moderate corrosion signs favorable to analysis by surface sensitive techniques was chosen. In the case of alkaline electrolyte (pH=11.5), due to general

corrosion of the Al matrix and lack of visible corrosion spots (pitting corrosion), the immersion time for thermally treated sample was 7 minutes and for polished sample was prolonged from 7 minutes to (7+30) minutes.

The OCP measured for the thermally treated sample is only 30 mV higher than for the pristine, polished Al-Cu alloy sample in near neutral 0.01 M NaCl＋0.3% vol H_2O_2 (pH≈6.2) electrolyte (Fig. 4-5). This small difference in the OCP between both samples indicates that the thermal treatments resulting in enlargement of the size of Cu-rich intermetallic particles has no marked influence on the electrochemical performances of the Al-Cu alloys. It should be noted that the alloy surface area exposed to the electrolyte is exactly the same and there is no significant difference in the thickness of the oxide layers present on both types of samples and thus changes in the OCP values are not expected. A small OCP decrease during the 7-minute-immersion test for both samples indicates minor surface modifications. The surface chemical and morphological modifications induced by immersion tests are discussed in the following parts.

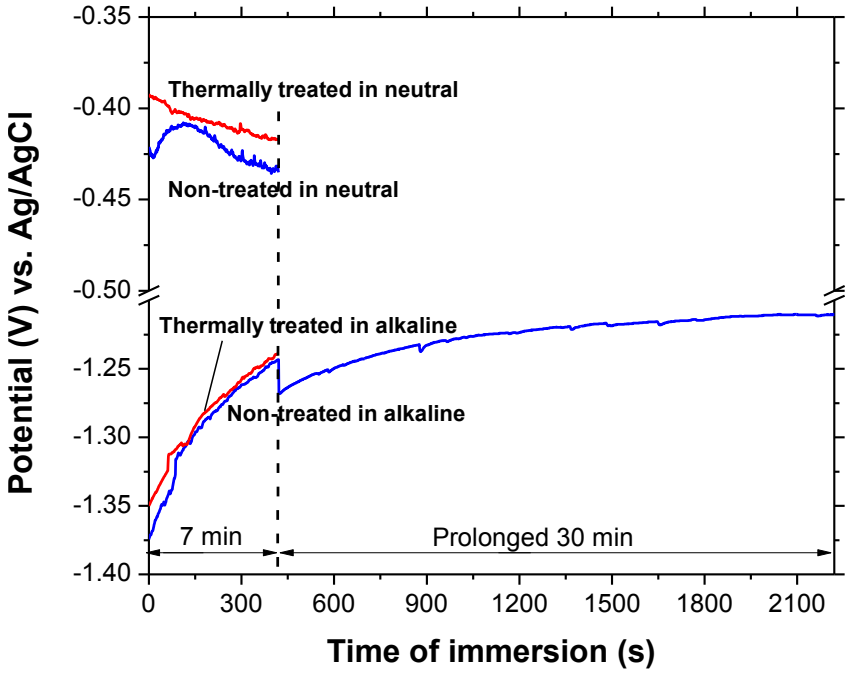

Fig. 4-5 The OCPs on both the polished and thermally treated Al-Cu (annealing at 540 °C & aging treatments at 300 and 450 °C) samples after immersions in a neutral and an alkaline electrolytes, respectively.

Much lower OCP of around -1.35 to -1.25 *vs.* Ag/AgCl was detected for both samples in the alkaline 0.01 M NaCl＋NaOH (pH=11.5) electrolyte (Fig. 4-5) compared with those in neutral electrolytes (with OCP of around -0.4 V *vs.* Ag/AgCl). This much lower OCP value in the alkaline electrolytes can be interpreted by the higher corrosion susceptibility of Al alloys and Al oxides in alkaline electrolytes (see the E-pH corrosion diagram discussed in the bibliographic chapter 1)[69-71]. Similar behavior have been reported on the pure Al (-0.7 V *vs.* SCE in a neutral solution, and -1.38 V *vs.* SCE in an alkaline solution) by Scully et al.[72-74]. As the immersions went on, both OCPs increased rapidly: for the thermally treated sample from -1.35 to -1.24 V *vs.* Ag/AgCl, and for the polished sample from -1.37 to -1.21 V *vs.* Ag/AgCl, respectively. The reason of this potential increase for both electrodes could be explained by the dissolution of the native Al oxide and Al matrix due to electrochemical attack by hydroxide ions resulting in the enrichment in Cu in the surface layer[75]. It should also be noted that the OCP for the thermally treated sample is only 20 mV higher than for the polished sample, consistent with the results in the neutral electrolytes. The immersion test for non-thermally treated sample was prolonged 30 min more due to not important, visible surface modifications. The prolonged immersion (of 30 min) shows a small potential increase from -1.26 to -1.2 V *vs*. Ag/AgCl indicating continuous surface modifications (*i.e.* oxide and Al matrix dissolution and surface copper ennoblement). The Cu enrichment confirmed by the surface characterization will be discussed hereafter.

4.3.3 Surface chemical modifications of the polished and thermally treated Al-Cu alloys after immersion tests

The first series of figures (Fig. 4-6(a) and (b)) present the Al2s, Cu2p O1s and Cu Auger XPS spectra obtained after the immersions of the polished (non-treated) and thermally treated samples in neutral electrolytes. The XPS data are also compiled in Tab.4-2. Due to the strong interference of Al2p and Cu3p (already discussed in

chapter 3), the Al2s core level was chosen instead of the Al2p for analysis of the Al-species. The Al2s core level for the polished sample can be fitted with two peaks: $Al2s_A$ (at 118.8 ± 0.1 eV, assigned to $Al(OH)_3$) and $Al2s_B$ (at 120.0 ± 0.1 eV, assigned to Al_2O_3). The Al_2O_3 film on aluminum alloy surface is prone to attract the hydrophilic groups in the solutions, which may promote the surface passivation by the formation of $Al(OH)_3$ or AlOOH[76,77]. Furthermore, it should be noted that an extra peak can be observed at around 117.0 ± 0.1 eV. This peak is not a metallic aluminium and it can be attributed to the strong charging effect related to formation of thick layer of corrosion products characterized by insulating properties. The charging effect can be also easily verified in the area of C1s core level (not shown here) where characteristic multiple carbon peak was observed.

The $Cu2p_{3/2}$ core level region is fitted with two peaks: $Cu2p_{3/2A}$ at 932.1 ± 0.1 eV, assigned to Cu_2O[78] and $Cu2p_{3/2B}$ at 934.0 ± 0.1 eV, assigned to CuO[79,80]. In addition, the presence of CuO can be confirmed by the characteristic shake-up satellite at 943.0 ± 0.1 eV[81,82]. The XPS analysis indicates that after corrosion the copper exists in a mixed oxidized form (CuO and Cu_2O), with a ratio of 43:57, respectively. The area of satellite peak corresponding to CuO was included into the calculation of the different copper oxides ratio. The Cu Auger signal is very low and too broad owing to the charging effect, hence, does not allow for a qualitative characterization. The higher intensity of Cu2p peak compared with that before immersion tests can be explained by the preferential dissolution of Al through the pitting corrosion mechanisms occurring around Cu-rich particles, resulting from the well-known electrochemical coupling of the cathodic particles and the anodic Al substrate[83-85].

In the O1s core level region, the peaks at 530.0, 531.2, 532.4 and 533.5 eV could be respectively ascribed to Cu oxides, Al oxides, hydroxyl groups or contaminants, and water molecules absorbed on the surface, respectively[86-89]. These XPS results indicate the formation of corrosion products mainly consisting of Al oxide and Al hydroxide rich in Cu oxides on the surface of non-treated sample after immersion in the neutral electrolyte.

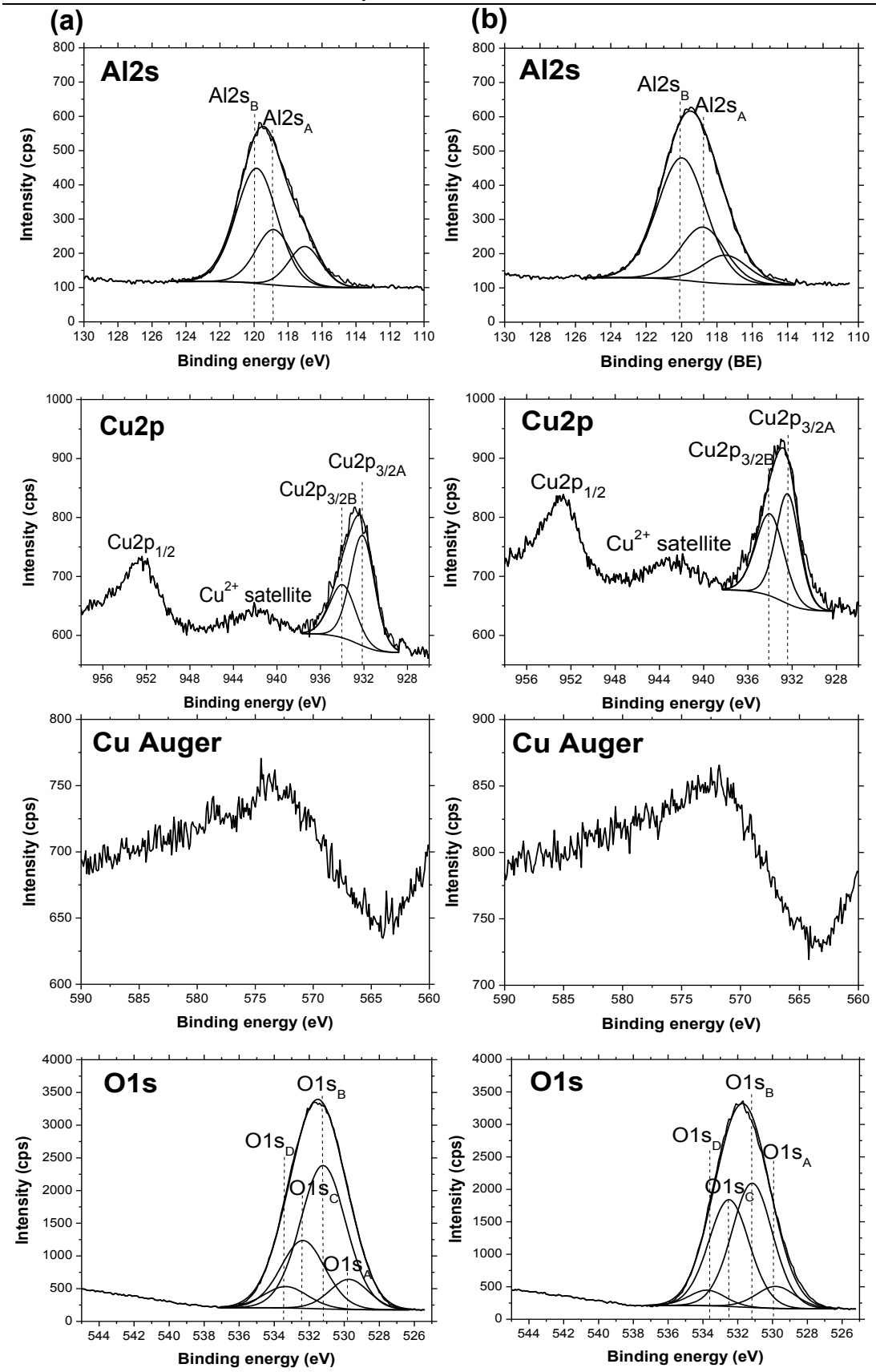

Fig. 4-6 Al2s, Cu2p, Cu Auger and O1s XPS spectra obtained from the polished sample (a) and thermally aged sample (annealing at 540 °C & aging treatments at 300 and 450 °C) (b) after immersion in the neutral solution.

A very low peak in the area of Cl2p at around 199.1 ± 0.1 eV (not shown here) can be attributed to some residual presence of NaCl not removed from the surface after rinsing. The presence of NaCl can be confirmed by the presence of Na1s peak.

Not very different XPS spectra were obtained on the surface of thermally treated sample attacked in neutral solutions (as shown in the Fig. 4-6(b) and in Tab.4-2). All the spectra (Al2s, Cu2p and O1s) obtained for the thermally treated sample can be fitted with similar peaks as those obtained for the non-treated sample, indicating the formation of similar corrosion products. However, it should be noted that here the ratio of CuO:Cu_2O is 52:48, which is different than in the case of non-treated sample (43:57), which may be related to enhanced corrosion and faster dissolution in the case of thermally treated sample.

The data of the high resolution main peaks of Al2s, $Cu2p_{3/2}$ and O1s core level spectra (BE and FWHM) are compiled in Tab.4-2. The $O1s_B$:$Al2s_B$ intensity ratios are 1.49 and 1.55 for the non-treated and thermally treated samples, respectively, which are close to the theoretical stoichiometry of Al_2O_3 (O:Al = 1.5). However, the $O1s_C$:$Al2s_A$ intensity ratios, 3.4 and 1.9 for the non-treated and thermally treated samples, respectively, are close to values expected for an aluminium hydroxide (3 for $Al(OH)_3$ or 2 for AlOOH), in agreement with the assignment of the oxygen peak to the aluminium.

After immersion in the alkaline electrolyte, the XPS spectra are significantly different, as shown in Fig. 4-7. It is seen from the Fig. 4-7(a) that the corrosion products layer on the non-treated sample surface is mainly composed of $Al(OH)_3$ (119.0 ± 0.1 eV) and the Al_2O_3 (120.1 ± 0.1 eV), similar to the case of immersion in the neutral solution. However, strong signals of Cu3s (with two peaks: BE at 122.6 ± 0.1 eV and 124.4 ± 0.1 eV), which overlap the Al2s spectra area, can be assigned to $Cu_2O/CuCl_2$ and CuO, respectively. Three peaks decomposed from the $Cu2p_{3/2}$ core level are assigned to the Cu_2O/CuCl, CuO and $Cu(OH)_2/CuCl_2$ [90]. From the Cu Auger spectra (as shown in the Fig. 4-7(a)), we could confirm the presence of CuO, Cu_2O

and Cu-Cl species[91,92]. This attribution was possible thanks to the reconstitution of this Cu Auger with the reference spectra of CuO and Cu_2O obtained in our laboratory for the synthetized thick oxide layers. The missing contribution was fitted with the additional peak corresponding to Cu-Cl. Moreover, the presence of Cu-Cl species is confirmed by the Cl2p core level, which can be decomposed into the peaks at 198.8 ± 0.1 and at 200.0 ± 0.1 eV assigned to the $Cl2p_{3/2}$ and $Cl2p_{1/2}$ spin orbit doublet of $CuCl_2$[93]. The Cl2p spin-orbit splitting (ΔeV) is about 1.6 eV, and the $Cl2p_{1/2}$:$Cl2p_{3/2}$ area ratio is 0.50 ± 0.01, both of which are consistent with the theoretical values[94,95]. Similar oxygen compounds can be observed on the surface after immersion in alkaline electrolytes as those observed after immersion in neutral electrolytes described above.

Tab. 4-2 Binding energies (BE) and full-widths at half maximum (FWHM) for Al2s, $Cu2p_{3/2}$ and O1s core level peaks after immersion in the neutral electrolyte.

Peaks	Non-treated		Thermally treated		Species
	BE (eV)	FWHM (eV)	BE (eV)	FWHM (eV)	
$Al2s_A$	118.9	2.6	118.8	2.7	$Al(OH)_3$/AlOOH
$Al2s_B$	120.0	2.9	120.1	3.0	Al_2O_3
$Cu2p_{3/2A}$	932.1	2.9	932.2	2.7	Cu_2O
$Cu2p_{3/2B}$	934.0	2.9	934.0	2.8	CuO
$O1s_A$	530.0	2.7	530.0	2.4	Cu oxides
$O1s_B$	531.2	2.9	530.9	3.0	Al_2O_3
$O1s_C$	532.4	2.9	532.1	3.0	Hydroxides/ contaminants
$O1s_D$	533.5	2.9	533.2	3.1	H_2O

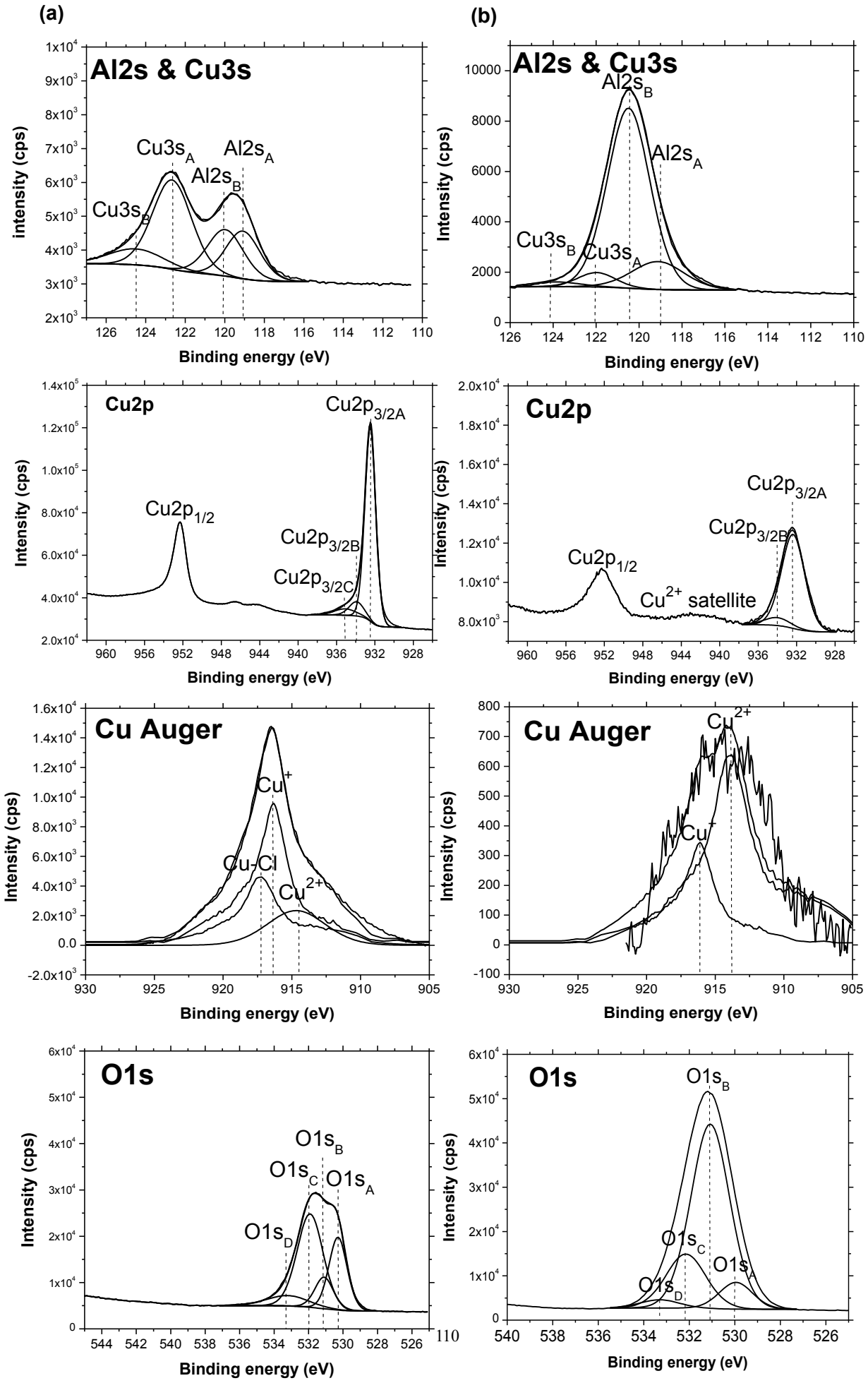
(a)
(b)
Al2s & Cu3s
Cu3s$_A$
Al2s$_A$
Al2s$_B$
Cu3s$_B$
Intensity (cps)
Binding energy (eV)
Cu2p
Cu2p$_{3/2A}$
Cu2p$_{1/2}$
Cu2p$_{3/2B}$
Cu2p$_{3/2C}$
Cu^{2+} satellite
Cu Auger
Cu$^+$
Cu-Cl
Cu^{2+}
O1s
O1s$_B$
O1s$_C$
O1s$_A$
O1s$_D$

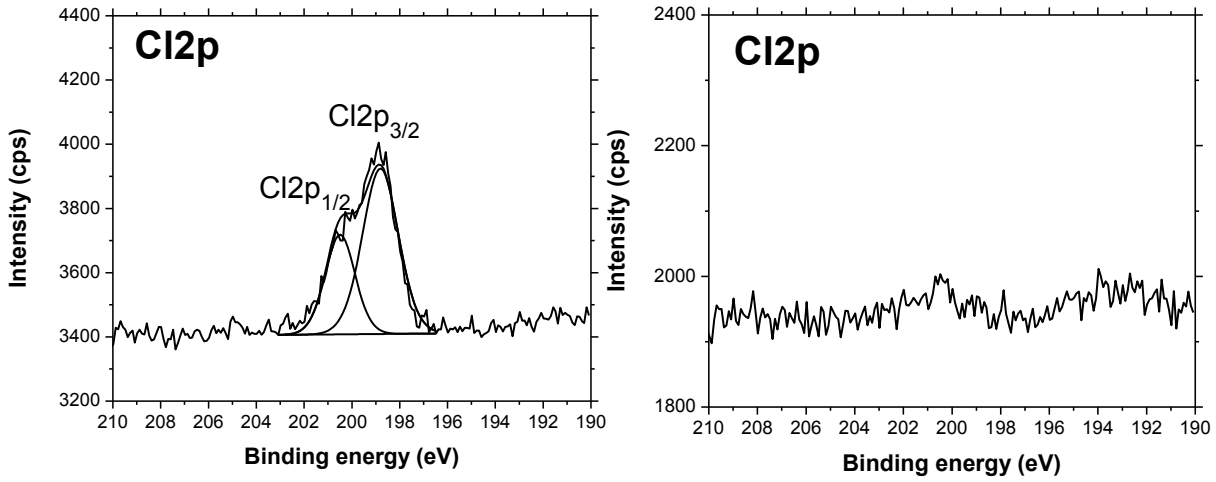

Fig. 4-7 Al2s, Cu2p, Cu Auger, O1s and Cl2p XPS spectra obtained for the pristine, polished Al-Cu sample (a) and thermally aged sample (annealing at 540 °C & aging at 300 and 450 °C) (b) after immersion in the alkaline electrolyte.

Significant differences can be observed in the XPS spectra obtained from the thermally treated sample after 7-minute-immersion in the alkaline electrolyte. As shown in the Fig. 4-7(b), the overlapping from the Cu3s spectra can still be observed in the Al2s spectra, but it is significantly attenuated. Both Cu3s peak and Cu2p spectra peak confirmed the presence of Cu oxides with a ratio of $CuO:Cu_2O$= 13:87. Furthermore, the presence of Cu_2O and CuO can be evidenced by the Cu Auger spectra (Fig. 4-7(b)). Large peaks in the area of Al2s region at around 119.0 ± 0.1 eV and 120.2 ± 0.1 eV are attributed to the formation of mixed $Al(OH)_3$ and Al_2O_3, respectively. The presence of aluminium and copper oxides and hydroxides was confirmed by the decomposition of O1s spectra as shown in the Fig. 4-7(b) and as depicted in Tab. 4-3. The quite weak Cl signal is related to the NaCl retains because of the same atomic percentage of Na and the binding energy of Cl2p peak (around 199.5 ± 0.1 eV, assigned to NaCl[96]).The data (BE and FWHM) of the high resolution main peaks of Al2s, O1s, $Cu2p_{3/2}$ and $Cl2p_{3/2}$ core level spectra for the Al-Cu samples after immersions in alkaline solutions are presented in Tab.4-3. The intensity ratios of O1s and Al2s peaks corresponding to the Al_2O_3 are 1.44 and 1.48 for the non-treated and thermally treated samples, respectively, suggesting the stoichiometry close to theoretical value of Al_2O_3. Besides, the $O1s_C$:$Al2s_B$ intensity ratios are 3.6 and 3.4 for

the non-treated and thermally treated samples, respectively, which are close to expected for an aluminium hydroxide (3 for $Al(OH)_3$ or 2 for AlOOH), indicating that the $O1s_C$ peak can be also assigned to some amounts of carbon contaminants.

Tab. 4-3 Binding energies (BE) and full-widths at half maximum (FWHM) for peaks of Al2s, $Cu2p_{3/2}$, O1s and $Cl2p_{3/2}$ core levels after immersion in the alkaline electrolyte.

Peaks	Non-treated		Species	Thermally treated		Species
	BE (eV)	FWHM (eV)		BE (eV)	FWHM (eV)	
$Al2s_A$	119.0	2.5	$Al(OH)_3$/AlOOH	119.1	3.0	$Al(OH)_3$/AlOOH
$Al2s_B$	120.1	2.5	Al_2O_3	120.3	3.5	Al_2O_3
$Cu2p_{3/2A}$	932.3	2.2	Cu_2O	932.3	2.3	Cu_2O
$Cu2p_{3/2B}$	933.9	1.9	CuO	933.8	2.0	CuO
$Cu2p_{3/2C}$	934.9	2.3	$CuCl_2$/$Cu(OH)_2$			
$O1s_A$	530.2	1.5	Cu oxides	530.2	1.7	Cu oxides
$O1s_B$	531.2	1.5	Al_2O_3	531.2	2.3	Al_2O_3
$O1s_C$	532.1	1.9	Hydroxides/ contaminants	532.2	2.5	Hydroxides/ contaminants
$O1s_D$	533.3	2.3	H_2O	533.4	2.7	H_2O
$Cl2p_{3/2}$	198.8	1.8	$CuCl_2$	199.5	3.5	NaCl

Furthermore, by comparing the atomic percentages of main species obtained from the XPS for the Al-Cu alloy samples (polished and thermally aged) after immersion in neutral and alkaline electrolytes it can be concluded that (as illustrated in the Fig. 4-8):

- no important differences in a quantity of different species can be observed as a function of thermal treatment after immersion in neutral electrolyte (Fig. 4-8 a) and high quantity of oxygen species would indicate a formation of thick corrosion layer rich in aluminium species and minor quantity of copper oxide compounds,

- the much higher at. % of copper can be observed on the surface sample after immersion in alkaline electrolyte indicating significant surface enrichment in copper and a preferential, general dissolution of Al matrix, which is in agreement with previous studies on the corrosion of binary Al-Cu alloys containing up to 6.7 at.% Cu in 0.1 M NaOH solution, showing that the corrosion proceeds with loss of Al species to the NaOH, while Cu is oxidized and redeposited in the corrosion product layer[97,98]; in alkaline electrolyte the important differences in the surface composition can be observed between polished and thermally aged sample showing much higher quantity of the copper on the surface of polished than on the surface of thermally aged sample; in the case of thermally aged sample the smaller copper surface enrichment can indicate to thicker corrosion layer rich in aluminium products; this different quantity of surface compounds can be related to different reaction mechanisms due to not the same size and distribution in-depth of copper-rich intermetallic particles as discussed in the previous part (Fig. 4-3 and 4-4).

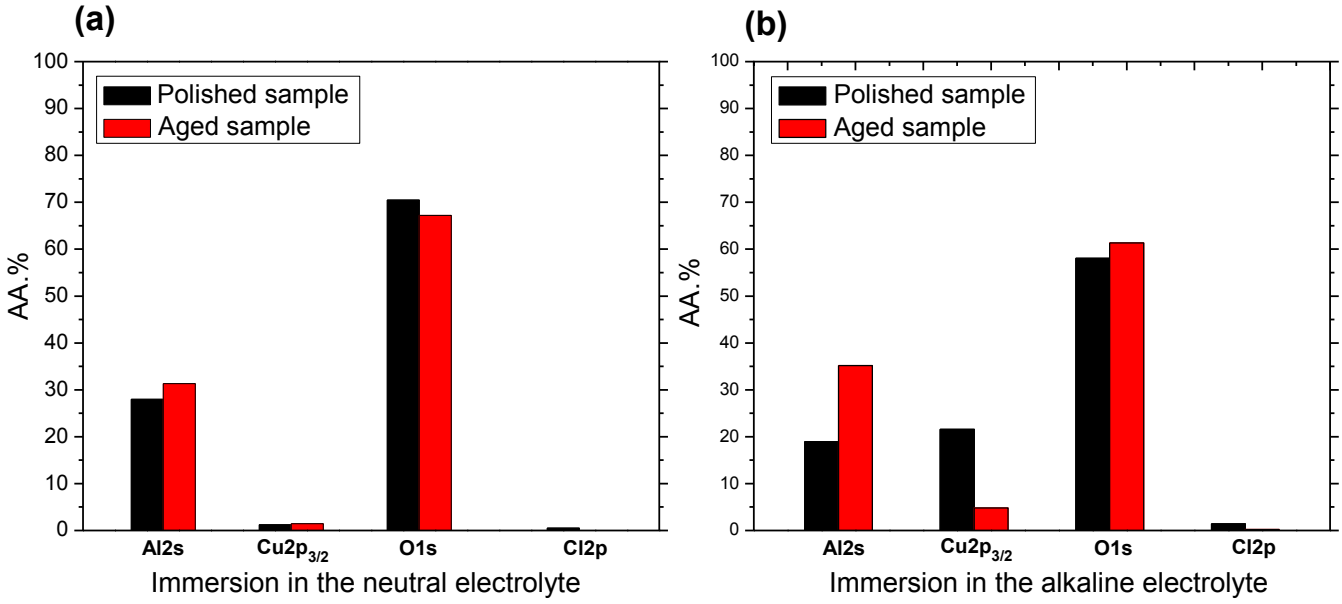

Fig. 4-8 Atomic percentages of main species Al2s, Cu2p$_{3/2}$, O1s and Cl2p present on the surface of both non-treated and thermally treated samples after immersions: (a) in the neutral electrolyte; (b) in the alkaline electrolyte.

The SEM images obtained from polished and thermally treated Al-Cu samples after exposed to neutral electrolytes show significant modifications with severe corrosion signs (Fig. 4-9(a) and (b)). In the case of polished Al-Cu alloy it can be concluded that preferential dissolution of Al occurred around the Cu-rich particles owing to the galvanic coupling (cathodic particle/Al matrix), which represented as pitting corrosion. Therefore, localized corrosion in the vicinity of the intermetallic particles (well known as trenching around particles) in the polished sample was observed. The similar results have been already reported showing the pitting around the second phase (*e.g.* S-phase) particles in the aluminium alloy AA 2024-T3 in NaCl solution[99,100]. It is well exhibited that the second phases, such as θ-phase, commonly exhibit cathodic electrochemical properties with respect to the matrix, which can easily lead to a preferential dissolution around these phases.

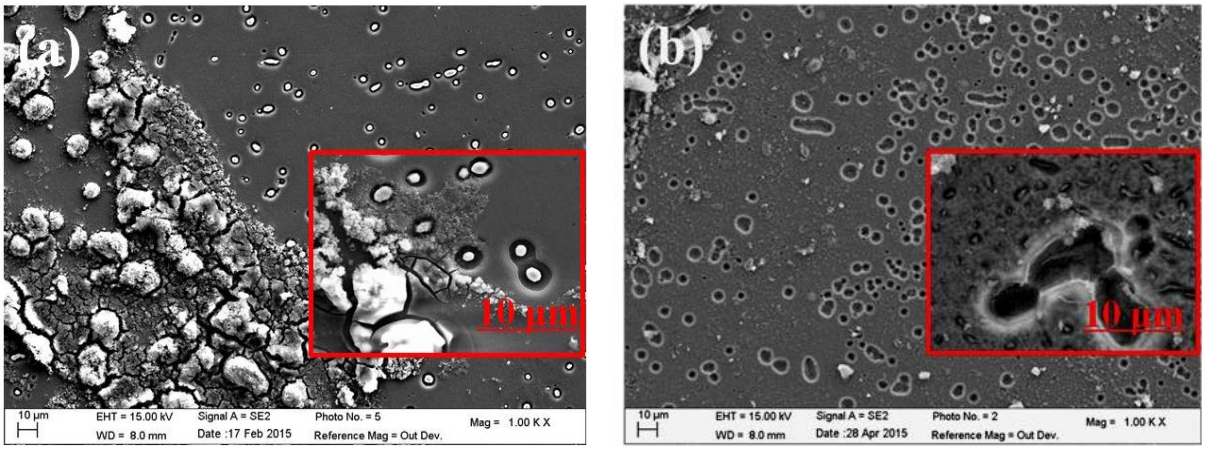

Fig. 4-9 SEM micrographs of samples after immersions in neutral electrolytes for 7 minutes: (a) the pristine, non-treated Al-Cu sample; (b) the Al-Cu thermally treated sample after annealing at 540 °C & aging treatments at 300 and 450 °C.

Hollow pits were found on the surface of the thermally treated samples (Fig. 4-9(b)). These pits can be formed in the thick layer of corrosion products beneath which the Cu-rich IMPs can be present. It is was confirmed by the ToF-SIMS results that during the annealing treatment Cu-rich intermetallics were dissolved into the substrate, and then precipitate during the thermal aging treatment prone to be on the Al-Cu alloy surface (namely, the oxide/metal interface)[101,102,103,104] (Fig. 4-4). For the

thermally treated sample, a short time (7 minutes) of immersion in the neutral solution is not sufficient for electrolyte and/or aggressive chloride ions to penetrate deeply into the interface region and form corrosion defects around the Cu-rich particles. It is possible that the defects are formed mostly at the regions where locally thinner oxide above the intermetallic particles (near the interfacial region) could provide initiation sites for the localized corrosion, leading to accumulation of chloride ions and local pH changes. The mechanism of dissolution will be clarified on the basis of ToF-SIMS results presented hereafter.

SEM images obtained for the polished and the thermally treated Al-Cu samples after immersion in alkaline electrolytes show totally different surface morphology (Fig. 4-10(a) and (b)). In alkaline electrolytes, protruded Cu-rich particles on the polished sample surface can be observed, likely resulted from thorough electrochemical anodic dissolution of Al oxide and Al matrix promoted by OH^- (overall corrosion reactions[105]: $Al + OH^- + 3/4O_2 + 3/2H_2O = Al(OH)_4^-$). However, for the thermally treated sample SEM images show dissolution mostly at grain boundaries. This is confirmed by ToF-SIMS results presented hereafter.

Our SEM results are consistent with the observations reported by many publications. For Al-Cu series alloys, in the neutral solutions containing Cl^-, the Cu-rich intermetallics as cathode would facilitate dissolution of the surrounding anodic Al matrix, hence pits are initiated around the Cu-rich intermetallics resulting in the preferential dissolution of active elements Al, leaving Cu-rich remnants[106-108]. In the alkaline solutions, the high pH promotes the dissolution of Al oxide on the Al-Cu alloy surface leading to the alkaline etching of Al substrate[109,110], as shown in the results (Fig. 4-10).

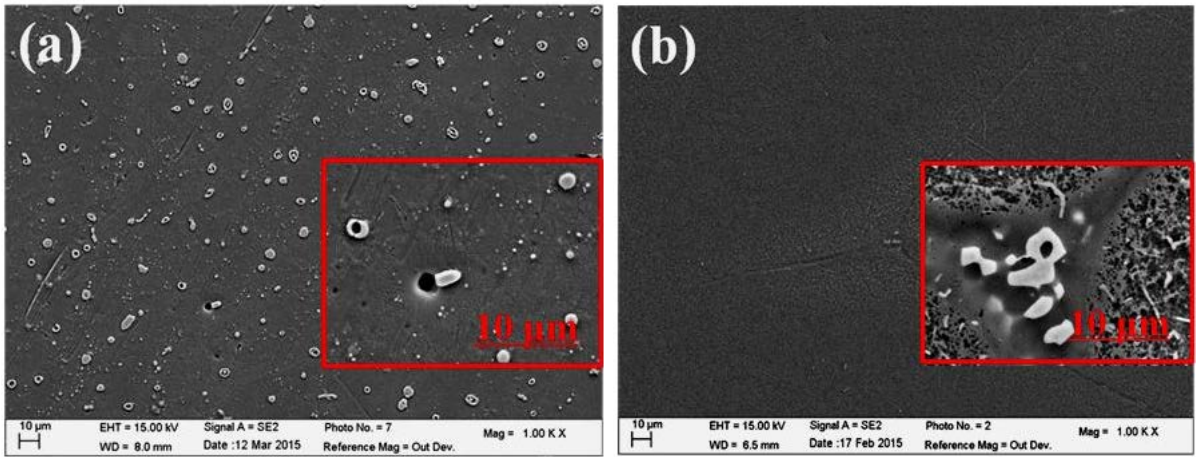

Fig. 4-10 SEM micrographs of samples after the immersions in alkaline solutions: (a) the pristine, non-treated Al-Cu sample after immersion for (7+30) minutes and (b) the Al-Cu thermally treated sample after annealing at 540 °C & aging treatments at 300 and 450 °C and immersion for 7 minutes.

ToF-SIMS negative ion profiles obtained on both samples after the immersion tests in neutral electrolytes containing chlorides show, as before immersion, three main regions:1) the Al oxide/corrosion layer, 2) the oxide/metal interface and 3) the metallic substrate (Fig. 4-11). A significant increase of sputtering time corresponding to the first oxide layer for the polished (over 5 times) and thermally treated (over 10 times) samples (Fig. 4-11(a)) when comparing to the negative ion profiles obtained for the Al-Cu alloy before immersion (Fig. 4-4(a)) can be observed. The longer sputtering times observed for the first (oxide) and the second (interface) region can be attributed to the formation of thick, rough and quite heterogeneous oxide layer composed of corrosion products. These data corroborates with the XPS results (Fig. 4-6(b)) showing thicker corrosion layer on the thermally treated sample. Moreover, the remarkable increase of Cu^- intensity in the Al oxide/corrosion layer region (increase of around one order of magnitude) can be related to the enrichment in Cu-like compounds resulting from the dissolution of Al matrix adjacent to Cu-rich intermetallic particles, which can be confirmed by the ToF-SIMS chemical mapping presented below (Fig. 4-12(a)).

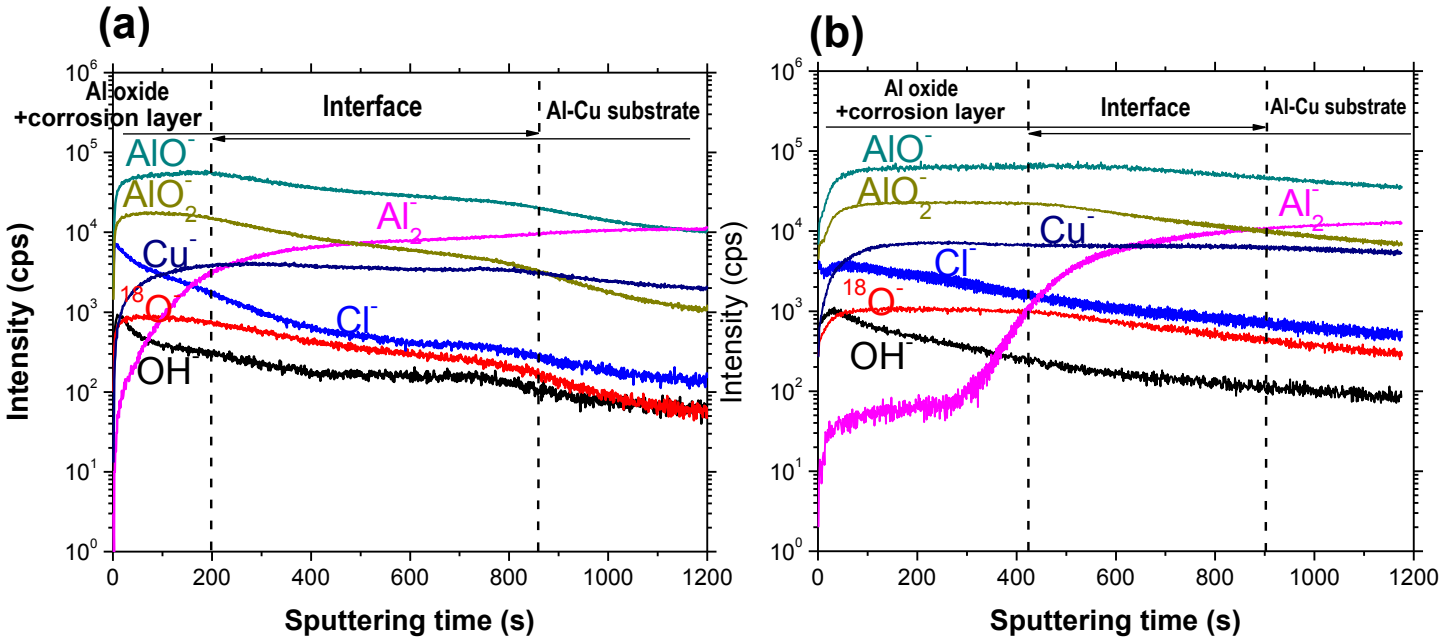

Fig. 4-11 ToF-SIMS negative ions depth profiles obtained on samples after immersion in neutral solutions for 7 minutes: (a) the non-treated sample; (b) the thermally treated Al-Cu sample after annealing at 540 °C & aging treatments at 300 and 450 ℃ .

The immersion of both samples in neutral, chloride-containing electrolytes leads also to intensity increase of OH^- principally within the oxide/corrosion layer region, which is also in agreement of the XPS results showing the formation of hydroxides. Furthermore, a slight intensity increase of Cl^- signal on the surface (from 200 cps to 600 cps) for the non-treated sample after immersion is consistent with the previous XPS observations (weak decomposed peaks assigned to chlorides). Here the ToF-SIMS depth profiles indicate that these corrosion products are not only present on the extreme surface but they penetrate in the bulk of the oxide/corrosion layer.

To have more insight into the corrosion mechanisms of model Al-Cu sample and the influence of thermal treatments (annealing and aging) performed on this alloy, the ToF-SIMS chemical maps were recorded on both samples after immersion tests (Fig. 4-12 presenting ToF-SIMS negative ion 100×100 μm^2 images). The ToF-SIMS images show very clearly different coverage and formation of chemically heterogeneous corrosion layer. Similarly to the ToF-SIMS images performed on the pristine, polished Al-Cu alloy and thermally treated Al-Cu alloy, the images presented below were obtained at different depth of sputtering: surface, interface and substrate

region chosen according the depth profiles (Fig. 4-11). Both samples present a large number of pits, which size is strongly influenced by the size of the intermetallic particles. The images performed at the extreme surface show principally the accumulation of oxygen-rich species, which can be related to formation of the layer rich in oxides and hydroxides (high intensity of O^-, AlO^- and OH^- ion signals). The high intensity of Cl^- signal can also point to NaCl retains at the extreme surface. It should be noted that with analysis performed at interface and substrate region the Cl^- ion signal becomes attenuated and the highest concentration of chlorides can be found at the most corroded zones. The zone with Al depletion observed at the interface region corresponds to the zone with oxygen (O^-) and oxide (AlO^-) and hydroxide (OH^-) enrichment. Finally, at the substrate region ((Fig. 4-12(a)) it can be observed that the high intensity large spots observed in O^-, AlO^- and OH^- ion maps overlap the high intensity smaller spots observed in Cu^- ion maps, which clearly indicate preferential dissolution of Al matrix nearby the Cu-rich intermetallic particles. This preferential dissolution phenomenon, resulting from the differences of electrochemical characteristics between the Cu-rich intermetallic particles and the surrounding Al matrix, was widely reported in the literature on the corrosion of aluminium alloy AA 2024-T3 in NaCl solutions[111-117].

Significant differences in the ToF-SIMS chemical images can be observed on the thermally treated sample after immersion tests (Fig. 4-12(b)). It can observed that in the area of surface region the oxides and hydroxides corrosion products are dominant and their concentration decreases with increasing sputtering time (substrate region) with the exception of large spots corresponding to intermetallic particles. The size and the form of corrosion spots account for the most important differences related to the influence of the thermal treatments (annealing and aging). From the images obtained at the interface region (Fig. 4-12(b)), it can be clearly observed that the pits are surrounded by the oxygen-rich species and that this high intensity O^- signals correspond also to high intensities of Cu^-. It can be then concluded that under the thick layer of oxide/hydroxide layer the accumulation of corrosion products (oxide

and copper) occurs principally in the vicinity of pits. With prolonged sputtering for the images performed at the substrate region it can be deduced that the middle parts of pits are filled with the oxygen and copper-like species and the presence of chlorine-species can be also confirmed. Outside of pitting spots, the Al-Cu alloy matrix shows principally a homogenous disctribution of metallic aluminium (constant intensity of Al_2^- signal), which is still rich in chlorine-like species confirming a penetration of chloride ions into the bulk (close to interface/substrate region). A penetration of chloride ions deep into the interface/substrate region is not so evident from the Cl-ion maps obtained for the pristine, polished Al-Cu sample (Fig. 4-12(a)). The intensity of Cl^- signal at the substrate region is very low. This can be related to formation of thicker (as also observed from ToF-SIMS depth profiles, Fig. 4-11(b)) and more porous corrosion layers on the thermally treated sample in comparistion to the layer formed on the pristine, polished Al-Cu alloy.

The ToF-SIMS images obtained on the thermally treated sample (Fig. 4-12(a)) allow also to conclude that the corrosion layer formed at the Al-Cu alloy matrix is not completely homogenous as it can be seen from the O^- and AlO^- ion images obtained in the substrate region where some high intensity spots with irregular shapes can be observed in the areas out of the areas corresponding to Cu-rich intermetallic particles. These irregular spots (with high intensity of O^- and AlO^- ions) can be superimposed with higher intensity of Cl^- ions, which could suggest that the thick oxide/hydroxide surface layer would favour an accumulation of chloride ions and corrosion initiation. It can be then concludedthat the Cu-rich intermetallic particles are the principal sites of corrosion initiation but not the only sites. In the case of SEM images (discussed above, Fig. 4-9(b)) the defects (pits) formed in the case of thermally treated sample has regular-in shape form similar to the defects detected in the ToF-SIMS images. However, the pits density observed in SEM images (Fig. 4-9 (b)) is not the same as the density defects observed in the case of ToF-SIMS images (Fig. 4-12 (b)). This can be related to different areas of characterisation chosen for the ToF-SIMS analysis, since pits on the corroded surface were not distributed homogeneously as shown in

the Fig. 4-9(b).

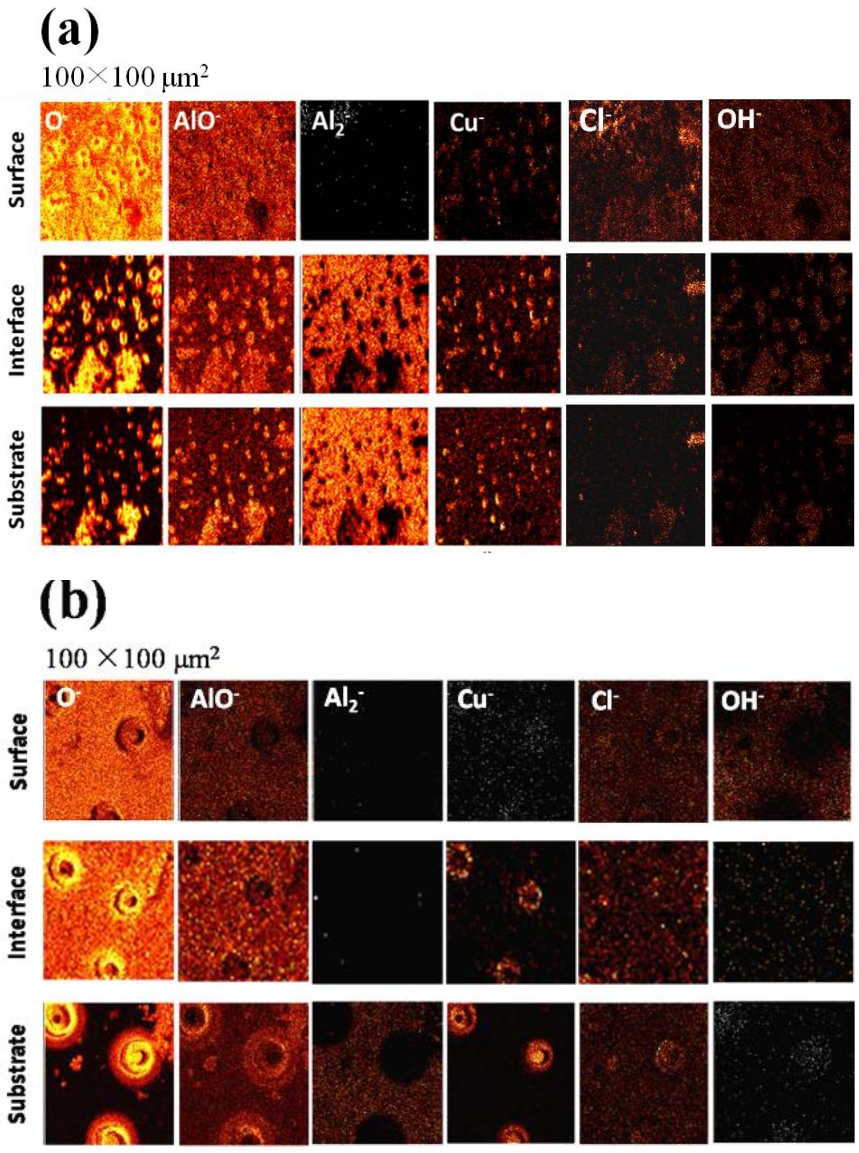

Fig. 4-12 ToF-SIMS negative ion images obtained on samples after the immersions in neutral solutions for 7 minutes: (a) the non-treated sample; (b) the thermally treated sample after annealing at 540 °C & aging at 300 and 450 °C.

A similar comparison was done on the polished and thermally treated samples after immersion in the alkaline electrolytes (ToF-SIMS negative ion profiles and images Fig. 4-13, Fig. 4-14, respectively). Here also, analogously to the ion depth profiles obtained on both samples after immersion in the neutral electrolytes, the marked increase of sputtering time for the first oxide/corrosion products layer (180 s

of sputtering) and the second interfacial layer (400 s of sputtering) can be observed (Fig. 4-13). This data are in agreement with the XPS data showing the formation of thick oxide and hydroxide layer as discussed in the previous part (Fig. 4-7). However, this increase is less important than in neutral electrolytes and there is no significant difference between both samples (Fig. 4-13(a) and (b)). The strong enrichment in Cu^- species and OH^- species can be confirmed by significant increase of the Cu^- (increasing from one to two orders of magnitude) and OH^- (increasing from two to three orders of magnitude) signals, and is much higher for thermally treated Al-Cu sample. These data show that the corrosion of Al-Cu alloy in the alkaline electrolytes proceeds through general dissolution of Al-matrix (Al oxide and Al substrate) and surface enrichment by Cu-species is observed. Much higher Cu-enrichment is observed after immersion in alkaline electrolyte than in neutral electrolyte, as shown by the XPS results discussed previously ((Fig. 4-7). It should be noted that the intensities of Cu^-, Cl^- and OH^- ions reach their maxima at around 50 s of sputtering time (for polished sample, Fig. 4-13(a)) and slightly higher for thermally treated sample (at around 80 s, Fig. 4-13(a)), revealing that the inner part of corrosion layer is rich in typical corrosion products (mixture of oxides and hydroxides, and also chlorides).

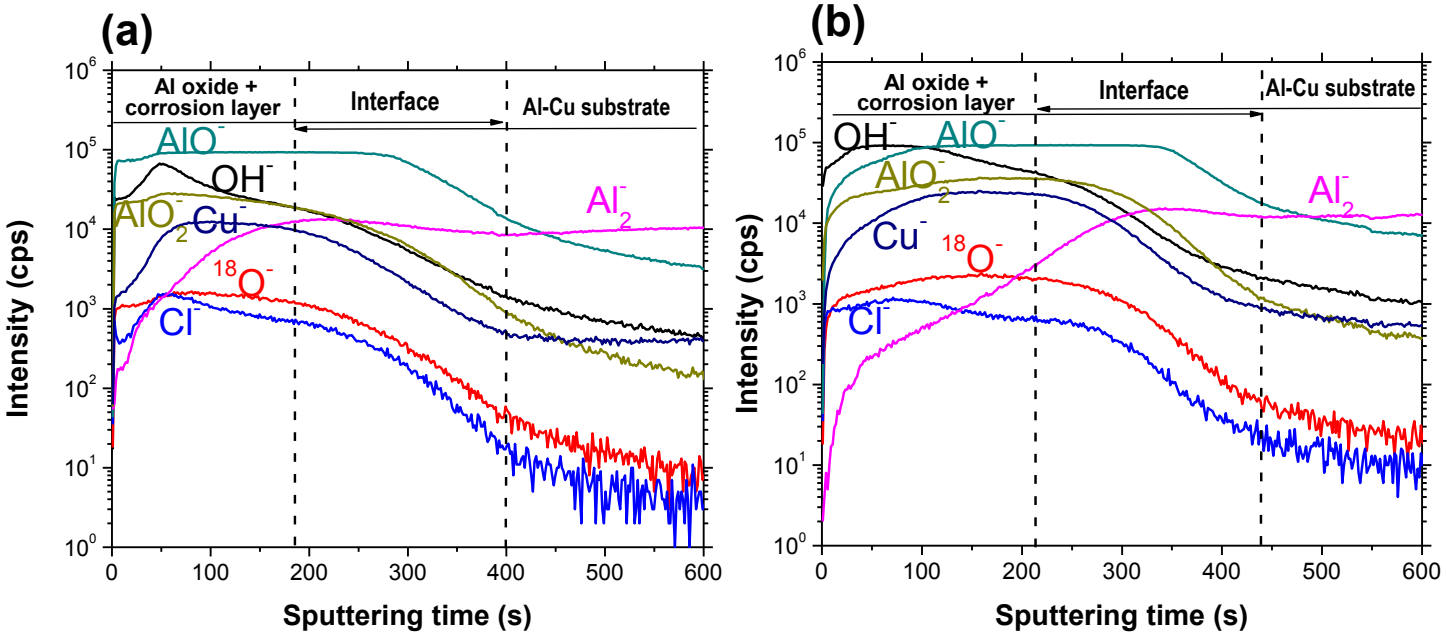

Fig. 4-13 ToF-SIMS negative ion depth profile obtained on samples after the immersions in alkaline solutions: (a) the non-treated sample for (7+30) minutes; (b) the thermally treated sample (annealing at 540 °C & aging at 300 and 450 °C) for 7 minutes.

The ToF-SIMS negative ion images (Fig. 4-14) obtained for both samples after immersion in alkaline electrolytes on show the high intensity O^-, AlO^- signals indicating to formation of oxygen-rich species on the extreme surface. Concerning the OH^- signal, the higher intensity can be observed after immersion of the thermally treated sample ((Fig. 4-14(b)) than pristine, polished sample (Fig. 4-14(a)), which can indicate to higher corrosion susceptibility of thermally treated sample. The pitting occurring on the polished sample (Fig. 4-14(a)) can be evidenced by comparing the sizes and densities of O^-, AlO^- and Cu^- signals. These higher intensity signals performed as preferential dissolution of Al matrix adjacent to the Cu-rich particles. However, the mechanism of dissolution is not the same as those observed on the pristine, polished Al-Cu alloy. Here, the strong Cu-enrichment is already observed in the surface region (Fig. 4-14(a)), where only copper rich spots corresponding to copper-rich intermetallic particles can be observed but also the clouds of high intensity Cu^- ion which can be attributed to dissolution of IMPs and redeposition of copper. With increased sputtering time the clouds of Cu-ion signal disappears and leaves behind the high intensity of Cu-rich spots corresponding to IMPs, meaning that dissolved and redeposited copper is present in the surface layer and the IMPs are not completely removed. These results are in perfect agreement with the SEM data showing the protruded Cu-rich IMPs (Fig. 4-10(a)) and also with the XPS data (Fig. 4-7(a)). However, ToF-SIMS mappings obtained for the thermally treated sample after immersion in the alkaline electrolyte (Fig. 4-14(b)) show significant differences. The general dissolution of Al oxide/substrate leads to revealing the grain boundaries and not the IMPs. The copper redeposition can be observed in the vicinity of the grain boundaries where probably Cu-rich intermetallics are precipitated during thermal treatment. These grain boundaries are preferential sites of corrosion attack when exposed to the alkaline electrolytes (as also observed by SEM, Fig. 4-10(b)).

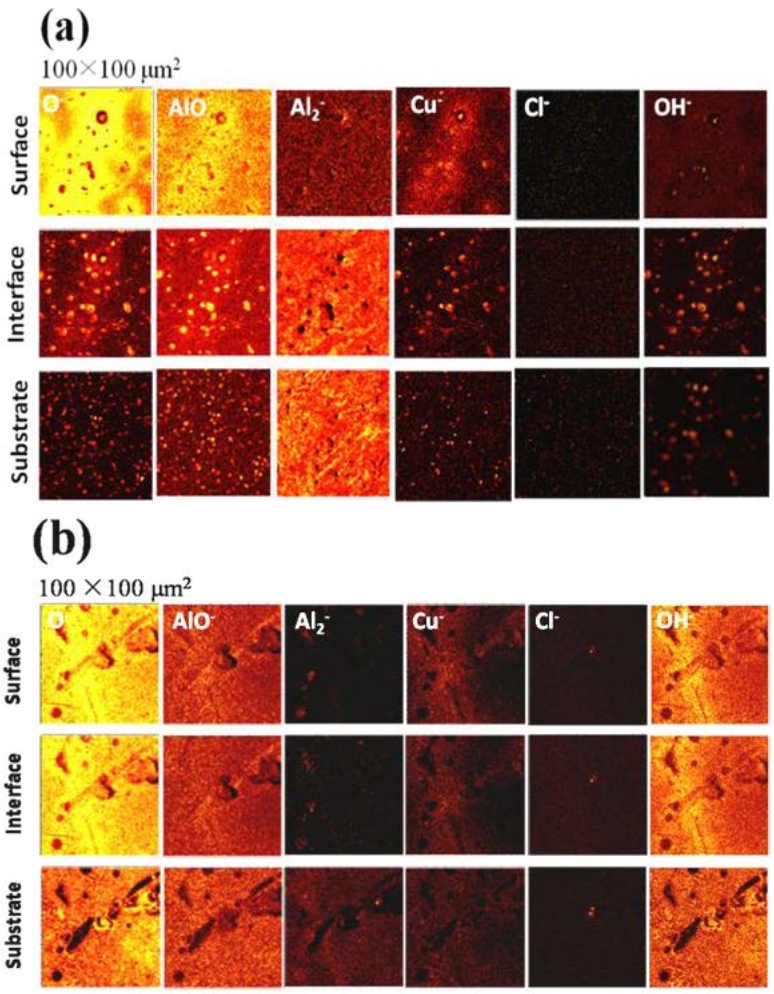

Fig. 4-14 ToF-SIMS negative ion images obtained on samples after the immersions in alkaline solutions: (a) the non-treated sample for (7+30) minutes; (b) the thermally treated sample (annealing at 540 °C & aging at 300 and 450 °C) for 7 minutes.

Based on presented results, it can be summarized that the intermetallic particles dissolved into the matrix in the annealing treatment, and precipitated mostly close to the oxide/substrate region during the aging treatment. It can be also concluded that the aging treatment leads to precipitation of the IMPs at the grain boundaries. The applied thermal treatment led to formation of large IMPs particles when compared to IMPs present in the non-thermally treated Al-Cu alloy.

In the neutral electrolyte containing Cl^-, pitting corrosion occurred at the adjacent areas of the Cu-rich particles in the case of the non-treated sample, whereas hollow pits formed on the thermally treated sample owing to the initiation sites for localized corrosion. The thermal treatments applied in this study led to lower corrosion

susceptibility with formation of thicker corrosion layer in neutral electrolyte and diffusion of chloride ions through this layer up to the substrate. The observation of the intermetallic particles formed during the thermal treatments allowed for characterization of different steps of pit formation:

1) the Cl^- ion penetration and preferential accumulation at the interface region in the areas corresponding to the Cu-rich IMPs,
2) corrosion initiation in the adjacent areas of the Cu-rich particles, and dissolution of Cu-rich intermetallic particles leading to copper redeposition,
3) formation of aluminium oxyhydroxide and redeposition at the rim of the pit covering the corroded areas of IMPs and also the Al-Cu matrix.

In the case of alkaline immersion, the general dissolution of Al oxide and Al-Cu alloy matrix was observed. The thermal treatment applied to the Al-Cu alloy had important influence on corrosion reaction mechanisms. For non-thermally treated alloy the dissolution resulted in protruding the Cu-rich IMPs, whereas for the thermally treated sample, the general dissolution of Al oxide and Al-Cu matrix led to the etching at grain boundaries, where Cu-rich intermetallics were concentrated. However, for both samples a clear copper enrichment on the sample surface was observed:

1) in the form of Cu-rich intermetallic particles and redeposited, formerly dissolved copper in the case of non-thermally treated, polished alloy,
2) in the form of redeposited copper, formerly dissolved copper from grain boundaries where the IMPs were concentrated.

4.4 Conclusions

(1) ToF-SIMS and XPS analysis indicate a slightly thicker Al oxide (about 8 nm) with Al hydroxides adsorption formed on the thermally treated (annealing at 540 °C & aging at 300 and 450 °C) Al-Cu alloy sample compared with the pristine, non-

treated sample (around 7 nm). In addition, a Cu-rich region at the oxide/metallic substrate interface was observed, the size and density of which corresponded to those of intermetallic particles (Al_2Cu, θ phase);

(2) The slightly nobler OCPs, obtained for the thermally treated samples during immersion in both the neutral electrolyte (around 20 mV higher) and the alkaline electrolyte (around 5 mV higher) can be related to the Cu-enrichment. More significant OCP increase observed in alkaline electrolytes for both polished and thermally treated samples can be attributed to faster general dissolution of Al oxide and Al matrix under high pH conditions resulting in the significant enrichment of Cu on the surface;

(3) After immersion in neutral electrolyte, severe pitting corrosion was observed on the non-thermally treated sample in the vicinity of the cathodic Cu-rich particles with respect to the anodic Al substrate, well known as trenching around particles, whereas hollow pits present at regions where the thinner oxide above large Cu-rich particles provided initiation sites for localized corrosion in the thermally treated sample. On the corroded surface of both the non-treated and treated samples, the formation of mixed layers composed of aluminium-copper oxides/hydroxides rich in Cu_2O and CuO were verified by the XPS analysis;

(4) In the alkaline electrolyte, general corrosion, performing significant etching of Al on both samples leads to protruding of Cu-rich intermetallic particles and exposure to the solution, which resulted in the localized corrosion in the adjacent area of these cathodic particles; more significant copper enrichment observed in the case of the polished sample than in the case of the thermally treated sample was attributed to different size and distribution in-depth of copper rich intermetallic particles before immersion tests;

Important increase of the corrosion layer products was confirmed in all immersion tests by XPS and ToF-SIMS. The XPS analysis indicated the formation of corrosion product layers composed of mixed aluminium oxides/hydroxides with significantly higher surface concentration of copper oxides/chlorides on the attacked surface of

non-treated sample in the alkaline electrolyte, while no copper chlorides was observed on the attacked surface of thermally treated sample in the alkaline electrolyte.

References

[1] I.J. Polmear, *Aluminum alloys—A century of age hardening*, Materials Forum, 28, 1-14 (2004)

[2] A. Guinier, *Nature*, 142, 569-570 (1938)

[3] S.C. Wang, M.J. Starink and N. Gao, *Scripta Mater.*, 54, 287-291 (2006)

[4] M. Hansen, *Constitution of Binary Alloys*, Mcgraw-Hill Book Company Inc., New York, 84-90 (1958)

[5] Z. Ahmad, *Recent Trends in Processing and Degradation of Aluminium Alloys*, InTech, Shanghai, 155-174 (2011)

[6] T.B. Massalski, *Bull. Alloy Phase Diagr.*, 1, 27-33 (1980)

[7] B. Geethaa, K. Ganesan, *Materials Today: Proceedings*, 2, 1200-1209 (2015)

[8] M. Voncina, A. Smolej, J. Medved, P. Mrvar and R. Barbič, *Mater. & Geoenviron.*, 57, 295-304 (2010)

[9] M.J. Starink, A.M. Zahra, *J. Mater. Sci. Lett.*,16, 1613-1615 (1997)

[10] M.J. Starink, A.M. Zahra, *J. Mater. Sci. Lett.*,16, 1613-1615 (1997)

[11] S. Abis, P. Mengucci, G. Riontino, *Mater. Sci. Eng.*, A134, 1175-1178 (1991)

[12] E.D. Boyes and F.L. Gai, *Proc. EMAG 75*, Academic Press, NY, 267 (1976)

[13] T. Abe, K. Miyazaki, and K. Hirano, *Acta Metall.*, 30, 57-366 (1982)

[14] M. Wada, H. Kita, and T. Mori, *Acta Metall.*, 33, 1631-1635 (1985)

[15] K. Hono, T. Satoh, and K. Hirano, *Philos. Mag.*, 53A, 495-504 (1986)

[16] R.J. Rioja and D.E. Laughlin, *Metall. Trans.*, 8A, 1257-1261 (1977)

[17] H.B. Aaron, H.I. Aaronson, *Acta Metall.*, 16, 789-798 (1968)

[18] M. Hass and J.Th.M. Hosson, *Scripta mater.*, 44, 281-286 (2001)

[19] R. Gronsky, P. Furrer, *Metall. Trans. A*, 12, 121-127 (1981)

[20] W.A. Cassada, G.J. Shiflet and S.J. Poon, *J. Microscopy*, 146, 323-335 (1987)

[21] J. Hong, *Modelling of grain boundary segregation, precipitation and precipitate-free zones of high strength aluminium alloys*, Loughborough University, 1994

[22] K.A. Son, N. Missert, J.C. Barbour, J.J. Hren, R.G. Copeland and K.G. Minor, *J.Electrochem.Soc.*,148, B260-B263 (2001)

[23] H. Habazaki, M.A. Paez, K. Shimizu, P. Skeldon, G.E. Thompson, G.C. Wood, X. Zhou, *Corros.Sci.*, 38, 1033 (1996)

[24] R.G. Buchheit, *J. Electrochem. Soc.*, 142, 3994-3996 (1995)

[25] S.S. Wang, I.W. Huang, L. Yang, J.T. Jiang, J.F. Chen, S.L. Dai, D.N. Seidman, G.S. Frankel, and L. Zhen, *J. Electrochem. Soc.*, 162, C150-C160 (2015)

[26] B.L. Hurley, S.Qiu and R.G. Buchheit, *J. Electrochem. Soc.*,158, C125-C131 (2011)

[27] J.R. Scully, D.E. Peebles, A.D. Romig, D.R. Frear, C.R. Hills, *Metall. Trans. A*,23A, 1365 (1990)

[28] Z. Szklarska-Smialowska, *Corros. Sci.*, 41, 1743–1767 (1999)

[29] *The behaviour of aluminium and its alloys*, Christian Vargel, Dunod, 1979

[30] N. Birbilis, and R.G. Buchheit, *J. Electrochem. Soc.*, 152, B140-B151 (2005)

[31] R.G. Buchheit, L.P, Montes, M.A. Martinez, J. Michael and P.F. Hlava, *J. Electrochem. Soc.*, 146, 4424-4428 (1999)

[32] T.J.R. Leclere and R.C. Newman, *J. Electrochem. Soc.*,149, B52 (2002)

[33] A.C. Vieira, A.M. Pinto, L.A. Rocha, S. Mischler, *Electrochim. Acta*, 56, 3821–3828 (2011)

[34] R. Ambat, E.S. Dwarakadasa, *J. Appl. Electrochem.*,24, 911-916 (1994)

[35] M. Yasuda, F. Weinberg and D. Tromans, *J.Electrochem.Soc.*,137, 3708-3715 (1990)

[36] J. R. Scully, R. P. Frankenthal, K.J. Hanson, D.J. Siconolfi, and J.D. Sinclair, *J. Electrochem. Soc.*,137, 1365 (1990)

[37] J. R. Scully, T. O. Knight, R. G. Buchheit, and D. E. Peebles, *Corros. Sci.*,35, 185 (1993).

[38] O. Schneider, G. O. Ilevbare, J. R. Scully, and R. G. Kelly, *J. Electrochem. Soc.*,151, B465 (2004)

[39] G.S. Chen, M. Gao, R.P.Wei, *Corros.*, 52, 8-15 (1996)

[40] J.R. Scully, K.O. Knight, R.G. Bucheit, D.E. Peebles, *Corros. Sci.*, 35, 185 (1993)

[41] R.G. Buchheit, R.P. Grant, P.F. Hlava, B. Mckenzie and G.L. Zender, *J. Electrochem. Soc.*, 144, 2621-2628 (1997)

[42] O. Schneider, G.O. Ilevbare, and J.R. Scully, *J.Electrochem.Soc.*,151, B465 (2004)

[43] G.O. Ilevbare, O. Schneider, R. G. Kelly, and J. R. Scully, *J. Electrochem. Soc.*,151, B453 (2004)

[44] J.R. Scully, K.O. Knight, R.G. Bucheit, D.E. Peebles, *Corros. Sci.*, 35, 185 (1993)

[45] J.R. Scully, D.E. Peebles, A.D. Romig, D.R. Frear, C.R. Hills, *Metall. Trans. A*, 23A, 1365 (1990)

[46] T.H. Muster, A.E. Hughes, G.E. Thompson, *Copper Distributions in Aluminium Alloys*, Nova Science Publishers Inc., New York, 9-23 (2009)

[47] K. Sieradzki, *J. Electrochem. Soc.*, 140, 2868-2872 (1993)

[48] P. Marcus, *Corrosion Mechanisms in Theory and Practice*, Third Edition, CRC Press, Boca Raton (2012)

[49] C. Blanc, B. Lavelle, and G. Mankowski, *Corros. Sci.*, 39, 495-510 (1997)

[50] A. Seyeux, G.S. Frankel, and P. Marcus, *J. Electrochem. Soc.*, 158, C165-C171 (2011)

[51] F. Wiame, V. Maurice, P. Marcus, *Surf. Sci.* 601, 1193–1204 (2007).

[52] S. Doniach, *Phys. Rev. B*, 2, 3898-3905 (1970)

[53] S.C. Wang, and M.J. Starink, *Int. Mater. Rev.*, 50, 193-215 (2005)

[54] S. Fu, D. Yi, H. Liu, Y. Jiang, B. Wang, Zh. Hu, *Trans. Nonferrous Met. Soc. China*, 24, 2282−2288 (2014)

[55] H. He, K. Alberti, T.L. Barr, J. Klinowski, *J. Phys. Chem*, 97, 13703 (1993)

[56] G. Moretti, G. Fierro, M.L. Jacono, P. Porta, *Surf. Interface Anal.*, 14, 325 (1989)

[57] P. Marcus, C. Hinnen, I. Ofefjord, *Surf. Interface Anal.*, 20, 923-929 (1993)

[58] Y.C. Kim, H.H. Park, J.S. Chun, W.J. Lee, *Thin Solid Films*, 237, 57 (1994)

[59] I. Ofefjord, H.J. Mathieu, P. Marcus, *Surf. Interface Anal.*, 15, 681 (1993)

[60] A.N. Mansour, *Surface Science Spectra*, 3, 202 (1994)

[61] A. Ayame, et al, *BunsekiKagaku*,40, 673 (1991)

[62] S. Moon, S. Pyun, Corrosion Science, 39, 399-408 (1997)

[63] J.P. Espinós, J. Morales, A. Barranco, A. Caballero, J.P. Holgado, and A.R. González-Elipe, *J. Phys. Chem. B*, 106, 6921-6929 (2002)

[64] P. Brand, H. Freiser, *Anal. Chem.*, 46, 1147 (1974)

[65] J.P. Espinós, P. Espinós, J. Morales, A. Barranco, A. Caballero, J.P. Holgado, and A.R. González-Elipe, *J. Phys. Chem. B*, 106, 6921-6929 (2002)

[66] P. Brand and H. Freiser, *Anal. Chem.*, 46, 1147 (1974)

[67] F.M. Capece, V. Di Castro, C. Furlani, G. Mattogno, *J. Electron Spectrosc.,* 27, 119 (1982)

[68] Y. Liu, G.E. Thompson, P. Skeldon, *Surf. Interface Anal.*, 36, 339 (2004)

[69] E. McCafferty, *Introduction to Corrosion Science*, Springer, New York, 2009

[70] W.G. Cook, R.P. Olive, *Corros. Sci.*, 58, 291-298 (2012)

[71] M.Sc. Ahmed Younis, *Protection of Aluminum Alloy (AA7075) from Corrosion by Sol-Gel Technique*, Technischen Universität Chemnitz, 30.08. 2011

[72] R.G. Buchheit, R.G. Kelly, N.A. Missert, B.A. Shaw, *Corrosion and Protection of Light Metal Alloys*, The Elctrochemical Society INC., Pennington, 2004

[73] J.R. Scully, D.E. Peebles, A.D. Romig Jr., D.R. Frear, and C.R. Hills, *Metal.Trans. A*, 23A, 2641-2655 (1992)

[74] S.I. Pyun, S.M. Moon, *J. Solid State Electrochem.*, 4, 267-272 (2000)

[75] J. R. Davis, *Aluminum and Aluminum Alloys*, ASM International, Ohio, 784 (1993)

[76] K. Naoi, M. Takeda, H. Kanno, M. Sakakura, A. Shimada, *Electrochim. Acta*, 45, 3413–3421 (2000)

[77] B. Zhou, Y. Wang, Y. Zuo, *Appl. Surf. Sci.*, 357, 735–744 (2015)

[78] T. Robert, G. Offergeld*, Phys. Status Solidi A,* 14, 277 (1972)

[79] N.S. McIntyre, M.G. Cook, *Anal. Chem.*, 47, 2208 (1975)

[80] G. Deroubaix, P. Marcus, *Surf. Interface Anal.,* 18, 39 (1992)

[81] G. Schon, *Surf. Sci.,*35, 96-108 (1973)

[82] N. Pauly, S.Tougaard, F.Yubero, *Surf. Sci.*, 620, 17-22 (2014)

[83] Y. Kim, R.G. Buchheit, P.G. Kotula, *Electrochim. Acta*, 55, 7367–7375 (2010)

[84] M. Bethencourt, F.J. Botana, M.J. Cano, M. Marcos, J.M. Sánchez-Amaya, L. González-Rovira, *Corros. Sci.*, 51, 518–524 (2009)

[85] C. Blanc, B. Lavelle, G. Mankowsk, *Corros. Sci.*, 39, 495–510 (1997)

[86] S. Anderson, J.W. Davenport, *Solid State Commun.,* 28, 677 (1978).

[87] H. Hopster, C.R. Brundle, *J. Vac. Sci. & Technol.*, 16, 548 (1979).

[88] S. Gredelj, A.R. Gerson, S. Kumar, G.P. Cavallaro, *Appl. Surf. Sci.*, 174, 240–250 (2001)

[89] T. Do, N.S. McIntyre, *Surf. Sci.*, 440, 438–450 (1999)

[90] T. Robert, G. Offergeld*, Phys. Status Solidi A,* 14, 277 (1972)

[91] A. Galtayries, J.P. Bonnelle, *Surf. Interf. Anal.*, 23, 171-179 (1995)

[92] J.C. Klein, C.P. Li, D.M. Hercules, and J.F. Black, *Appl. Spectrosc.,* 38, 729-734 (1984)

[93] W. Sesselmann, T.J. Chuang, Surf. Sci. 176, 32 (1986)

[94] S. Murali Krishna, K. Sureshkumar, Thomas S. Varley, D. H. Nagaraju, T. Ramakrishnappa, *The Royal Society of Chemistry*, 6, 8698-8705 (2014)

[95] W. Gutowski, H. Dodiuk, *Recent Advances in Adhesion Science and Technology in Honor of Dr. Kash Mittal*, CRC Press, 1 edition, Boca Raton, FL, 2013

[96] Y. Uwamino, A. Tsuge, T. Ishizuka, H. Yamatera, *Bull. Chem. Soc. Jpn.*, 59, 2263 (1986)

[97] Y. Liu, A.M. Arenas, P. Skeldon, G.E. Thompson, H. Habazaki, K. Shimizu, P. Bailey, T.C.Q. Noakes, *Corros. Sci.*, 48, 1874 (2006)

[98] Y. Liu, M.A. Arenas, S.J. Garcia-Vergara, T. Hashimoto, P. Skeldon, G.E. Thompsoa, H. Habazaki, P. Bailey, T.C.Q. Noakes, *Corros. Sci.*, 50, 1475-1480 (2008)

[99] M. Shao, Y. Fu, R. Hu, C. Lin, *Mater. Sci. Eng.*, A344, 323-327 (2003)

[100] A.E. Hughes, A. Boag, A.M. Glenn, D. McCulloch, T.H. Muster, C. Ryan, C. Luo, X. Zhou, G.E. Thompson, *Corros. Sci.*, 53, 27-39 (2011)

[101] C.R. Brooks, *Heat treatment, structure and properties of nonferrous alloys*, ASM International, 1982

[102] J.W. Martin, *Precipitation Hardening*, Second Edition, Butterworth-Heinemann, 1998

[103] K.G. Karthikeyan, H.A. Elliott, J. Chorover, *J. Colloid Interf. Sci.*, 209, 72-78 (1999)

[104] H.W. Guo and S.T. Dunham, *2007 MRS Spring Meeting*, Materials Research Society, 2007

[105] J. R. Davis, *Aluminum and Aluminum Alloys*, ASM International, Ohio, 784 (1993)

[106] V. Guillaumin, G. Mankowski, *Corros. Sci.*, 41, 421–438 (1998)

[107] D.G. Harlow, R.P. Wei, *Eng. Fract. Mech.*, 59, 305–325 (1998)

[108] G.S. Chen, M. Gao, R.P. Wei, *Corros.*, 52, 8–15 (1996)

[109] Y. Liu, M. A.Arenas, S.J. Garcia-Vergara, et al, *Corros. Sci.*, 50, 1475-1480 (2008)

[110] O. Schneider, G.O. Ilevbare, J.R. Scully and R.G. Kelly, *J. Electrochem. Soc.*, 151, B465-B472 (2004)

[111] A. Boag, A.E. Hughes, A.M. Glenn, T.H. Muster, D. McCulloch, *Corros. Sci.*, 53, 17-26 (2011)

[112] G.S. Chen, M. Gao, R.P. Wei, *Corros.*, 52, 8-15 (1996)

[113] J.R. Scully, K.O. Knight, R.G. Bucheit, D.E. Peebles, *Corros. Sci.*, 35, 185 (1993)

[114] G.O. Ilevbare, O. Schneider, R. G. Kelly, and J. R. Scully, *J. Electrochem. Soc.*, 151, B453 (2004)

[115] J.R. Scully, K.O. Knight, R.G. Bucheit, D.E. Peebles, *Corros. Sci.*, 35, 185 (1993)

[116] P. Leblanc, G.S. Frankel, *J. Electrochem Soc.*, 149, B239-B247 (2002)

[117] C.M. Liao, J.M. Olive, M. Gao, R.P. Wei, *Corros.*, 54, 451-458 (1998)

Chapter 5 Corrosion protection of the model Al-Cu alloy by ALD alumina thin film coatings

The corrosion protection of Al-4.87wt.% Cu model alloy by a thin, 20 nm-thick alumina ALD layer is presented in this chapter. A detailed surface chemical and morphological characterization shows a significant improvement of corrosion resistance of the coated alloy samples. As expected, the ALD alumina layer in alkaline electrolytes is not as stable as in neutral electrolytes, and undergoes dissolution. However, regardless of the pH of electrolyte, the Al_2Cu particles present in the Al-Cu alloy remain intact, and no trenching around them was observed either in neutral or alkaline electrolytes. The application of a compact, conformal alumina layer made by ALD can be an alternative for the corrosion protection of aluminium alloys not requiring prior removal of the intermetallic particles.

5.1 Introduction

As discussed in the bibliographic chapter and in the previous chapter 3 presenting research results on thermal treatments, the Al_2Cu second phase particles (θ-phase) present in the Al-Cu alloys reduce their corrosion resistance, owing to the galvanic coupling between the copper and the surrounding matrix promoting the localized corrosion[1-4]. These copper-rich zones are more noble/cathodic than the surrounding aluminum matrix, and are generally considered to be the initiation sites for localized corrosion in an environment containing aggressive ions, *e.g.* Cl^-[5-9].

To avoid this problem, there are many anti-corrosion treatments such as anodizing, chemical conversion treatments or organic coatings[10-13]. The chemical conversion treatment is applied widely due to advantages of low cost, simple process, and the stability of the treatment solution. Chromium chemical conversion (CCC), the most widely used, however, will be banned because the hexavalent chromium is toxic[14]. So new, non-hexavalent chromium-based processes, *e.g.* trivalent chromium process (TCP)[15] or phosphate conversion process have been developed[16,17]. However, the TCP has a complex composition and poor stability and, in addition, trivalent chromium may be converted to hexavalent chromium[18, 19], which limits its applications. The phosphate conversion coating is to some degree thick and rough, and calls for a long time heating on the solutions to keep it stable leading to a significant consumption of electricity and time[20]. As the final stage of corrosion protection, organic paints are often applied to the aluminium alloys[21].

Atomic Layer Deposition (ALD) can be an interesting alternative to thin conversion coatings. ALD treatment has recently been described as a promising technique for the surface treatment of metals and alloys, and has already shown its versatility in industrial uses[22]. Application of ALD for corrosion protection has been studied by the group of Physical Chemistry of Surfaces (PCS) at CNRS-Chimie ParisTech on different materials such as carbon steel, stainless steel, copper, and aluminium[23-32]. According to our knowledge the investigation of the protection

performance of ALD coatings for the Al-Cu alloys containing Cu-rich intermetallic particles (IMPs) has been rarely reported. The thin alumina layers (10–50 nm) deposited on the aluminium Al2024-T3 alloys by plasma-enhanced and thermal ALD at a temperature range of 50–150 °C showed that the 50 nm films were the least porous (<0.5%), and offered the best corrosion-resistance[33]. Similar reports by Härkönen *et al.*[34,35] confirmed that the thicker alumina ALD coating (over50 nm) deposited on the aluminium Al2024-T3 alloys offered better corrosion protection performances and lower porosities during the neutral salt spray tests (NSS) and electrochemical measurements (decrease of corrosion current density and increase of the pitting resistances (R_{pit})).

In this chapter, the corrosion efficiency of a 20 nm-thick alumina ALD layer deposited on the Al-Cu alloy with Cu-rich precipitates was evaluated by surface analytical techniques such as x-ray photoelectron spectroscopy (XPS), time-of-flight secondary ion mass spectrometry (ToF-SIMS), and atomic-force microscopy (AFM). The coating stability and the chemical and structural coating modifications during the immersion tests in neutral and alkaline electrolytes containing chloride ions were investigated. In addition scanning electron microscopy (SEM) was used to evaluate the morphology of the coated and non-coated Al-Cu alloys before and after immersion tests.

5.2 Experimental

Substrate preparation. Before processing, the Al-Cu model alloy samples (*Goodfellow,* with 4.87wt.% Cu as measured by energy dispersive X-ray spectrometry (EDX)) in the form of discs (Φ=1cm) were polished on SiC papers (#1200; #2400; #4000) with water, and then on cloth with alumina suspensions (OP-AN, ESCIL Inc.) up to 0.3 μm. The samples were cleaned separately with acetone, ethanol and pure millipore water (resistivity＞18 MΩ cm) in an ultrasonic bath for 5 minutes, 3 minutes, and 1 minute, respectively.

ALD coatings preparation. Al_2O_3 (20 nm) coatings were deposited on the Al-Cu polished alloy substrates (as described above) at 250 °C with a Picosun SUNALE R-150 ALD reactor. Trimethyl aluminium (TMA, $Al(CH_3)_3$) (Chemtura (AXION® PA 1300, purity 99.9%) and water (ultra-pure with resistivity > 18 MΩ cm) were used as precursors. The ALD reactor was operated with a constant nitrogen flow at a pressure of about 5 mbar. The deposition rate was about 0.1 nm cycle^{-1}. The pulse time was 0.1 s for both TMA and H_2O. The purge time with nitrogen (> 99.999%) was 5 s each time after application of each precursor. After the deposition the coated samples were cooled to 100 °C in the ALD reactor (for approximately 4 hours) before exposition of the samples to laboratory air. The deposited film thickness was measured by means of X-ray Reflectivity (XRR) using Panalytical X'Pert Pro MPD diffractometer. The thickness was measured from a silicon wafer coated simultaneously with the substrates and modeled with X'Pert Reflectivity. 200 deposition cycles correspond to coating thickness of 20 nm.

Immersion tests. The pristine, non-coated and alumina ALD coated Al-Cu model alloy samples were immersed in a near neutral electrolyte containing 0.01 M NaCl＋ 0.3% vol H_2O_2 (pH≈6.2) and in an alkaline electrolyte containing 0.01M NaCl＋ NaOH (pH=11.5). The electrolytes were prepared with ultra-pure Millipore® water and reagent grade chemicals (NaCl Analar Normapur analytical reagent, VWR® BDH Prolabo®). The open circuit potential (OCP) was recorded during the immersion tests. The OCP measurements were performed using the three-electrode electrochemical cell: a working electrode (non-coated or coated Al-Cu sample), a counter electrode (Pt wire) and a reference electrode (Ag/AgCl), using an Autolab/PGSTAT128N instrument. The surface of working electrode area was delimited to 0.29 cm^2 by a Viton O-ring. The pristine Al-Cu samples were immersed in the near neutral electrolyte for 7 minutes and in the alkaline electrolyte for (7+30) minutes, while the samples coated with ALD layers were immersed in both the near neutral and alkaline electrolyte for longer time (45 minutes) to assess their durability.

X-ray Photoelectron Spectroscopy. A Thermo Scientific ESCALAB 250 X-ray

Photoelectron spectrometer (XPS) with an Al Kα monochromated radiation (hv= 1486.6 eV), was used to analyze the surface chemical composition of the sample. The pressure in the analysis chamber was kept at 1×10^{-9} mbar. The Al Kα monochromatized source was operated at 15kV and the samples were analyzed at 90° as a take-off angle normal to the surface. Survey spectra (BE=0~1060 eV) were recorded with a pass energy of 100 eV. The high-resolution spectra (C1s, O1s, Al2p, Cu2p) were recorded with a pass energy of 20 eV and a resolution of 0.1 eV. All spectra were calibrated versus binding energy (BE) of hydrocarbons (C1s at 285.0 eV). Spectra were recorded and analyzed using the Thermo Scientific™ Avantage Software (version 5.954). For curve fitting and decomposition, a Shirley-type background subtraction was used and the shape of fitting curves was determined by a 70% Gaussian/30% Lorentzian distribution, typical for the spectra fitting for metal/oxides[36,37].

Time-of-Flight Secondary Ion Mass Spectrometry. Time-of-Flight Secondary Ion Mass Spectrometry (ToF-SIMS) was employed to analyze the distribution of chemical species using a ToF-SIMS V spectrometer (ION TOF GmbH-Munster, Germany). The analysis chamber was maintained at about 1×10^{-9} mbar. A pulsed Bi^+ 25 keV, delivering 1.1 pA over a 100×100 μm^2 area. Depth profiling was performed by interlacing analysis with sputtering using a 2 keV Cs^+ sputter beam over a 300×300 μm^2 area with 100 nA target current. Chemical mapping was performed using a primary Bi^+ ion delivering 0.2 pA and a 2 keV Cs^+, sputter beam over a 100×100 μm^2 area with 0.1 pA target current. Negative ion profiles were recorded because of their higher yield when emitted from oxide matrices. Data acquisition and post-processing analyses were performed using the Ion-Spec commercial software version 4.1.

Atomic Force Microscopy. Atomic Force Microscopy (AFM) imaging in acoustic AC mode (Frequency=321.3 kHz, and amplitude=8.89 V) was performed in air, at room temperature using an Agilent 5100 microscope (Agilent Technologies). Topographic AFM images of the surface were acquired (mapping of the topography of the surface in x, y and z directions). Stiff SiN type cantilevers from Applied

Nanostructures, with a force constant of 50 N/m and a tip radius lower than 10 nm were employed.

Scanning Electron Microscope. Scanning Electron Microscope (SEM) images of the pristine Al-Cu and the coated Al-Cu surface with ALD layer before and after immersion were obtained with a Carl Zeiss Ultra 55 Field Emission Scanning Electron Microscope (FE-SEM, Germany).

5.3 Results and discussions

5.3.1 Surface characterization of the pristine and alumina-coated Al-Cu alloy samples

The chemical surface characterization of the Al-Cu model alloy sample after polishing (by means of XPS) was presented in details in chapter 3. It was concluded that the surface of the polished Al-Cu model alloy is covered by a thin aluminium oxide layer and aluminium hydroxide ($Al(OH)_3$ and AlOOH) layer of 7.5 nm. The presence of metallic copper on the surface of Al-Cu alloy was also evidenced.

The XPS performed on the 20 nm alumina ALD layer deposited on the Al-Cu alloy (shown hereafter in Fig. 5-6 for the sake of comparison) shows only one principal Al2p peak corresponding to the aluminium oxide. The O1s/Al2p ratio close to 1.5 indicates the theoretical stoichiometry of Al_2O_3 of the ALD layer.

The pristine Al-Cu alloy sample exhibits after polishing a microstructure that consists of a number of intermetallic particles as shown in Fig. 5-1(a). The electron diffraction (EDX) analysis confirms the presence of Al_2Cu intermetallic particles (θ-phase) with a composition Cu/Al= 33/66 [at.%]. Particles with diameters ranging between 2 and 5μm are also evidenced by AFM, as seen in Fig. 5-1(b). It can be noticed that the polishing scratches are cut off by the Al_2Cu particles, indicating the more important hardness of the particle with reference to the surrounding aluminium matrix. These Cu-rich intermetallic particles, visible clearly on the surface of polished sample (Fig. 5-1(b)), cannot be observed by AFM on the ALD coated Al-Cu samples anymore (Fig. 5-1(c)). The ALD coated Al-Cu surface is homogeneously covered by

aluminium oxide layer characterized by small grains with a RMS roughness of 12.8 nm. The roughness of the coated sample is only slightly higher than the polished Al-Cu alloy with RMS=10.4 nm.

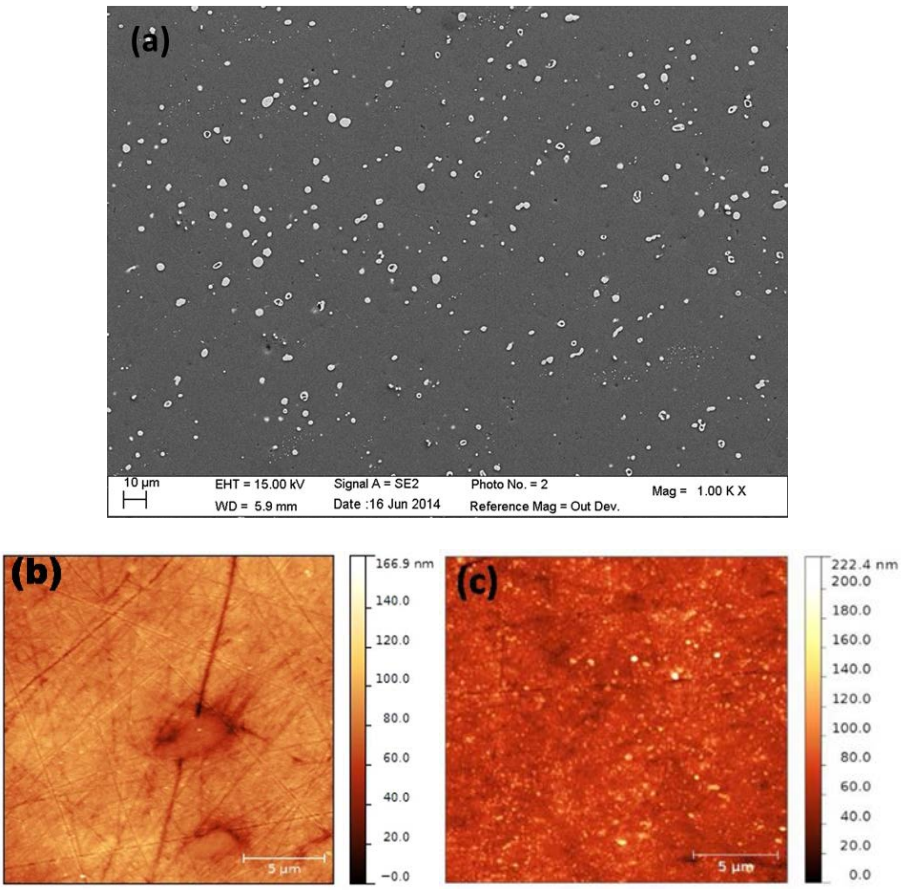

Fig. 5-1 SEM(a)and AFM (b) images performed on the polished Al-Cu model alloy surface and(c) AFM image of the Al-Cu model alloy surface coated with20 nm alumina ALD layer.

ToF-SIMS negative ion depth profiles and images for both non-coated and coated Al-Cu samples are shown in Fig. 5-2. For both samples, three main regions, the aluminium oxide region (characterized by high and relatively constant intensities of AlO^-, AlO_2^- and $^{18}O^-$), the oxide/metal interfacial region and the metallic substrate region (identified by a large and constant Al_2^- signal), can be identified. The presence of some Cl-like and OH-like contaminations can be also observed on the surface of the polished sample, which intensities decrease with increasing sputtering time. A detailed description of the ToF-SIMS depth profiles of the polished Al-Cu alloy sample was given in the chapter 3. Significant differences observed for the coated and

non-coated Al-Cu alloy samples are related to the sputtering time of the first region and to the presence of Cu ion signal and its intensity in the first region.

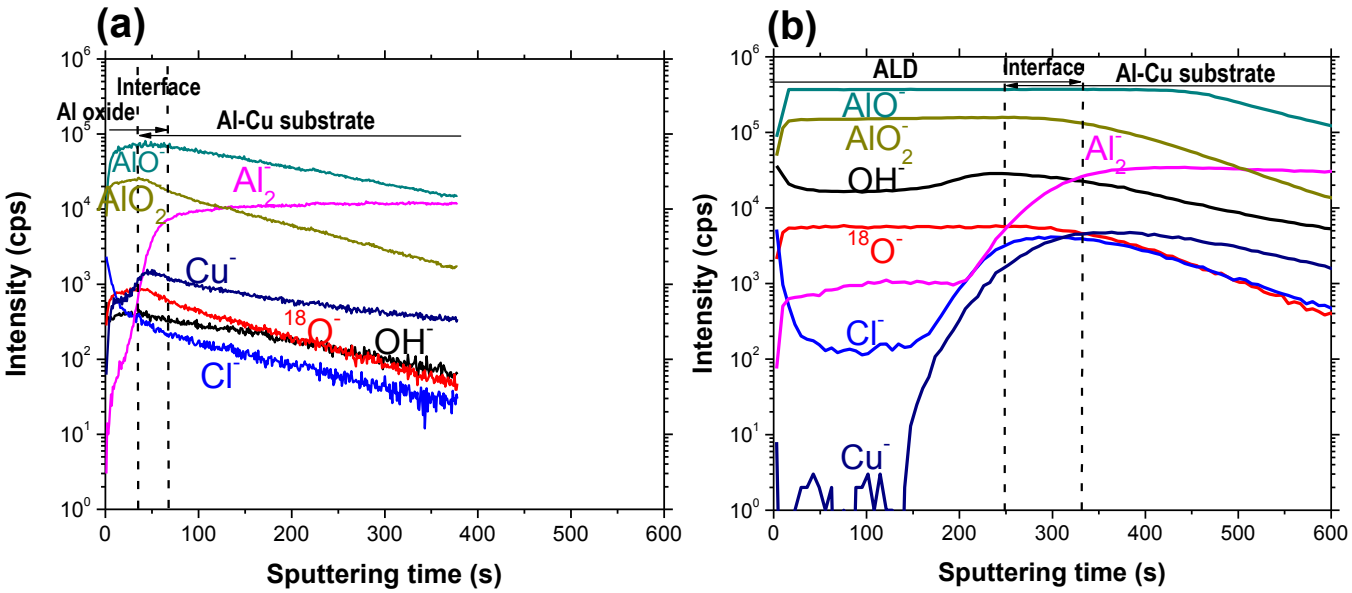

Fig. 5-2 ToF-SIMS negative ion depth profiles obtained on:(a) the pristine non-coated Al-Cu alloy sample; (b) the coated Al-Cu sample (20 nm thick ALD alumina layer).

The marked increase of the sputtering time for the ALD coated sample from 25 s (for non-coated, Fig. 5-2 (a)) to 250 s (for coated, Fig. 5-2 (b)) confirms the presence of a much thicker ALD Al_2O_3 oxide layer than the native Al_2O_3 oxide as already observed by the AFM (Fig. 5-1(c)) and the XPS data (discussed above). However, 250 s is a much longer sputtering time, than would be expected from the sputtering time observed for the native aluminium oxide layer. This longer than expected sputtering time observed for the ALD layer can result from its different structure and higher density. It should be also noted that the extremely low intensity of Cu ion signal in the first oxide region can be related to formation of a uniform and conformal ALD layer, blocking the exposition of the intermetallic particles present on the polished Al-Cu alloy. The intensity increase of the Cu^- ion profile can be observed already from 150 s of sputtering pointing to segregation of Cu-rich intermetallic particles at the native oxide layer/substrate interfacial region before the ALD deposition. The ToF-SIMS chemical mapping performed on both non- and coated samples presented hereafter confirm this hypothesis. The Cl and OH-like contaminations are mainly detected on

the extreme surface of the ALD layer and the higher intensities can also be observed in the interfacial region (which can be attributed to the contaminations not removed from the polished Al-Cu surface before ALD deposition). Quite high OH ion profile intensity in the bulk of the ALD coating can be attributed to existence of pores in the coating layer as discussed in previous studies [24,206,31].

The ToF-SIMS negative ion 100×100 μm^2 chemical images have been performed on both the non-coated sample (Fig. 5-3(a)) and on the alumina ALD coated sample (Fig. 5-3(b)) at different depth of sputtering corresponding to the extreme surface of the native oxide layer or the ALD alumina oxide coating, to the interfacial region (oxide/substrate interface) and in the area corresponding to the metallic substrate. The schematic illustrations presenting the cross sections of the analyzed regions corresponding to different depth analyses are presented in Fig. 5-3.

The images obtained from the extreme surface of the non-coated sample (Fig. 5-3 (a)) show a homogeneous native aluminium oxide film on the pristine, polished Al-Cu sample. However, the presence of small intermetallic particles can be evidenced by a weak Cu^- signal intensityin the surface layer after polishing. This surface state of the pristine Al-Cu alloy sample after polishing was already observed in the previous analysis and described in chapter 3. The images obtained from the surface of the ALD coated sample ((Fig. 5-3 (b)) also show a homogeneous Al oxide with a low porosity and high coating density, which can be confirmed by no visible signal of Cu ions. The coating inhomogeneity can be detected at higher sputtering time corresponding to the interfacial and substrate regions. From the ToF-SIMS images performed in the substrate region it is visible that the spots corresponding to high intensity of O^- and AlO^- signals can be superimposed with the dark spots in the Al_2^- chemical mappings and slightly higher intensities in the Cu^- ion maps. These observations can be explained by formation of the Cu-rich intermetallic particles covered by the external coat built on the native aluminium oxide. This structure of intermetallic particles was already described in the chapter 3 of this manuscript as the core-shell structure. The images of the OH^- and Cl^- (not presented here) show rather homogenous signal

intensities decreasing with increasing sputtering time. Much higher OH^- signal intensity was observed on the surface of the ALD coated sample than on the non-coated alloy.

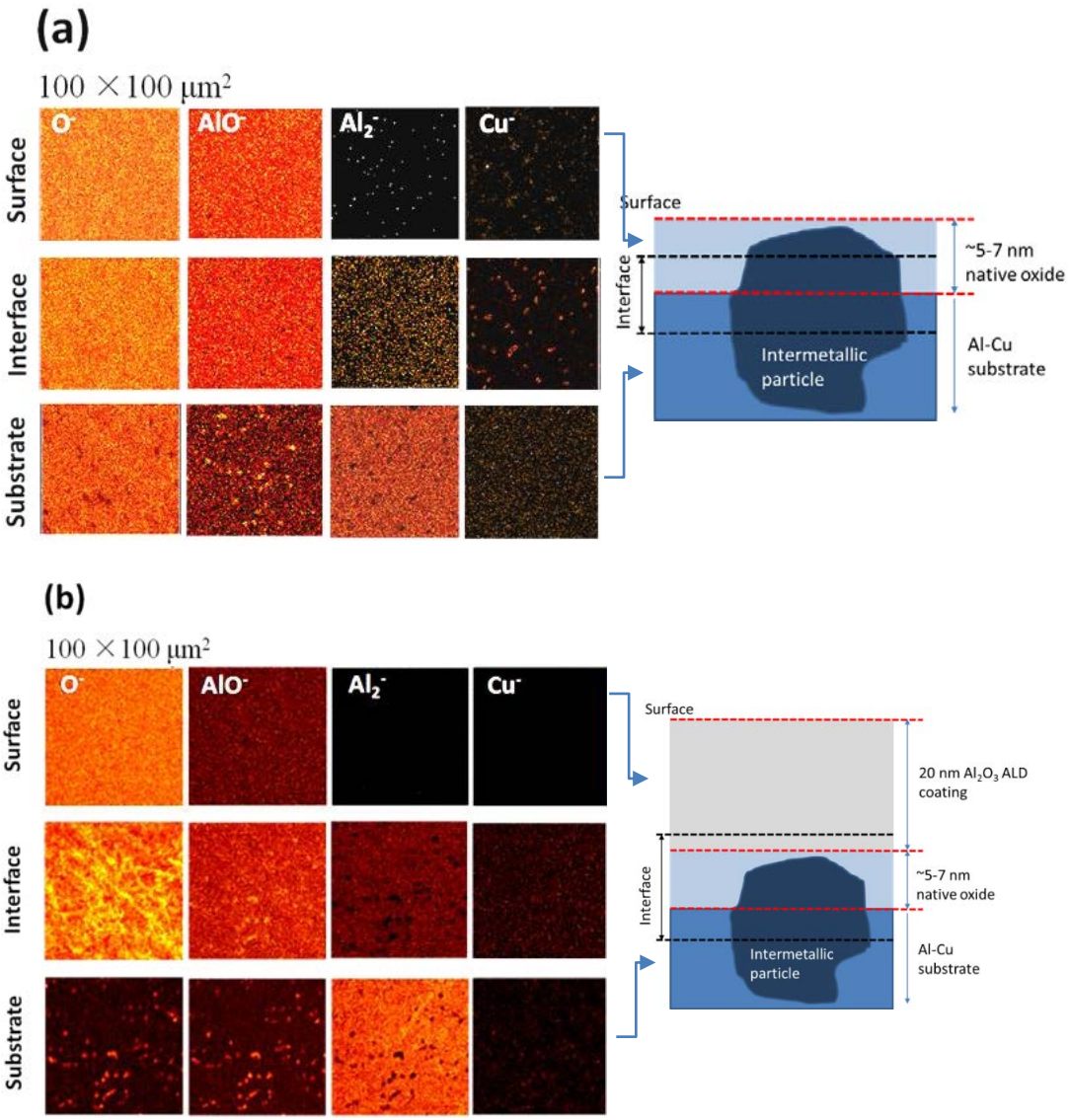

Fig. 5-3 ToF-SIMS negative ion images and schematic illustrations (on the right) presenting the cross sections of the analyzed regions corresponding to different depth analyses obtained on:(a) the pristine non-coated Al-Cu; (b) the alumina ALD coated (20 nm) Al-Cu sample.

5.3.2 Corrosion resistance of the alumina ALD coated Al-Cu alloys – immersion tests

As described in the chapter 3, a series of immersion tests were carried out for the pristine Al-Cu alloy in neutral and alkaline electrolytes (at different time ranging from

7 to around (7+30) minutes) for measurement optimization in order to be able to observe the first signs of corrosion initiation and to control the surface state by surface sensitive techniques. Finally, the 7-minute-immersion test in the case of neutral chloride electrolyte was chosen for pristine, non-coated Al-Cu alloy samples due to moderate surface modifications (pitting corrosion) of Al-Cu alloy as observed by optical microscope. In the case of alkaline electrolyte (pH=11.5), due to general corrosion of the Al matrix and lack of visible corrosion spots (pitting corrosion), the immersion time was prolonged from 7 minutes to (7+30) minutes for non-coated pristine Al-Cu alloy samples. In the case of ALD alumina coated samples, the immersion time was in total 45 minutes for both neutral and alkaline electrolytes.

During all immersion tests for the pristine, non-coated and ALD alumina coated samples the OCP was controlled (Fig. 5-4). In the case of a near neutral electrolyte containing 0.01 M NaCl＋0.3% vol H_2O_2 (to increase the oxidability?) (pH≈6.2), the immersion tests for the pristine non-coated Al-Cu sample was stopped after 7 min (as mentioned above). However, for the Al_2O_3 ALD coated sample the immersion was performed for 45 minutes due to stable OCP and no corrosion signs observed by optical microscope and ToF-SIMS analyses at the intermediate time (7 or 15 minutes). The OCP for the ALD alumina coated sample is around 100-60 mV lower than the OCP measured for the non-coated sample. The presence of Cu-rich intermetallic particles (as discussed above) on the surface of the pristine, non-coated sample can be a reason of a nobler OCP (+0.24 V_{SCE} versus -1.42 V_{SCE} in standard reduction potential). During the 7 min of immersion the 40 mV in OCP variations for the non-coated Al-Cu alloy in comparison to very stable OCP for the ALD alumina coated alloy sample were observed for all immersion times. The OCP of the ALD coated sample remained constant up to around 30 min of immersion indicating a stable behavior of the 20 nm alumina coating in neutral chloride electrolyte. The slow decrease of the OCP from -0.5 V (at 30 min of immersion) to -0.56 V (after a total 45-min-immersion) can indicate a decrease of the ALD coating corrosion resistance.

The difference in the OCP for the pristine (non-coated) and ALD alumina coated

sample is much larger in the case of the immersion test performed in the alkaline electrolyte 0.01 M NaCl＋NaOH (pH=11.5) (Fig. 5-4(b)). Both coated and non-coated Al-Cu alloy show lower OCPs in alkaline electrolytes than in neutral electrolytes, confirming higher corrosion susceptibility of aluminium, and aluminium alloys and aluminium oxides at high pH (as know from Pourbaix diagram and as discussed in the bibliographic chapter 1)[38,39]. However, the much higher OCP observed for the ALD alumina coated sample (around -0.68 V during around 30 min of immersion) than that of the non-coated sample (around -1.34 to -1.24 V) in the alkaline electrolytes means a beneficial protective effect of the Al_2O_3 ALD layer.

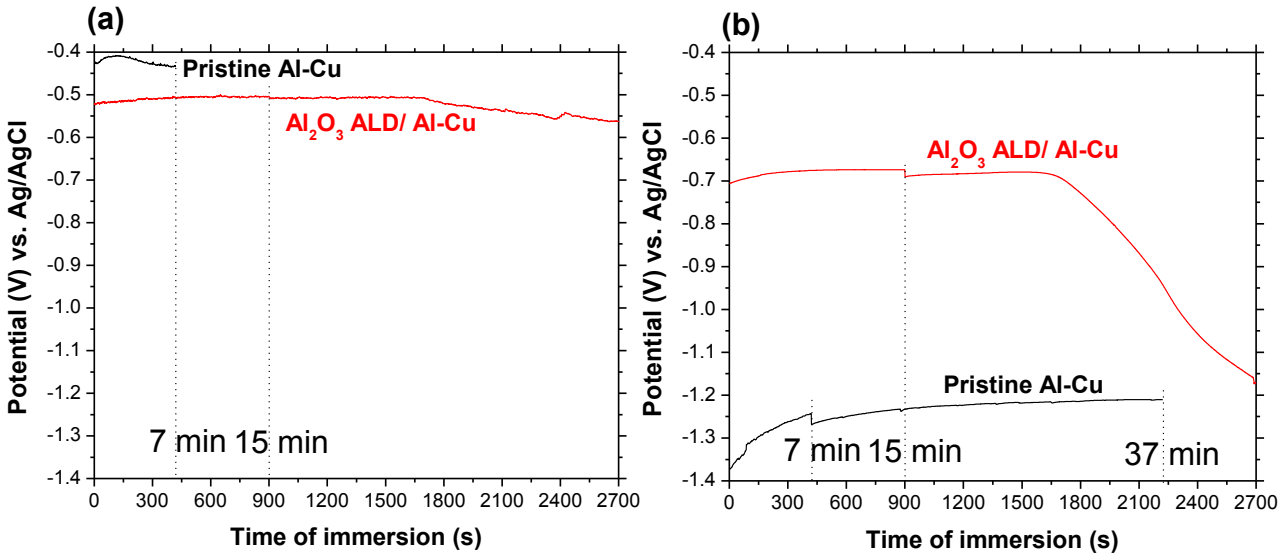

Fig. 5-4 The OCP results obtained for the pristine, non-coated Al-Cu alloy sample and the Al-Cu sample coated by 20 nm ALD Al_2O_3 layer in:(a) a neutral 0.01 M NaCl＋0.3% vol. H_2O_2 (pH≈6.2) electrolyte (b) an alkaline 0.01 M NaCl＋NaOH (pH=11.5) electrolyte.

In the case of the coated alloy a severe decrease of the OCP from -0.68 to -1.13 V can be observed from 30 min of immersion to 45 min of immersion, while in the case of non-coated alloy an increase from -1.37 to -1.21 V is observed during 37 min of immersion. Both variations: decrease and increase of the OCPs in the case of coated and non-coated Al-Cu alloy, respectively, indicate corrosion, which, depending on the sample, occurs according to different mechanisms. The potential increase observed for the non-coated sample during immersion in the alkaline electrolyte can be related to surface ennoblement in Cu due to severe dissolution of Al matrix.

In the first stages the corrosion is related to the dissolution of the oxide film (native aluminium oxide layer or ALD alumina coating) owing to electrochemical attack by hydroxide ions OH^- according to anodic dissolution of aluminium (Eq. 5-1) and cathodic reduction of oxygen, which can occurs at the copper-containing phases (Eq. 5-2)[40]:

$$Al + 4OH^- = Al(OH)_4^- + 3e^- \quad \text{Eq. 5-1}$$

$$3/4O_2 + 3/2H_2O + 3e^- = 3OH^- \quad \text{Eq. 5-2}$$

The possible reaction can be also the water reduction reaction:

$$3H_2O + 3e^- = 3/2H_2 + 3OH^- \quad \text{Eq. 5-3}$$

The overall corrosion reaction is:

$$Al + OH^- + 3/4O_2 + 3/2H_2O = Al(OH)_4^- \quad \text{Eq. 5-4}$$

However, in the case of electrolyte containing chloride ions, pitting corrosion can occur. The known, possible reaction mechanisms are presented in the bibliographic part (chapter 1). Here, we will present the surface characterization of non-coated and ALD alumina coated Al-Cu alloy and confirm possible reaction mechanisms.

5.3.3 Surface characterization of non-coated and coated Al-Cu alloys after immersion tests

As already mentioned, the chemical surface characterization of the pristine, non-coated Al-Cu alloy sample was presented in details in chapter 4. After immersion in neutral chloride electrolytes of the non-coated alloy, the XPS analysis shows formation of thick layer of corrosion products as indicated by Al2p and Cu2p core levels presented in Fig. 5-5(a). The evidence of the formation of the thick layer is a complete attenuation of the Al2p peak at lower binding energy (72.7 ± 0.1 eV) corresponding to metallic aluminium[41,42]. The corrosion products formed on the

surface of non-coated Al-Cu electrode are a mixture of Al oxide (at 75.7 ± 0.1 eV)[43-45], Al hydroxide ($Al(OH)_3$ or AlOOH) (at 74.6 ± 0.1 eV)[46,47], as shown in the Fig. 5-5(a). The decrease of Cu2p can be observed with simultaneous displacement of the Cu2p (Fig. 5-5(b)). The decomposition of the $Cu2p_{3/2}$ shows a formation of copper compounds such as Cu_2O (at 932.3 ± 0.1 eV) [48,49], and CuO (at 933.9 ± 0.1 eV)[50-54] (Fig. 5-5(c)). The presence of oxidized CuO is confirmed by the shake-up satellite peak expected at 943.0 ± 0.1 eV[55,56].

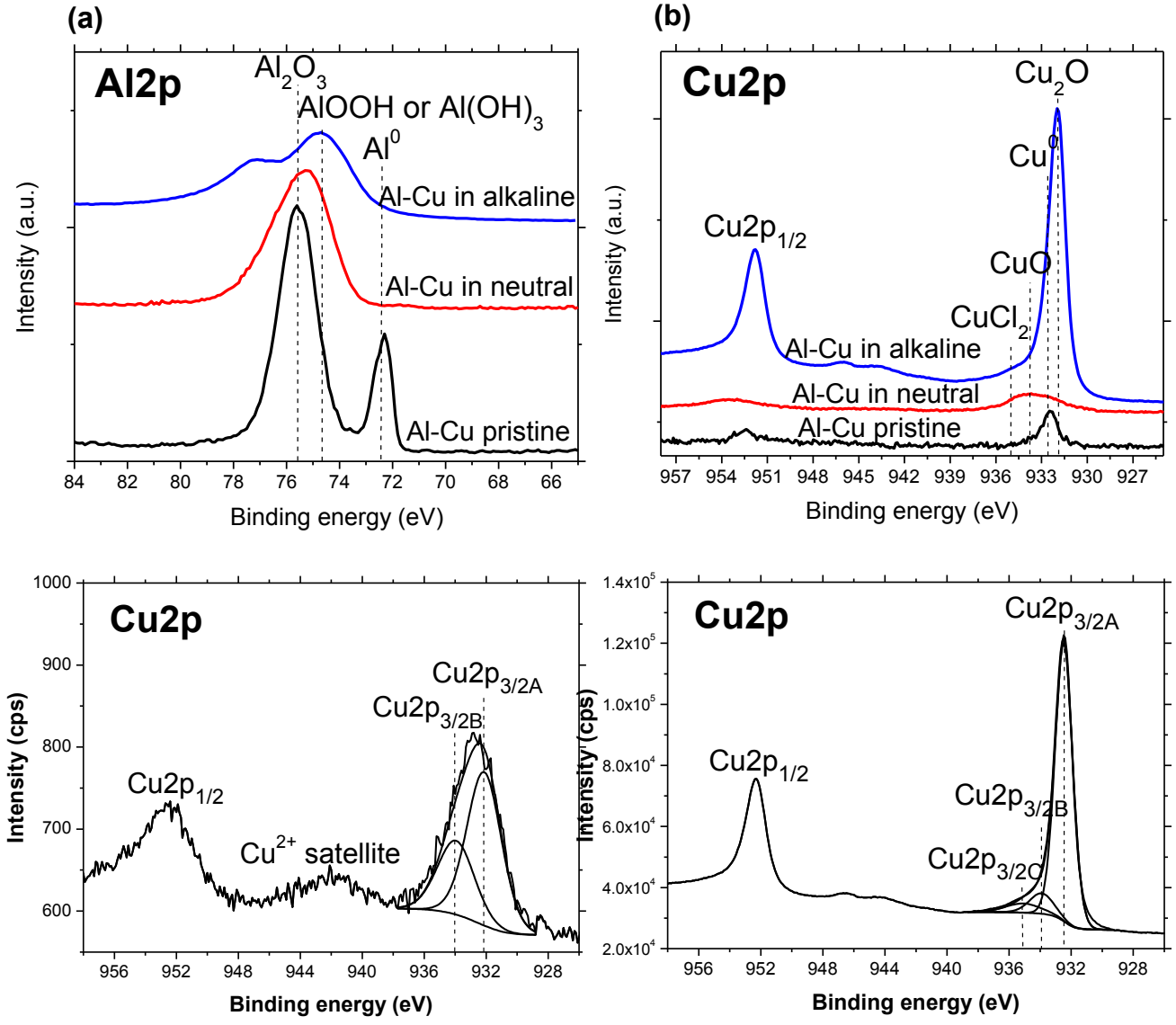

Fig. 5-5 XPS spectra of Al2p(a) and Cu2p(b) obtained for the pristine, non-coated Al-Cu sample and after immersion tests in the neutral and alkaline electrolytes and Cu2p peak decomposition for the non-coated Al-Cu sample after immersion in the neutral (c) and alkaline (d) electrolytes.

After immersion in the alkaline electrolyte, the surface of non-coated Al-Cu alloy does not show the significant signs of corrosion by optical microscope. However, the Al2p core level presented in Fig. 5-5 (a) shows a disappearance of the Al peak corresponding to aluminium metal (Al2p at 72.7 ± 0.1 eV) and similarly to neutral electrolyte the large peak at around 75 eV, which can be attributed to hydroxides and oxides indicates the formation of thick corrosion layer. However, in the case of immersion in alkaline electrolyte a more intense peak at the higher binding energy of around 75.9 ± 0.1 eV and 78.4 ± 0.1 eV in the region of Al2p core level spectra corresponding to $Cu3p_{3/2}$ and $Cu3p_{1/2}$ can be observed[57-59]. The presence of high intensity copper peak is confirmed in the region of Cu2p (Fig. 5-5 (d)). The decomposition of $Cu2p_{3/2}$ shows the presence of Cu_2O and CuO and some presence of copper hydroxides and/or chlorides as discussed in details in chapter 4. The high intensity of copper peak indicates significant surface enrichment in copper and a preferential, general dissolution of Al matrix in the case of Al-Cu alloy corrosion in the alkaline electrolyte. This is in agreement with previous studies on the corrosion of binary Al-Cu alloys containing up to 6.7 at.% Cu in 0.1 M NaOH solution[60,61].

No surface modification of the 20 nm alumina ALD layer can be observed from the XPS data (Al2p core level spectra) as shown in Fig. 5-6. The ALD alumina layer is still present (with the O/Al ratio corresponding to the theoretical stoichiometry of Al_2O_3) on the surface of the Al-Cu alloy regardless of the severe conditions of immersion tests performed either in neutral or alkaline electrolytes containing chloride ions. In order to have more insight into the coating characteristics after the immersion tests, ToF-SIMS ion depth profiles and chemical mapping will be presented and discussed below.

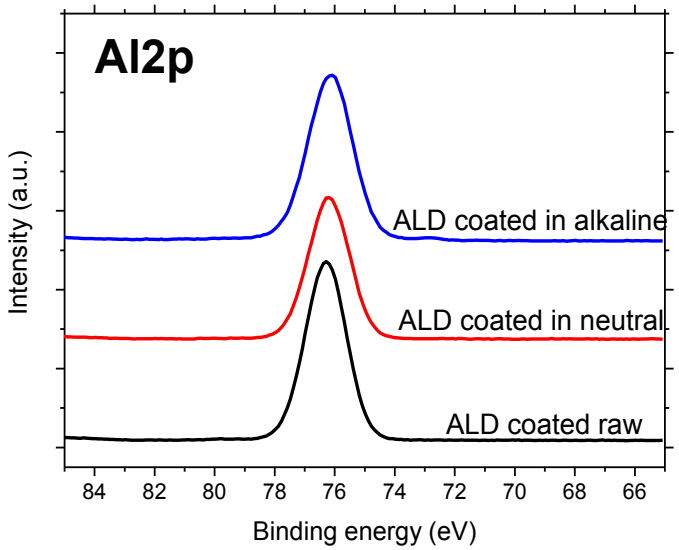

Fig. 5-6 XPS spectra of Al2p obtained for the ALD alumina coated Al-Cu sample before and after immersion tests in the neutral and alkaline electrolytes.

Fig. 5-7 shows the ToF-SIMS negative ion depth profiles obtained on the non-coated sample and the coated sample after the immersion in neutral electrolyte containing chloride ions. As before immersion, three main regions can be distinguished in the profiles of both samples: the Al oxide/corrosion layer, the oxide/metal interfacial region and the metallic substrate region. After immersion of the non-coated alloy the significant increase of sputtering time necessary to reach the substrate region (of around 10 times higher than the sputtering time of the oxide layer present on the pristine Al-Cu alloy, Fig. 5-2(a)) can be attributed to the thickness increase of the oxide/corrosion product layer. The large interface evidences the augmented surface roughness and formation of inhomogeneous corrosion layer. Moreover, the significant intensity increase of Cu signal in the first Al oxide/corrosion layer region (from few hundreds for the pristine alloy to over 3500 counts for the alloy after immersion) can be related to the enrichment in Cu compounds resulting from the dissolution of Al-Cu alloy matrix and Cu-rich intermetallic particles, which will be confirmed by the ToF-SIMS chemical mapping presented hereafter (Fig. 5-8(a)).

The most important modification of the alumina coated Al-Cu sample induced by

immersion in neutral electrolyte is a decrease of sputtering time of the ALD layer from 250 s (for the coated sample before immersion, Fig. 5- 2(b)) to around 100 s (for the sample after immersion, Fig. 5-7 (b)). Two hypothesis related to sputtering time decrease can be proposed:

1) the coating thickness decreases with a dissolution rate 0.0015 nm/s,

2) the sputtering yield of the coating exposed to the neutral electrolyte increases due to the modification of the bulk coating and formation of pores.

It should be emphasized that the immersion did not result in important chemical modifications of the ALD alumina coated sample, except the low intensity (around 10 counts) of the Cu^- signal detected in the beginning of sputtering time (not observed on the ALD alumina coated sample before immersion, Fig. 5-2(b)). This low intensity copper signal can be attributed to the Cu-rich intermetallic particles, due to the formation of more porous ALD layer leading to the corrosion initiation in the vicinity of the Cu-rich intermetallic particles at the alumina ALD layer/substrate interface. As already mentioned in our previous works by Harkonen *et al.*[62], alumina dissolution is triggered by the penetration of the solution via cracks/pinholes through the ALD coating to the substrate surface where oxygen reduction takes place. These cracks/pinholes provide paths for invasion of aggressive ions, such as Cl^-, and penetrating up to the interface into the inner passive Al oxide layer. In the case of Al-Cu alloy the preferential sites of the oxygen reduction would be the sites of Cu-rich intermetallic particles. A more clear insight into the possible corrosion mechanisms can be elucidated on the basis of ToF-SIMS chemical mapping performed on the non-coated and coated aluminium alloys after immersion tests (presented hereafter).

Cl^- ions are observed on the surfaces of both non-coated and coated samples. Few order of magnitude higher Cl^- ion intensity can be observed in the beginning of the sputtering time for the non-coated Al-Cu sample after immersion than before immersion test, which indicates formation of chloride components already observed by XPS as presented above. However, no significant changes compared with those before immersion test can be observed in Cl^- ion profile for the alumina ALD coated

sample. In addition, enrichment of OH^- can be observed principally at the non-coated surface, indicating the formation of hydroxide compounds, already reported by the XPS described above.

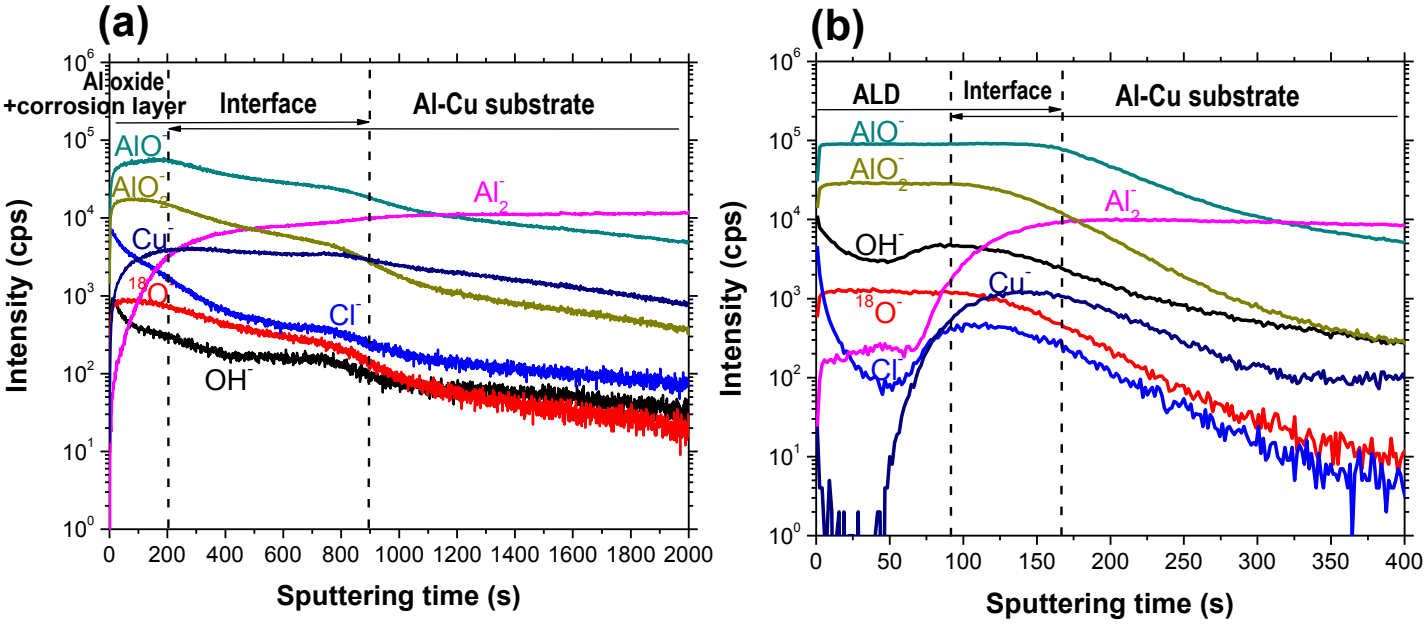

Fig. 5-7 ToF-SIMS negative ion depth profilesobtained on: (a) the non-coated Al-Cu alloy sample after immersion in neutral electrolytes, (b) the ALD alumina coated Al-Cu sample after immersion in neutral electrolytes.

Fig. 5-8 shows the ToF-SIMS negative ion images obtained on the non-coated sample (a) and the ALD alumina coated sample (b) after immersion in near neutral electrolyte containing chloride ions. These chemical maps clearly show a significant difference in the corrosion behaviour of the non-coated (a) and coated samples (b). Without any deep analysis it can be quickly concluded that the dense, conformal ALD layer with nanometer thickness (20 nm) is enough to protect the Al-Cu alloy sample against the severe corrosion rapidly occuring on the non-coated alloy sample in the neutral electrolyte containing aggressive (Cl^-) ions. As seen in the Fig. 5-8(a), a severe pitting corrosion occurred during the immersion in the neutral electrolyte, which was discussed in details in chapter 4. The "o-ring-like" pits with sizes ranging between 2 and 5 μm and with a density of about 0.003 μm^{-2} (30 pits per 100×100 μm^2), are observed at the spots which are enriched with Cu. These ring-like pits where high

intensities of O^- and AlO^- ions accompanied with high intensities of Cl^- and OH^- are observed, as basic compounds of corrosion products as observed by XPS (Fig. 5-5) can be formed due to preferential dissolution of Al matrix nearby the Cu-rich intermetallic particles. This preferential dissolution phenomenon, resulting from the differences of electrochemical characteristics between the intermetallic particles and the surrounding substrate, was widely reported in the literature in the case of the corrosion of aluminium alloy AA 2024-T3 in NaCl solutions as discussed in the bibliographic chapter 1[63-70]. However, these ToF-SIMS chemical maps indicate that the corrosion of Al-Cu alloy is strongly influenced by the distribution of Cu-rich intermetallic particles. Despite the formation of thick layer of corrosion products, the ToF-SIMS images performed at different depths (*i.e.* in the interfacial region) allow us to conclude that the intermetallics are preferential sites for corrosion initiation. The copper compounds observed as corrosion products by XPS (Fig. 5-5) originate from the Al-Cu intermetallic particles and the distribution of these products is not homogenous on the surface of the corroded Al-Cu alloy.

For the alumina ALD coated sample (Fig. 5-8(b)) the same, uniform signal intensities observed in the ToF-SIMS images for O^- and AlO^- ion signals indicate very limited electrochemical activity and good corrosion resistance of the ALD layer (as already observed by XPS, Fig. 5-5). However, appearance of small spots in the image of Cu^- ion on the surface of the ALD alumina coated sample (Fig. 5-8(b) confirms the low intensity observed already in the ion depth profiles in the beginning of the sputtering time as discussed above (Fig. 5-7 (b)). The presence of Cu species on the surface of the ALD coated sample after immersion can be indicative of the enhanced electrochemical activity of Cu-rich intermetallic particles. The copper spots observed on the surface can be superimposed with the higher intensity spots of O^- and AlO^- ions and black spots in Al_2^- ion image (corresponding to deficiency of metallic aluminium) in the interfacial region. The low signal observed in the case of Cl^- and OH^- maps does not indicate any particular coating modifications. These results would allow to conclude that the alumina ALD can undergo small modifications during prolonged

time of immersion in neutral electrolytes. The electrochemically active sites for the alumina ALD coated Al-Cu sample would be the presence of the Cu-rich intermetallic particles at the ALD/substrate interface and chloride ions in the neutral electrolyte. Then, this electrochemical activity can lead to coating porosity and/or small general dissolution of the alumina as stated above.

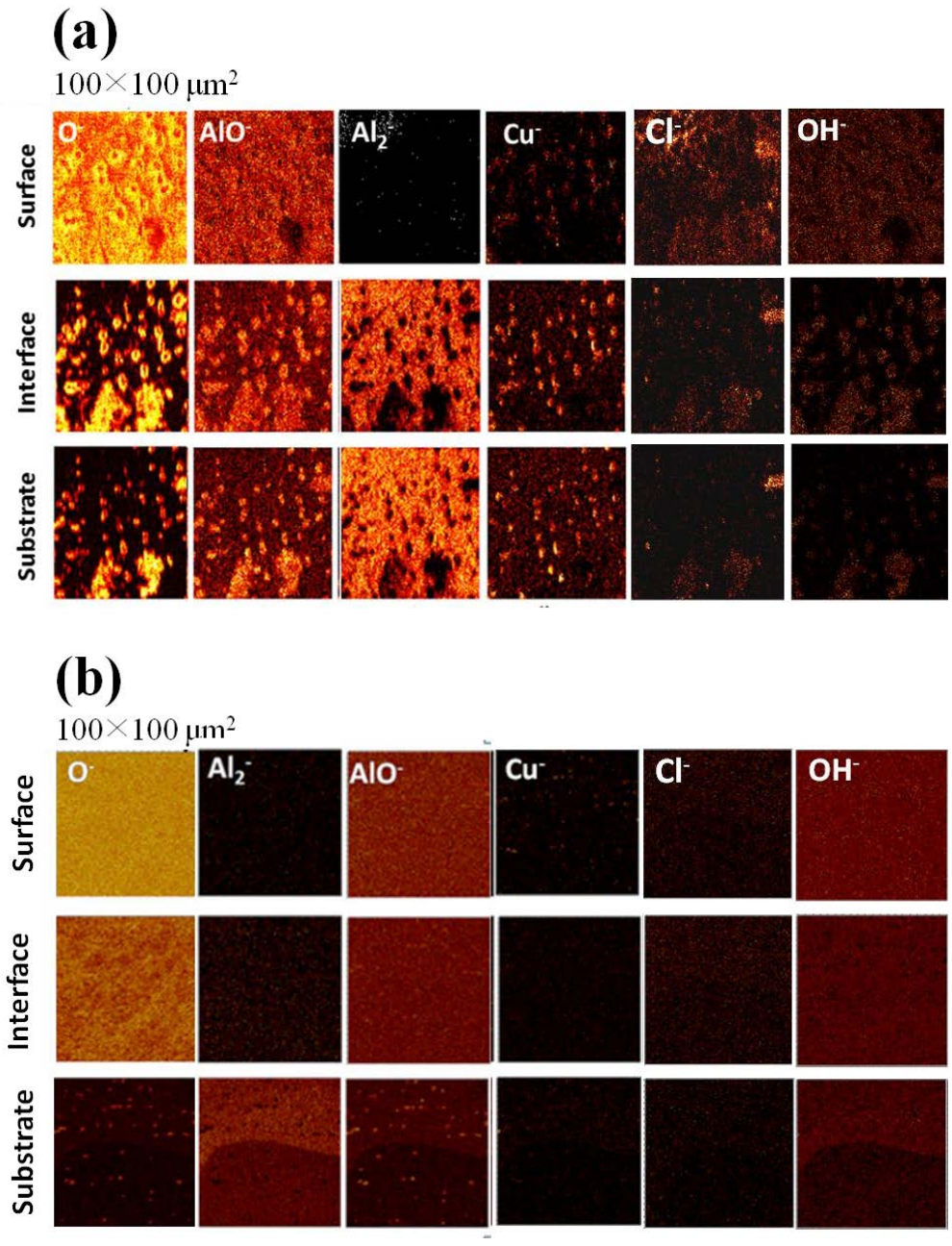

Fig. 5-8 ToF-SIMS chemical mapping obtained on: (a) the non-coated Al-Cu alloy sample after immersions in neutral electrolyte, (b) the ALD alumina coated Al-Cu sample after immersions in neutral electrolyte.

Similar comparison between non-coated and alumina ALD coated Al-Cu alloy samples was done after immersion in the alkaline electrolyte. Fig. 5-9 shows ToF-SIMS negative ion profiles obtained on both the non-coated Al-Cu sample and the ALD alumina coated Al-Cu sample after the immersion in the alkaline electrolyte containing chloride ions. As shown in the Fig. 5-9(a), the significant increase of the Cu^- ion signal (up to 10^4 counts) can be observed when compared to the pristine sample (with intensity of around 10^3 counts, Fig. 5-2), indicating significant chemical modifications and serious corrosion of the sample surface induced by the immersion in the alkaline electrolytes. However, it should be noted that the enrichment in copper is not observed at the extreme surface of the corrosion layer. The maximum intensity of the Cu^- ion profile is at around 50 s of sputtering time, which would suggest that the corrosion layer is composed of oxygenated species at the extreme surface and the Cu-like species and the Cu-rich intermetallic particles are found underneath this layer. The Cu^- ion profile is remarkably different for the Al-Cu sample corroded in alkaline electrolyte (Fig. 5-9(a)) as compared to Cu^- in the profile for the Al-Cu sample corroded in neutral electrolyte (Fig. 5-7(a)), where the intensity stable with sputtering time is only around two orders magnitude higher ($2*10^3$ counts, Fig. 5-7(a)) with reference to Cu^- ion intensity for pristine Al-Cu alloy.

These changes point to different corrosion mechanisms of Al-Cu alloy as a function of electrolyte pH, as already expected from literature but also to formation of corrosion layers with different structures and different chemical composition (as confirmed above by the XPS data, Fig. 5-5). Moreover, significant intensity increases of OH^- and Cl^- ion signals are observed either in the first oxide layer region or in the interfacial region for both non-coated and coated samples, which indicates the formation of corrosion products containing hydroxide and chloride species, as confirmed by the previous XPS results (Fig. 5-5) and the following ToF-SIMS mapping results (Fig. 5-10). It should be noted that the OH^- signal is much stronger after immersion in the alkaline than in the neutral electrolytes.

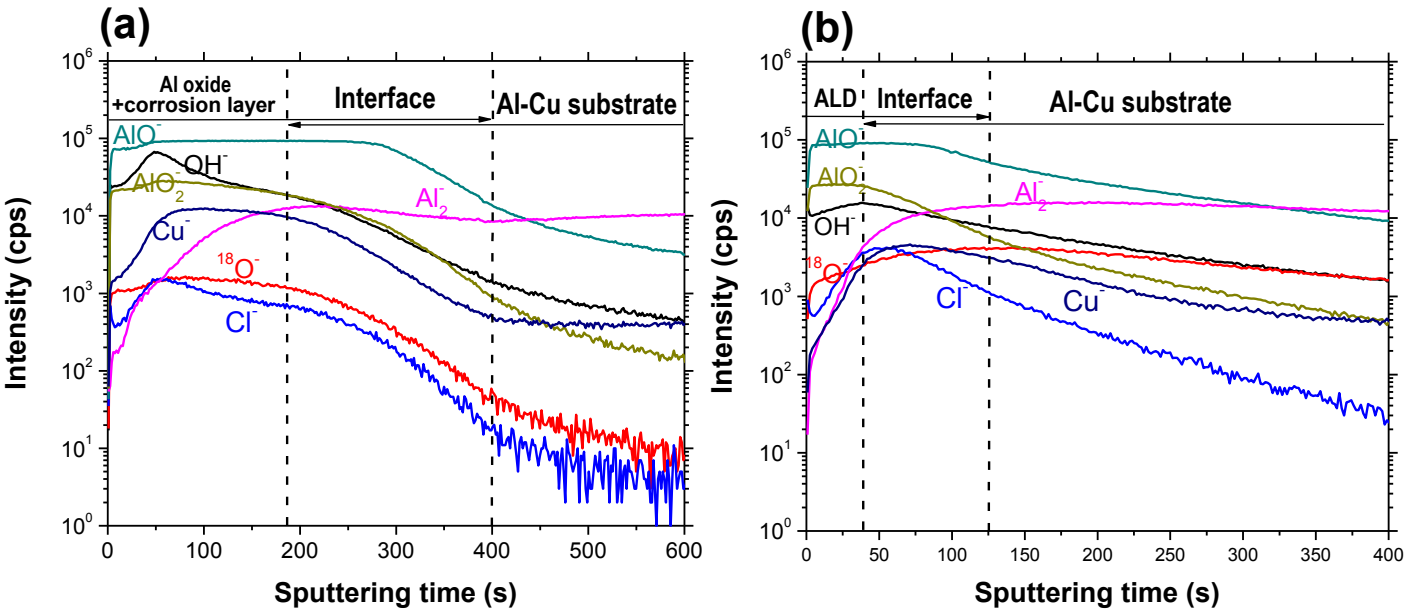

Fig. 5-9 ToF-SIMS negative ion depth profiles obtained on: (a) the non-coated Al-Cu alloy sample after immersions in alkaline electrolyte, (b) the ALD alumina coated Al-Cu sample after immersions in alkaline electrolyte.

ToF-SIMS ion depth profiles obtained for the Al-Cu alloy immersed in alkaline electrolyte corroborate with the ToF-SIMS images presented in Fig. 5-10(a). The first series of ToF-SIMS images corresponding to the extreme surface show non homogenous distribution of O^- and AlO^- species. These areas correspond also to higher intensity of Cu^- signal, which can be attributed to Cu-like species including copper oxides (as observed by XPS, Fig.5-5(d)). The obtained images suggest less significant pitting corrosion and more important general corrosion of the aluminium matrix and formation of ~~"a~~ more uniform" corrosion layer on the whole surface with exception of Cu-rich intermetallic particles. At the interface region, once the first corrosion layer is sputtered, the alloy matrix is more homogenous, however the clear spots of Cu^- ions appear together with AlO^- and O^- ions along with the black spots of Al_2^- ions. The Cu-rich particles are protruded from the aluminium matrix. The differences in the ion contrasts (clear spots of Cu^-, AlO^- and O^- ions and dark spots of Al_2^-) can be explained by the preferential oxidation/dissolution of the Cu-rich intermetallic particles at the oxide/substrate interface. This kind of preferential oxidation was already observed previously, however induced not by the

electrochemical processes, but by the thermal aging at low oxygen pressure, as discussed in chapter 3. With increased sputtering time, closer to substrate region (Fig. 5-10(b)), the size of the spots decreases showing depletion in the intermetallic particles and/or their decreased electrochemical activity related to their obstructive contact with electrolyte/aggressive ions.

The immersion in alkaline electrolyte of the alumina ALD coated Al-Cu alloy leads to significant ALD coating layer dissolution, which can be deduced from the important decrease of sputtering time from 250 s (for the ALD coated sample before immersion, Fig. 5-2(b)) to around 30 s (for the sample after immersion, Fig. 5-9 (b)). In this case, similarly to neutral electrolytes, the general or localized corrosion can occur. Taking into account the immersion time (45 min) of the alumina ALD coated Al-Cu sample and the sputtering time measured by ToF-SIMS, the dissolution rate of the Al_2O_3 ALD was calculated to be 0.1 nm/s, which is much higher than those observed in neutral electrolyte (0.007 nm/s). The other significant modification is an important increase of the Cu^- intensity in the bulk of the ALD layer (Fig. 5-9 (b)). The Cu^- intensity increases from 10^2 counts (in the beginning of sputtering) and reaches the intensity of around $3.5*10^3$ in the interfacial region, which is equivalent to the intensity of the Cu-ion signal observed for the ALD coated sample before immersion tests (Fig. 5- 2(b)). This slope, profile of Cu-ion signal in the first region of sputtering (ALD layer) would correspond to the Cu-rich intermetallic particles exposed through the porous, defective structure of the ALD layer.

It must be noted that the ToF-SIMS ion images obtained from the ALD alumina coated Al-Cu alloy (Fig. 5-10(b)) do not show significant modifications. The homogenous intensity ion signals obtained at the surface and at the interface region suggest the general dissolution of ALD alumina layer. Usually decreasing intensity of $^{18}O^-$ signal with sputtering time (as observed in Fig. 5-2, 5-7 and 5-9(a)), here shows increasing intensity at the interface region. This phenomenon can be related to uniform corrosion and to redistribution of corrosion products within the pores of dissolved/undergoing dissolution of ALD alumina layer. The intermetallic particles

should also play their roles, in this process of coating degradation, which can be confirmed from slightly higher intensity of Cu^- signal at the interface region and intensification of this signal at the near substrate region (Fig. 5-10b). However, these huge clear spots are not the Cu-reach intermetallic particles as those revealed by dissolution of non-coated sample in alkaline (Fig.5-10(a)) or neutral electrolytes (Fig. 5-8(a)). These big Cu-rich spots can be superimposed with the blurred spots of O^-, AlO^- and OH^- attributed to diffusion of corrosion products. These ToF-SIMS images confirm once again a not-localized character of corrosion but privileged generalized corrosion occurring within the bulk of the ALD layer most probably at the interfacial region.

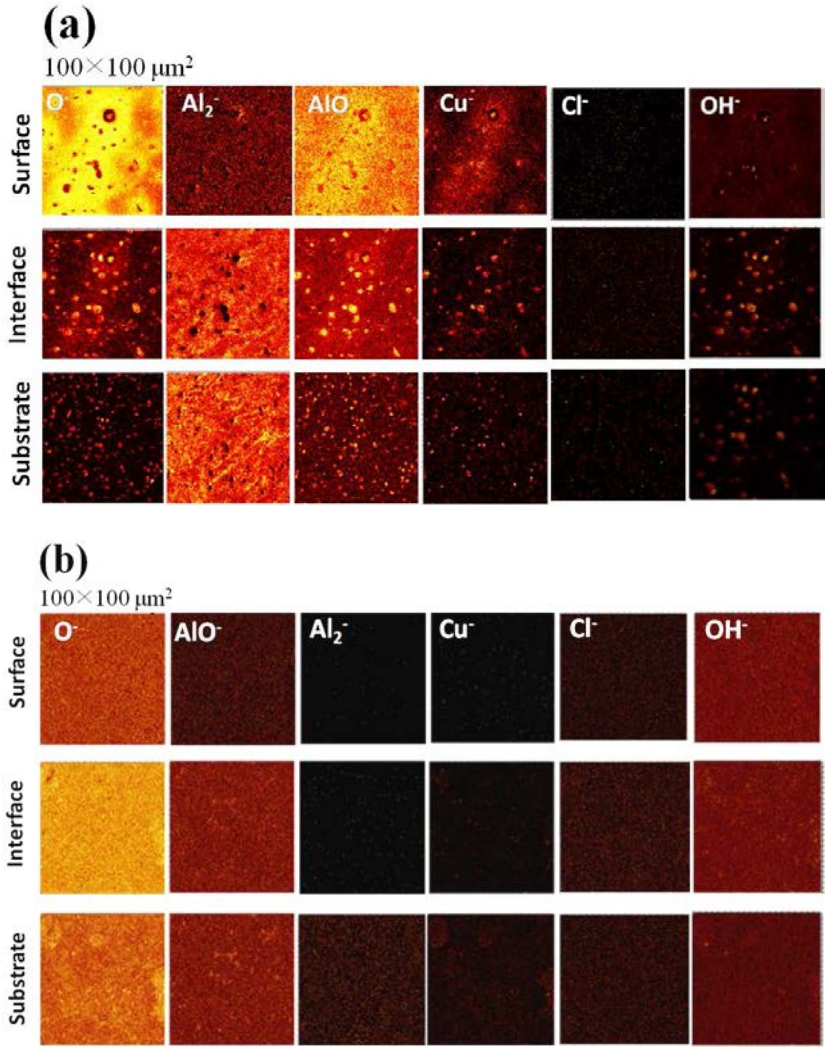

Fig. 5-10 ToF-SIMS chemical mapping obtained on: (a) the non-coated Al-Cu alloy sample after immersion in alkaline electrolyte, (b) the ALD alumina coated Al-Cu sample after immersions in alkaline electrolyte.

The SEM micrographs of the non-coated (a,b) and the ALD alumina coated Al-Cu alloy (c,d) after immersion tests in the neutral and alkaline electrolytes containing Cl^- ions are shown in Fig. 5-11. As observed in the Fig. 5-11(a), the dissolution of Al occurred around the Cu-rich intermetallic particles owing to the galvanic coupling (cathodic particle/Al matrix). These SEM images obtained on the Al-Cu alloy after immersion in neutral electrolyte are in agreement with the ToF-SIMS images (Fig. 5-8(b)). The advantages of the ToF-SIMS chemical mapping at different thickness is the possibility to discriminate the surface products accumulated around the intermetallic particles which are present beneath this surface corrosion layer in the interface region. Small pits and large deposits resulting from corrosion can also be observed on this non-coated alloy surface. Similar phenomenon related to the pitting around the second phase (*e.g.* S-phase) of the aluminium alloy AA 2024-T3 in NaCl solution has been reported in the literature[71,72]. It confirms that the second phases, such as θ-phase and S-phase, commonly exhibit active electrochemical properties with respect to the matrix, which can easily lead to a preferential dissolution around these phases.

The SEM images recorded on the thin ALD alumina coating exposed to neutral electrolyte do not evidence any significant modifications (Fig. 5-11(c)), which could lead to the conclusion that this layer works as a good barrier layer for the aggressive electrolyte containing chloride ions. However, is can be deduced on the basis of other results presented above (ToF-SIMS depth profiles) that the ALD coating is not completely inert and can undergo dissolution.

In the case of alkaline electrolytes, non-coated and coated Al-Cu alloy (Fig. 5-11(b) and (d), respectively), the formation of protruded Cu-rich intermetallic particles can be observed, which appears through dissolution of Al oxide and Al matrix. These observations are in agreement with the results obtained by the ToF-SIMS measurements (Fig.5-10(a)). A number of visible pits or defects, with size from few to few dozens of millimeters, are observed on the coated sample surface after immersion in the alkaline electrolyte (Fig. 5-11(d)). However, these defects are not detectable by

ToF-SIMS (Fig. 5-10(b)).

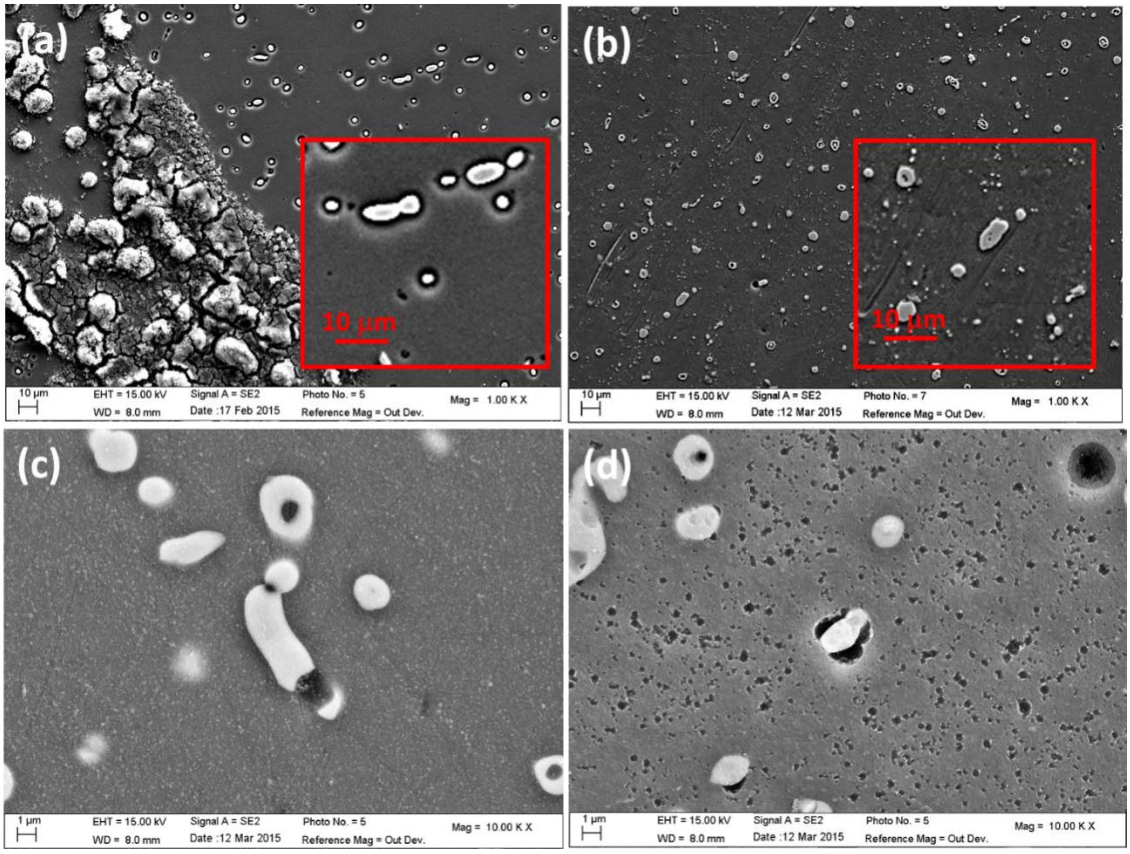

Fig. 5-11 SEM images obtained after immersions in neutral electrolytes for (a) the non-coated Al-Cu sample, (b) the alumina ALD coated Al-Cu sample and after immersion in alkaline electrolyte for (c) the non-coated Al-Cu sample and (d) the alumina ALD coated Al-Cu sample.

Based on the presented results, schematic illustrations of corrosion process of Al-Cu sample coated with the Al_2O_3 ALD film in the neutral and the alkaline solutions are presented in the Fig. 5-12 and Fig. 5-13, respectively. Cu-rich intermetallic particles already exist in the Al-Cu alloy after polishing, and can be located at the interface region. In the neutral electrolyte containing Cl^-, the non-coated Al-Cu can undergo pitting corrosion, which occurs in the areas of the Cu-rich particles. However, the thin alumina ALD layer deposited on the surface of the Al-Cu alloy results in significant improvement of the corrosion resistance: no corrosion occurred at the oxide/substrate interface in the neutral solution containing Cl^- despite the

presence of intermetallic particles. The Al_2Cu particles remained intact, and no trenching around them was observed as observed on the ALD coated sample. However, decrease of the ALD coating thickness (with a dissolution rate of ~ 0.007 nm/s) and the formation of some defects induced by penetration of the electrolyte and the chloride ions can be observed (Fig. 5-12(b), (c)). The local dissolution can be initiated due to diffusion of aggressive ions through the coating defects, then lead to local decrease of pH at the coating-substrate interface, and therefore the coating dissolution and local delamination of alumina coating. If the duration of immersion was extended to longer enough, the coating detachment, breakdown and loss could be assisted upon immersion in aqueous solution by an electrochemically-induced delamination mechanism, including oxygen reduction occurring in the area of intermetallic particles and anodic dissolution of aluminium alloy.

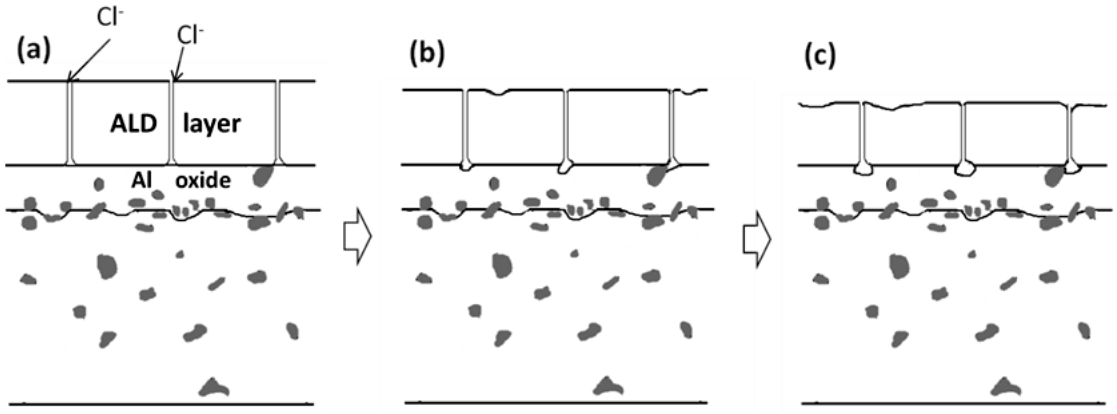

Fig. 5-12 Schematic illustrations of corrosion processes of Al-Cu sample with the ALD coating during neutral immersion: (a) the alumina ALD coated Al-Cu sample, (b) the initiation of corrosion, (c) the corrosion development with the coating thickness decrease and the pits propagation at the alumina ALD/substrate interface.

Immersion in the alkaline electrolyte causes obvious damage the ALD layer deposited on the Al-Cu alloy was observed after (Fig. 5-13). The OH^- promoted the corrosion, by decreasing the thickness of the alumina coating and enlarging the cracks/pinholes, resulting in general dissolution of the ALD layer at significant dissolution rate of ~0.1 nm/s. The presence of Cu-rich particles at the ALD coating/substrate interface can provide initial sites of corrosion, leading to preferential dissolution of the substrate in the vicinity of particles. However, this mechanism was

not really verified here. The intermetallic particles present beneath the thin ALD layer are not modified. The ALD alumina layer has still a protective corrosion protection function for Al-Cu alloy even in the alkaline pH. It is obvious that to stop completely a dissolution of the ALD alumina layer, other ALD coatings, such as TiO_2 or Ta_2O_5 - stable in a wider range of pH, should be deposited as a top-coating.

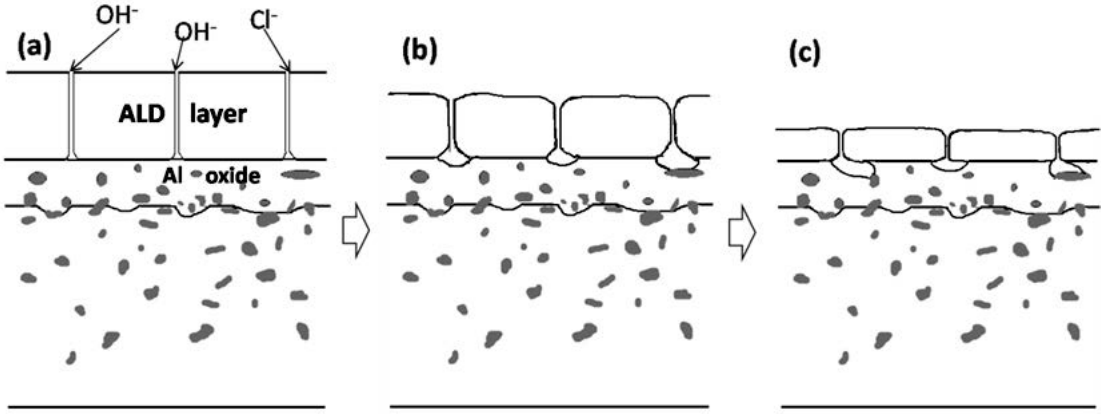

Fig. 5-13 Schematic illustrations of corrosion process of the Al-Cu sample with the ALD coating during alkaline immersion: (a) the alumina ALD coated Al-Cu sample, (b) the initiation of general corrosion and enlarging of channels; (c) further general corrosion combined with decrease of the coating thickness.

5.4 Conclusions

(1) AFM, SEM, and ToF-SIMS show the formation of a complete and homogeneous 20-nm-thick Al_2O_3 coating deposited from trimethyl aluminium ($Al(CH_3)_3$, TMA) and H_2O on the surface of the Al-4.87wt.% Cusample including the Al_2Cu intermetallic particles.

(2) Both coated and non-coated Al-Cu alloy show lower OCPs in alkaline electrolytes than in neutral electrolyte confirming higher corrosion susceptibility of aluminium alloys at high pH;

The much higher OCP observed for the ALD alumina coated sample (around -0.68 V *vs.* Ag/AgCl) than that of the non-coated sample (around -1.34 to -1.24 V *vs.* Ag/AgCl) in the alkaline electrolytes means a beneficial protective function of the Al_2O_3 ALD layer;

(3) A severe pitting corrosion was observed on the pristine Al-Cu samples undergoing by a well known trenching mechanism around the Cu-rich particles leading to formation a mixture of aluminium-copper oxide/hydroxide layer rich in Cu_2O and CuO, after 7-minute-immersion in the neutral chloride electrolytes, whereas no significant corrosion was observed on the ALD coated samples immersed in the same solution for (45) minutes indicating beneficial, protective function of the ALD coating applied to the Al-Cu alloys;

(4) A general corrosion was observed in a case on the non-coated Al-Cu samples in the alkaline electrolytes containing Cl^- after (7+30)-minute-immersion. XPS results, obtained on the surface of the Al-Cu alloy after immersion in alkaline electrolytes containing chloride ions, reveal significant preferential dissolution of Al matrix and surface enrichment of Cu. The ALD alumina layer showed degradation (dissolution of the ALD layer in depth and along the cracks/pinholes) induced by immersion in alkaline electrolytes even though the Al-Cu substrate remained relatively well preserved.

(5) The presence of Cu-rich particles beneath the ALD layer can provide initial sites for localized corrosion as suggested in this study but the thin alumina, conformal ALD layer provides already efficient corrosion protection for aluminium alloys. It should be emphasized that the ALD layer can be a good alternative for Al-Cu surface pretreatments, which does not necessarily requires a removal of intermetallic particles from the alloy surface.

(6) To stop completely a dissolution of the ALD alumina layer, other ALD coatings, stable in a wider range of pH, could be deposited as a top-coating.

References

[1] S.C. Wang, M.J. Starink and N. Gao, *Scripta Mater.*, 54, 287-291 (2006)

[2] K.A. Son, N. Missert, J.C. Barbour, J.J. Hren, R.G. Copeland, K.G. Minor, *J. Electrochem. Soc.*,148, B260-B263 (2001)

[3] T.H. Muster, A.E. Hughes, G.E. Thompson, *Copper Distributions in Aluminium Alloys*, Nova Science Publishers Inc., New York, 9-23 (2009)

[4] H. Habazaki, M.A. Paez, K. Shimizu, P. Skeldon, G.E. Thompson, G.C. Wood, X. Zhou, *Corros. Sci.*, 38, 1033 (1996)

[5] J.R. Scully, R.P. Frankenthal, K.J. Hanson, D.J. Siconolfi and J.D. Sinclair, *J. Electrochem. Soc.*,137, 1365 (1990)

[6] O. Schneider, G.O. Ilevbare, and J.R. Scully, *J. Electrochem. Soc.*,151, B465 (2004)

[7] W.M. Carroll, C.B. Breslin, *Brit. Corros. J.,* 26, 255 (1991)

[8] P.L. Cabot, F.A. Centellas, J.A. Garrido, E. Perez, H. Vidal*, Electrochim. Acta,* 36, 179-187 (1991)

[9] S. Jasty and A. J. Epstein, *Polym.Mater. Sci. Eng.*, 72, 565 (1995)

[10] R.S. Razavi, *Recent Researches in Corrosion Evaluation and Protection*, InTech, Shanghai, 2012

[11] M. Sheffer, A. Groysmanb, D. Mandler, *Corros. Sci.*, 4, 2893-2904 (2003)

[12] A.J. Epstein, J.A.O. Smallfield, H. Guana, M. Fahlman, *Synth. Met.,* 102, 1374-1376 (1999)

[13] D.W. DeBerry, *J. Electrochem. Soc.*, 132, 1022 (1985)

[14] E. Akiyama, A.J. Markworth, J.K. Mccoy, G.S. Frankel, L. Xia, R.L. Mccreery, *J. Electrochem. Soc.,* 150, B83-B91 (2003)

[15] H.L. Jamese, *Plat. Surf. Finish.*, 86, 40-42 (1999)

[16] D. Ende, W. Kessler, D. Oelkrug, R. Fuchs, *Electrochim. Acta*, 38, 2577-2580 (1993)

[17] T.A. Markley, J.I. Mardel, A.E. Hughes, B.R.W. Hinton, A.M. Glenn and M. Forsyth, *Mater. Corros.*, 62, 836-840 (2011)

[18] V.S. Protsenko, F.I. Danilov, *Clean Technologies and Environmental Policy*, 16, 1201-1206 (2004)

[19] X.C. Dong, P. Wang, S. Argekar, D.W. Schaefer, *Langmuir*, 26, 10833-10841 (2010)

[20] X. Sun, D. Susac, R. Li, K.C. Wong, T. Foster, K.A.R. Mitchell, *Surf. Coat. Tech.*, 155, 46-50 (2002)

[21] D.A. Wrobleski, B.C. Benicewicz, K.G. Thompson, and C.J. Bryan, *ACS Polymer Preprints,*35, 265 (1994)

[22] M. Leskela, M. Ritala, *Thin Solid Films*, 409, 138-146 (2002)

[23] B. Diaz, E. Harkonen, J. Swiatowska, V. Maurice, A. Seyeux, P. Marcus, M. Ritala, *Corros. Sci.*, 53, 2168-2175 (2011)

[24] B. Díaz, J. Światowska, V. Maurice, A. Seyeux, B. Normand, E. Härkönen, M. Ritala, P. Marcus, *Electrochim. Acta*, 56, 10516-10523 (2011)

[25] B. Diaz, E. Harkonen, V. Maurice, J. Swiatowska, A. Seyeux, M. Ritala, P. Marcus, *Electrochim. Acta*, 56, 9609-9618 (2011)

[26] B. Díaz, J. Światowska, V. Maurice, A. Seyeux, E. Härkönen, M. Ritala, S. Tervakangas, J. Kolehmainen, P. Marcus, *Electrochim. Acta*, 90, 232-245 (2013)

[27] B. Díaz, E. Härkönen, J. Światowska, A. Seyeux, V. Maurice, M. Ritala, P. Marcus, *Corros. Sci.*, 56, 208-217 (2014)

[28] S. Mirhashemihaghighi, J. Swiatowska, V. Maurice, A. Seyeux, L.H. Klein, E. Salmi, M. Ritala, P. Marcus, *Electrochim. Acta*, 193, 7-15 (2016)

[29] E. Härkönen, S.E. Potts, W.M.M. Kessels, B. Díaz, A. Seyeux, J. Światowska, V. Maurice, P. Marcus, G. Radnóczi, L. Tóth, M. Kariniemi, J. Niinistö, M. Ritala, *Thin Solid Films*, 534, 384-393 (2013)

[30] E. Härkönen, S. Tervakangas, J. Kolehmainen, B. Díaz, J. Światowska, V. Maurice, A. Seyeux, P.Marcus, M. Fenker, L. Tóth, G. Radnóczi, M. Ritala, *Mater. Chem. Phys.*, 147, 895-907 (2014)

[31] S. Mirhashemihaghighi, J. Światowska, V. Maurice, A. Seyeux, L.H. Klein, E. Härkönen, M. Ritala, and P. Marcus, *J. Electrochem. Soc.,* 162, 31-C384 (2015)

[32] B. Diaz, E. Harkonen, V. Maurice, J. Swiatowska, A. Seyeux, M. Ritala, P. Marcus, *Electrochim. Acta*, 56, 9609-9618 (2011)

[33] S.E. Potts, L. Schmalz, M. Fenker, B. Díaz, J. Światowska, V. Maurice, A. Seyeux, P. Marcus, G. Radnóczi, L. Tóth, W.M.M. Kessels, *J. Electrochem. Soc.*, 158, C132-C138 (2011)

[34] E. Härkönen, M. Ritala, L. Schmalz, M. Fenker, B. Diaz, J. Światowska, B. Normand, V. Maurice, P. Marcus, *J. Electrochem. Soc.,* 216th ECS Meeting, Abstract, 2009

[35] E. Härkönen, I. Kolev, B. Díaz, J. Światowska, V. Maurice, A. Seyeux, P. Marcus, M. Fenker, L. Toth, G. Radnoczi, M. Vehkamäki, and M. Ritala, *ACS Appl. Mater. Interfaces*, 6,1893-1901 (2014)

[36] B.V. Crist, *Handbook of Monochromatic XPS Spectra*, XPS International, CA, 2004

[37] S. Doniach, *Phys. Rev. B*, 2, 3898-3905 (1970)

[38] R.G. Buchheit, R.G. Kelly, N.A. Missert, B.A. Shaw, *Corrosion and Protection of Light Metal Alloys*, The Electrochemical Society INC., Pennington, 2004

[39] S.I. Pyun, S.M. Moon, *J. Solid State Electrochem.*, 4, 267-272 (2000)

[40] J. R. Davis, *Aluminum and Aluminum Alloys*, ASM International, Ohio, 784 (1993)

[41] C. Hinnen, D. Imbert, J.M. Siffre, P. Marcus, *Appl. Surf. Sci*. 78, 219 (1994)

[42] T.J. Sarapatka, *J. Phys. Chem.*, 97, 11274 (1993)

[43] P. Marcus, C. Hinnen, I. Ofefjord, *Surf. Interface Anal.*, 20, 923-929 (1993)

[44] Y.C. Kim, H.H. Park, J.S. Chun, W.J. Lee, *Thin Solid Films*, 237, 57 (1994)

[45] I. Ofefjord, H.J. Mathieu, P. Marcus, *Surf. Interface Anal.*, 15, 681 (1993)

[46] H. He, K. Alberti, T.L. Barr, J. Klinowski, *J. Phys. Chem.*, 97, 13703 (1993)

[47] G. Moretti, G. Fierro, M.L. Jacono, P. Porta, *Surf. Interface Anal.*, 14, 325 (1989)

[48] S.W. Gaarenstroom, N. Winograd, *J. Chem. Phys.*, 67, 3500 (1977)

[49] J.C. Klein, C.P. Li, D.M. Hercules, J.F. Black, *Appl. Spectrosc.*, 38, 729 (1984)

[50] J.P. Espinós, J. Morales, A. Barranco, A. Caballero, J.P. Holgado, and A.R. González-Elipe, *J. Phys. Chem. B*, 106, 6921-6929 (2002)

[51] P. Brand, H. Freiser, *Anal. Chem.*, 46, 1147 (1974)

[52] J.P. Espinós, P. Espinós, J. Morales, A. Barranco, A. Caballero, J.P. Holgado, and A.R. González-Elipe, *J. Phys. Chem. B*, 106, 6921-6929 (2002)

[53] P. Brand and H. Freiser, *Anal. Chem.*, 46, 1147 (1974)

[54] F.M. Capece, V. Di Castro, C. Furlani, G. Mattogno, *J. Electron Spectrosc.,* 27, 119 (1982)

[55] G. Schon, *Surf. Sci.*, 35, 96-108 (1973)

[56] N. Pauly, S. Tougaard, F. Yubero, *Surf. Sci.*, 620, 17-22 (2014)

[57] A.N. Mansour, *Surf. Sci. Spectra*, 3, 202 (1994)

[58] A. Ayame T. Kitagawa, *Bunseki Kagaku*,40, 673 (1991)

[59] S. Moon, S. Pyun, *Corros. Sci.*, 39, 399-408 (1997)

[60] Y. Liu, A.M. Arenas, P. Skeldon, G.E. Thompson, H. Habazaki, K. Shimizu, P. Bailey, T.C.Q. Noakes, *Corros. Sci.*, 48, 1874 (2006)

[61] Y. Liu, M.A. Arenas, S.J. Garcia-Vergara, T. Hashimoto, P. Skeldon, G.E. Thompsoa, H.Habazaki, P. Bailey, T.C.Q. Noakes, *Corros. Sci.*, 50, 1475-1480 (2008)

[62] E. Harkonen, S.E. Potts, W.M.M. Kessels,B.Diaz, J. Swiatowska, V. Maurice, P. Marcus, G. Radnoczi, L. Toth,*Thin Solid Films*, 534, 384-393 (2013)

[63] A. Boag, A.E. Hughes, A.M. Glenn, T.H. Muster, D. McCulloch, *Corros. Sci.*, 53, 17-26 (2011)

[64] G.S. Chen, M. Gao, R.P. Wei, *Corros.*, 52, 8-15 (1996)

[65] J.R. Scully, K.O. Knight, R.G. Bucheit, D.E. Peebles, *Corros. Sci.*, 35, 185 (1993)

[66] G.O. Ilevbare, O. Schneider, R. G. Kelly, and J. R. Scully, *J. Electrochem. Soc.*, 151, B453 (2004)

[67] J.R. Scully, K.O. Knight, R.G. Bucheit, D.E. Peebles, *Corros. Sci.*, 35, 185 (1993)

[68] J.R. Scully, D.E. Peebles, A.D. Romig, D.R. Frear, C.R. Hills, *Metall. Trans. A*, 23A, 1365 (1990)

[69] P. Leblanc, G.S. Frankel, *J. Electrochem Soc.*, 149, B239-B247 (2002)

[70] C.M. Liao, J.M. Olive, M. Gao, R.P. Wei, *Corros.*, 54, 451-458 (1998)

[71] M. Shao, Y. Fu, R. Hu, C. Lin, *Mater. Sci. Eng.*, A344, 323-327 (2003)

[72] A.E. Hughes, A. Boag, A.M. Glenn, D. McCulloch, T.H. Muster, C. Ryan, C. Luo, X. Zhou, G.E. Thompson, *Corros. Sci.*, 53, 27-39 (2011)

Chapter 6 Conclusions and perspectives

In this work, Al-4.87wt.% Cu polycrystalline alloy samples were employed to investigate the **influence of thermal aging treatment** at low oxygen pressure $p=1.0\times10^{-7}$ mbar **on the surface modifications** using surface analytical techniques (*in situ* XPS and ToF-SIMS, **chapter 3**). Then, in **chapter 4**, the Al-Cu samples were prepared by annealing treatment at 540 °C in vacuum ($p=1.0\times10^{-5}$ mbar) to obtain the solid solution, and then aging treatment at 300 °C followed by 450 °C in air to form the Cu-rich intermetallic particles. The **influence of this thermal treatment on the corrosion behaviour of Al-Cu alloy** in the neutral electrolyte ($pH\approx6.2$) and the alkaline electrolyte (pH=11.5) containing aggressive Cl^- ions was investigated. Surface analytical techniques (XPS and ToF-SIMS) were combined with microscopic (SEM and AFM) analytical techniques to explore the corrosion mechanisms of the thermally treated Al-Cu samples with Cu-rich intermetallics in the neutral and alkaline solutions, compared with the non-treated, polished Al-Cu samples. Finally in **chapter 5**, the **corrosion protection of Al-Cu** alloy samples by 20 nm-thick **Al_2O_3 coatings deposited by atomic layer deposition (ALD)** was investigated. The aim of this study was also to assess whether significant improvement on the corrosion resistance could be observed without prior removal of the Cu-rich intermetallic particles usually applied in industry on aluminium alloys before deposition of conversion corrosion protection coatings.

In the first part of this thesis (in **Chapter 3**), surface and depth profile analysis (*in situ* XPS and ToF-SIMS) were used to study thoroughly the influence of thermal aging treatment (from 300 °C to 400 °C) at low oxygen pressure (UHV, $p=1.0\times10^{-7}$ mbar) on the surface modifications of the Al-4.87wt.% Cu alloy, such as the oxide

growth, the chemical modifications at oxide/substrate interface and evolutions of the Cu-rich intermetallic particles. XPS showed that the thickness of aluminium oxides grew thicker as a function of thermal treatments from 300 °C to 400 °C, whereas a concentration of Cu near the surface (at the oxide/substrate interface) first decreased from around 33.1 to 23.6 at.% attributed to low diffusion rate of Cu atoms from the bulk to the surface/interface region at the beginning stage of thermal treatments (from 300 °C to 350 °C), and then during the last stage of heating at higher temperatures (from 350 °C to 400 °C), slightly increased from 23.6 at.% to 26.3 at.%. This increase was attributed to the higher diffusion rate of Cu atoms from bulk of Al-Cu alloy to the interface region (oxide /substrate) at higher temperatures (>350 °C).

Furthermore, the decrease of O1s peak area at the beginning stage of thermal treatments (300 °C) indicated the dehydration and/or decomposition of hydroxide layer (formerly present at the native alumina surface), while a slight decrease of O1s peak area at 400 °C was attributed to the reduction of Cu oxides with CO under high-temperature conditions, or preferential aluminium oxidation and segregation of Cu/Cu oxides at surface defects or at grain boundaries or at oxide/substrate interface region.

In addition, the total area (metal + oxide and hydroxide) of the Al2p spectra was constant over the oxidation, suggesting the limited segregation of Al to the surface, which is in agreement of results on other binary alloy (oxidation of α-brass $Cu_{0.7}Zn_{0.3}$(111)), where no Zn segregation was observed).

ToF-SIMS profiling identified three zones: the oxide surface, the oxide/metal interface and the metal Al-Cu substrate for both non-treated, and thermally treated samples. ToF-SIMS imaging confirmed the existence of Cu-rich intermetallics in the non-treated Al-Cu sample, which grew bigger during the thermal treatment. Moreover, thermal treatments of Al-Cu alloy underwent via the preferential oxidation of Al, resulting in the growth of the aluminum oxide layer, and accumulation/growth of Cu-rich intermetallic at the oxide/metal interfacial region, evidenced by the ToF-SIMS mapping. These ToF-SIMS results are in perfect agreement with the XPS data.

In the second part (**Chapter 4**), the pristine, non-treated and the thermally treated (annealed at 540 °C for 1 h at $p=1.0\times10^{-5}$ mbar and aged at 300 °C for 10 h followed by 450 °C for 5 min in air) Al-4.87wt.% Cu samples, were exposed to immersion tests in the neutral electrolyte (pH=6.2) and the alkaline electrolyte (pH=11.5) containing aggressive Cl^- ions using the three-electrode system. SEM and ToF-SIMS confirmed the formation of much bigger Cu-rich intermetallic particles due to thermal treatment (sizes ranging 1-5 μm for non-treated samples and sizes of 5-20 μm for thermally treated samples). XPS indicated a slight increase of Al oxide thickness (from 7 nm to 8 nm), as well as the presence of the oxidized Cu after thermal treatments.

The nobler OCPs (around dozens mV higher), obtained for the thermally treated samples during immersion in both neutral and alkaline electrolytes was attributed to the Cu-enrichment. More significant OCP increase (higher slope) observed in alkaline electrolytes for both polished and thermally treated samples was attributed to faster general dissolution of Al oxide and Al matrix under high pH conditions resulting in the remarkable enrichment of Cu on the surface.

After immersion in neutral electrolytes for 7 minutes, a severe pitting corrosion was observed on the non-treated sample in the vicinity of the cathodic Cu-rich particles with respect to the anodic Al substrate, whereas hollow pits presenting the initiation sites for the localized corrosion (proving by the locally thinner oxide above the big-size Cu-rich particles in the thermally treated sample) were evidenced in the case of thermally treated sample. On the corroded surface of Al-Cu alloys the formation of mixed layers composed of aluminium-copper oxides and hydroxides rich in Cu_2O and CuO were verified by the XPS analysis.

In the case of alkaline immersion, the general dissolution of Al oxide and Al-Cu alloy matrix was observed. The thermal treatment applied to the Al-Cu alloy had important influence on corrosion mechanisms. For the non-thermally treated alloy the dissolution resulted in protruding the Cu-rich particles (immersion duration= 37 min), whereas for the thermally treated sample (immersion duration= 7 min), the general dissolution of Al oxide and Al-Cu matrix led to the etching at grain boundaries, where

Cu-rich intermetallics were accumulated. However, for both samples the clear surface copper enrichment was observed. XPS reported significant surface modifications on the non-treated sample: formation of a mixed aluminium-copper oxide and hydroxide layer rich in Cu_2O, CuO, and $CuCl_2$ deposits. Nevertheless, $CuCl_2$ deposit was not detected by the XPS in the corrosion products on the thermally treated sample after attack in the alkaline electrolyte.

The last part of this thesis (**Chapter 5**), the corrosion protection of model Al-4.87wt.% Cu alloy by 20-nm-thick Al_2O_3 coatings deposited by atomic layer deposition (ALD) was studied. The alloy/ALD samples were corroded in the neutral electrolyte (pH=6.2), and in the alkaline electrolyte (pH=11.5) containing aggressive Cl^- ions.

The AFM and ToF-SIMS analyses of pristine, coated alloys showed the formation of a complete and homogeneous 20-nm-thick Al_2O_3 coating deposited from trimethyl aluminium ($Al(CH_3)_3$, TMA) and H_2O on the surface of the Al-Cu alloy, beneath which small Cu-rich particles were presented. The immersion tests showed lower OCPs from the ALD coated Al-Cu alloy in the alkaline electrolyte (around -0.68 V *vs.* Ag/AgCl) than that in the neutral electrolyte (around -0.52 V *vs.* Ag/AgCl), confirming higher corrosion susceptibility of coated Al-Cu alloys at high pH. However, in the alkaline electrolytes the much higher OCP observed for the ALD coated sample (around -0.68 V *vs.* Ag/AgCl) than that of the non-coated sample (around -1.34 to -1.24 V *vs.* Ag/AgCl) means lower corrosion susceptibility of Al-Cu alloys at high pH beneficial to the protection of ALD alumina film.

After immersion in the neutral solution containing Cl^- ion for 7 minutes, a severe pitting corrosion was observed on the non-coated Al-Cu samples well known trenching around the Cu-rich particles (as already observed in a previous chapter), whereas in the same electrolyte after (15+30)-minute-immersion, no significant corrosion was observed on the ALD coated samples suggesting the corrosion resistance of alumina ALD layer on the Al-Cu alloy, without prior removal of the Cu-

rich particles. These particles remained intact, without any significant corrosion signs observed by SEM and ToF-SIMS imaging.

However, general corrosion was observed on the surface of the non-coated Al-Cu alloy in the alkaline electrolytes containing Cl^- after (7+30)-minute-immersion. XPS results revealed significant preferential dissolution of Al matrix and surface enrichment of Cu (as also underlined in previous chapter). The ALD alumina layer showed degradation (dissolution of the ALD layer in depth and along the cracks/pinholes) induced by immersion of the alumina in the alkaline electrolyte even though the Al-Cu substrate remained relatively well preserved. For longer time of immersion, the presence of Cu-rich particles at the oxide/substrate interface may provide initial sites for the localized corrosion, leading to preferential dissolution of the substrate in the vicinity of Cu-rich IMPs like the case observed on the non-coated Al-Cu samples.

The systematic studies have demonstrated the negative effects of Cu-rich intermetallics on the corrosion resistance of the Al-4.87wt.% Cu alloy in the aggressive environments, no matter with or without thermal treatments. However, these studies demonstrate that the formation of a good quality alumina layer deposited by ALD on the Al-4.87wt.% Cu alloy is beneficial for its corrosion resistance, without prior removal of the intermetallic particles.

New several perspectives can be proposed for future work:

i. The study on surface modifications and corrosion mechanisms of commercial Al-Cu alloys, *e. g.* aluminium AA 2024 alloy, employed with surface analytical techniques (XPS, ToF-SIMS) combined with microscopic (SEM, AFM) analytical techniques. The surface characterization should be combined with a thorough electrochemical investigation on the corrosion assess using diversified electrochemical techniques, such as cyclic voltammetry (CV), Electrochemical Impedance Spectroscopy (EIS) and also application of local

electrochemical techniques could be interesting. For a better understanding the corrosion mechanisms the model Al-Cu alloy could be also used (like this applied in this thesis) by means of classical electrochemical methods and local electrochemical techniques.

The material of interest copper-rich aluminium alloys (AA2xxx) are widely used in aerospace industry. These alloys contain alloying elements such as Cu, Fe or Mg. These alloying elements are necessary to improve the mechanical properties of these alloys by precipitation of the intermetallic phases (IMP) as discussed in the bibliographic chapter. The presence of some intermetallic particles can result in a loss of corrosion resistance of the aluminium alloys because the electrochemical behaviour of IMP is different than the aluminium matrix: they can be either cathodic (like Al_2Cu, Al_7Cu_2Fe *etc*.) or anodic (Al_2CuMg, $MgZn_2$, Mg_2Si) with respect to the surrounding aluminium matrix. Moreover, the behaviour of the particle can change from anodic to cathodic during the interaction with the electrolytes because of selective dissolution of the most active element from the intermetallic (e.g. Mg from Al_2CuMg phase). Different surface pre-treatments are applied to these alloys, *i.e.*: alkaline degreasing in order to remove organic contaminations but also some part of the native oxides from the surface and acid desmutting (deoxidizing) process in an aggressive acid bath for removing the IMP near the surface and the rest of the native oxide layer. The influence of these pre-treatments on the surface state of the aluminium alloys and their corrosion properties are still not well understood.

ii. *In situ* thermal treatments and ageing of Al-Cu model alloy and its influence on chemical composition and corrosion resistance in new surface analysis platform available in the PCS group. This platform is equipped with the following principal parts: surface preparation by ion sputtering, annealing,

deposition, or exposition to gaseous phases, surface characterisation by XPS, UPS, LEED, STM, with possibility of analysis at different temperature or exposition to different gas pressure (UHV or near ambient pressure), surface treatments in liquid phase (classical electrochemical methods) or surface analysis at atmospheric pressure (SPM *ex* or *in situ* electrochemical methods: AFM, STM) in glove box.

A model, pure Al-Cu alloy, which can be poly- or single crystalline (with Cu of around 4-5 wt.% similar to AA2024) with well-prepared surface (mechanically and electrochemically polished) should be used. Thermal treatment at different temperatures ranging from 200°C to 450°C can be applied to follow the *in situ* the chemical modifications by XPS and Auger analyses and the nano-crystalline modifications can be followed by *in situ* STM or AFM studies.

The main objectives of these studies would be:

- To investigate the influence of thermal treatment on the chemical modifications as a function of temperature and oxygen pressure of Al-Cu alloy.
- To investigate the mechanisms of formation of the intermetallic particles Al2Cu.
- To investigate the kinetics of the oxide growth.
- To follow the structural modification at the nanometric and the atomic level (for the single-crystalline samples).
- To study the surface hydroxylation as a function of the thermal treatments (presence of oxides, the oxide thickness, presence of intermetallic particles).
- To study the material ageing at defined conditions (i.e. influence of the thermal ageing on the stability of the intermetallic particles and the stability and properties of the oxide layer).

iii. The new ways of corrosion protection of aluminium alloys. Development of new ways of corrosion protection is also governed by new European REACH and RoHS restrictions (described above) aiming at application of environmentally friendly products. Very good from corrosion point of view chromium-based coatings (containing Cr(VI)) characterized by self-healing properties must be completely removed from industrial applications and replaced by new coatings by 2017. This is a big challenge not only for industry but also for research because many aspects related to corrosion protection by Cr(VI)-free systems are far from being efficient in terms of corrosion protection in order to meet the high aeronautic and the automotive industry standards.

The application of very thin, nanometer-thick protective coatings by ALD method is a new and very interesting domain (developed in a frame of the Corral project since 2008 in the PCS group and presented also in this manuscript in chapter 5). These types of coatings can be bi- or even multi-functional and apart their good corrosion resistant properties they can be applied also as decorative layers, sub- or top-coatings. One of the perspective would be develop a new chemically stable thin ALD layers as already mentioned in the last chapter 5 of this thesis. The dissolution of alumina layers can be blocked by a deposition of titanium or tantalum oxide layers. The ALD technology allows also for the coating developments not only with a different chemistry but also with a different architecture: nanolaminate coatings or mixture coatings (which corrosion efficiency was also studied on steel substrates in the PCS group). Thus, the application of this method of corrosion protection can be a new and nice alternative for all chemically deposited conversion layers.

Abbreviations and acronyms

AA	Aluminium alloy(s)
AFM	Atomic force microscopy
ALD	Atomic layer deposition
a.u.	Arbitrary unit
BE	Binding energy
CCC	Chromium conversion coating
EDX	Energy dispersive x-ray spectroscopy
ESCA	Electron spectroscopy for chemical analysis
exp	exponential function
FE-SEM	Field emission scanning electron microscope
FWHM	Full width at half maximum
IMP or IMPs	Intermetallic particles
LP	Low pressure
KE	Kinetic energy
OCP	Open circuit potential
RMS	Root mean square
SCE	Saturated calomel electrode
SEM	Scanning electron microscopy
ToF-SIMS	Time-of-flight secondary ion mass spectrometry
TCP	Trivalent chromium processes
UHV	ultra-high vacuum
VB	Valence band
XPS	X-ray photoelectron spectroscopy

Acknowledgements

I would like to express my sincere gratitude to:

First and foremost, my supervisors, Prof. Dr. Philippe Marcus, and Dr. Jolanta Światowska for accepting me as a PhD student in your group, and for your guidance, encouragement, support and excellent inspiration;

My co-authors, Dr. Sandrine Zanna, Pascal David, Dr. Antoine Seyeux, Dr. Lorena H. Klein, for your guidance, sharing your knowledge, inspiring discussions and fruitful collaborations;

The secretaries, Sylvie Gandziarski, Marie-Jose Michel for your helps with the administrative matters;

All the present and former members in Equipe de Physico-Chimie des Surfaces at Institut de Recherche de Chimie Paris, CNRS - Chimie ParisTech, Bingbing, Hao, Remi, Anne-ilham, Hu, Mohamed, Emna, Shadi, Marion, Zuzana, Elise, Mari, Qi, Toni, Feng, Elie, Catarina, Mathieu, Thomas, Blanca, … for sharing the good times and happy hours in Paris;

The Chinese Scholarship Council (CSC) for the financial support;

Finally, my family, for your selflessness and understanding; without your love and support, I may not be able to earn this degree.

Jun TAO
Campus Pierre et Marie Curie
04/2016

Surface composition and corrosion behavior of an Al-Cu alloy

Al-Cu alloys are the most widely used heat treatable alloy for the aircraft materials, machine parts, and structural materials mainly due to their high strength to weight ratio and good mechanical properties. However, the Cu-rich precipitations (Al_2Cu intermetallic particles present as the most important strengthening phase), have negative effects on the corrosion performances of them. In this thesis, Al-Cu model alloy was employed to investigate the influence of thermal aging treatments in ultra-high vacuum (UHV) on the chemical modifications of the alloy using surface analytical techniques (XPS, ToF-SIMS). *In situ* XPS and ToF-SIMS characterizations showed that thermal treatments of Al-Cu alloy underwent via the preferential oxidation of Al, resulting in the growth of the aluminum oxide layer, and accumulation/growth of Cu-rich intermetallic at the oxide/metal interfacial region. Then, in a next chapter, the Al-Cu alloy samples thermally treated in a dedicated setup (at 540 °C in vacuum (1.0×10^{-5} mbar) and aged at 300 °C in air) were exposed to the neutral (pH≈6.2) and the alkaline electrolyte (pH=11.5) containing Cl^- ions. After immersion the surface characterization indicated different corrosion mechanisms influenced by aging. In neutral electrolyte trenching on the polished sample *vs*. hollow pits on the aged sample were observed due to formation of defects as initiation sites of the corrosion in the vicinity of the intermetallic particles (at the oxide/substrate interface) covered by a thick oxide layer. However, in alkaline electrolytes, corrosion of the polished and aged samples showed the general dissolution of aluminium matrix, which resulted in a formation of protruded Cu-rich intermetallics. Then, in the next stages after general corrosion, the preferential dissolution of matrix surrounding Cu-rich intermetallics occurred. However, grain boundaries of aged samples were also etched because of the matrix distribution at the grain boundaries, which was not observed on the corroded surface of polished samples. Formation of mixed aluminium-copper oxide/hydroxide layers rich in Cu_2O, CuO and/or $CuCl_2$ deposits were found by XPS on the corroded surface. The last part of the thesis presents the corrosion protection of the Al-Cu alloy by nanometer-thick (20 nm) Al_2O_3 ALD layer (atomic layer deposition). This study was performed to confirm whether significant improvement of corrosion resistance of Al alloys can be observed without a prior removal of intermetallic particles. Immersion of the alumina coated Al-Cu alloy in neutral electrolytes containing Cl^- ions showed good corrosion resistance, while lots of pits were observed by SEM on the Al-Cu sample after immersion in alkaline electrolytes although no chemical surface modifications were observed by XPS. It was indicated that the OH^- promoted the corrosion, by enlarging the cracks/pinholes and dissolving the ALD layer by decreasing its thickness and increasing its porosity.

Keywords: Al-Cu alloy; corrosion; intermetallic particles; thermal treatment; ALD film; XPS; ToF-SIMS; SEM; OCP;

Jun TAO

Institut de Recherche de Chimie Paris, CNRS – Chimie ParisTech (UMR 8247),
11 rue Pierre et Marie Curie, 75005 Paris, France